Mondragon Unibertsitatea

DOCTORAL THESIS

EFFECT OF INDEPENDENTLY CONTROLLED CLAMPING LOADS ON TOROIDAL TYPE CONTINUOUSLY VARIABLE TRANSMISSIONS CONSIDERING THE INFLUENCE OF CONTACT SCALE AND SPINNING

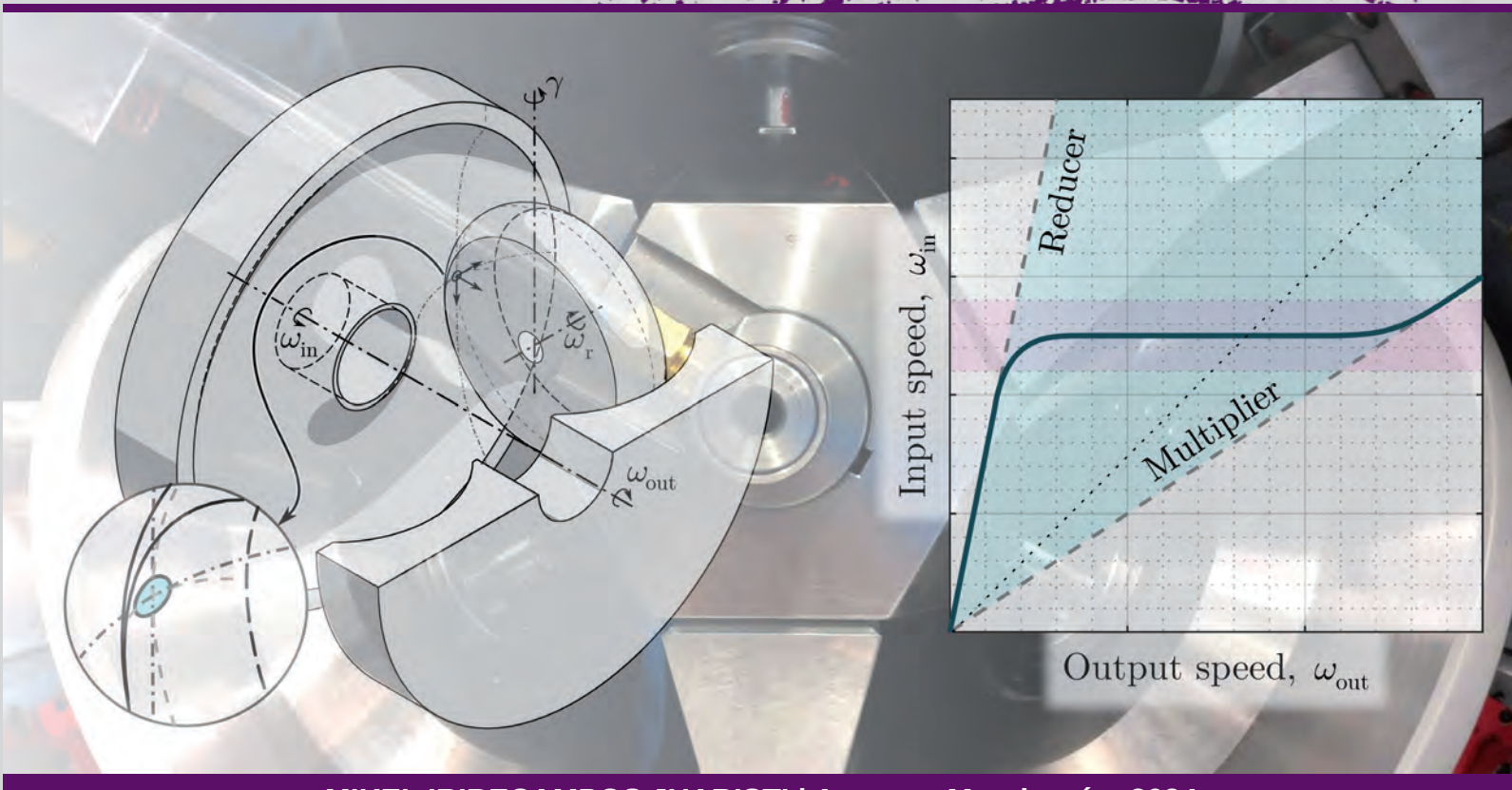

MIKEL IRIBECAMPOS JUARISTI | Arrasate-Mondragón, 2024

Mondragon Unibertsitatea
Goi Eskola Politeknikoa

Effect of independently controlled clamping loads on Toroidal type Continuously Variable Transmissions considering the influence of contact scale and spinning

Author:
Mikel Iribecampos Juaristi

Supervisors:
Dr. Jon Larrañaga Amilibia
Dr. Aitor Arana Ostolaza

Structural Mechanics and Design Research Group
Mechanics and Industrial Production Department
Mondragon Goi Eskola Politeknikoa - Mondragon Unibertsitatea

A Thesis submitted in partial fulfilment of the requirements for the degree of Doctor of Philosophy in Engineering

January 2024

“Puntu eta koma izan nahi nuke, nola egin dakienak bakarrik erabil nazan. Geldi dadin, baina ez betiko;”
Oihana Arana

Bidelagun izan zaretenoi,
maitasunez

ABSTRACT

To increase the energy efficiency of a system, Continuously Variable Transmissions (CVTs) enable to steadily adapt its transmission ratio in a smooth manner. Among the different existing mechanisms, Toroidal type CVTs (T-CVTs) consist of input and output discs conforming a toroidal-shaped cavity with rollers positioned in between where torque transmission occurs across two contact points: one, between the input disc and the rollers, and the other one, between the rollers and the output disc. For effective power transmission through these contact points, high normal loads are required to increase lubricated traction and to this aim, clamping devices are employed. Despite the differences in geometry and kinematic behaviour of each point, historically both contacts have been subject to equal loads; thus, differences may be expected when loads are adapted to local conditions. Therefore, the main objective of this thesis is to predict and evaluate the efficiency of T-CVTs by independently controlling the clamping loads at the input and the output contact points.

In these transmissions requiring high traction, the occurrence of large-scale interfaces and spinning motion tends to decrease traction. However, the combined impact of these phenomena has not been thoroughly studied. That is why a semi-analytical model to predict traction coefficient at the disc-roller contact points was developed. Results reveal that the traction coefficient increases under low-scale and low-spin velocities, which depicts a favourable scenario for torque transmission.

Moreover, a global analytical model to predict traction equilibrium and efficiency of full T-CVTs has been developed, considering independently controlled clamping loads at each contact point. Results indicate that the efficiency of this transmission decreases under, both, low and high longitudinal sliding conditions. Indeed, clamping loads influence the longitudinal sliding in the contact points while it has been observed that each point behaves differently due to scale effects.

Finally, a T-CVT prototype was designed to validate the proposed models and to measure experimentally the efficiency and longitudinal sliding under variable working conditions; achieving very similar trends to those obtained by previous analytical models. The main innovation of the prototype involves independent control of the input and the output clamping loads. In this way, under low torque conditions, the lowest tested clamping load achieved the highest efficiency, albeit with a lower maximum transmissible torque. Experimental measurements reveal that the input clamping load affects the efficiency of the output point. In other words, overclamping the input point, increases power losses, reducing the energy reaching to the output point. Finally, it is concluded that the transmission efficiency experiences an improvement when the clamping forces are independently controlled in contrast with current equal clamping force control methods.

LABURPENA

Sistema baten efizientzia energetikoa handitzeko, transmisio aldakor jarraiek (CVT) beren transmisio erlazioa etengabe leuntasunez egokitzea ahalbidetzen dute. Dauden mekanismoen artean, toroidal motako CVTak (T-CVT) sarrerako eta irteerako diskoek, eta horien artean sortzen den barrunbe toroidalean dauden arrabolek osatzen dute, non momentuaren transmisioa bi ukitze punturen bidez gertatzen den: bata, sarrerako diskoaren eta arrabolen artekoa, eta bestea, arrabolen eta irteerako diskoaren artekoa. Ukitze puntuetan potentziaren transmisioa eraginkorra izan dadin indar normal altuak behar dira lubrifikatutako trakzioa (marruskadura) handitzeko, horretarako estutze gailuak erabiltzen dira. Puntu bakoitzaren geometrian eta portaera zinematikoan ezberdintasunak egon arren, gaur arte bi ukitze puntuetan indar normal berdina kontsideratu izan ohi da; nolanahi dela ere, desberdintasunak espero daitezke kargak baldintza lokaletara egokitzen direnean. Beraz, tesi honen helburu nagusia T-CVTen efizientzia iragarri eta ebaluatzea da, sarrerako eta irteerako ukitze puntuetan esku hartzen duten estutze indarrak modu independentean kontrolatuz.

Trakzio handia behar duten transmisio horietan, eskala handiko gainazalek eta *spin* mugimenduak trakzioa murrizteko joera dute. Hala ere, bi fenomeno horien efektu konbinatua ez da sakon aztertu. Horregatik, eredu erdianalitiko bat garatu da, disko eta arrabolen arteko ukitze puntuetako trakzio koefizientea iragartzeko. Emaitzek erakusten dutenez, trakzio koefizientea kontaktuko tamaina baxutan eta *spin* abiadura txikian handitzen da, momentua transmititzeko egokia izanik.

Gainera, T-CVTen trakzio oreka eta efizientzia aurreikusteko eredu analitiko global bat garatu da, eta ukitze puntu bakoitzeko estutze kargak modu independentean kontrolatu dira. Emaitzek adierazten dute transmisio horren efizientzia murriztu egiten dela, bai irristadura longitudinal baxu, zein altuko baldintzetan; estutze kargek ukitze puntuetako irristaduran eragiten dutelarik. Aldiz, ikusi da puntu bakoitzak modu desberdinean jokatzen duela eskala efektuen ondorioz.

Azkenik, T-CVT prototipo bat diseinatu da proposatutako ereduak balioztatzeko eta lan-baldintza ezberdinetan efizientzia eta irristadura longitudinala esperimentalki neurtzeko. Gainera ereduetatik lortutako joera oso antzekoak lortu dira. Prototipoaren berrikuntza nagusia da, sarrerako eta irteerako estutze indarrak modu independentean kontrolatzea. Ikusi da, momentu baxuko baldintzetan, entseatutako estutze karga txikienarekin efizientzia handiena lortu dela, nahiz eta transmititu daitekeen gehieneko momentua txikiagoa izan. Neurketa esperimentalen arabera, sarrerako estutze kargak irteerako puntuaren portaerari eragiten dio. Beste era batera esanda, sarrerako puntuaren gehiegizko estutzeak potentzia galerak areagotzen ditu, irteerako puntura iristen den energia murrizten delarik. Azkenik, ondorioztatu da transmisioaren eraginkortasuna hobetu egiten dela estutze indarrak modu independentean kontrolatzen direnean, estutze indar berdinak kontrolatzeko egungo metodoekin alderatuta.

RESUMEN

Para aumentar la eficiencia energética de un sistema, las transmisiones variables continuas (CVT) permiten adaptar constantemente su relación de transmisión de forma suave. Entre los distintos mecanismos existentes, las CVT de tipo toroidal (T-CVT) constan de discos de entrada y salida que conforman una cavidad de forma toroidal donde se sitúan los rodillos, la transmisión de par se produce a través de dos puntos de contacto: uno, entre el disco de entrada y los rodillos, y otro, entre los rodillos y el disco de salida. Para que la transmisión de potencia a través de estos puntos de contacto sea eficaz, se requieren cargas normales elevadas para aumentar la tracción (fricción) lubricada, y para ello se emplean dispositivos de apriete. A pesar de las diferencias en la geometría y el comportamiento cinemático de cada punto, históricamente ambos contactos han estado sometidos a cargas normales iguales, por lo que cabe esperar diferencias cuando las cargas se adaptan a las condiciones locales. Por lo tanto, el objetivo principal de esta tesis es predecir y evaluar la eficiencia de las T-CVT controlando de forma independiente las cargas de apriete en los puntos de contacto de entrada y salida.

En estas transmisiones donde se requiere una gran fuerza de tracción, la aparición de interfaces a gran escala y el movimiento de *spin* tienden a disminuir la tracción. Sin embargo, el impacto combinado de estos fenómenos no se ha estudiado a fondo. Por ello, se ha desarrollado un modelo semianalítico para predecir el coeficiente de tracción en los puntos de contacto disco-rodillo. Los resultados revelan que el coeficiente de tracción aumenta a superficies de contacto pequeñas y baja velocidad de *spin*, lo cual representa un escenario favorable para la transmisión de par.

Además, se ha desarrollado un modelo analítico global para predecir el equilibrio de tracción y la eficiencia de las T-CVT, considerando cargas de apriete controladas independientemente en cada punto de contacto. Los resultados indican que la eficiencia de esta transmisión disminuye tanto en condiciones de deslizamiento longitudinal bajo como alto; de hecho, las cargas de apriete influyen en el deslizamiento longitudinal de los puntos de contacto. Asimismo, se ha observado que cada punto se comporta de forma diferente debido a los efectos de escala.

Finalmente, se ha diseñado un prototipo de T-CVT para validar los modelos propuestos y medir experimentalmente la eficiencia y el deslizamiento longitudinal bajo diferentes condiciones de trabajo. Consiguiendo tendencias muy similares a las obtenidas por los modelos previos. La principal innovación del prototipo consiste en el control independiente de las cargas de apriete de entrada y de salida. Se ha visto que en condiciones de par bajo, la mayor eficiencia se ha alcanzado mediante la carga de apriete menor ensayada, aunque con un par máximo transmisible inferior. Las mediciones experimentales revelan que la carga de apriete de entrada afecta a la eficiencia del punto de salida. En otras palabras, un apriete excesivo del punto de entrada aumenta las pérdidas de potencia, reduciendo la energía que llega al punto de salida. Finalmente, se concluye que la eficiencia de la transmisión experimenta una mejora cuando las fuerzas de apriete se controlan independientemente, en comparación con los métodos actuales de control de fuerzas de apriete iguales.

ACKNOWLEDGEMENTS

First of all, I would like to express my greatest gratitude and appreciation to my supervisors Jon Larrañaga Amilibia and Aitor Arana Ostolaza as well as to Ibai Ulacia Garmendia for the implication and support in the project. I would also like to acknowledge the support received from Eñaut Errazkin, Julen Maskariano, Pello Alberdi, Fermin Estanga, Aratz Iturgaitz and Eneko Ariztegi for their work designing, assembling and testing the developed CVT prototype. My sincere thanks also go to Patricia, for responding resolutely procedures that we have rushed to the last minute, while she has other responsibilities.

This research work is funded by CIRMET project, which has received funding from the European Union's Horizon 2020 research and innovation programme under grant agreement No 820670. For this reason, I would like to thank the opportunity they gave me to carry out this research project. In addition, I would also like to acknowledge the work performed to the members of the project, Iker Cuñado and Gorka Urchegui from MSI for the support on the control cabinet of the CVT and data acquisition and Mattia Baraldi from ARC for the developed torque meters. I would also like to thank Javier Calviño from Enerbasque and Mikel Merchan and Pablo Casado from Tecnalia for the work performed in the European project and the time we have expended together during these years.

Doktoregaien gelan topatu garen danoi be eskertzia gustauko jaten, elkarrekin ein dogun harremana lankide izatetik baino gehixau izatera heldu dalako. Eskerrik asko Eli eta Ibarretxe, etxian hartu ninduzutelako, baitxa luze eta sendo hitz egin izan dogun egun horreingatik, horiek barik ez zan berdina izango. Baitxa buleguan koinzidirutako gainontzeko doktoregai danei: Abedul, Nora, Eneritz, Ane, Sergio, Laura, Xuban, Asier, Agirre, Mikel, David, Aurea, Ainara, David, Ander, Pello, Jonro, Eli, Imanol, Arjun, Antton, Gurutz, Julen eta Ainhoari.

Bukatzeko, urte hauetan eskolatik kanpo bidelagun izan zaretenoi ezin zaitxuztet ahaztu. Rosa, azken urtian tesitura honi frente eitxeko emandako laguntzagatik, eskerrik asko! Baitxa lan orduetatik kanpo nire kontakizunak estoikoki entzun doztazuenoi: Bizarñoñiko eta ostiraletako lagunei, momentuengatik, eskerrik asko! Bide batez, eskerrik beruenak familixari ematia gustauko jaten: amari, aitari, Joneri, Igorri eta baitxa berriki heldu dan Mareni be. Zuek barik ez nauke honi aurre eitxeko indarrik aukiko ta, zorretan nau zuekin.

Eskerrik asko!

DECLARATION OF ORIGINALITY

I hereby declare that this dissertation and the work described in it are the product of my own work and that, to the best of my knowledge, it contains no previously published material except where due acknowledgement has been made in the text as noted by citations. This PhD thesis has not been submitted for any other degree or diploma of Mondragon Unibertsitatea or other institute of higher education. The copyright of this document including data, figures, tables and text rests with the author and all the assistance received in preparing it have been acknowledged. Researchers are free to copy, distribute or transmit the thesis on the condition that they attribute it properly, that they do not use it for commercial purposes and that they do not alter, transform or build upon it.

Mikel Iribecampos Juaristi
Arrasate, January 2024

CONTENTS

LIST OF FIGURES

LIST OF TABLES

LIST OF SYMBOLS

a	mm	Contact ellipse semimajor axis
b	mm	Contact ellipse semiminor axis
b_1	GPa^{-1}	Yasutomi parameter
b_2	(-)	Yasutomi parameter
c	J/kgK	Heat capacity
e	mm	Toroidal minimum radius
h	mm	Film thickness
h_c	mm	Central film thickness
h_m	mm	Minimum film thickness
i	(-)	Transmission ratio
i_ideal	(-)	Ideal transmission ratio
i_real	(-)	Real transmission ratio
k	(-)	Toroid aspect ratio
k_c	1/m	Torque clamping load ratio
k_e	(-)	Ellipticity parameter
m_r	(-)	Number of toroidal cavities
n_r	(-)	Number of rollers
n	(-)	Carreau shear thinning power law exponent
p	MPa	Pressure
p_H	MPa	Hertzian pressure
$\dot{q}$	$\mathrm{W/m}^2$	Heat generation rate
r	mm	Radius
r_0	mm	Toroidal curvature radius
r_r	mm	Roller curvature radius
r_d	mm	Disc radius
r_b	mm	Ball radius
u_e	mm/s	Entrainment speed
u_b	mm/s	Speed of the ball
u_d	mm/s	Speed of the disc
u_r	mm/s	Speed of the roller
v	m/s	Speed
v_s	m/s	Sliding speed
A_H	mm^2	Hertzian contact area
A_1	°C	Yasutomi parameter
A_2	GPa^{-1}	Yasutomi parameter

Br	(-)	Brinkman number
C_1	(-)	Yasutomi parameter
C_2	°C	Yasutomi parameter
C_f	(-)	Experimental torque correction factor
C_T	(-)	Film thickness reduction factor due to shear heating
C_ST	(-)	Film thickness reduction factor due to shear thinning
C_sp	(-)	Film thickness reduction factor due to spin motion
C_m	(-)	Torque coefficient of churning losses
Cr	(-)	Creep (sliding) coefficient
CR	(-)	Conformity ratio
E	Pa	Solid elastic modulus
$E*$	Pa	Effective elastic modulus
E_{ff}	(-)	Efficiency
F	N	Force
F'	N	Dimensionless relative thermal expansivity of the free volume
F_c	N	Clamping force
F_c0	N	Initial preload
F_n	N	Normal load
F_t	N	Traction force
F_r	N	Force reaction on the roller
G	(-)	Dimensionless material parameter
G_S	Pa	Lubricant shear coefficient
H	(-)	Dimensionless film thickness
K	W/mK	Thermal conductivity
L	(-)	Moes dimensionless parameter
M	(-)	Moes dimensionless parameter
N	RPM	Rotational speed in revolutions per minute
Pe	(-)	Peclet number
P	W	Power
P_in	W	Input power
P_out	W	Output power
P_CL	W	Contact power loss
P_D	W	Disc power loss
P_R	W	Roller power loss
P_LS	W	Longitudinal sliding power loss
P_SP	W	Spinning power loss
R	mm	Curvature radius
Re	(-)	Reynolds number
R_e	mm	Effective curvature radius
R_x	mm	Curvature radius in x-direction

R_y	mm	Curvature radius in y-direction
R_fl	$\mathrm{m^2K/W}$	Thermal resistance for flash temperature rise
R_f	$\mathrm{m^2K/W}$	Thermal resistance for fluid heating
S_p	(-)	Dimensionless spin ratio
SRR	(-)	Slide to roll ratio
SRR_in	(-)	Slide to roll ratio of the input point of the T-CVT
SRR_out	(-)	Slide to roll ratio of the output point of the T-CVT
SRR_global	(-)	Slide to roll ratio of the entire T-CVT
T	Nm	Torque
T_s	Nm	Spinning torque
T_l	Nm	Loading torque
T_be	Nm	Bearing frictional torque
T_rr	Nm	Rolling frictional torque
T_sl	Nm	Sliding frictional torque
T_drag	Nm	Drag loss torque
T_ch	Nm	Churning torque
U	(-)	Dimensionless speed parameter
V	$\mathrm{m^3}$	Volume
W	(-)	Dimensionless load parameter
Ws	(-)	Weissenberg number
O	(-)	Contact interface centre
P	(-)	Spin pole position
Q	(-)	A point inside the Hertzian contact interface
α	$\mathrm{GPa^{-1}}$	Pressure-viscosity coefficient
α_0	$\mathrm{GPa^{-1}}$	Conventional pressure-viscosity coefficient
$\alpha*$	$\mathrm{GPa^{-1}}$	Reciprocal asymptotic isoviscous pressure-viscosity coefficient
α_B	$\mathrm{GPa^{-1}}$	Secant pressure-viscosity coefficient
α_Θ	(-)	Heat partitioning
β	°	Tilting angle of the rotation axis of the ball
β_K	$\mathrm{°C^{-1}}$	Temperature coefficient (viscosity index)
Γ	°	Elliptical integral
γ	°	Roller tilting angle
$\dot{\gamma}$	1/s	Shear strain rate
δ	mm	Elastic deflection due to normal loads
ε	(-)	Simplified elliptic integral
η	Pa s	Viscosity
η_0	Pa s	Viscosity ($\Theta = 40$°C)
η_g	Pa s	Low shear viscosity at glass transition
η_L	Pa s	Low shear viscosity
η_G	Pa s	Generalized viscosity

θ	°	T-CVT roller angle
Θ	°C	Temperature
Θ_0	°C	Supply temperature
Θ_{g0}	°C	Temperature at glass transition
κ	W/(mK)	Thermal conductivity
λ	(-)	Film thickness ratio (lubrication regime)
Λ	(-)	Pressure - Limiting shear stress coefficient
μ	(-)	Traction coefficient
ν	(-)	Poisson's ratio
ν_{visc}	m^2/s	Kinematic viscosity
ρ	kg/m^3	Density
σ	(-)	Spin ratio
σ_q	µm & nm	Root mean square surface roughness
τ	Pa	Shear stress
τ_{L0}	GPa	initial Limiting Shear Stress
τ_{LSS}	GPa	Limiting Shear Stress
φ	°	Sliding vector angle with respect to rolling direction
χ	m^2/s	Thermal diffusivity
ω	rad/s	Angular speed
ω_{in}	rad/s	Input angular speed
ω_{out}	rad/s	Output angular speed
ω_r	rad/s	Roller angular speed
ω_d	rad/s	Disc angular speed
ω_b	rad/s	Ball angular speed
ω_s	rad/s	Spinning angular speed

LIST OF ACRONYMS

BCH	S50 base oil [1,1-(1,1,3-trimethyl-1,3-propanediyl)bis-cyclohexane]
CIRMET	Acronym of the H2020 project
CMM	Coordinate Measuring Machine
CVT	Continuously Variable Transmission
EHL	Elasto Hydrodynamic Lubrication
FBD	Free Body Diagram
MGEP	Mondragon Goi Eskola Politeknikoa (faculty of engineering)
MTM	Mini Traction Machine (ball on disc tribometer)
ORC	Organic Rankine Cycle
RCF	Rolling Contact Fatigue
RECUWASTE	Acronym of CIRMET project Waste Heat Recovery System
S50	Santotrac 50 lubricant
T9	Shell Turbo 9 lubricant
T-CVT	Toroidal type Continuously Variable Transmission
WHRS	Waste Heat Recovery System

1 INTRODUCTION

"Ideiek euria bezala etorri behar dute, ez trumoiak eta ekaitza bezala"
"Ideas should come like rain, not like thunder and storm"
Joxe Azurmendi

1.1 MOTIVATION

Continuously Variable Transmissions (T-CVTs) are mechanisms were transmission ratio can be adapted continuously within a range in order to work in the most efficient condition of a system [1]. Toroidal type CVTs (T-CVTs) are based on an input disc, an output disc and a number of power rollers placed in a toroidal cavity between both discs as represented in Figure 1.1a. The rollers are the responsible to transmit the energy from the input disc to the output one and the transmission ratio shifting is made changing the tilting angle of the rollers, γ angle (see Figure 1.1b). This capability enables to adapt the transmission ratio to the optimum working condition (maximum efficiency) of a system, thus, decreasing the power losses which is an important environmental concern to reduce the excessive energy waste of recent years.

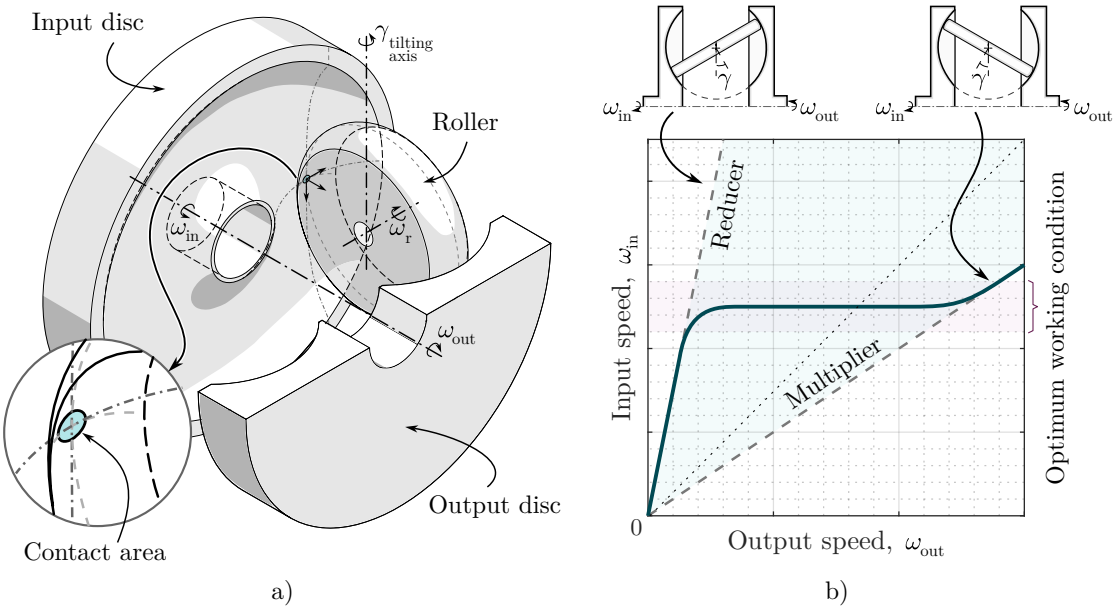

Figure 1.1: a) Isometric view of a Toroidal type Continuously Variable Transmission with a single roller in the toroidal cavity and b) a representation of the transmission ratio shifting, maintaining the input speed constant and varying the output speed.

Several studies have been published in relation to the energy saving potential of these mechanisms [1–4], where the energy consumption may be lowered from 3 to 7% even if the efficiency of this kind of transmission is lower than conventional geared transmissions [5]. Furthermore, CVTs may be used in many applications such as internal combustion or electric/hybrid vehicles [5, 6], wind power generators [7], bicycles [8, 9] and flywheel charging and discharging mechanisms [10–13]. Hence, due to the high energy saving capacity of these transmission mechanisms, the present thesis focuses on the their efficiency optimization.

Power transmission of T-CVTs is carried out by means of lubricated traction[1] forces between the aforementioned components. It is already known that traction forces strongly depend on the normal loads [14, 15], therefore, clamping devices are used in T-CVT transmissions with the purpose of adapting the normal loads during operation as a function of the torque that has to be transmitted [16]. These loads have direct effect on the performance of the transmission [17] hence, a proper clamping load increases the efficiency of the mechanism. Additionally, as a consequence of the normal loads on the point contacts, elastic deflection of the components occur and a large contact interface with a high pressure is generated.

Even if lubricants are commonly used to reduce friction losses [18], in T-CVTs, they are used to transmit torque by lubricated traction, thus, avoid direct metal to metal contact increasing the durability of the rolling components [19, 20]. The lubricated traction loads are determined by the Elastohydrodynamic (EHL) lubrication regime. It consists on a lubricant fluid film separating the rolling components in contact [21], and, the traction forces are transmitted by the shear stresses of the lubricant [22]. These stresses are governed by the lubricant viscosity and sliding motion. On one hand, the viscosity of the lubricant increases as a consequence of the high contact pressure on the contact interface. On the other hand, sliding motion is required to shear the film and thus generate traction. Consequently a certain amount of sliding is required to transmit torque by lubricated traction. Nevertheless, since sliding is a power loss source and equilibrium have to be achieved controlling the clamping loads of the transmission.

Regarding lubricated traction, the literature review (presented in the next chapter) has recently revealed that large contact interface sizes decrease the lubricated traction, which is a phenomena occurring in T-CVTs [23]. Furthermore, a characteristic kinematic behaviour of T-CVTs is spin motion, which increases the sliding distribution on the contact interface which, decreasing traction and increasing power losses [24]. Both phenomena, large interfaces and spin motion occur together in the contact points of T-CVTs.

As it will be detailed in the next chapter, historically, both contact points of the transmission are equally loaded, but, differences between their working conditions may be expected in terms of EHL conditions, spin motion and contact scale. The objective of this thesis is therefore to predict and evaluate the efficiency of this kind of transmission under independently controlled input and output variable clamping load conditions; both, numerically and experimentally, considering the combined effects of spin motion and contact scale on traction and efficiency.

[1] In this thesis the word traction is used for the friction force, since friction is a general term and traction is referred to the tangential force transmitted across an interface between two bodies.

1.2 STRUCTURE OF THE DOCUMENT

The document has been divided into seven chapters represented in Figure 1.2.

Chapter 1, Introduction, provides the motivation of the current study, a description of CVT transmissions, emphasizing their working principle and key characteristics. At the end of the chapter the structure of the document is defined.

Chapter 2, Literature review, encompasses studies related to T-CVT transmissions. It focuses on the phenomena occurring at the contact points between the components, including kinematics and traction, crucial for these transmissions' proper function. The chapter concludes with a critical analysis of the scientific literature, identifying research opportunities for the present thesis.

Chapter 3, Hypothesis and Objectives, include scientific contribution of the current work in form of hypothesis based on the critical review presented. Afterwards, some objectives are stated in order to answer the hypothesis.

Chapter 4, Traction prediction model, describes the model that has been generated to predict the traction coefficient acting on rolling and sliding contacts with spin typical in CVT mechanisms. The combined effect of spin motion and interface size on the effective traction has been studied since both occur together in T-CVTs.

Chapter 5, T-CVT efficiency prediction model, contains the model that has been developed to predict the efficiency of full T-CVT transmissions as a function of the applied clamping loads and torque to be transmitted. The traction prediction model generated in the previous chapter is used to determine the traction and longitudinal sliding equilibrium of the transmission. Furthermore, independently controlled input and output variable clamping loads were analysed to determine their effect on the performance of T-CVT transmissions.

Chapter 6, Experimental study, contains measurements carried out with a T-CVT prototype designed and manufactured in this thesis with the main peculiarity of independently controlling the input and output clamping loads.

Chapter 7, Conclusions and Future Work, describes a compilation of the main conclusions inferred from the performed work as well as some insights for future work. Moreover, at the end of the chapter the dissemination activities performed during this period are stated.

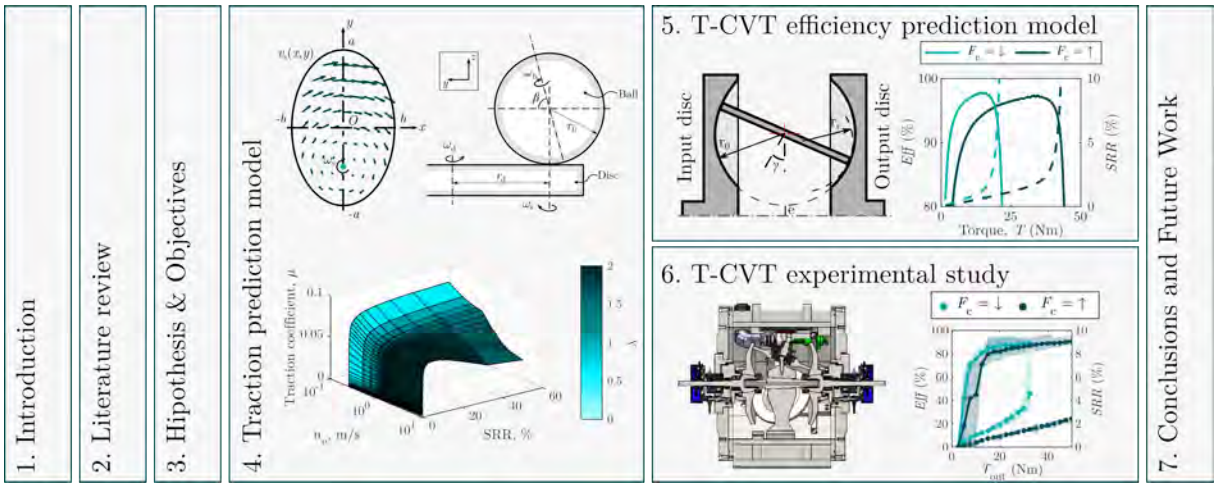

Figure 1.2: Structure of the PhD thesis.

2 LITERATURE REVIEW

"When we can't think for ourselves,
we can always quote"
Ludwig Wittgenstein

This chapter resumes the main studies that have been carried out in the topic of T-CVTs and lubricated traction with spin. The chapter has been divided in five sections. Firstly, the generalities and the working principle of T-CVTs are explored together with the effects that spin and contact scale have on lubricated traction. Subsequently, the works regarding the modelling of lubricated traction are presented. In the third section studies regarding the modelling of T-CVT transmissions are presented. Afterwards, experimental measurements of T-CVTs that have been published are presented. Finally, a critical review of the literature is carried out in order to infer some conclusions and determine some research opportunities.

2.1 TOROIDAL TYPE CVTS AND LUBRICATED TRACTION

This section has been divided into two parts, firstly, the generalities of T-CVTs are presented, then the study focuses on lubricated traction and how it is affected by spin motion and contact scale.

2.1.1 *Toroidal type CVTs*

Toroidal type Continuously Variable Transmissions are mechanisms where torque is transmitted between its components by means of heavy loaded, lubricated, rolling, sliding and spinning point contacts between disc and rollers. Torque transference is carried out from the input disc to the rollers and from the rollers to the output disc, and the transmission ratio is shifted tilting the rollers (γ angle in Figure 2.1), thus the relation between the input and output radius changes [25, 26].

Normal loads are required to transmit torque by traction, therefore, variable clamping mechanisms are developed in order to adapt the normal load during operation [16]. Additionally, lubricated traction is governed by the EHL lubrication regime (later explained in this chapter), nevertheless, it is noteworthy that longitudinal sliding is essential to generate traction forces [27]. Hence, in the following pages the geometry of the transmission, the clamping devices and their effects and finally the kinematics of the transmission are presented to understand the operation of this type of transmissions.

Geometry of a T-CVT

Different kind of T-CVT transmissions may be distinguished regarding the disposition of the rollers [27]. The most common disposition is the full toroidal CVT, which has the rollers placed on the centre of the toroidal cavity as represented in Figure 2.1a. Another disposition is the half toroidal disposition, where the rollers are no longer placed on the centre of the toroidal cavity since they are moved along their rotation axis as illustrated in Figure 2.1b. The main advantage of the later is that spinning speed decreases (later analysed in this section) which is a characteristic power loss source of this kind of transmission. Additionally, a modification of the full toroidal disposition was proposed [28], combining two rollers in the toroidal cavity, hence, the spin losses were considerably decreased (neglected in the 1:1 transmission ratio) and the rotation direction of the input and output discs was in the same direction. Other studies published other geometries that are no longer toroidal such as the logarithmic CVT, that eliminate the spin across the entire range of transmission ratio [29–32]. Another disposition, is the ball CVT [33, 34], it has a similar performance as the T-CVT but instead of rollers, ball are placed between both discs where thee is no longer any toroidal cavity, tilting the rotation axis of the balls, the effective radius of them change and hence the transmission ratio. In addition, other disposition that differ from the conventional ball CVT is the Constant Power CVT [35, 36], which is a passively actuated CVT that changes the transmission ratio as a function of the torque to be transmitted, maintaining constant the relation between speed and torque (constant power). However, the current thesis focuses on the full toroidal disposition.

Geometrically, the torque that a T-CVT can transmit depends on the number rollers placed inside the toroidal cavity and the number of toroidal cavities of the transmission (one or two) [27, 37]. Increasing the number of rollers, more contact points are involved in the torque transmission, dividing the traction load in more points, therefore, the transmissible torque increases. Similarly, an additional coaxial toroidal cavity enables to duplicate the number of rollers and consequently the torque transmission is duplicated.

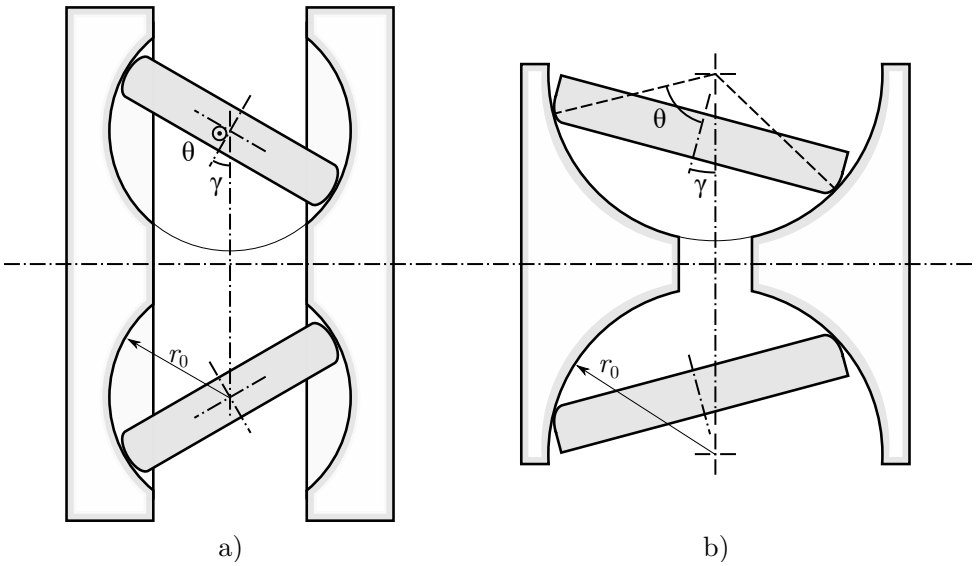

Figure 2.1: Schematic representation of the a) full and b) half T-CVT. Adapted from [38].

Clamping mechanisms

Variable clamping mechanisms have been developed in order to adapt the normal load acting in the contact points as a function of the working conditions. Mainly, two clamping devices have been identified, passive and active systems. The passive systems are based on loading cams [16], where, as a function of the torque that has to be transferred (loading torque), the clamping load is adapted. The clamping load applied on the transmission by this kind of passive mechanisms is proportional to the torque that has to be transmitted as determine by Equation 2.1 [39].

$$F_c = k_c \cdot T_l + F_{c0} \tag{2.1}$$

where F_c is the clamping load, k_c is the relation between the torque and clamping load, T_l is the loading torque (usually the input torque) and F_{c0} is the initial preload (clamping without torque).

Active clamping devices though, are usually based in hydraulic systems where the hydraulic pressure is converted into clamping load [17]. This devices have been usually used to test the behaviour of this kind of transmission as a function of the clamping load, nevertheless, they require an additional controller. Additionally, the generated normal loads affects the transmission performance. On one hand, the literature has shown that in the conditions where the applied force is too low, gross slip happens, thus no torque transmission is achieved. On the other hand, overclamped conditions lead to decrease the transmissions efficiency as a result of frictional losses. Figure 2.2 shows some power loss measurements as a function of torque under four clamping load conditions. On one hand, the figure shows a gradual increase in power losses while torque increases, they attributed it to the increase on the longitudinal sliding. On the other hand, the figure depicts that at any torque condition the power losses are higher under higher clamping load conditions. Therefore, they concluded that by mean of the optimum clamping of the transmission the efficiency could be optimized in 1-2% instead of clamping it at a nominal traction coefficient of 0.055. However, the opposite was concluded in other studies [40], where it was said that efficiency increases with clamping, fatigue life decreases though as a result of the high contact pressures.

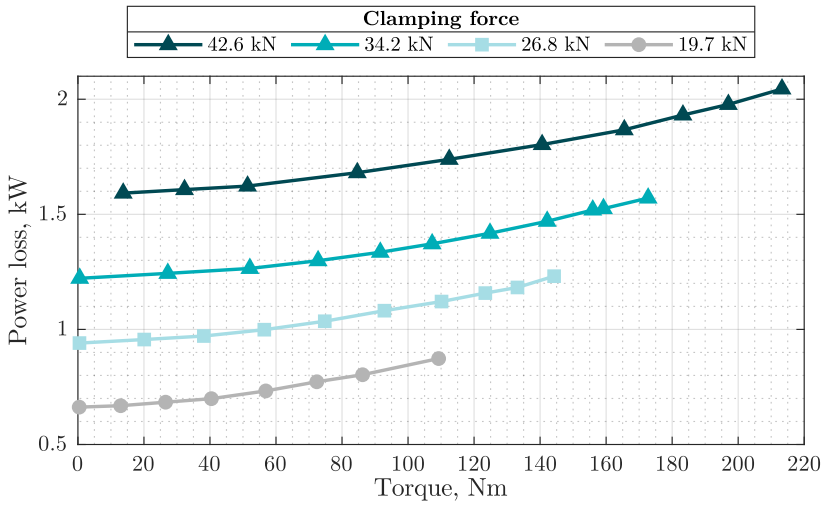

Figure 2.2: Power losses as a function of torque to be transmitted under four clamping load conditions. Adapted from [17].

Furthermore, the normal loads acting on the point contacts between disc and rollers cause elastic deformations of the components and consequently a contact interface is created [41]. As a function of the curvatures of the components, the contact interface may be even circular (spherical components in contact) or even elliptical. In addition, as a result of the elastic deformation a parabolic distribution of the contact pressure appears in the interface. Regarding Toroidal type CVTs, the contact interface that could be found in these transmission mechanisms is high, up to $a = 4.2$ mm (semimajor axis) and $b = 1.1$ mm (semiminor axis) [42]. Besides, the maximum contact pressure that may appear on the contact interfaces may be up to 3.5 GPa [43, 44].

A geometrical parameter influencing the contact conditions in such transmissions is the Conformity Ratio (CR). This ratio establishes a connection between the toroidal cavity curvature (r_0) and the roller curvature in the y-direction (r_r). Some authors [38], has demonstrated the significant impact of this parameter on transmission performance. On one hand, it has been suggested that higher conformity ratios lead to increase torque capacity, which is desirable to maximize the transmissible torque. On the other hand, the studies have concluded that, under these conditions, transmission efficiency decreases. A low CR is associated with reduced torque capacity but increased efficiency; in Figure 2.3, the efficiency of transmissions is depicted as a function of torque. The figure illustrates that low conformities result in higher efficiency, specially under low torque conditions. However, the maximum torque achievable is lower compared to high conformity conditions. Geometrical optimization studies for such transmissions [3, 45, 46] indicate that, under specific conditions, high conformity ratios are preferable to maximize the transmissible torque, while other scenarios may require low conformities. Nevertheless, the optimum efficiency condition was found to be at the analysed minimum conformity ratio, $CR = 0.5$.

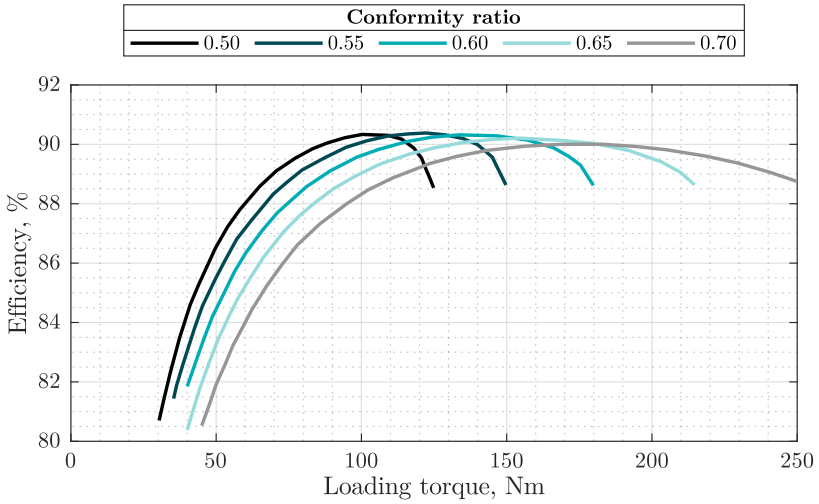

Figure 2.3: Efficiency as a function of loading torque for different conformity ratios. Adapted from [38].

Kinematics

Since torque is transmitted by lubricated traction (later studied in this chapter), it is noteworthy that strongly depends on the shearing of the lubricant, therefore, a certain amount of longitudinal sliding occur between the components in contact. Figure 2.4 illustrates three different disposition

of rolling components. On one hand, Figure 2.4a illustrates a pure rolling and longitudinal sliding disposition. Rolling speed refers to the speed of both components in the same direction, usually determined by the entrainment speed (see Equation 2.2). Longitudinal sliding, though, is the difference between the linear speed of each component in the same direction to rolling, in T-CVTs a small amount of longitudinal sliding occurs always to allow the torque transmission [27]. The longitudinal sliding occurring on the contact is determined by the creep coefficient Cr or the slide to roll ratio SRR[1].

Additionally, Figure 2.4b shows a combination of rolling, longitudinal sliding and spin motion, which is a rotational sliding motion distribution with the rotation axis normal to the contact interface characteristic of machine elements such as angular contact ball bearings, roller bearings [48, 49] and T-CVTs [27]. Additionally, Figure 2.4c shows the side slip condition, which it may appear in T-CVTs during the transmission ratio shifting [50].

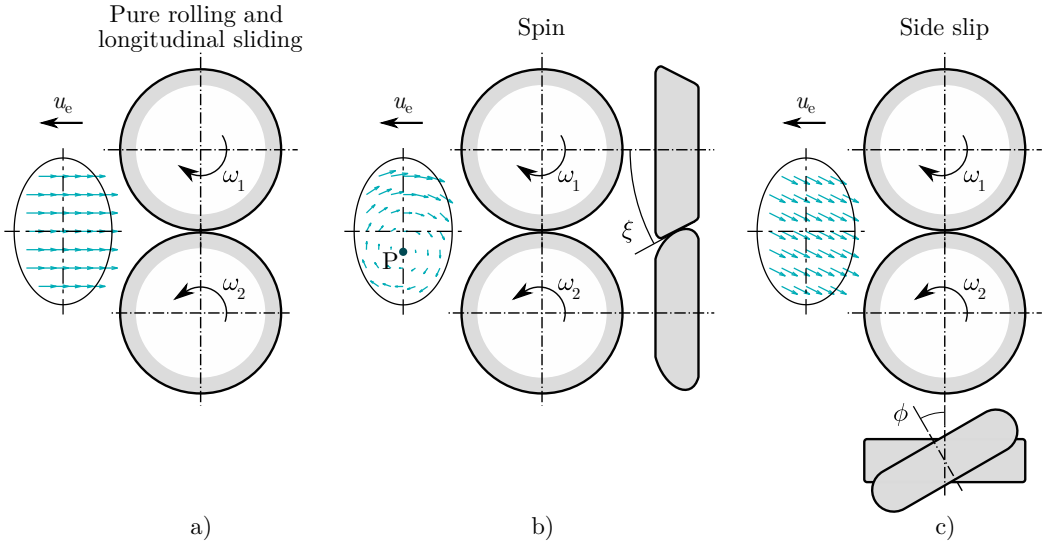

Figure 2.4: Sliding speed distribution representation on the contact interface as a function of the disposition of the rolling components, where a) represents a pure rolling and sliding distribution, b) is a combination of rolling, longitudinal sliding and spin and c) illustrates a condition with side slip. Adapted from [51].

[1] The longitudinal sliding considered in this kind of transmissions is usually represented as the creep coefficient Cr [27, 28, 47]. Nevertheless, in the field of lubricated traction the slide to roll ratio SRR definition is used. While SRR relates the sliding speed with the entrainment speed (mean rolling speed of both components), the Cr relates the sliding speed with the input speed. However, both parameters are related as shown in Equations 2.2, 2.3 and 2.4.

$$u_e = \frac{u_1 + u_2}{2} \tag{2.2}$$

$$SRR = \frac{v_s}{u_e} = 100 \cdot \frac{2 \cdot (u_1 - u_2)}{u_1 + u_2} \tag{2.3}$$

$$Cr = \frac{v_s}{u_1} = \frac{u_1 - u_2}{u_1} \tag{2.4}$$

where, u_e is the entrainment speed, u_1 the speed of the fastest components, u_2 the speed of the slowest component, SRR the slide to roll ratio and Cr the creep coefficient.

Spin is generated as a consequence of the disposition of the rolling components in contact [51]. Figure 2.5 determines the spinning speed occurring in a contact pair where the radius of both components in contact is equal. According to their analysis, a contact pair would have no spin when the tangent line of the contact interface intersects in the same point with both axis of rotation of the components. The equation to calculate the spinning speed for any disposition is shown in Equation 2.5 considering that the radius of both rolling components is equal.

$$\omega_s = \omega_A \cdot \sin(\theta) - \omega_B \cdot \sin(\gamma - \theta) \tag{2.5}$$

with ω_s, ω_A and ω_B the spinning speed, and rotational speed of component A and B respectively. Similarly, the γ angle represents the angle between the rotational axis of both components and θ the angle between the axis of component A and the tangent line to the contact interface as represented in Figure 2.5.

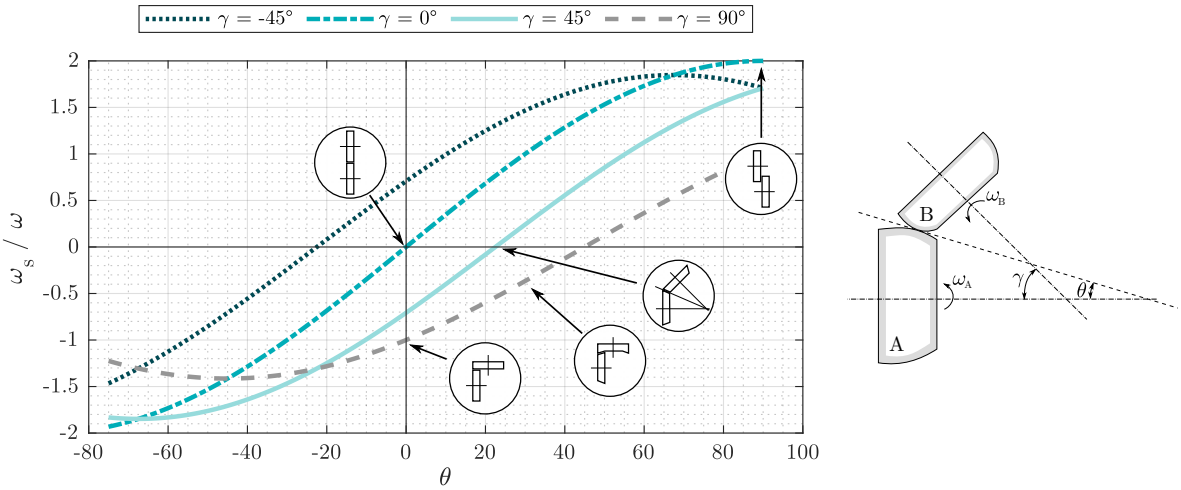

Figure 2.5: Spinning speed as a function of the disposition of the rolling components. Adapted from [51].

In order to quantify the spin acting in the contact interface different dimensionless parameters have been defined. The parameters are shown in Table 2.1. For that purpose different authors considered different parameters such as the contact interface size; where a and b are the semi axis of the contact ellipse or R_x which is the effective curvature of the components in rolling direction and the rolling speed, u_e. Nevertheless, there is no a single unified definition.

In the field of T-CVTs the spin coefficient term is commonly used [27, 28]. The calculation method of the spin coefficient for different transmission dispositions as a function of the transmission ratio is defined in Equation 2.6.

$$\sigma = \frac{\omega_s}{\omega_d} = \sin(\theta + \gamma) - (1 - Cr) \cdot \frac{1 + k - \cos(\theta + \gamma)}{\tan(\theta)} \tag{2.6}$$

where, σ is the spin coefficient, ω_s and ω_d the spinning and disc speed respectively, γ the inclination angle of the rollers and θ the angle from the roller tilting axis to the point contacts (90° for the full T-CVT). The spin coefficient comparison for three different kind of toroidal type CVT are shown in Figure 2.6 for the input and output contact points separately for a condition without longitudinal sliding ($Cr = 0$).

Table 2.1: Different dimensionless spin parameters found in the literature.

Loewenthal et al. [51]	$S_{\mathrm{pL}} = C \cdot \frac{\omega_{\mathrm{s}} \cdot \sqrt{a \cdot b}}{u_{\mathrm{e}}}$
Taniguchi et al. [52]	$S_{\mathrm{pT}} = \frac{2 \cdot \omega_{\mathrm{s}} \cdot R_{\mathrm{x}}}{u_{\mathrm{e}}}$
Porras-Vazquez et al. [53]	$S_{\mathrm{pP}} = \frac{2 \cdot \omega_{\mathrm{s}} \cdot a}{u_{\mathrm{e}}}$
Poon et al. [54]	$S_{\mathrm{pP}} = \frac{\omega_{\mathrm{s}} \cdot b}{u_{\mathrm{e}}}$
Zou et al. [55]	$S_{\mathrm{pZ}} = \frac{\eta_0 \cdot \omega_{\mathrm{s}}}{E^*}$

Figure 2.6a, reflects the variation of the spin coefficient on the input point of the transmission as a function of the transmission ratio while Figure 2.6b shows the spin coefficient of the output point. The figure reveals that the spin coefficient is zero when the transmission ratio is one for the Double full T-CVT, they concluded that a proper design of a T-CVT allows to reduce spin losses over a wide range of transmission ratios. Moreover, the Full T-CVT is the one with the highest spin coefficient, which suffers from spinning motion in every transmission ratios while the Half Toroidal CVT has two no-spin transmission ratio points. Furthermore, the figure shows that the condition with the maximum spin coefficient occurs at 1:1 transmission ratio.

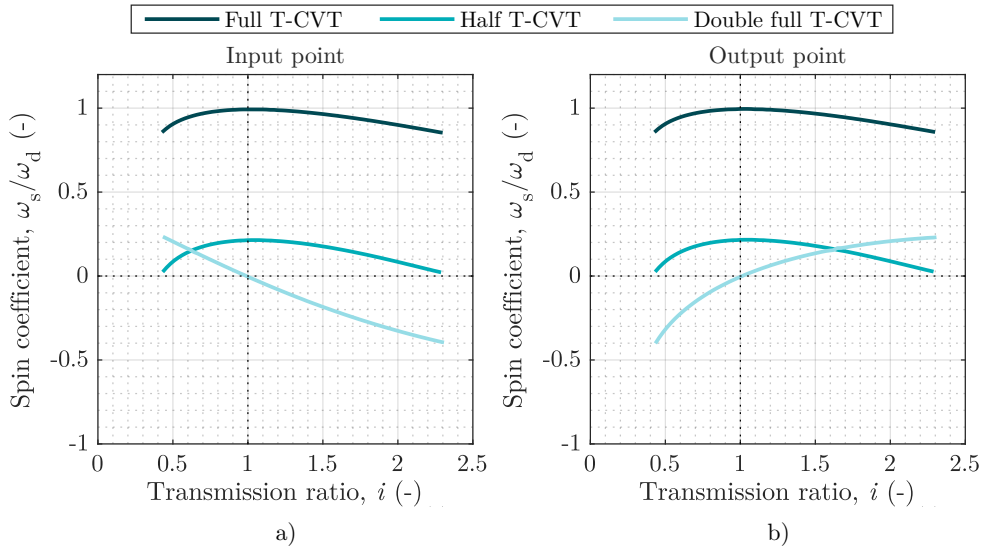

Figure 2.6: The spin coefficient at the a) input and b) output contact points as a function of the ideal transmission ratio. Adapted from [28].

Furthermore, a spin pole occurs in rolling and longitudinal sliding contacts with spin. It is defined as the point where the linear speed of both components in contact is equal. As a function of the longitudinal sliding happening on the rolling and sliding contact, the spin pole moves from the centre of the contact interface. Equation 2.7 defines the distance from the centre of the contact interface to the position of the spin pole [51] (point P in Figure 2.4b).

$$\mathrm{P} = \frac{v_{\mathrm{s}}}{\omega_{\mathrm{s}}} \tag{2.7}$$

2.1.2 *Spin and scale effects in lubricated traction*

Lubricated traction

In T-CVTs torque is transmitted by traction forces across a lubricant fluid film separating the rolling components in contact, known as Elastohydrodynamic lubrication (EHL). This lubrication regime was established in 1945 since different solutions where proposed for the lubricant film in non-conformal contacts [21]. This lubrication regime considers the deformation of the contacting bodies as a result of the applied normal load. Therefore, due to the high pressure on the contact interface the viscosity of the lubricant increases considerably [56].

On one hand, rolling speed generates the film thickness since lubricant is introduced to the contact interface. Film thickness is defined by the lubricant properties in the inlet of the contact [57]. On the other hand, it is widely known that lubricated traction varies as a function of the shearing of the lubricant fluid film separating both components, which in fact is determined by the sliding speed. Therefore, lubricated traction is usually represented as a function of longitudinal sliding (Slide to roll ratio, SRR). In addition, EHL traction is determined by the properties of the lubricant inside the Hertzian contact region, therefore, its rheology plays an important role [58]. Furthermore, spin motion and scale effects affect the traction coefficient, the effects of these two phenomena are explained in the following pages.

Figure 2.7 shows a 3D traction coefficient map as a function of entrainment speed and SRR, the following regions are identified [59, 60]:

- Under low longitudinal sliding conditions, there is a linear increase in traction while sliding increases, it represents the Newtonian region where the shear stresses increase linearly with shearing.
- Larger increase in SRR generates non-Newtonian effects in the lubricant film where a non linear increase in traction is shown. The lubricant suffers shear thinning, which is considered to be a decrease in viscosity as a result of the shear stresses. Therefore, the slope of the traction curve decreases.
- The sliding between the rolling components in contact lead to increase the contact temperature [61]. Therefore, at high longitudinal sliding conditions the viscosity of the lubricant decreases as a result of the contact temperature rise, consequently, the traction coefficient decreases. As represented in Figure 2.7 traction decreases more under high entrainment speed conditions as a consequence of the increase in temperature rise at higher speed.
- There is a maximum traction limit where lubricant shear stresses no longer increase while shearing increases. It is considered as a plastic yield of the lubricant fluid film at high contact pressure conditions. This is known as a limiting shear stress. Nevertheless, it is a topic that it is still under discussion in the scientific community [62].
- At low entrainment speed conditions, since the lubricant fluid film decreases, contact between the asperities of the solids may occur which represents the mixed lubrication regime [63–65]. In these conditions an increase of the traction coefficient occurs since part of the traction load is carried by the solids (boundary lubrication regime [58, 66]). The condition to occur mixed lubrication are still under discussion in the literature since similar surface roughness may be achieved by a different surface topography [67, 68]. The lubrication regime is determined by the Stribeck curve [69].

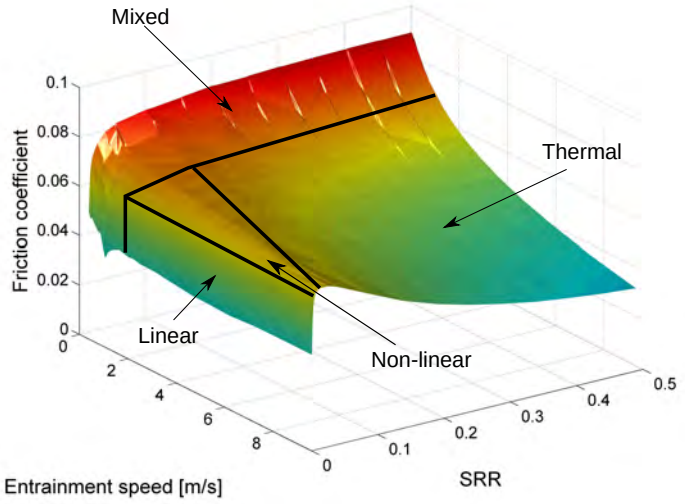

Figure 2.7: 3D traction coefficient map as a function of entrainment speed and slide to roll ratio where different regions are identified [59].

Influence of spin motion in lubricated traction

This section focuses on the resume of the studies published regarding the effects that spin motion has on rolling and longitudinal sliding EHL contacts. On one hand, many researchers agreed that spinning motion has no or little influence on the pressure distribution and central film thickness of the lubricant, this may be because the film thickness and pressure distribution is mainly defined by rolling speed [52, 55]. Moreover, the film thickness is defined by the lubricant properties at the inlet of the contact. However, spinning affects the film thickness distribution and reduces the minimum film thickness, therefore, it should be considered in terms of asperity contacts in order to determine the lubrication regime [70]. On the other hand, traction is defined by the lubricant rheology in the Hertzian zone of the contact interface, therefore, spinning affects the traction coefficient [57].

It is known that spin motion decreases the traction coefficient [24], specially while the spin pole (pure rolling line) is inside the Hertzian contact region. At low longitudinal sliding conditions, the spin pole is inside the contact interface; while longitudinal sliding increases it moves from the surface centre until it leaves the Hertzian contact region. Therefore, it has already been said that in order to increase traction coefficient, the spin to roll ratio should be kept to the minimum [54, 71].

A specific tribometer for high scale spin induced rolling and sliding contacts was found in the literature [72–74]. This tribometer can measure the frictional loads as well as temperatures and film thickness distribution. In their studies they mentioned that spinning motion decreases the traction coefficient as a result of two main phenomena. On one hand, as a result of the sliding motion happening in the contact interface, shear thinning happens and thus the traction decreases. On the other hand, the additional sliding increases the thermal effects of the contact surface and thus the viscosity decreases and thereby traction. Furthermore, their experimental setup is able to measure the transversal (perpendicular to rolling) traction, they concluded that it is almost null as the sum of the shear stresses in transversal direction are self balanced.

The development of a special twin disc was published where spin motion may be included together with rolling and longitudinal sliding [47, 75]. Their analysis was based on implementing a new model to estimate the effective shear stresses on the contact interfaces. Two traction measurements are shown in Figure 2.8, with and without spin under 3 GPa of maximum Hertzian contact pressure, 70 m/s of input speed (fastest component) and 120°C of lubricant temperature. The figure shows lower traction coefficient under the condition with spin in low longitudinal sliding conditions (low Cr). However, as longitudinal sliding increases, both traction curves converge into an equal traction coefficient, which coincides with the findings of other studies [24, 76].

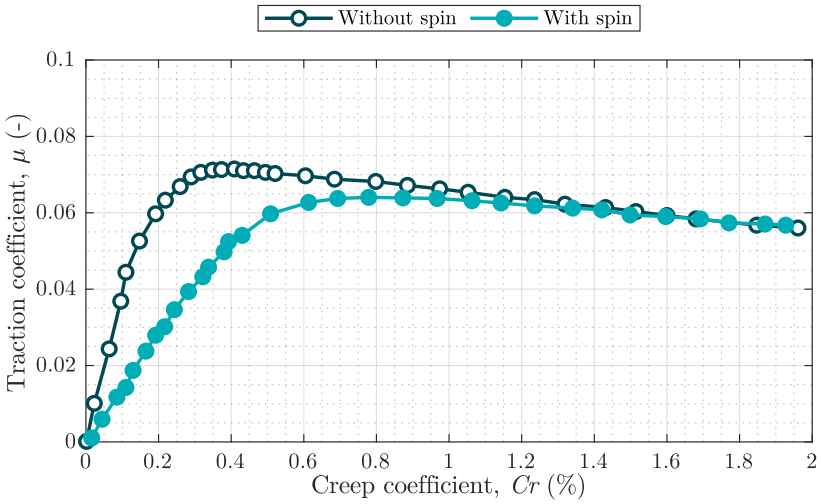

Figure 2.8: Traction curve with and without spin motion under $u_1 = 70$ m/s, $p_H = 3$ GPa and $\Theta_0 = 120$ °C. Adapted from [75].

Scale effect in traction coefficient

Recently, a discussion regarding the influence that the contact interface size has in the traction coefficient has been of interest of several researchers [23, 77, 78]. It has to be pointed out that spinning motion was not considered in these publications. They saw that the traction coefficient increases while the contact interface size decreases at comparable conditions—speed, pressure and temperature.

Firstly, Bergseth et al. [77] analysed the influence of the contact size by both, a ball-on-disc and a twin-disc tribometer disposition. Their analysis was focused on the influence of the surface roughness in traction. Therefore, even if they mentioned that the traction results differ by a factor of two between their results it can be a possibility that different EHL scenarios were compared. The lubrication regime should be carefully determined. Since rough surfaces were used in their measurements, the lubrication regime may affect the measurements.

Accordingly, other study analysed the differences in measurements between two comparable test rigs under comparable EHL conditions [23] for different contact scale. Their study was based on some previous studies published by Plint et al. [79]. The analysis was carried out by a ball-on-disc with a contact curvature in rolling direction of $R_x \cong 10$ mm and a twin-disc with an equivalent radius of $R_x \cong 30$ mm. They analysed both the isothermal behaviour (numerically) and the thermal behaviour experimentally and they mentioned that even if traction differences were obtained under isothermal conditions they could not explain the differences in

the measurements, where the largest interface size tested was the condition with the lowest traction coefficient as represented in Figure 2.9. Therefore, they concluded that the difference source was the thermal behaviour of the contacts.

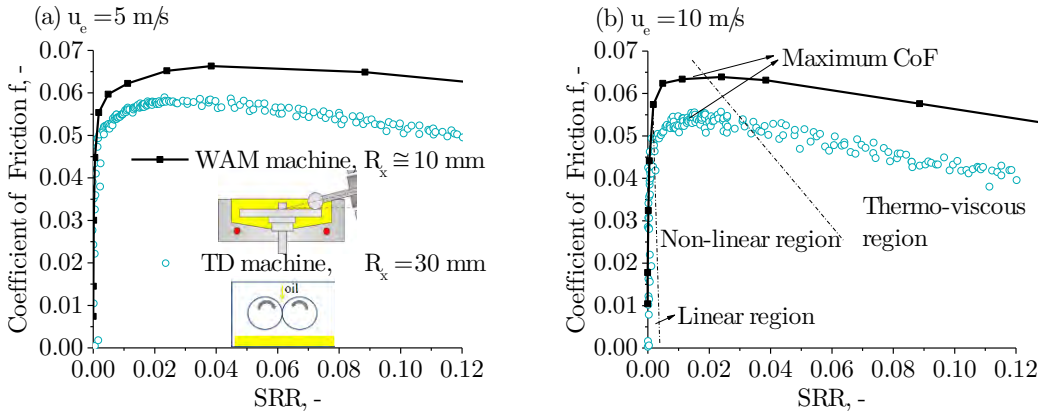

Figure 2.9: Traction curves measured with two test rigs in different geometrical configurations at constant mean contact pressure, speed and supplied oil temperature for Squalane lubricant, a) $u_e = 5$ m/s and b) $u_e = 10$ m/s. Adapted from [23].

In addition, they mentioned that the shear rate is no longer Couette flow for large contact sizes and that shear localization appears in thicker film shapes (see Figure 2.10). However, recent studies made on Molecular Dynamics said that the lubricant shearing in EHL conditions may be plug flow instead of shear localization [80].

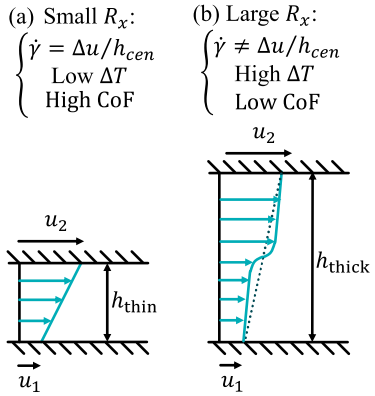

Figure 2.10: Shear strain rate on the fluid film for different contact scale (film thickness) conditions [23].

Moreover, a discussion to the aforementioned study was published [78]; they mentioned that the results should be carefully studied in order to reach to a true conclusion. They concluded that there may be three reasons in the difference source such as different EHL conditions, where the effective curvature radius affects the film thickness. The pervasive presence of thermal effects and mixed lubrication in some of the tested cases since as a consequence of the roughness of the samples and the film thickness the tests were carried out at the limits of the lubrication regime. Nevertheless, these difference sources in traction are important to be considered in the characterization of lubricants, however, in the characterization the experimental setup used may have an important impact as mentioned in the reply [81].

2.2 PREDICTION MODELS OF LUBRICATED TRACTION

With the aim of predicting the traction coefficient, several lubricated traction prediction models have been proposed, which are mainly based on calculating the shear stresses of the lubricant film [82–84] and integrating them to calculate the traction coefficient as shown in Equation 2.8.

$$\mu = \frac{\iint \tau_x \, \mathrm{d}x \, \mathrm{d}y}{F_\mathrm{n}}, \text{ where } \tau_x = \min\left[\dot{\gamma} \cdot \eta_\mathrm{G}(p, \Theta, \dot{\gamma}), \tau_\mathrm{LSS}\right] \tag{2.8}$$

where μ is the traction coefficient, τ is the shear stress, $\dot{\gamma}$ is the shear strain rate, η_G is the generalized viscosity and τ_LSS is the limiting shear stress. These models can be (i) empirical, (ii) numerical or (iii) analytical. The prediction of the traction forces is crucial for the design and optimization of T-CVT transmissions [85].

Empirical traction prediction models are developed based on traction measurements. Using a tribometer to measure many traction curves in multiple working conditions, these models determine the traction coefficient in each working condition via regression [86]. Although spin can not be directly measured in conventional tribometers, its effect on traction can be predicted using such methods. One approach involves dividing the contact interface in different parallel strips in the rolling direction and determining the traction coefficient based on the condition of each strip [54].

Numerical traction prediction models, on the other hand, consider the physical phenomena occurring inside the contact region. These have undergone significant improvements in recent years, in particular solving Reynold's flow equation together with load, energy, and elasticity balance equations. However, numerical methods can be subject to some convergence issues and incur considerable computational costs [72–74, 87–90]. The equation governing the motion of a fluid in space and time is the Navier-Stokes equation. Nevertheless, after some simplifications such as neglecting inertia forces and the thin film assumption the Reynolds equation is achieved [91] shown in Equation 2.9.

$$\frac{\partial}{\partial x}\left(\frac{\rho h^3}{12\eta}\frac{\partial p}{\partial x}\right) + \frac{\partial}{\partial y}\left(\frac{\rho h^3}{12\eta}\frac{\partial p}{\partial y}\right) - \frac{\partial}{\partial x}\left(\left(u_{1,x} + u_{2,x}\right)\rho h\right) - \frac{\partial}{\partial y}\left(\left(u_{1,y} + u_{2,y}\right)\rho h\right) = 0 \tag{2.9}$$

where, the components of the equation represent a variation on pressure p and variation of speed u along x and y axis, spinning motion would be considered as the speed in transverse direction to rolling.

Computational numerical solution methods are required to solve the Reynolds equation [92–94]. However, with the purpose to have some engineering approaches of the central and minimum film thickness, simple analytical expressions were defined by means of adjusting the numerical results [95]. These are simple and time efficient analytical models suitable for machine elements with multiple EHL working conditions. The first analytical expression for circular contacts was given by Hamrock and Dowson in 1976 for circular contacts under isothermal and fully flooded conditions and lubricated by a Newtonian fluid; it is still widely used [21, 96]. Afterwards other expressions were defined considering different ellipticity and working conditions [97–99]. Spin motion is only considered in the equations proposed by Zou et al. [55], nevertheless, later studies revealed that spin motion does not affect the central film thickness [70].

The ellipticity ratio, the rolling direction, the lubricants viscosity ranges and so on affects the film thickness. Therefore, it is important to choose the film thickness formula correctly. A recent study [100] made an analysis of the suitability of different film thickness formulas comparing the results with a quantitative T-EHL analysis across a wide range of EHL conditions. Theyconcluded that the best results were obtained by the Chittenden film thickness equations for the central film thickness and the Nijenbanning and Chevalier combination for the minimum film thickness.

These analytical models provide accurate results for engineering purposes [58, 101–105]. Spin motion was considered in some of them, however, for the sake of simplicity, this kind of models usually locate the spin pole position independently from real kinematic behaviour giving rise to non-feasible solutions [106], rheological models do not account for high pressure viscosimetry [107] and the thermal calculation usually considers a constant, contact size independent, friction coefficient in the contact area [108]. Additionally, analytical traction prediction models are based on the mean Hertzian contact pressure. However, under high contact pressure conditions, the difference between the maximum and mean pressure may exceed 1 GPa and particularly, when spin occurs this models are not suitable [109].

2.3 T-CVT EFFICIENCY PREDICTION MODELS

In order to calculate the efficiency of this kind of transmissions, one of the mostly cited model is the one published by Carbone et al. [27]. It is a pure analytical approach of the transmissions efficiency was carried out. Similar models were used by other researchers [3, 28, 39, 45, 46, 110–112]. Firstly, the geometry of the transmission is determined to follow with the definition of its kinematics. Then, the forces and reactions between the components of the transmission are calculated, subsequently, the loading and the contact interface and pressures were conducted by the Hertzian contact model. Then, the hydrodynamic traction was modelled without considering thermal behaviour of the lubricant. The traction coefficient and torque induced by the spinning motion was modelled by the integration of the shear stresses across the Hertzian contact region as shown in Equation 2.10 and 2.11. In their analysis, the normal loads acting in both point contacts—input and output points—were considered equal, nevertheless, traction coefficient and spinning torque acting in each point contact was calculated independently. However, differences between the behaviour of each of the contact points were not discussed.

$$\mu_{\mathrm{i}} = \tilde{a}_{\mathrm{i}} \cdot \tilde{b}_{\mathrm{i}} \int_0^1 \mathrm{d}R \cdot \int_0^{2\pi} \tilde{\tau}_{\mathrm{x,i}} \cdot R \cdot \mathrm{d}\psi \tag{2.10}$$

$$\tilde{T}_{\mathrm{i}} = \frac{\tilde{a}_{\mathrm{i}} \cdot \tilde{b}_{\mathrm{i}}}{\Re \cdot \tilde{r}_{\mathrm{i}}} \int_0^1 \mathrm{d}R \cdot \int_0^{2\pi} \left(\tilde{a}_{\mathrm{i}} \cdot \tilde{\tau}_{\mathrm{y,i}} - \tilde{b}_{\mathrm{i}} \cdot \tilde{\tau}_{\mathrm{x,i}} \right) \cdot R^2 \cdot \mathrm{d}\psi \tag{2.11}$$

with $\tilde{a}$ and $\tilde{b}$ the dimensionless semimajor and semiminor axis of the contact ellipse, $\tilde{\tau}$ the dimensionless shear stress and $\Re$ is the load parameter $(((\pi E' r_0^2)/(6F_{\mathrm{n}}))^{1/3})$.

Regarding the efficiency determination of the transmission, it is calculated with Equation 2.12 [27]. They separated two efficiency loss sources, the torque efficiency and the sliding efficiency.

$$Eff = Eff_T \cdot Eff_v = \frac{r_{\mathrm{in}} \cdot T_{\mathrm{out}}}{r_{\mathrm{out}} \cdot T_{\mathrm{in}}} \cdot \frac{r_{\mathrm{out}} \cdot \omega_{\mathrm{out}}}{r_{\mathrm{in}} \cdot \omega_{\mathrm{in}}} \tag{2.12}$$

where Eff, Eff_T and Eff_v are the global efficiency, torque efficiency and speed efficiency respectively. Additionally, T and ω reflect the torque and angular speed and r represents the radius of the transmission (the subscript in and out reflect the input and output shafts of the transmission respectively). The equation shows that the torque efficiency is based on the differences on the input and output torque; differences come from the spinning torque generated in the contact points and the torque of the bearings of the rollers. The speed efficiency though, comes from the relation between the input and output linear speeds; in fact, longitudinal sliding occurring in the contact points. It has to be pointed out that lubricant churning losses of the rollers were not considered in their model. Additionally, of the discs (bearing sealing components and churning) were not included either.

The spin motion effects on contact efficiency had been also studied in the literature. It is an important aspect to consider it in the field of T-CVTs. Since the nature of spin is an additional sliding speed distribution on the contact interface, it is expected to increase the power losses. Figure 2.11 shows the contact efficiency for three conditions published in the literature, one without spin motion and two spinning speed conditions [24]. Results showed that under pure rolling and longitudinal sliding condition the highest efficiency is achieved at zero longitudinal sliding (there would be no sliding speed on the contact interface). Increasing spin leads to decrease the contact efficiency specially under low longitudinal sliding conditions. Furthermore, the contact efficiency values tend to converge under high longitudinal sliding conditions correspondingly to a traction curve. This trend was attributed the by the cited author as a consequence of the position of the spin pole, where under low longitudinal sliding conditions, spin increases the power losses and causes the efficiency drop, however, once the spin pole is no longer inside the Hertzian contact region its effects are negligible.

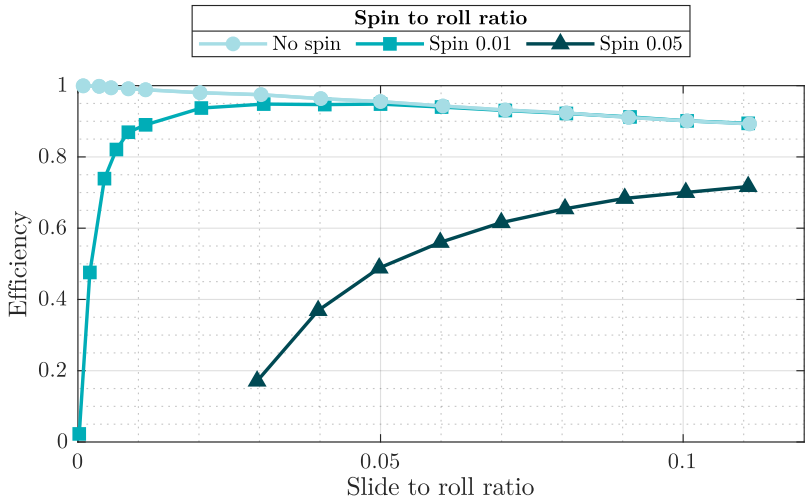

Figure 2.11: Contact efficiency under three spinning conditions. Adapted from [24].

Regarding contact efficiencies subjected to rolling and longitudinal sliding with spin, it was said that [90] showed that high conformities decreased the transmissible power as well as the efficiency. This finding is in accordance with the afore shown effect of the conformity ratio on the performance of T-CVTs [38, 45]. In this kind of rolling contacts, different power loss sources may be distinguished [113]. The expression to calculate the contact power losses Equation 2.13. Different sliding kinematics are distinguished in the equation in order to determine which is the predominant power loss source as a function of the conditions on the contact.

$$P_{\mathrm{CL}} = \int_S \left(\tau_{\mathrm{zx}} \cdot v_{\mathrm{s,x}} + \tau_{\mathrm{zy}} \cdot v_{\mathrm{s,y}}\right) \mathrm{d}S = \underbrace{v_{\mathrm{s,x,0}} \cdot F_{\mathrm{x}}}_{\text{Longitudinal sliding}} + \underbrace{v_{\mathrm{s,y,0}} \cdot F_{\mathrm{y}}}_{\text{Transversal sliding}} + \underbrace{\omega_{\mathrm{s}} \cdot T_s}_{\text{Spin motion}} \tag{2.13}$$

where P_{CL} reflects the contact power loss, τ and v_{s} are the shear stress and sliding speed distribution respectively and S is the surface area. The power loss equation is distinguished in the three sliding components that occur in the contact surface. On one hand, sliding ($v_{\mathrm{s,x,0}}$) and traction load (F_{x}) in longitudinal direction —in same direction to rolling (x-direction)—calculated on the centre of the contact interface (subfix 0) determine the longitudinal sliding power losses. The losses generated by the sliding in transversal direction to rolling on the centre of the surface are the transversal losses, these will appear when side slip occurs on the contact interfaces (see Figure 2.4c). Finally, the spinning losses are the ones generated by the spinning speed (ω_{s}) and spinning torque (T_{s}).

2.4 EXPERIMENTAL MEASUREMENTS OF T-CVTS

Few experimental measurements of T-CVTs have been published in the literature. Generally, the tests are carried out in specific test benches were the transmission is positioned within a energy source (commonly an electric motor) and a brake (commonly a generator), different working conditions such as speed, torque and transmission ratio may be adapted to test the performance of the transmission. Numerical T-CVT performance trends were compared to experimentally measured efficiency results [114]. In order to compare experimental and modelled efficiency results, they subtracted the power losses from gear and bearings to the measurements. They mentioned that the traction coefficient determination is critical for the determination of the power transmission of this kind of transmission [115, 116]. Walker et al. [117] tested the transmission kind that comprises two rollers in a single toroidal cavity (the double full T-CVT of Figure 2.6). In their analysis the clamping forces were directly proportional to the input torque; applied by a loading cam system. Their measurements demonstrated that the efficiency was up to 96% at 1:1 transmission ratio (no spin condition) for a traction coefficient of 0.07.

Meyer [118] tested the traction behaviour of T-CVTs. For that purpose they developed a CVT prototype comprising two rollers in a single toroidal cavity. The clamping force was controlled by an hydraulic cylinder, however, the clamping of the transmission was carried out only from one side of the transmission, thus both contacts were equally loaded. Figure 2.12 shows the transmission prototype used in their measurements, where and angular contact ball bearing is used to clamp the discs by means of the applied hydraulic pressure.

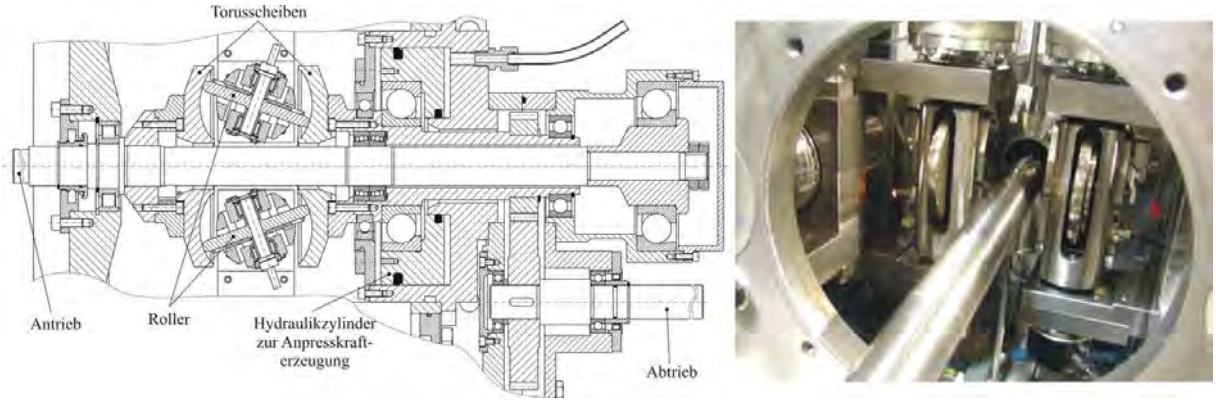

Figure 2.12: a) Drawing of the measured transmission and b) a picture of the tested T-CVT [118].

The measured traction coefficient as a function of the longitudinal sliding measured in the CVT is depicted in Figure 2.13. Traction, and consequently torque capacity, is directly related with sliding motion. While longitudinal sliding increases the traction coefficient increases also, this is in accordance with the lubricated traction behaviour, later studied in this chapter. Nevertheless, the figure shows that the traction coefficient decreases increasing the contact pressure, which it is the opposite to the conventional behaviour of the lubricated traction [119]. In addition, the figure reveals that the traction coefficient acting on the half toroidal CVT disposition is higher than the one acting on the full toroidal CVT disposition, which is in accordance with the traction curves depicted by other studies for T-CVT transmission mechanisms [27].

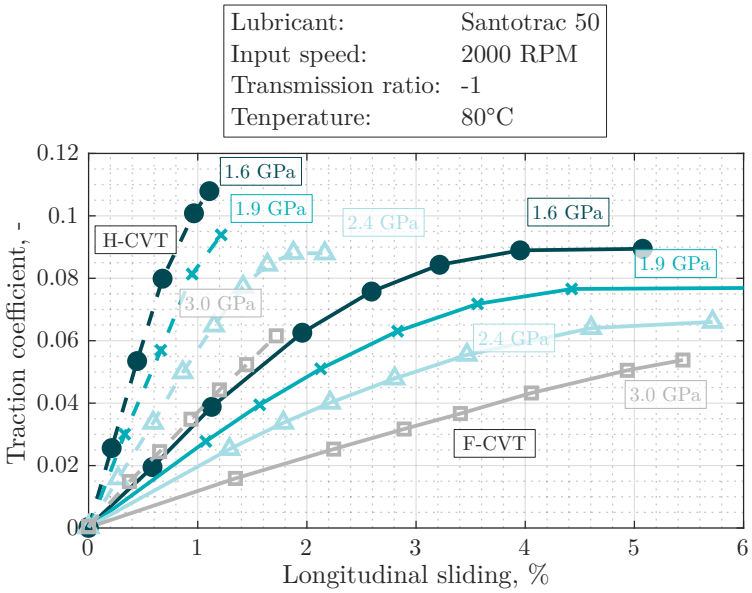

Figure 2.13: Traction coefficient measurements by a half (H-CVT) and a full (F-CVT) toroidal type CVTs for different clamping conditions. Adapted from [118].

2.5 CRITICAL REVIEW

The literature review has revealed that the clamping loads acting in the point contacts of T-CVT transmissions plays an important role in the working performance of the mechanism [17]. It has been identified that a certain amount of longitudinal sliding is also required since torque is transmitted by means of lubricated traction forces. Additionally, this sliding is controlled by clamping loads. Traction acts in two point contacts in this kind of transmissions, firstly energy is transmitted from the input disc to the rollers; subsequently, it is transmitted from the rollers to the output disc. However, it has been seen that the same normal load is usually considered in both point contacts and differences may be found in their working conditions in terms of EHL.

Additionally, it has been stated that elastohydrodynamic lubrication regime is the responsible of generating the traction forces on the point contacts of this kind of transmission. In this kind of lubrication regime it is known that traction is severally affected by the working conditions such as contact pressure, lubricant shearing and temperature [21]. It is worth mentioning that some studies stated the importance of considering the thermal behaviour of transmission lubricants [120]. It has also been identified that lubricated traction is sensitive to the longitudinal sliding; shearing of the lubricant fluid film is required to have traction forces, therefore a certain amount of longitudinal sliding is essential [83].

Recently, the effects of the contact interface size has been under discussion in the literature [23]. It has been revealed that large contact interfaces lead to decrease the lubricated traction under comparable EHL conditions; which is a common scenario on T-CVT transmission systems where the semimajor axis of the contact interface may be up to 4.2 mm [42]. Note, that spin motion was not analysed in the published studies.

Furthermore, literature has revealed that spin motion is a characteristic kinematic behaviour that occurs together with rolling and longitudinal sliding in the contact points of this kind of transmission [51]. It has been revealed that this kinematics affects the traction behaviour as well as the power losses of the transmission. In addition, it has been seen in the literature that the optimum efficiency condition appears at a certain longitudinal sliding condition [24]. Efficiency decreases under both, too low longitudinal sliding conditions; which may be caused by the overclamping effect on T-CVT transmissions and in high longitudinal sliding conditions as a result of the longitudinal sliding.

Research opportunities

The critical review has provided some insights into the research opportunities in relation to the effects of the clamping loads on the efficiency of T-CVTs. Some of the most relevant ideas are summarized as follows:

- The quantification of the effects on efficiency by independently controlled input and output clamping load of the T-CVT transmissions.
- The definition of the effects that the transmission ratio has on the contact behaviour of each of the point contacts acting in a T-CVT transmission.
- The analysis of the effects of the clamping load in the contact interface scale and its influence on traction equilibrium.
- The determination of the combined effect of the spinning speed and contact size under comparable conditions in EHL traction coefficient.

3 HYPOTHESIS AND OBJECTIVES

"We do not describe the world we see, we see the world we can describe"
Rene Descartes

3.1 HYPOTHESIS

Based on the research opportunities stated in the critical review of the literature, the following hypothesis has been formulated:

> *Independently controlled input and output clamping loads will increase the efficiency of T-CVT transmissions in comparison with equally loaded input and output points, due to the influence of the contact interface size.*

3.2 OBJECTIVES

With the purpose of verifying the hypothesis, the main objective of the present PhD thesis is as follows:

> *To predict and evaluate the performance of toroidal type continuously variable transmissions by means of independently controlled clamping forces, focusing on the contact interface size and spin motion effects on lubricated rolling and sliding traction.*

With this aim the following research objectives are defined:

O.1: To predict the traction coefficient in rolling and longitudinal sliding contacts points considering the combined effect between the contact interface size and spin motion.

O.2: To evaluate the efficiency and traction performance—equilibrium of the longitudinal sliding—of toroidal type CVT transmission mechanisms as a function of the applied clamping load and torque to be transmitted.

O.3: To design, manufacture and assemble a T-CVT prototype enabling to independently control the input and output clamping loads and experimentally validate the hypothesis.

4 TRACTION PREDICTION MODEL

"The two most powerful warriors
are patience and time"
Lev Tolstoy

This chapter contains the work performed regarding the model generated to predict the traction coefficient of rolling and longitudinal sliding contacts considering the combined effects of spin motion and contact scale. Afterwards, this traction prediction model will be used in the T-CVT performance prediction model to determine the traction coefficient acting in the contact points between disc and rollers. Contact conditions such as contact pressure, kinematics and lubricant rheology affect the performance of this kind of contact pairs, where two phenomena—spin motion and large size interfaces—occur together. As a consequence, a wide range of EHL conditions may appear in such transmissions, for that purpose a time efficient model is required to calculate the performance of the transmission in many working conditions.

At the beginning of the chapter the model is described considering all the parameters that affect the traction coefficient. Subsequently, the model validation is presented, for this purpose, both, experimental traction measurements by a ball on disc tribometer and literature published traction measurements were used. Afterwards, an analysis of the combined effect of contact scale and spin motion is presented, which is a phenomena occurring in the contacts points of a T-CVT transmission that affects their performance and efficiency. For that purpose, three case studies are presented for different scale and spinning speed scenarios under comparable conditions. Finally, at the end of the chapter the conclusions inferred from the performed work are presented.

4.1 DESCRIPTION OF THE TRACTION PREDICTION MODEL

4.1.1 *Generalized traction prediction model*

Lubricated rolling and sliding non-conformal contacts are defined by the EHL theory [121]. This lubrication regime is a hydrodynamic lubrication regime with the peculiarity of the non-negligible elastic deflection of the components in contact as a result of the normal loads. Due to the rolling motion of the components in contact, the lubricant is introduced to the contact generating a fluid film that separates and protects the components. Traction is transmitted by a thin lubricant film, therefore it is determined by the shear stresses of the fluid film. It is known that the film thickness is determined by the lubricant properties at the inlet of the contact while traction is determined by the properties of the lubricant confined inside the Hertzian contact region [84], therefore, the rheology of the contact plays an important role. Additionally, friction between the components generates heat, which affects the rheology of the lubricant and thus traction.

Under high normal load conditions, the EHL pressure distribution on lubricated rolling point contacts resembles that of smooth dry contact and the film thickness shape within the contact region approximates to a constant value [122]. In such conditions, the EHL lubrication problem can be stated with the Ertel-Grubin approach [103]. This method is employed in the semi-analytical traction prediction model developed in this study.

Figure 4.1 illustrates a lubricated elliptical contact interface in which the semi-minor axis is oriented to the rolling velocity component and aligned with the x-axis. The position of the spin pole is included to generalize the model to arbitrary contact conditions. Point O refers to the geometric origin of the contact ellipse while point P indicates the spin pole position.

Film thickness distribution inside the contact region is considered constant and equal to the central film thickness value h_c. While, The pressure distribution $p(x, y)$, contact area A_H, and gap outside the interface $h(x, y)$, follow the Hertzian solution for general elliptical contacts. For an arbitrary contact point Q inside the interface, local fluid traction $\tau(x, y)$ depends on local fluid pressure $p_f = p(x, y)$, film thickness h_c, and kinematic conditions. Besides, spin affects the sliding speed distribution inside the Hertzian contact region and the sliding direction φ plays an important role on the traction determination.

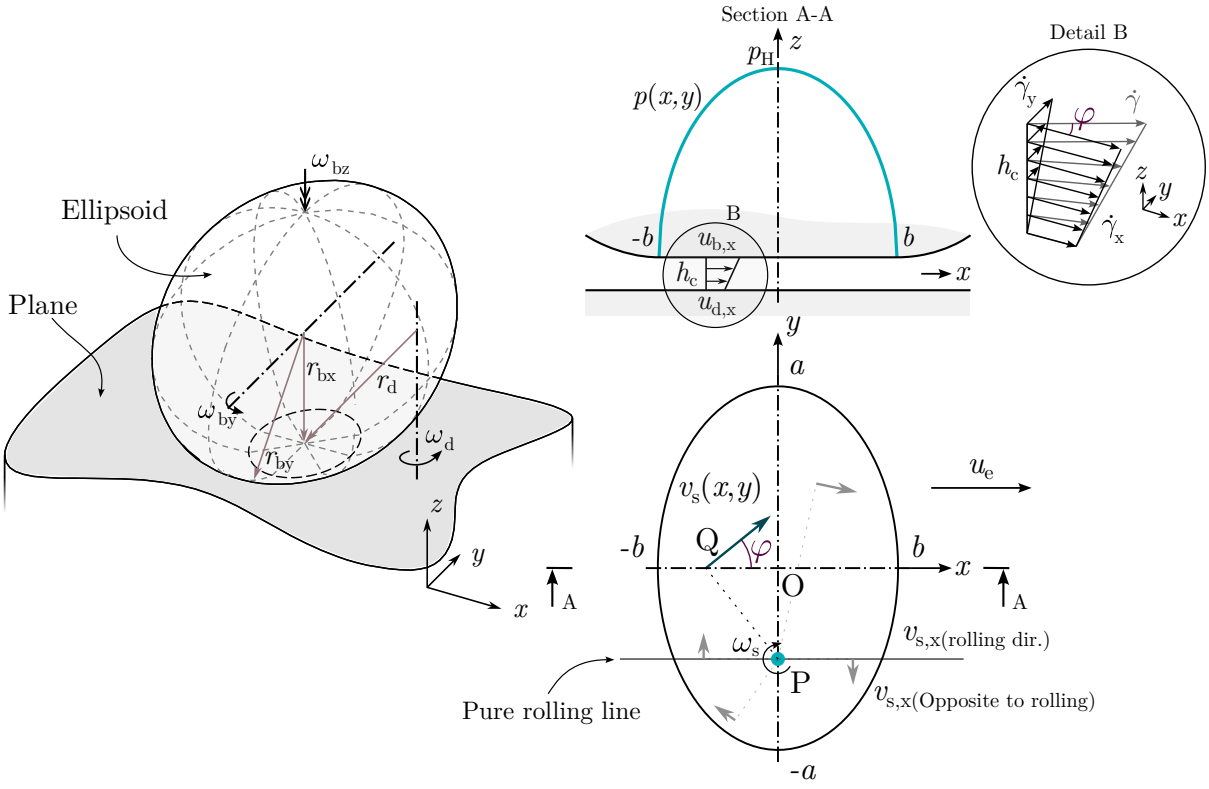

Figure 4.1: Detail of a rolling and longitudinal sliding contact with spin motion.

4.1.1.1 *Contact mechanics*

In order to calculate the local deformations, each body can be considered as an elastic half-space loaded over a small elliptical region of its plane surface [123, 124]. By this simplification, generally followed in contact stress theory, the highly concentrated contact stresses are treated separately from the general distribution of stress in the two bodies which arises from their shape and the way in which they are supported [125]. The method proposed by Hertz in 1882 is widely used due to its simplicity. Even if the integration may be difficult, the results are simple analytical equations to calculate the deformations [121]. Hertz contact theory is derived from the analytical solution of elasticity theory equations [126] under half-space approximation:

- Surface are infinitely large half-spaces.
- Pressure profile is parabolic (which assumes that the shape of the bodies in contact can also be approximated well with parabolic shapes, e.g., sphere, ellipse or a cylinder).
- All the assumptions of the classical theory of elasticity apply (small strain, homogeneous material).
- Surfaces in contact are ideally smooth. Surface roughness is neglected.

The general elliptical contact represents almost all the contact interfaces. The equation of the semiaxis of the elliptical contact interface as well as the Hertzian maximum pressure equation are shown in Table 4.1.

Table 4.1: Hertz contact model equations [126].

Semimajor axis (a)	Seminor axis (b)	Hertzian pressure
$a = \left(\frac{6 \cdot k_e^2 \cdot \varepsilon \cdot F_n \cdot R_e}{\pi \cdot E^*}\right)^{1/3}$	$b = \left(\frac{6 \cdot \varepsilon \cdot F_n \cdot R_e}{\pi \cdot k_e \cdot E^*}\right)^{1/3}$	$p_H = \frac{3 \cdot F_n}{2 \cdot \pi \cdot a \cdot b}$

where $\varepsilon = 1.0003 + 0.5968 \cdot (R_y / R_x)$ represents the simplified elliptic integral and $k_e = 1.0339 \cdot (R_x / R_y)^{0.636}$ the ellipticity parameter. Similarly, E^* represents the effective elasticity modulus defined as shown in Equation 4.1 and R_e is the effective curvature radius calculated as shown in Equation 4.2.

$$\frac{1}{E^*} = \frac{1}{2}\left[\frac{1-\nu_1}{E_1} + \frac{1-\nu_2}{E_2}\right] \tag{4.1}$$

$$\frac{1}{R_e} = \frac{1}{R_x} + \frac{1}{R_y} = \left(\frac{1}{R_{x,1}} + \frac{1}{R_{x,2}}\right) + \left(\frac{1}{R_{y,1}} + \frac{1}{R_{y,2}}\right) \tag{4.2}$$

where, E is the elasticity modulus (Young's modulus) of the solids in contact, ν is the Poisson's ratio and R is the curvature of the contact in x-direction and y-direction of each component in contact respectively. It is worth mentioning that as represented in Figure 4.2, the semiminor axis of the contact is aligned with rolling motion, therefore, the simplified elliptic integral ε and the ellipticity parameter k_e are calculated inversely to what is is commonly stated, where the semi major axis is usually in x-direction.

The pressure distribution inside the Hertzian contact region is a parabolic shaped distribution given by Equation 4.3, represented in Figure 4.3.

$$p(x,y) = p_{\mathrm{H}} \cdot \sqrt{1 - \frac{x^2}{b^2} - \frac{y^2}{a^2}}, \quad \text{for } (x,y) \in A_{\mathrm{H}} \tag{4.3}$$

The maximum elastic deflection δ of the contact pair is calculated by Equation 4.4.

$$\delta = \Gamma \left[\frac{9}{2 \cdot R_{\mathrm{e}} \cdot \varepsilon} \cdot \left(\frac{F_{\mathrm{n}}}{\pi \cdot k_{\mathrm{e}} \cdot E^*} \right)^2 \right]^{1/3} \tag{4.4}$$

with the Γ elliptical integral determined as $\Gamma \approx 1.5277 + 0.6023 \cdot \ln(R_{\mathrm{y}}/R_{\mathrm{x}})$.

The gap between the bodies in contact becomes zero within the Hertzian contact region, while the gap between the bodies in contact outside the contact zone may be determined by the approximation shown in Equation 4.5 [124].

$$\delta_z^p = \frac{1}{2 \cdot \pi \cdot E^*} \cdot \left(L - M \cdot y^2 - N \cdot x^2 \right) \tag{4.5}$$

where δ_z^p represents the surface displacement outside the Hertzian contact region which is used to determine the gap between both components in contact:

$$L = \pi \cdot b \cdot p_{\mathrm{H}} \cdot \Gamma \tag{4.6}$$

$$M = \frac{\pi \cdot b \cdot p_{\mathrm{H}}}{a^2 \cdot e^2} \left[\Gamma - \varepsilon \right] \tag{4.7}$$

$$N = \frac{\pi \cdot b \cdot p_{\mathrm{H}}}{a^2 \cdot e^2} \left[\frac{a^2}{b^2} \varepsilon - \Gamma \right] \tag{4.8}$$

with, $e = 1 - 1/k^2$, for $a > b$.

4.1.1.2 *Kinematics*

Different kinematic behaviours is distinguished in this kind of contacts. On one hand, rolling motion represents the linear speed of both components in the same direction, this speed introduces lubricant to the contact and therefore it is essential to generate a lubricant fluid film separating both components in contact. On the other hand, sliding motion is determined by the difference in speed of the components in contact. Sliding is essential to generate shear stresses and therefore traction on the contact interface. Furthermore, two different sliding motion types may be distinguished in machine elements such as angular contact ball bearings or T-CVTs—longitudinal sliding and spinning sliding. Longitudinal sliding is the sliding that occurs in the same direction to rolling motion, while spinning speed a circular sliding speed distribution with the rotation axis normal to the contact interface.

The rolling speed is commonly determined by the entrainment speed, which is the mean rolling speed of both components defined in Equation 4.9.

$$u_{\mathrm{e}} = \frac{u_{1,\mathrm{x},0} + u_{2,\mathrm{x},0}}{2} \tag{4.9}$$

where, u refers to the linear speed, the subscript e refers to the main rolling direction (x-direction) and the subscript 1 and 2 refers to the components in contact respectively; the subscript 0 determines to the speed on the centre of the contact interface (point O in Figure 4.2).

The longitudinal sliding of the contact is defined by the sliding on the centre of the contact interface. This motion is important because it generates the shearing of the lubricant fluid film in rolling direction and in fact, traction. Usually, the sliding motion is represented by the dimensionless slide to roll ratio parameter defined in Equation 4.10.

$$SRR_{\mathrm{x},0} = 100 \cdot \frac{v_{\mathrm{s,x},0}}{u_{\mathrm{e}}} = 100 \cdot \frac{2 \cdot (u_{1,\mathrm{x},0} - u_{2,\mathrm{x},0})}{u_{1,\mathrm{x},0} + u_{2,\mathrm{x},0}} \tag{4.10}$$

where, $v_{\mathrm{s,x},0}$ is the sliding speed in the centre of the contact interface in x-direction, and u_{e} is the entrainment speed.

Spin motion is a circular sliding distribution with the rotation axis normal to the contact interface [51]. The spinning speed occurring between two rolling components depends on the disposition of the components (studied in Chapter 2, Figure 2.5). In order to quantify it, a spin to roll ratio is commonly used in the literature; defined in Equation 4.11 [53, 70, 127].

$$S_{\mathrm{p}} = \frac{\omega_{\mathrm{s}} \cdot \sqrt{a \cdot b}}{u_{\mathrm{e}}} \tag{4.11}$$

where, ω_{s} is the spinning angular speed, a and b are the elliptical semi-axes of the contact interface and u_{e} is the entrainment speed.

In conditions where both, longitudinal sliding and spinning occur together a spin pole appears and its position varies as a function of the longitudinal sliding. The spin pole is considered to be the point where the linear speed of both components is equal (point P in the sliding speed distribution shown in Figure 4.2). Therefore, from vector composition the spin pole position $\overline{\mathrm{PO}}$ and local sliding speed distribution $v_{\mathrm{s}}(x, y)$ can be computed. The former is determined from the overall sliding speed calculated at the centre of the contact while the latter additionally depends on the distance from the centre of the contact to the evaluated point Q on the contact interface. Equations 4.12 and 4.13 summarize the results.

$$\vec{\omega}_{\mathrm{s}} \times \overrightarrow{\mathrm{PO}} = \vec{v}_{\mathrm{s}}(0,0) \quad \rightarrow \quad |\overrightarrow{\mathrm{PO}}| = \frac{\vec{v}_{\mathrm{s}}(0,0)}{\vec{\omega}_{\mathrm{s}}} \tag{4.12}$$

$$\vec{v}_{\mathrm{s}}(x,y) = \vec{\omega}_{\mathrm{s}} \times \overrightarrow{\mathrm{PQ}} = \vec{\omega}_{\mathrm{s}} \times \left(\overrightarrow{\mathrm{PO}} + \overrightarrow{\mathrm{OQ}}\right) \tag{4.13}$$

The resulting sliding speed distribution of Figure 4.2 leads to several conclusions to understand the effects of spinning in traction, which are as follows:

- Not all the sliding speed vectors are aligned with entrainment speed and that the sliding speed on the centre of the contact interface O represents the longitudinal sliding.
- The sliding vectors above the spin pole are in same direction to rolling motion, which are required to generate traction. While the sliding vectors below the spin pole are in opposite direction to rolling, which increase and power losses and do not help in traction.
- Sliding components in y-direction are self cancelled since the sliding in positive direction at $-b$ point is cancelled with the sliding in negative direction in $+b$.

- Due to the disposition of the rolling components, the spin pole has to be at any point in y-axis and $x = 0$. The location of the spin pole varies as a function of the longitudinal sliding

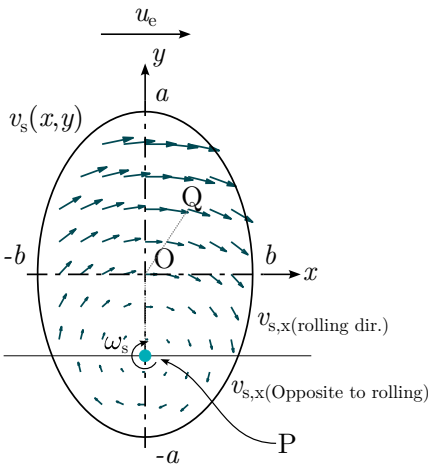

Figure 4.2: Sliding speed distribution representation on an elliptical contact interface where longitudinal sliding and spin occur together.

4.1.1.3 *Lubricant fluid film thickness*

It is known that the film thickness shape is a horse-shoe shaped with a central film thickness and a minimum film thickness in the outlet of the contact as represented in Figure 4.3. However, in this model constant film thickness approximation has been considered following the Chittenden's central film thickness formula [97].

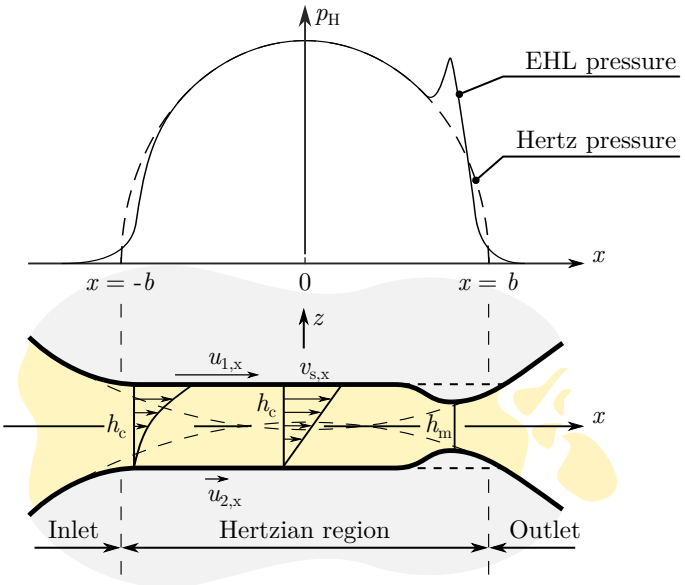

Figure 4.3: EHL film thickness and pressure distribution representation in rolling direction where the coordinate system has been represented in the middle of the contact interface and in the mid-plane of the fluid film. Adapted from [119].

This model has been selected since it has been proven that it reveals best results over a wide range of EHL conditions [100] (see Equation 4.14). The film thickness is defined by the lubricants properties in the inlet of the contact [128, 129].

$$\frac{h_c}{R_y} = 4.31 \cdot G^{0.49} \cdot U^{0.68} \cdot W^{-0.073} \cdot \left(1 - e^{-1.23(R_y/R_x)^{2/3}}\right) \tag{4.14}$$

The G, U and W represent the dimensionless material, speed and load parameters respectively, the equations to calculate them are shown in Table 4.2. The pressure-viscosity coefficient, α is studied later in the rheology section in this chapter [57]. Note that in Equation 4.14 the central film thickness is related to the curvature in y-direction since the semimajor axis is oriented in y-direction.

Table 4.2: Dimensionless parameters for the film thickness calculation [100].

Speed, U	Material, G	Load, W
$\frac{\eta_0 \cdot u_e}{E^* \cdot R_e}$	$\alpha \cdot E^*$	$\frac{F_n}{E^* \cdot R_x^2}$

The film thickness have been correlated with experimental data published in the literature for the selected lubricants (presented later in this chapter; see Table 4.6). Figure 4.4 shows the obtained results which showed good agreement in the obtained results with an average error of 9.52% for S50 lubricant and 9.23% for T9 lubricant. In addition the maximum difference on the obtained film thickness was 19 nm for S50 and 34 nm for T9.

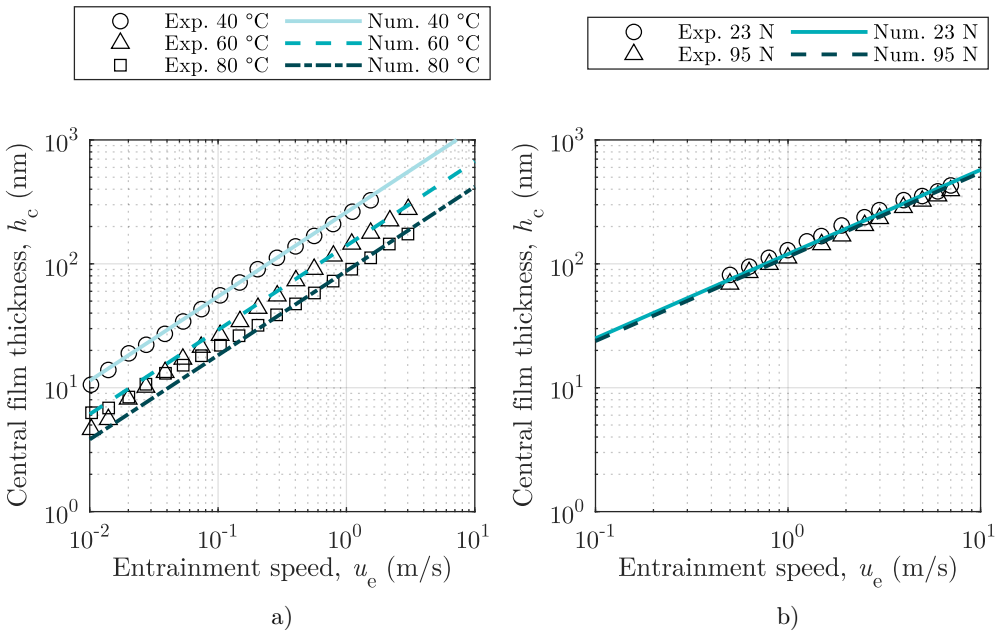

Figure 4.4: Measured and predicted central film thickness for a) Santotrac 50 and b) Shell T9 lubricant (experimental results obtained from [130, 131]).

Additionally, two film thickness reduction factors were considered which determine correction factors as a result of the working conditions happening in the contacts. On one hand, Equation 4.15 reflects the inlet shear heating which is a consequence of the heating of the lubricant at the inlet as a result of possible convection of the lubricant in opposite direction to rolling in the lubricant meniscus [132].

$$C_{\mathrm{T}} = \frac{1 - 13.2\,(p_{\mathrm{H}}/E^{*})\,B_{\mathrm{r}}^{0.42}}{1 + 0.213\,(1 + 2.23 \cdot SRR^{0.83})\,B_{\mathrm{r}}^{0.64}} \tag{4.15}$$

where, B_{r} is the Brinkman number calculated as shown in Equation 4.16. Here, the changes of the lubricant viscosity as a function of temperature is considered.

$$Br = -\frac{\partial \eta}{\partial \Theta}\frac{u^2}{K_{\mathrm{oil}}} \tag{4.16}$$

On the other hand, the film thickness reduction caused by the lubricant's shear thinning is determined by Equation 4.17 [133]. There the film reduction at high shear rate conditions are considered, therefore this equations mainly depends on the SRR value.

$$C_{ST} = \frac{1}{\left\{1 + 0.79[(1 + SRR)Ws]^{1/(1+0.2\cdot SRR)}\right\}^{3.6(1-n)^{1.7}}} \tag{4.17}$$

where, n is the power-law component in the Carreau shear thinning equation (later studied in this chapter) and Ws is the Weissenberg number defined as shown in Equation 4.18, where, $h_{\mathrm{c,iso}}$ is the central film thickness at isothermal condition.

$$Ws = \frac{u_{\mathrm{e}} \cdot \eta_0}{h_{\mathrm{c,iso}} \cdot \tau_{\mathrm{c}}} \tag{4.18}$$

The corrected central film thickness (h'_{c}) is calculated by Equation 4.19 where the correction factors C_{T} and C_{ST} are multiplied to the film thickness (h_{c}) value obtained from Equation 4.14.

$$h'_{\mathrm{c}} = h_{\mathrm{c}} \cdot C_{\mathrm{T}} \cdot C_{\mathrm{ST}} \tag{4.19}$$

Additionally, the literature has revealed that spin motion does not affect the pressure distribution and central film thickness of EHL contacts [52, 134, 135], however, the minimum film thickness decreases. Therefore, minimum film thickness reduction factor due to spinning has been considered in the determination of the lubrication regime with the purpose to ensure that the tested working conditions were under the full film lubrication regime. A minimum film thickness reduction factor was proposed by Porras-Vazquez et al. [53, 127] defined in Equation 4.20.

$$C_{\mathrm{sp}} = 0.26 \cdot \left(e^{0.27\cdot S_{\mathrm{p}}} - e^{-0.1\cdot S_{\mathrm{p}}}\right) \tag{4.20}$$

where, S_{p} is the spin to roll defined as $2 \cdot \omega_{\mathrm{s}} \cdot a/u_{\mathrm{e}}$ (circular contact in Equation 4.11). The minimum film thickness considering spinning motion is calculated as $h_{\mathrm{m,sp}} = (1 - C_{\mathrm{sp}}) \cdot h_{\mathrm{m,ns}}$, where, the subscript sp means with spinning motion and the subscript ns means without spinning.

4.1.1.4 *Rheology*

The lubricants rheology considers the changes in lubricant properties as a result of the operation conditions such as temperature, pressure or shear stresses. The main parameter that determines the shear stresses that a lubricant fluid film can transmit, is the viscosity of the lubricant. In this section these parameters are studied.

Newtonian viscosity

The viscosity of a fluid changes a sa function of pressure and temperature. This is considered as the Newtonian viscosity and usually represented as low shear viscosity η_{L}. Different models have been proposed to predict the Newtonian viscosities: starting from the Barus [136] and Roelands [137], which are no longer used since it have been proven that they lead to an error for pressures higher than 0.5 GPa since exponential behaviour is considered [138]. Mainly two different models are used to date, the Vogel like model [131] and the Yasutomi model [139]. The improved Yasutomi is a free volume equation that does not need the equation of state to correlate the viscosity with pressure and temperature. For that purpose, this study the improved Yasutomi model has been used (see Equation 4.21) [140].

$$\eta_{\mathrm{L}} = \eta_{\mathrm{g}} \exp\left[\frac{-2.303 \cdot C_1(\Theta - \Theta_{\mathrm{g}}) \cdot F'}{C2 + (\Theta - \Theta_{\mathrm{g}} \cdot F')}\right] \tag{4.21}$$

where, η_{L} is the low shear viscosity, η_{g} is the low-shear viscosity at glass transition, Θ_{g} is the glass transition temperature ($\Theta_{\mathrm{g}} = \Theta_{\mathrm{g0}} + A_1 \ln(1 + A_2 \cdot p)$), which varies with pressure, and F' is the dimensionless relative thermal expansivity of the free volume ($F' = (1 + b_1 \cdot p)^{b_2}$). Figure 4.5 shows the results obtained from the improved Yasutomi model for the selected two lubricants. In addition, experimental low shear viscosity values as a function of pressure for different temperature conditions are also represented and the results show good agreement between the results.

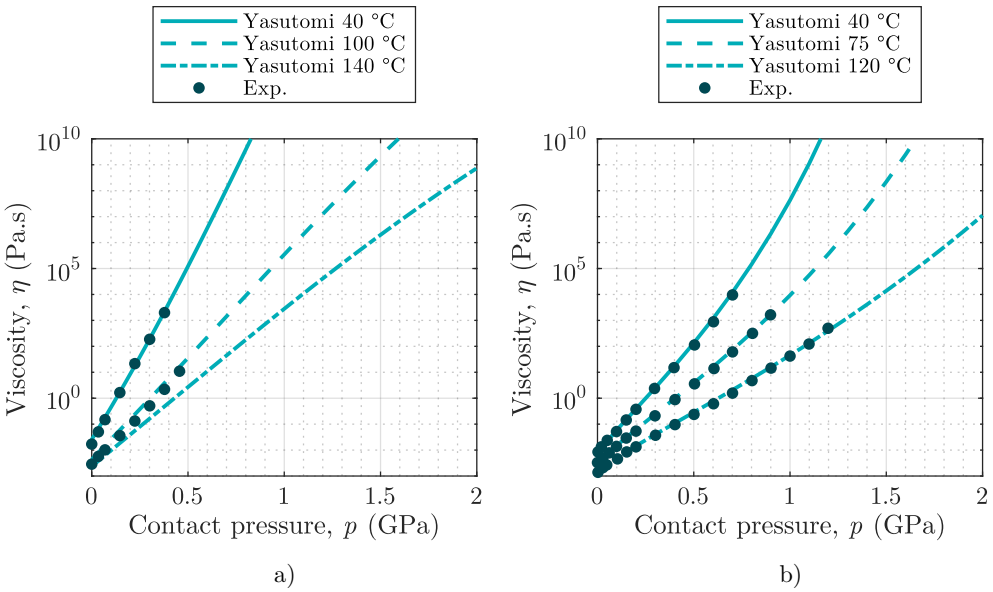

Figure 4.5: Newtonian viscosity validation for a) S50 (BCH) [141] and b) T9 [131].

The relation between pressure and viscosity was related by a pressure-viscosity coefficient. It is no longer useful for the viscosity calculation inside the Hertzian contact region [142], for the film thickness calculation though are widely used which is determined by the lubricant values in the inlet of the contact [58]. There are different pressure viscosity coefficient definitions, two of them are shown in Table 4.3. However, the definition of the pressure viscosity coefficient is still an issue under discussion in the scientific community [143].

Table 4.3: Pressure viscosity coefficient definitions [57].

Secant pressure-viscosity coefficient	$\alpha_B = \frac{\ln(\eta_L(p)) - \ln(\eta_L(0))}{p}$
Reciprocal asymptotic isoviscous pressure-viscosity coefficient	$\alpha^* = \left[\int_0^\infty \frac{\eta_L(p=0)dp}{\eta_L(p)}\right]^{-1}$

Different studies regarding the determination of the pressure viscosity coefficient based on film thickness measurements were carried out [130, 144, 145]. Which is of great importance since they are used for its calculation. Table 4.4 shows the pressure viscosity coefficient obtained from film thickness measurements of S50 lubricant for 0.5 GPa of Hertzian contact pressure.

Table 4.4: Pressure viscosity coefficients of Santotrac 50 lubricant for different temperatures [130].

Temperature (°C)	40°C	60°C	80°C
dynamic viscosity, η_0 (Pa·s)	$26.81 \cdot 10^{-3}$	$12.68 \cdot 10^{-3}$	$6.92 \cdot 10^{-3}$
Pressure viscosity coefficient, α (GPa^{-1})	28.2	23.0	19.3

Two different pressure viscosity coefficient formulations are compared in Figure 4.6. It shows how the secant pressure viscosity coefficient best matches to the literature published data. Accordingly, the film thickness results (shown in Figure4.4) lead to better results by means of the secant pressure viscosity coefficient formulation, therefore, in the film thickness calculation of this model the secant pressure viscosity definition has been used.

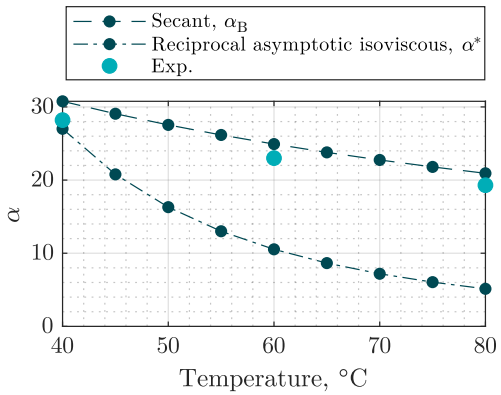

Figure 4.6: Comparison of different pressure viscosity coefficient definitions for Santotrac 50 with experimental data published in the literature [130].

Non-Newtonian viscosity

The non-Newtonian rheology considers the variations on the lubricants viscosity as a function of the shear strain rate and/or shear stress [146] (further explained in this chapter). Different models to reflect the non-Newtonian behaviour are available in the literature such as the Carreau power-law model [147] and the Eyring sinh-law model [56]. In this study, the non-Newtonian behaviour is modelled by means of the Carreau equation (see Equation 4.22) [131, 148]. This model considers the changes in lubricant viscosity as a function of the shearing of the lubricant fluid film, where the viscosity decreases while the shear stresses increases. It have to be pointed out that lubricant additives may affect the non-Newtonian behaviour of the lubricant, which is something that happens with the Santotrac 50 traction lubricant, which has two Newtonian regions [149], a double modified Carreau-Yasuda equation was proposed.

$$\eta_{\mathrm{G}} = \eta_{\mathrm{L}} \left[1 + \left(\frac{\tau}{G_{\mathrm{S}}} \right)^2 \right]^{\frac{1-(1/n)}{2}} \tag{4.22}$$

where, η_{G} si the generalized viscosity and η_{L} si the low shear viscosity (the one obtained from the Newtonian model). τ is the shear stress, G_{S} is the shear modulus of the lubricant and n is the power law exponent.

The validation of the non-Newtonian behaviour of Santotrac 50 and Shell T9 has been carried out based on the measurements published in the literature [131, 149, 150]. Results showed good agreement for the base oil of S50 (BCH) and T9 lubricant, while some differences in the Newtonian region were achieved for the S50 lubricant as a result of the second Newtonian region and the effects of the additives [149].

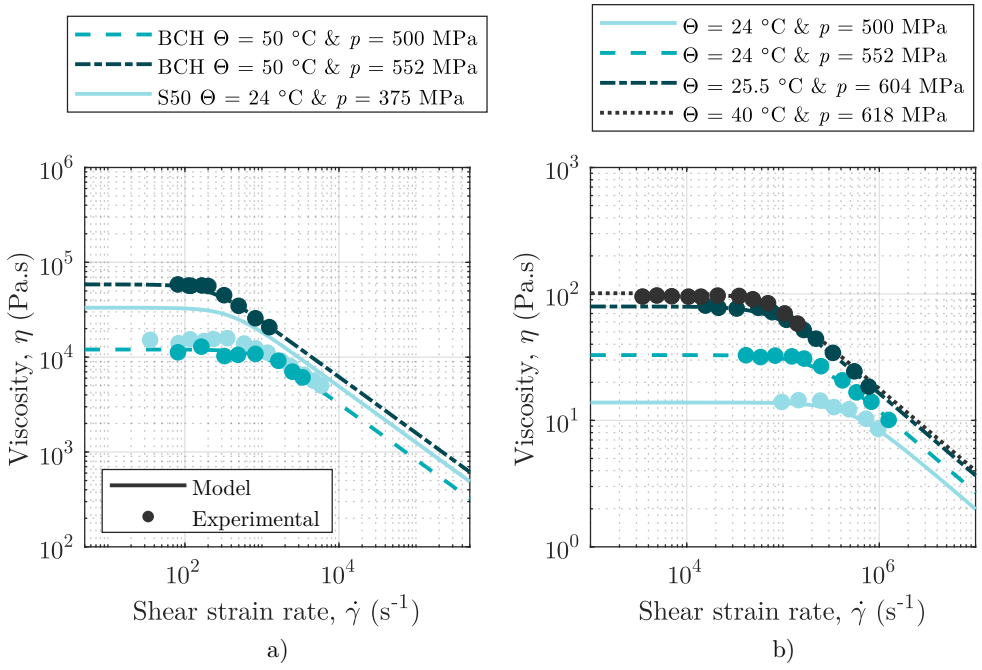

Figure 4.7: Non-Newtonian rheology of a) S50 (BCH) [141, 149] and b) T9 lubricant [131].

Limiting Shear Stress

Literature mentions that there is a plastic yield on the shear stresses of a lubricant, usually known as Limiting Shear Stress (LSS) [22, 151]. This region represents that shear stresses of the lubricant no longer rise increasing shear strain rate. According to Limiting Shear Stress analysis published by Bair [57], it is shown that the limiting shear stress is achieved earlier in the centre of the contact interface and it is achieved later in the outer region of the interface. It has to be pointed out that the limiting shear stress problem is not resolved yet. It is still one of the challenges of the EHL field to make accurate predictions of the traction coefficient [59, 151]. Different models to determine the limiting shear stress are proposed as a function of the lubricant that has to be modelled. Commonly, the model used to calculate the limiting shear stress is determined by the traction coefficient measured at very high contact pressures, the maximum traction coefficient measured is used as the limiting shear stress-pressure coefficient Λ. Therefore, the limiting shear stress is calculated as shown in Equation 4.23.

$$\tau_{\mathrm{LSS}} = \Lambda \cdot p \tag{4.23}$$

However, for Santotrac 50 lubricant that model is no longer feasible according to several authors [152–156]. The Limiting Shear Stress of S50 is modelled by Equation 4.24.

$$\tau_{\mathrm{LSS}} = \tau_{\mathrm{L0}} + \Lambda \cdot p \tag{4.24}$$

Both equations are similar, nevertheless, the limiting shear stress of S50 has a τ_{L0} value. Therefore, as stated by several authors, the maximum traction coefficient of Santotrac 50 decreases with pressure [152–158]. Figure 4.8 depicts the limiting shear stress values as a function of pressure published in the literature by several authors. Based on the presented data the values of τ_{L0} and Λ may be determined adjusting the values (further presented in Table 4.6).

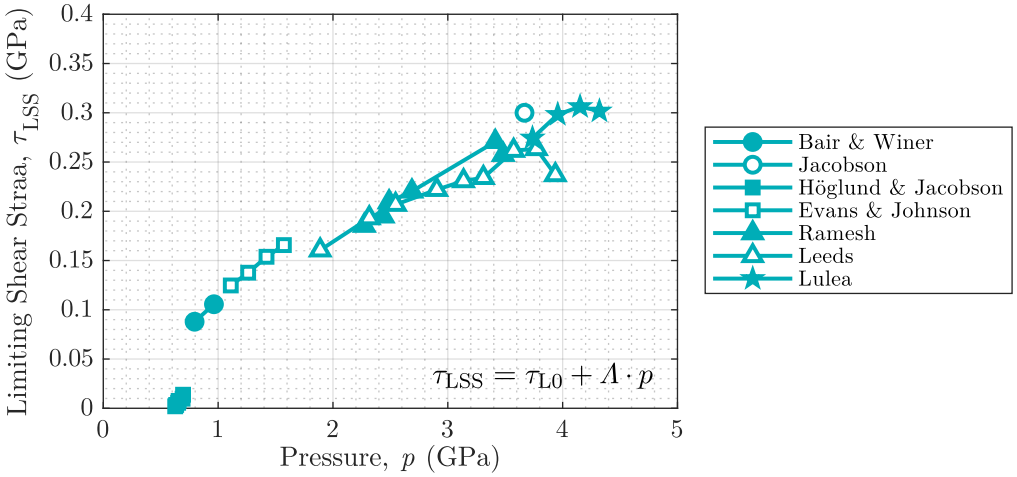

Figure 4.8: Limiting shear stress adjustment for S50 lubricant based on literature published data [157].

4.1.2 *Isothermal traction calculation*

The shear strain rate represents the shearing of the lubricant fluid film. Where according to the sliding vectors in x and y-direction the shearing may be distinguished in this two components. The shearing in each direction would be the responsible of generating the shearing in the corresponding direction. Nevertheless, it has to be pointed out that the shear strain rate affects the rheological behaviour of the lubricant regardless the direction, therefore the resultant shear strain rate is represented in Equation 4.27.

$$\dot{\gamma}_{\mathrm{x}}(x,y) = \frac{\partial u_{\mathrm{x}}}{\partial z} \approx \frac{v_{\mathrm{s,x}}(x,y)}{h} \tag{4.25}$$

$$\dot{\gamma}_{\mathrm{y}}(x,y) = \frac{\partial u_{\mathrm{y}}}{\partial z} \approx \frac{v_{\mathrm{s,y}}(x,y)}{h} \tag{4.26}$$

$$\dot{\gamma}^2 = \dot{\gamma}_{\mathrm{x}}^2 + \dot{\gamma}_{\mathrm{y}}^2 \tag{4.27}$$

The shear strain rate represents the shearing of the lubricant confined inside the Hertzian contact region. In the equations shown above the Couette flow was represented. Which defines the shearing of the lubricant was the relation between the sliding speed and the film thickness. Nevertheless, the Poiseuille flow has been neglected there since no variations in temperature were considered along the fluid film (both where represented in Figure 4.3). Different flows may occur in the contact and it is subjected to assumptions since it can not be measured [80, 159]. Assuming that there is no temperature variation, and thus, shear stress variation along the fluid film (in z-direction), it may be assumed that the shear strain rate is Couette flow. In order to calculate other shear strain distributions numerical calculations of the temperature distribution should be considered, which complicates the calculation considerably [103].

The shear stress of the lubricant is determined by the lubricant shear strain rate. Figure 4.9 shows depicts the shear stress evolution as a function of the shear strain rate where different region are identified.

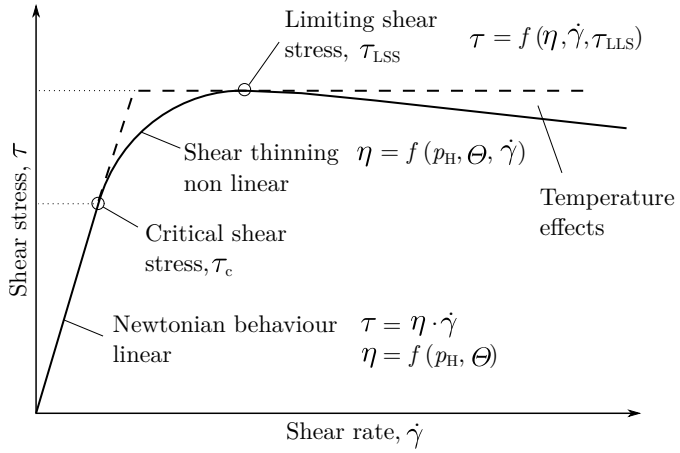

Figure 4.9: Lubricant shear stress as a function of the shear strain rate and the identification of the different regions on the curve. Adapted from [84].

Under low shear strain rate conditions. the figure represents a linear increase in shear stress which corresponds to the Newtonian behaviour of the lubricant fluid film. Further increase in the lubricant shearing shows a decrease in lubricant's viscosity and a corresponding decrease in the traction curve slope, this trend is related to a non-Newtonian behaviour of the lubricant known as shear thinning. A gradual decrease on the shear stresses is identified under high shear strain rate conditions, which corresponds t the increase on lubricants temperature due to the sliding and the subsequent decrease on viscosity and consequently shear stress. Nevertheless, a maximum traction coefficient is achieved in this kind of contacts that correspond to the Limiting Shear Stress, a plastic yield of the lubricant fluid film that determines the maximum shear stress that a lubricant can afford, from that point on, the shear stresses no longer increase with shearing of the lubricant.

In addition, since spinning motion appears in the contact interface, the sliding direction is no longer aligned with rolling direction, therefore a similar behaviour may happen with the shear stresses, that may be divided in x and y-direction as a function of the sliding speed distribution. A representation of the shear stress distribution for a rolling, longitudinal sliding and spinning condition is represented in Figure 4.10. It is represented how in pure rolling condition ($SRR = 0\%$) the shear stresses in positive would be cancelled with the shear stresses in negative in the other side of the contact. However, while longitudinal sliding increase, the shear stresses in x-direction are no longer symmetric according to the horizontal axis of the contact surface while the shear stresses in y-direction are maintained symmetric according to the vertical axis.

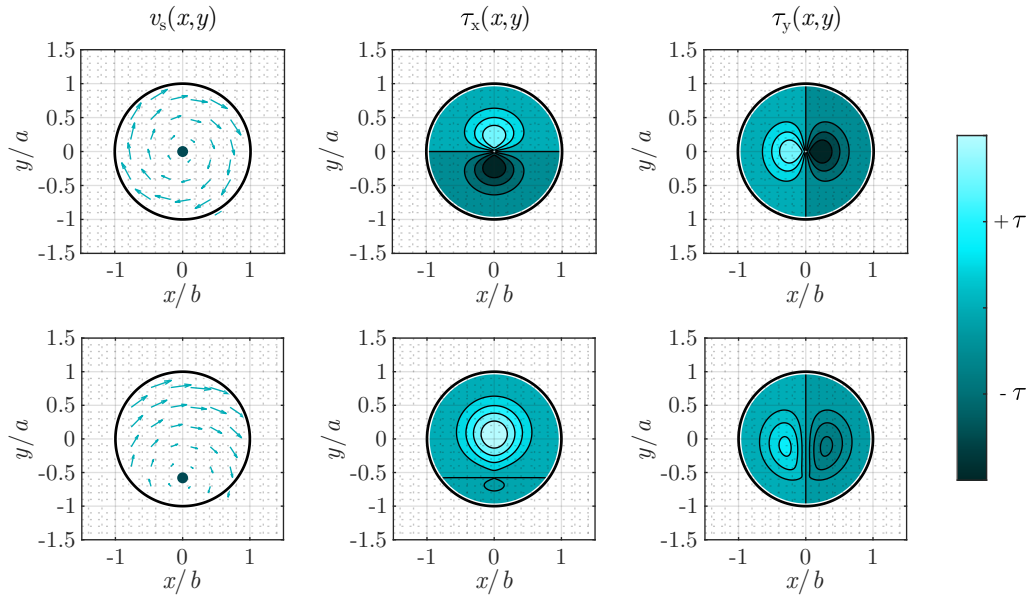

Figure 4.10: Dimensionless shear stress distribution in x and y-direction on the contact interface occurring spin motion for (top) $SRR = 0\%$ and (bottom) $SRR > 0\%$ (shear stresses in scale).

In the EHL regime, friction is caused by shearing of the fluid film confined in the contact interface. Hence, friction force can be calculated by integrating the shear stress across the contact area. The non-Newtonian shear stress τ in the lubricant is a function of the strain rate $\dot{\gamma}$, which depends on the sliding speed $v_s(x, y)$ and the non-Newtonian viscosity $\eta_G(p, \Theta, \dot{\gamma})$. Furthermore, if the limiting shear stress coefficient Λ is considered, fluid pressure $p(x, y)$ affects the maximum traction attainable [151]. Therefore, local fluid behaviour is limited by the relationship between shear rate and pressure distributions. As the rheology of the lubricant is modelled by means of

the Carreau non-Newtonian equation [147], the general mathematical formulation for traction prediction in a isothermal EHL contact is shown in Equation 4.28 and Equation 4.29. In spin conditions, since the sliding speed distribution is no longer aligned with rolling speed, there may appear some traction in transversal direction. The φ angle denotes the angle of the local sliding speed direction to the main rolling speed (x-direction) represented in Figure 4.1.

$$\mu_{\mathrm{x}} = \frac{1}{F_{\mathrm{n}}} \cdot \iint_{A_{\mathrm{H}}} \tau_{\mathrm{x}} \cdot \mathrm{d}A_{\mathrm{H}} = \frac{1}{F_{\mathrm{n}}} \cdot \int_{-b}^{b} \int_{-a}^{a} \left[\min\left(\dot{\gamma} \cdot \eta_{\mathrm{G}},\ \Lambda \cdot p\right)\right] \cdot \cos\varphi \cdot \mathrm{d}x \cdot \mathrm{d}y \tag{4.28}$$

$$\mu_{\mathrm{y}} = \frac{1}{F_{\mathrm{n}}} \cdot \iint_{A_{\mathrm{H}}} \tau_{\mathrm{y}} \cdot \mathrm{d}A_{\mathrm{H}} = \frac{1}{F_{\mathrm{n}}} \cdot \int_{-b}^{b} \int_{-a}^{a} \left[\min\left(\dot{\gamma} \cdot \eta_{\mathrm{G}},\ \Lambda \cdot p\right)\right] \cdot \sin\varphi \cdot \mathrm{d}x \cdot \mathrm{d}y \tag{4.29}$$

4.1.3 *Contact temperature determination*

At point contacts working under high load and/or sliding speed conditions significant temperature increase may occur [160]. The changes in temperature may alter the properties of the lubricant affecting the characteristics of the interface. The temperature rise can increase more than hundred degrees Celsius in a rubbing of a small area between the solids in a short period of time [124]. This temperature rise is known as flash temperature. Nevertheless, temperature rise in the lubricant film may be an important factor since heat is mainly generated by viscous dissipation and subsequent then transferred into the solids. Additionally, sliding generated by spin affects the local shear stresses and consequently the contact temperature is affected. The thermal model is based mostly on resolving the energy equation which shown in Equation 4.30 for the lubricant [161]. The energy equation of the solids is equal without the adiabatic compression and the heat generation terms which are negligible in the solids and considering the density, specific heat and thermal conductivity of the solids.

$$\underbrace{\rho C_p \left(u\frac{\partial \Theta}{\partial x} + v\frac{\partial \Theta}{\partial y} + w\frac{\partial \Theta}{\partial z}\right)}_{\text{Heat convection}} = \underbrace{K_f \left(\frac{\partial^2 \Theta}{\partial y^2} + \frac{\partial^2 \Theta}{\partial z^2}\right)}_{\text{Heat conduction}} - \underbrace{\frac{\Theta}{\rho}\frac{\partial \rho}{\partial \Theta}\left(u\frac{\partial p}{\partial x} + w\frac{\partial p}{\partial y}\right)}_{\text{Adiabatic compression}} + \underbrace{\eta\left[\left(\frac{\partial u}{\partial z}\right)^2 + \left(\frac{\partial v}{\partial z}\right)^2\right]}_{\text{Heat generation}} \tag{4.30}$$

where, Θ is the temperature, p the hydrodynamic pressure, ρ the lubricant density, and C_{p} and K_f the specific heat and thermal conductivity of the lubricant [162]. The four terms in Equation 4.30 stand for, from left to right, the heat convection, the heat conduction, the work of adiabatic compression, and the energy of viscous dissipation (heat generation), respectively [124, 163].

Different approximations have been proposed in order to simplify the calculation procedure because solving the energy equation requires numerical methods and high computational cost. Following the Tevaarwerk's mid-shear plane hypothesis [107] it is possible to derive an alternative equation to the fluid and solid energy equations. To overcome such situation, lubricant temperature rise within the contact is calculated combining the energy equation in the lubricant film with the point heat source integration method by Carslaw and Jaeger [164]. It assumes a heat source moving on the surface of the semi infinite body in x-direction. For any point Q in the contact region, the temperature of the film is calculated assuming that the heat is only conducted in the z direction and neglecting convection from the oil. Applying heat balance to the contact interface, the film temperature distribution can be expressed as:

$$\Theta_f(x,y,z) = \Theta_{\mathrm{b},1} + \iint_{A_\mathrm{H}} \alpha_\Theta \cdot \dot{q} \cdot [R_{\mathrm{fl},1} + R_\mathrm{f}]\,\mathrm{d}A_\mathrm{H} = \Theta_{\mathrm{b},2} + \iint_{A_\mathrm{H}} (1-\alpha_\Theta) \cdot \dot{q} \cdot [R_{\mathrm{fl},2} + R_\mathrm{f}]\,\mathrm{d}A_\mathrm{H} \quad (4.31)$$

where, θ_b is a constant value representing the bulk temperature of the solid, α_Θ is the heat partitioning coefficient, $\dot{q}$ is the heat source of arbitrary shape due to the local fluid shear distribution and R_fl and R_f are the thermal resistances for flash temperature rise and fluid heating respectively. The former, is computed from the analytical solution for quasi-steady state surface temperature distribution due to a moving heat source $\dot{q}(x,y)$ in a semi-infinite homogeneous medium by Carslaw and Jaeger [164] while the latter can be derived applying the energy equation and Fourier's law to a given lubricant differential area. Both solutions are presented in Equations 4.32 and 4.33 respectively.

$$R_{\mathrm{fl,i}}(x,y) = \frac{1}{2 \cdot \pi \cdot K_\mathrm{i} \cdot \sqrt{x^2+y^2}} \exp\left(-\frac{u_\mathrm{e}}{2 \cdot \chi_\mathrm{i}} \cdot \left(\sqrt{x^2+y^2} - x\right)\right) \quad (4.32)$$

$$R_\mathrm{f}(z) = \frac{1}{2 \cdot K_\mathrm{oil}} \cdot \left(\frac{h_\mathrm{c}}{2} - z\right) \quad (4.33)$$

with $\dot{q}(x,y) = \tau(x,y) \cdot v_\mathrm{s}(x,y)$ the heat generated due to shearing of the fluid, K_i is the thermal conductivity of the solid and χ the thermal diffusivity. Assuming that the heat partitioning in the interfaces is constant and equal to $\alpha_\Theta = 0.5$, the bulk temperature of the solids is equal to that of the oil bath Θ_0 and it is simplified. In such conditions the fluid temperature distribution in the mid plane can be computed as a space convolution between $\dot{q}(x',y')$ and $R(x-x',y-y')$ which can be solved by FFT methods [165, 166] after discretization on a uniform grid [167, 168] (see Equation 4.34). The calculation method is detailed in Appendix A. Figure 4.11 shows a representative mid film temperature rise distribution.

$$\Theta(x,y) = \mathrm{IFFT}\left\{\mathrm{FFT}(\dot{q}) \cdot R(x,y)\right\} \quad (4.34)$$

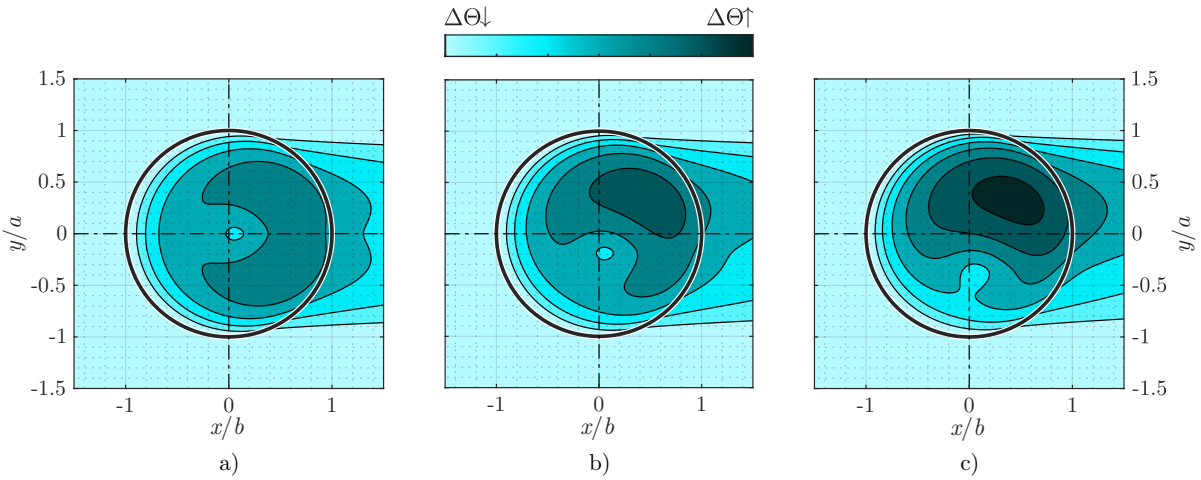

Figure 4.11: Temperature rise distribution for a rolling, longitudinal sliding and spinning contact for a) $SRR = 0\%$, b) $SRR > 0\%$ and c) $SRR \gg 0\%$.

4.1.4 *Calculation procedure*

The flowchart shown in Figure 4.12 shows the procedure followed to determine the variables governing traction, which are as follows:

1. Determine input variables of the model considering the mechanical properties, geometries, disposition, and speed of the components, together with the supply temperature and the rheological properties of the lubricant.
2. Determine contact interface size and contact pressure distribution by means of the Hertzian contact model.
3. Calculate sliding speed distribution for a range of imposed longitudinal sliding conditions to generate a traction curve as a function of longitudinal sliding.
4. Determine film thickness and shear strain rate distribution.
5. Calculate viscosity distribution in the contact region based on pressure, temperature, and kinematics.
6. Determine shear stresses and integration of shear stresses to calculate traction load.
7. Calculate changes in temperature distribution due to shearing of the lubricant fluid film.
8. Repeat operations 5, 6, and 7, updating the contact temperature distribution until stabilized ($\Delta\Theta(x,y)_{\max} \leq 1°\text{C}$)

In the calculation two steel components in contact were considered (instead of in the validation of the film thickness, since measurements are made by glass discs [92]). The most commonly used steel in rolling and sliding components is the AISI 52100 (100Cr6) through hardened steel [169] (Table 4.5).

Table 4.5: Properties of the solids in contact.

Steel AISI 52100 [169–172]			
Elasticity modulus	E	GPa	210
Poisson's ratio	ν	(-)	0.3
Density	ρ	kg/m^3	7800
Thermal conductivity	K	W/mK	21
Specific heat	c	J/kgK	460

In addition, two lubricants have been selected for the analysis—Shell Turbo9 and Santotrac 50 traction lubricant. The lubricant properties are shown in Table 4.6.

- Santotrac 50 traction lubricant was selected because it is widely used in T-CVT transmissions [141, 149, 173–175]. It is a specific high traction fluid.
- Shell T9 lubricant was selected because it is an accurately characterized lubricant in the scientific literature and because traction curves with spin motion were published for this specific lubricant [57, 72, 73, 131, 139, 176].

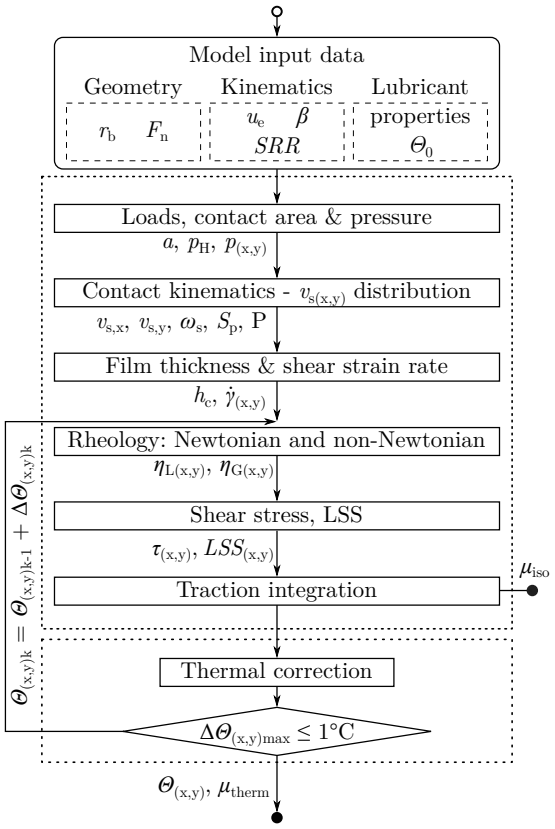

Figure 4.12: Semi-analytical traction prediction model.

Table 4.6: Properties of the selected lubricants.

			Santotrac 50	**Shell T9**
Viscosity (Θ = 40°C)	η_0	Pa·s	0.02681	0.008
Density (Θ = 40°C)	ρ_0	kg/m^3	886	872
Yasutomi parameters	$A1$	°C	166	188.86
	$A2$	GPa^{-1}	0.846	0.719
	$b1$	GPa^{-1}	5.96	8.2
	$b2$	(-)	-0.8392	-0.5278
	$C1$	(-)	15.82	16.09
	$C2$	°C	16.13	17.38
	Θ_{g0}	°C	-58.46	-83.2
	η_g	Pa·s	$1{\cdot}10^{12}$	$1{\cdot}10^{12}$
Shear modulus	G_s	MPa	13	7
Power law exponent	n	(-)	0.41	0.35
LSS constant	τ_{L0}	(GPa)	0.016	0
LSS-pressure coefficient	Λ	(-)	0.091	0.083
Thermal conductivity	K_{oil}	W/mK	0.104	0.1114

4.2 VALIDATION OF THE TRACTION PREDICTION MODEL

The traction coefficient validation has been made both, based on literature published data and experimental traction measurements for the afore mentioned two lubricants.

4.2.1 *Validation by traction measurements*

The traction coefficient calculation of Santotrac 50 lubricant has been carried out based on some traction measurements carried out on a MTM ball on disc tribometer. Figure 4.13 shows the setup of the tribometer. It consists on a ball and a disc pressed one against the other where the speed of both components may be controlled with the purpose of adapting the entrainment (u_e) and longitudinal sliding (SRR) accordingly. Besides, the normal load acting between both components and the temperature of the lubricant bath is controlled to determine the EHL conditions. Since the MTM was designed to measure the traction coefficient of rolling and longitudinal sliding contacts, spin motion should be avoided. For that purpose, the inclination angle of the axis of rotation of the ball is designed to achieve a disposition without spin motion.

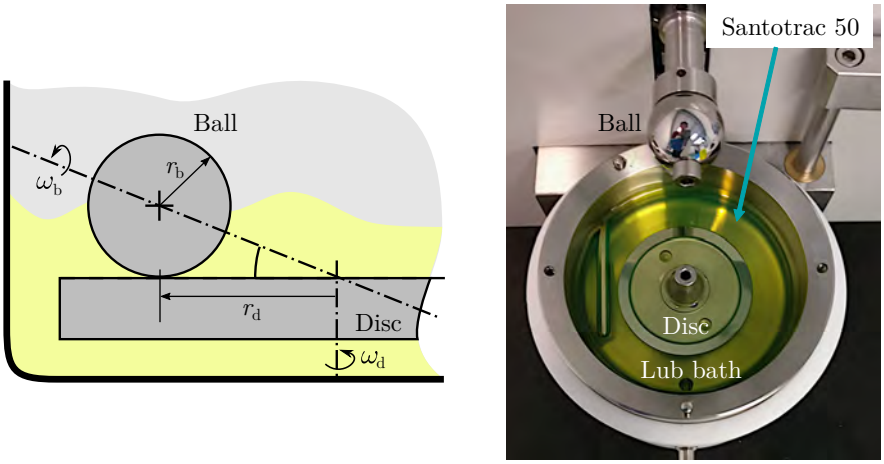

a) b)

Figure 4.13: a) MTM tribometer disposition and b) a photograph of the tribometer.

Traction measurements over a wide range of working conditions were carried out for three contact pressure conditions, two entrainment speed scenarios and two lubricant bath temperature conditions determined in Table 4.7. The same working conditions were modelled in the developed traction prediction model. The correlation of the measurements of Santotrac 50 traction lubricant with the results obtained from the model are shown in Figure 4.14. Note that Bair et al. [177] investigated the effect of lubricated traction at low longitudinal sliding conditions which is the working condition found at T-CVTs. Commonly, the Newtonian slope of the measured traction is lower than the modelled one [83, 88]. The measured traction coefficient curve has ben corrected by Equation 4.35 under low longitudinal sliding conditions in order to neglect the longitudinal sliding caused by the shearing of the solids and consider only the SRR of the lubricant.

$$SRR = SRR_{visc} + \frac{\mu}{m} \tag{4.35}$$

where SRR is the measured slide to roll ratio, SRR_{visc} is the SRR corresponding to the lubricant (lubricant shearing), μ is the traction coefficient and m is the linear traction gradient, that at low longitudinal sliding conditions where the dry traction curve resembles to the lubricated traction $m \approx G_s/p_H$ (G_s is the shear modulus of the solid). This gradient does not depend on rolling speed or temperature [177].

Table 4.7: Working conditions for Santotrac 50 correlation by measurements on a MTM tribometer.

u_e	[0.5, 2.5] m/s
d_b	3/4" (19.05 mm)
r_d	21.18 mm
F_n	[18, 35.25, 68.8] N
p_H	[0.8, 1, 1.25] GPa
a	[0.104, 0.130, 0.162] mm
Θ_0	[30, 80]°C
SRR	[0% to 50%]

The correlation between the traction curves are shown in Figure 4.14. Although traction has some differences between predicted and measured curves, the traction trend seems to be properly determined. In one hand, the predicted curve shows that the maximum traction decreases while the contact pressure increases, which was a trend that was also observed in the literature [157, 158], however, this trend has not been observed in the measurements. In addition, the obtained results have a mean error of 10% and a maximum error that does not exceed 0.015 in traction coefficient.

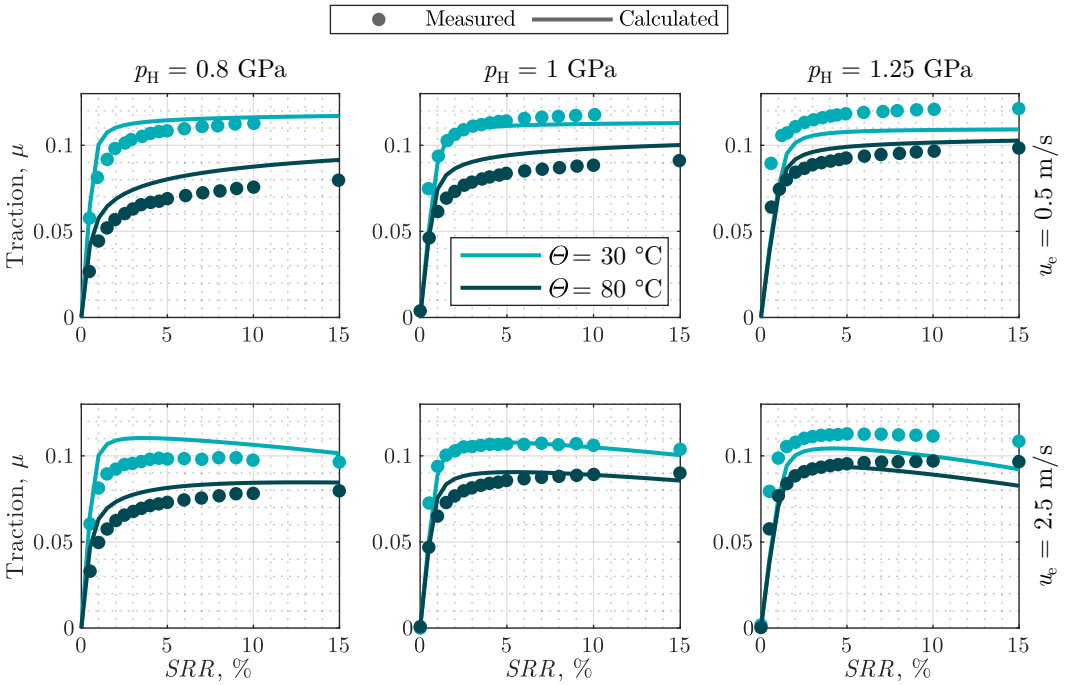

Figure 4.14: Correlation of measured and calculated traction curves for Santotrac 50.

4.2.2 *Traction validation by literature*

In order to identify the feasibility of the model for contact conditions considering spin motion traction measurements with spin published in the literature were considered. These measurements where carried out in the working conditions shown in Table 4.8 by means of the *Tribogyr* machine; a ball on disc tribometer to test large size interfaces subjected to rolling, longitudinal sliding and spin motion [178].

Table 4.8: Working conditions for Shell T9 correlation [73].

u_e	2 m/s
r_b	[12.5, 80] mm
r_d	50 mm
β	[86, 88, 88.5]°
F_n	1500 N
p_H	0.845 GPa
a	0.92 mm
Θ_0	30°C
SRR	[-45% to 45%]
ω_s ($SRR_{x,0} = 0\%$)	[397, 755, 991] rad/s

Figure 4.15 shows the correlation between the results obtained from the traction prediction model and the experimental ones published in literature [73] considering spin motion. The Figure illustrates that the model accurately reflects the trends of the experimental traction coefficient data. The maximum difference in traction coefficient does not exceed 0.014, while the average difference is only 0.005.

- Increasing the spin (β angle) results in a reduction in traction across all slide to roll ratio conditions.
- Differences in traction between the three spinning speed conditions are more considerable at low longitudinal sliding conditions since spin motion affects more considerably at this working range.
- Under high longitudinal sliding conditions, the results of the traction coefficient converge on the same value regardless of the spinning speed condition. This is particularly evident in the SRR = -45% condition for both experimental and numerical results. It has to be remarked that the β = 0°condition does not converge to the same traction value for high longitudinal sliding conditions since the experimental results from the literature were carried out under a different scale condition (r_b = 12.5 mm). As a result, variations in thermal behaviour are expected, leading to differences in the obtained results. These findings align with similar observations in the literature, where it has been demonstrated that interfaces with smaller sizes exhibit higher traction coefficients due to lower thermal heating [23].
- Under positive longitudinal sliding conditions, the traction coefficient values do not completely converge in high sliding conditions as happens for the negative sliding condition (e.g., 88°and 88.5°). This is a result of the variation of the spin speed as a function of longitudinal sliding, which occurs due to the adjustment of the speed of the components

to maintain a constant input speed across different longitudinal sliding speeds. Therefore, the spin pole position at positive and negative longitudinal sliding conditions cannot be directly compared. The spin pole locations are shown subsequently for both longitudinal sliding directions, which highlights the differences in traction under positive and negative longitudinal sliding conditions.

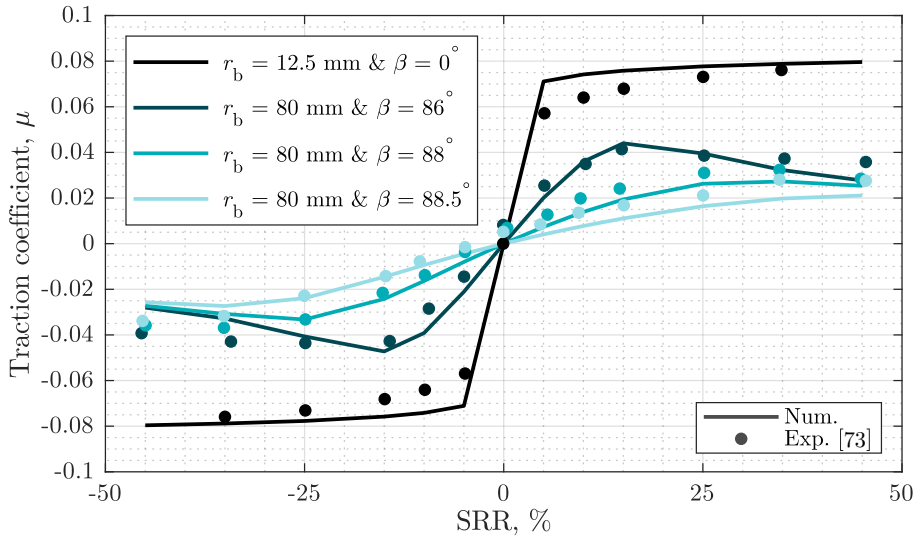

Figure 4.15: Correlation of Shell T9 traction results (experimental results from [73]).

Figure 4.16 shows the sliding speed distribution for the three spinning conditions at SRR = -45% and SRR = 45%. The following following working trends were identified:

- In negative longitudinal sliding conditions, the spin pole P moves in the positive y-direction, while in positive longitudinal sliding, it moves in the negative y-direction. The differences in spin pole distance between positive and negative longitudinal sliding conditions occur because the rotational speed of the disc and ball are adjusted to maintain a constant entrainment speed when the longitudinal sliding speed is changed. As a result, the spinning speed is no longer constant as a function of longitudinal sliding.

- The spinning speed is greater under positive longitudinal sliding conditions because the speed of the ball is accelerated, bringing the spin pole closer to the contact centre. Since the spin pole remains inside the Hertzian contact region for the SRR = 45% the traction coefficient values do not converge in an equal value.

The obtained traction trends are in accordance with what Ehret et al. mentioned [24]. It was stated that traction coefficient is affected while the spin pole is inside the Hertzian contact region. Therefore, based on the spin pole positions shown in Figure 4.16, it can be explained why the traction coefficient at SRR = -45% converge in a same traction coefficient while the traction coefficient at SRR = 45 % are still different. The spin pole of the β = 88.5°condition is still inside the Hertzian contact region, therefore, the obtained traction coefficient is lower than the traction coefficient of the other two conditions.

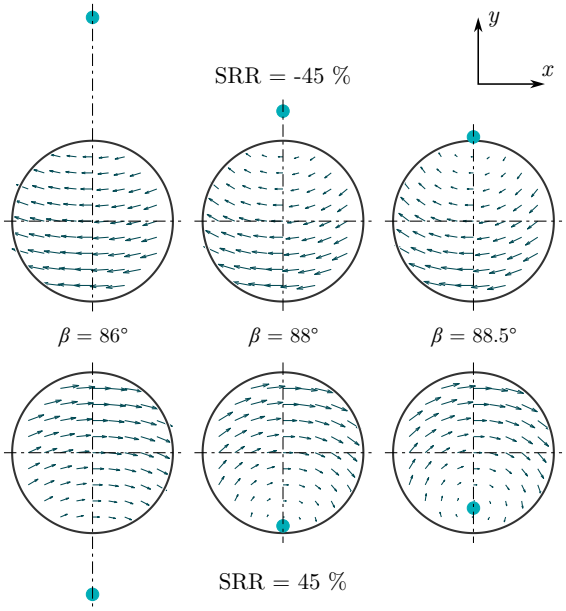

Figure 4.16: Sliding speed distribution on the contact surfaces for (top) SRR = -45% and (bottom) SRR = 45%.

4.3 COMBINED EFFECT OF SPIN AND CONTACT SIZE

Different case studies have been defined in order to analyse how the contact interface size affects the traction coefficient and contact efficiency of rolling, sliding and spinning contacts at comparable conditions. Shell T9 lubricant was used on this analysis. For that purpose the component disposition shown in Figure 4.17 was considered, which is a generalization of the different spinning contact types by Loewenthal [51, 178].

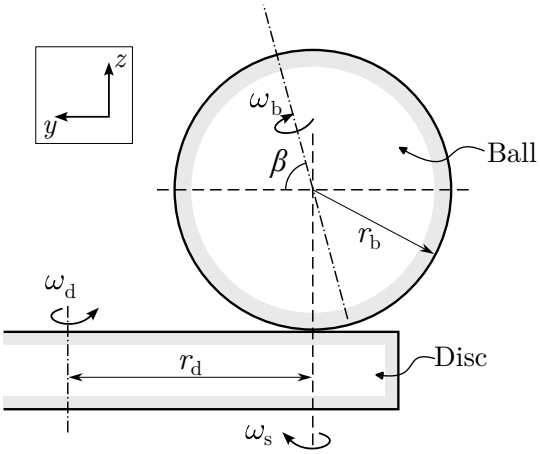

Figure 4.17: A ball on disc disposition in which spinning motion may be controlled by the β angle.

From Figure 4.17 is easy to deduce that the rolling speed of the disc in the centre of the contact interface is $u_d = \omega_d \cdot r_d$ while of the ball depends on the tilting angle with $u_b = \omega_b \cdot r_b \cdot \cos(\beta)$. Thus, the overall rolling and sliding speeds would be calculated as $u_e = (u_b + u_d)/2$ and $v_s = u_b - u_d$ respectively. However, local fluid conditions is affected by spinning motion as

the rotational speed of the disc and the ball are not equal, the spinning speed is given by Equation 4.36.

$$\omega_s = \omega_d + \omega_b \cdot \sin(\beta) \tag{4.36}$$

where, ω_b and ω_d are th rotational speed of the ball and the disc respectively and β is the tilting angle of the rotation axis of the ball.

In order to determine the traction coefficient at different contact scale and spinning speed conditions, the entrainment speed, the contact pressure and the supply temperature of the lubricant were maintained constant by means of changing the normal load and disposition of the components. Three different cases will be studied which are explained as follows and the testing conditions are determined in Table 4.9:

1. Equal spin to roll ratio conditions. At this condition, the spin to roll ratio has been maintained constant for three different scale conditions by means of adapting the spinning speed. The relation between the contact interface size and spinning speed has been maintained constant.
$$S_p = \frac{\omega_s \cdot a}{u_e} = \frac{(\omega_s/2) \cdot (2 \cdot a)}{u_e} \tag{4.37}$$
2. Equal spinning speed conditions. This condition, the spinning speed has been maintained equal and the curvature of the components were adapted. Therefore, only the interface size was the difference between the modelled conditions.
3. Equal spinning speed and normal load conditions. This last case corresponds to a condition where the results are no longer comparable from the EHL point of view since the contact pressure is different. Therefore, the rheological behaviour is considerably altered. Nevertheless, it represents a condition that may be realistic on the T-CVT working conditions since the torque capacity is defined by the normal load and not by the contact pressure.

Table 4.9: The modelled working conditions for each case study.

Parameter	1	2	3
u_e	2 m/s	2 m/s	2 m/s
r_b	[20, 40, 80] mm	[20, 40, 80] mm	[20, 40, 80] mm
r_d	50 mm	50 mm	50 mm
β	84°	[84, 87, 88.5]°	[84, 87, 88.5]°
F_n	[155.3, 621, 2484.2] N	[155.3, 621, 2484.2] N	621 N
p_H	1 GPa	1 GPa	[1.59, 1, 0.63] GPa
a	[0.27, 0.54, 1.09] mm	[0.27, 0.54, 1.09] mm	[0.43, 0.54, 0.69] mm
Θ_0	30°C	30°C	30°C
SRR	[0% to 50%]	[0% to 50%]	[0% to 50%]
ω_s ($SRR_{x,0} = 0\%$)	[991, 495, 248] rad/s	991 rad/s	991 rad/s

4.3.1 *Equal spin to roll ratio*

Figure 4.18 shows the isothermal and thermally corrected traction curves calculated at equal spin to roll ratio conditions. For that purpose, both, spin speed and contact interface size were changed at each condition, thus maintaining the relation in the three conditions equal. In one hand, the isothermal curves show similar trends in the three conditions, therefore it reveals that the spin to roll ratio correctly represents the contact behaviour. Nevertheless, the thermally corrected traction results show lower traction coefficient while contact scale increases, where differences are more considerable at high longitudinal sliding conditions. In addition, the thermally corrected traction shows that the maximum traction coefficient decreases while the contact interface size increases.

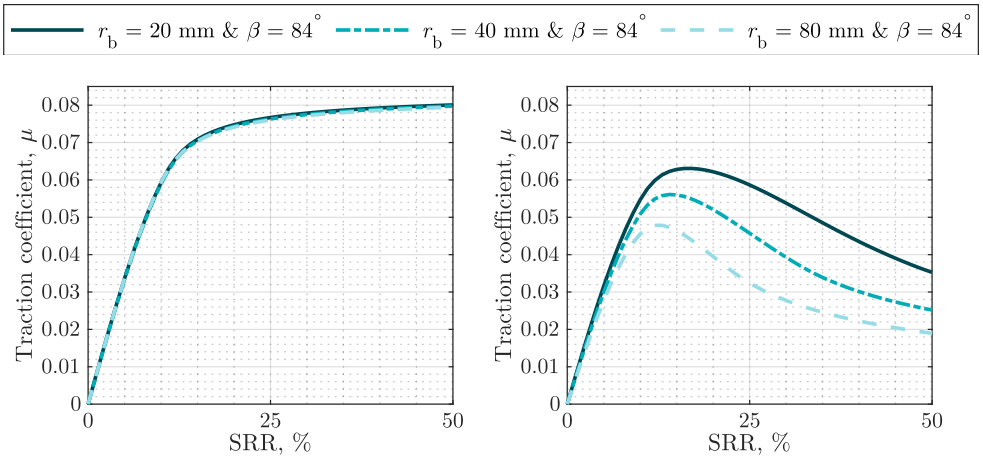

Figure 4.18: Traction coefficient for equal spin to roll ratio conditions in a) isothermal and b) thermal conditions.

Figure 4.19 shows different kinematic parameters as a function of longitudinal sliding such as spin speed, spin to roll ratio, spin pole position and dimensionless spin pole position (P/a).

- Firstly, the figure shows how the spinning speed increases together with longitudinal sliding for the three contact radius conditions. The variation in spin speed happens as a result of the changes in the rotational speed of the disc and the ball. In order to maintain the entrainment speed constant while longitudinal sliding changes, the spinning speed is affected. Nevertheless, the variation of the spinning speed is proportional in the three conditions.

- The figure shows how the spin to roll ratio is equal for the analysed three conditions since the large size interface has low spinning speed and vice versa. In addition, the variation in spin to roll ratio is almost equal in the three conditions making the traction results comparable.

- Since the spin speed is no longer equal in the three scale conditions, the spin pole moves from the centre of the contact interface at different speeds. In the small size interface, the spin pole moves slower than in the large size interface, therefore, the spin pole reaches the contact interface boundary at equal longitudinal sliding in the analysed three conditions. Therefore, the dimensionless spin pole position is equal in the analysed three cases.

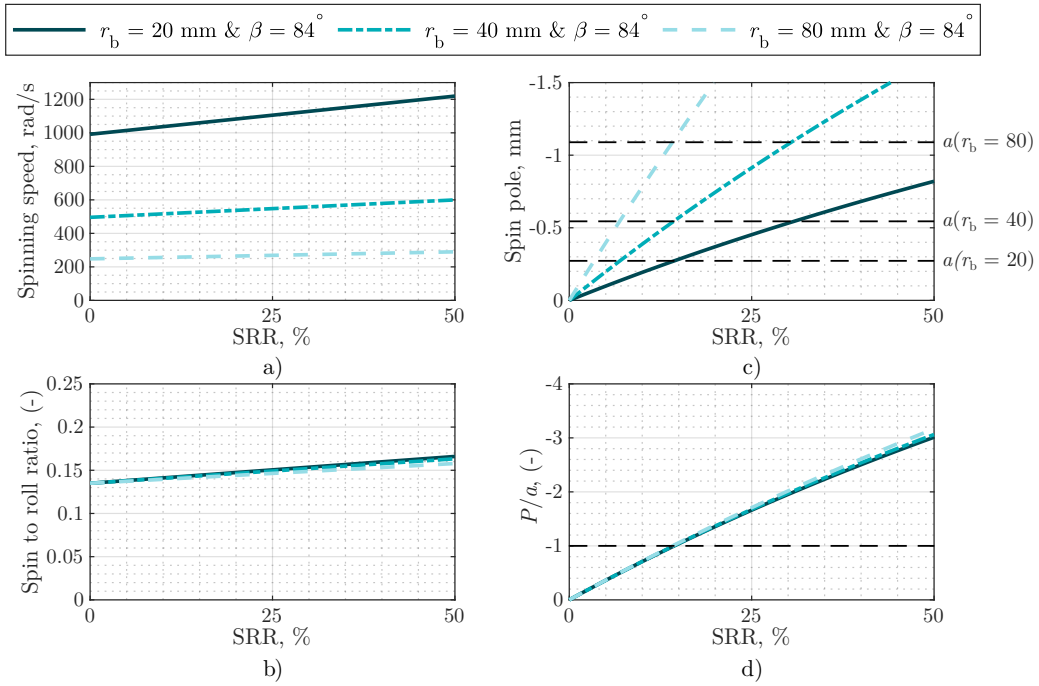

Figure 4.19: a) Spinning speed, b) spin to roll ratio, c) spin pole position and d) relation between spin pole and interface size as a function of longitudinal sliding for three contact interface conditions under equal spin to roll ratio conditions.

Figure 4.20 plots the sliding speed, isothermal shear stress, temperature rise, and thermally corrected shear stress in the rolling direction on the contact interface when SRR equals 10 %. The sliding speed distribution indicates that the position of the spin pole is equal in the three scale conditions. This corresponds with Figure 4.19d, in which the relationship between the spin pole position and the interface radius is equal. Therefore, it can be seen that since the relationship between the spinning speed and contact interface radius is equal, the sliding speed values across the contact interface are equal, i.e., $v_s(x/a, y/a)_{R20} = v_s(x/a, y/a)_{R40} = v_s(x/a, y/a)_{R80}$. As the sliding speed distribution is equal across the contact interface, the viscosity distribution would also be similar in the three scale conditions. Therefore, the second row of Figure 4.20 shows the shear stresses for the isothermal condition, which are equal in the three scale conditions.

The third row of Figure 4.20 depicts the temperature rise distribution on the mid plane generated by the shearing of the lubricant. The figure clearly shows that the temperature distribution coincides with the sliding speed distribution. On the one hand, the temperature at the outlet increases as a result of the rolling direction of the components in contact. On the other hand, the temperature rise in the negative y-region is smaller than in the positive y-region. This behaviour is a result of the spin motion. Since there is no heat generation in the spin pole position (no sliding speed) the temperature increase near this region is lower.

The corrected temperature distribution decreases the viscosity of the lubricant, and thus changes in shear stresses are expected. The bottom row of Figure 4.20 presents the thermally corrected shear stress distribution in the rolling direction. It can be observed that the shear stresses of the large interface are lower than those of the small interface. Hence, the traction coefficient of the large interface can be expected to be lower than the low scale, as also reported in Figure 4.18.

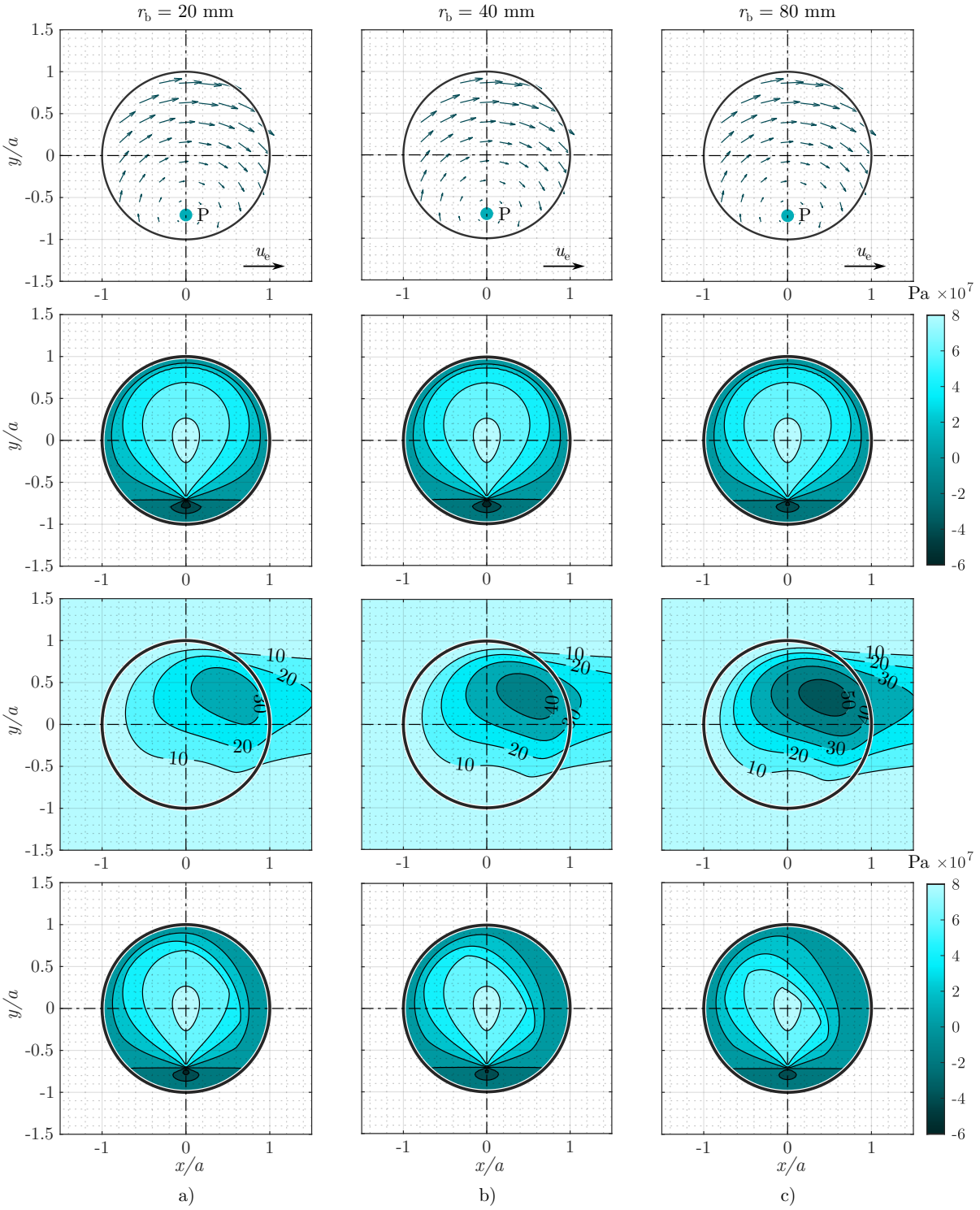

Figure 4.20: (From top to bottom) Surface sliding speed distribution, isothermal shear stresses in the rolling direction, temperature rise distribution and thermal shear stress under equal spin to roll ratio conditions for $SRR = 10\%$ and a) $r_b = 20$ mm, b) $r_b = 40$ mm, and c) $r_b = 80$ mm.

This case study revealed that the spin to roll ratio represents correctly the kinematic behaviour of the spinning circular contacts, nevertheless, since the interface size affects the thermal behaviour of the contact, the traction coefficient is influenced by the scale effect.

4.3.2 *Equal spinning speed*

Figure 4.21 shows the traction curves for the equal spinning speed and different contact interface size conditions. For that purpose, the β angle was adapted in order to achieve the same spinning speed in the three scale conditions. In this case, differences were achieved at isothermal analysis, which reveals that the differences are not only a result of the different thermal behaviour. Nevertheless, the traction differences increase in the thermally corrected traction curves. The traction results show that the larger the contact interface the lower the traction coefficient.

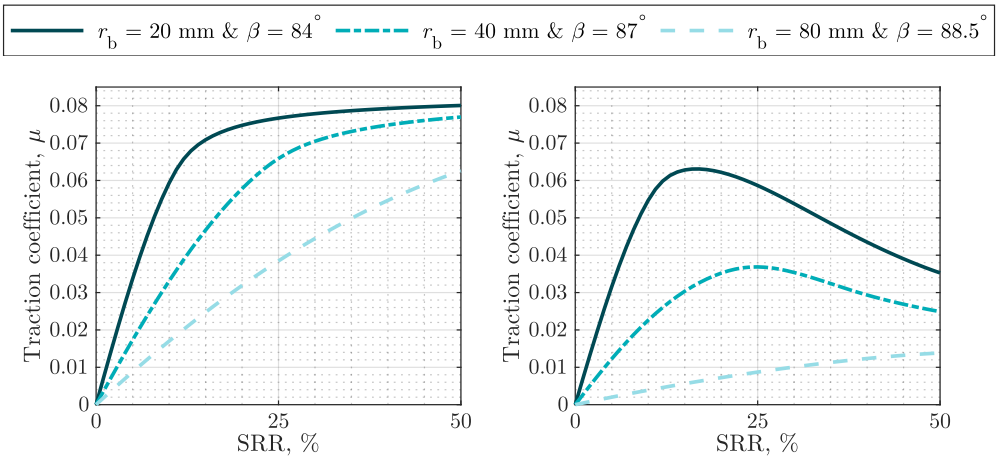

Figure 4.21: Traction coefficient for equal spinning speed in a) isothermal and b) thermal conditions.

Figure 4.22 shows the main kinematic parameters as a function of longitudinal sliding. It reveals that the spinning speed is equal in the three scale conditions, therefore, the spin to roll ratio is no longer equal. In addition, since the spinning speed is equal, the position of the spin pole as a function of longitudinal sliding is equal in the three for the three contact sizes. Therefore, it leaves the contact interface at different longitudinal sliding values. The spin pole would leave the contact interface at greater longitudinal sliding conditions for the large size interface. Therefore, the dimensionless spin pole position is no longer equal for the three conditions.

Figure 4.23 depicts the sliding speed distribution on the contact interface for $SRR = 10\%$. The figure clearly shows that the spin pole position changes in proportion to the interface size, which corresponds to Figure 4.22c, in which the spin pole position was shown to be equal in the three conditions. Hence, since the spinning speed is equal, the sliding speed values at the contact boundaries are different, because the speed of the large size interface is higher. In this case, the sliding speed distribution is related as $v_s(x,y)_{R20} = v_s(x,y)_{R40} = v_s(x,y)_{R80}$. Moreover, as the spin pole is closer to the contact interface for the large scale condition, more sliding appears in the opposite direction to rolling, and thus, traction is affected.

The second row of Figure 4.23 shows the isothermal shear stress distribution on the contact interface. As expected, more shear stresses can be observed in the negative x-direction of the largest interface, and thus less traction can be expected after the integration. This is in agreement with the results depicted in Figure 4.21.

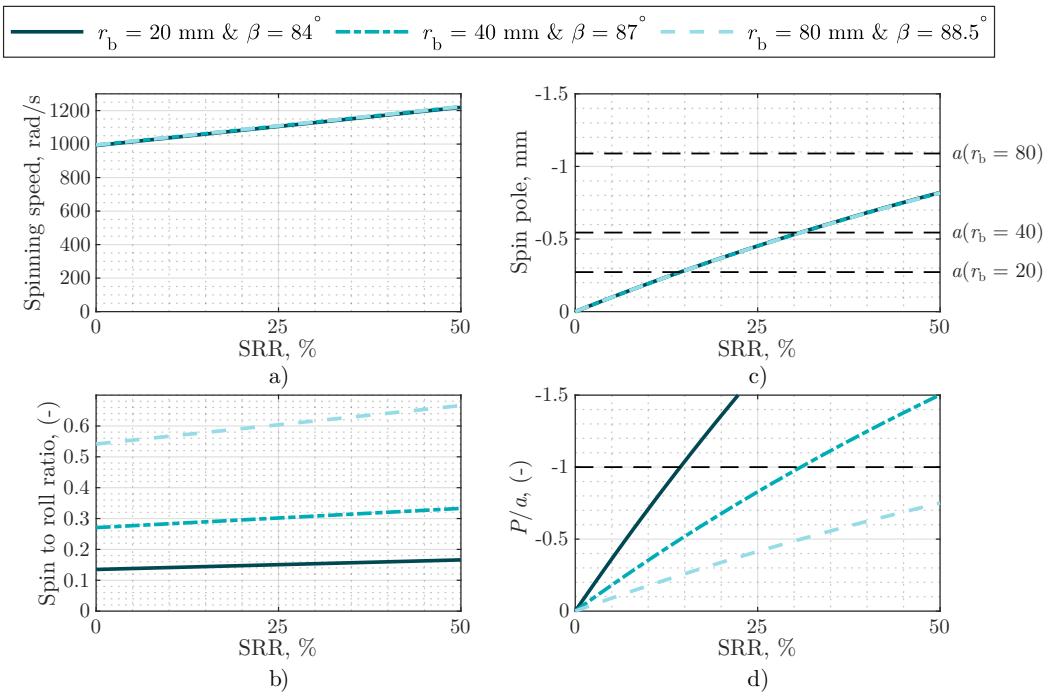

Figure 4.22: a) Spinning speed, b) spin to roll ratio, c) spin pole position and d) dimensionless spin pole position as a function of longitudinal sliding under equal spinning speed conditions.

The distribution of temperature rise on the contact interfaces is reported in the third row of Figure 4.23. As expected, the rise in temperature is greater on the large interface than the small one, which leads to a larger decrease in viscosity, and thus traction. Since the spin pole is closer to the contact interface for the largest contact size, the temperature distribution changes. This shows that the temperature rise near the spin pole is low, which is the result of the lack of sliding at that point. On the other hand, it also indicates that an increase in temperature corresponds to an increase in the size of the contact interface.

The bottom row of Figure 4.23 shows the distribution of thermally corrected shear stress distribution in the rolling direction for the three scale conditions. The findings indicated a greater decrease of the shear stresses on the largest contact interface, consequently resulting in a substantially greater decrease in the traction coefficient.

Shear stresses in the positive direction lead to an increase in the traction coefficient, while shear stresses in the negative direction result in a decrease. It can thus be concluded that in the integration process, the shear stresses in the positive direction are cancelled by the shear stresses in the negative, which has a resultant effect on the traction coefficient. Nevertheless, all these shear stresses generate energy dissipation, which increases the contact power loss, thereby decreasing the efficiency.

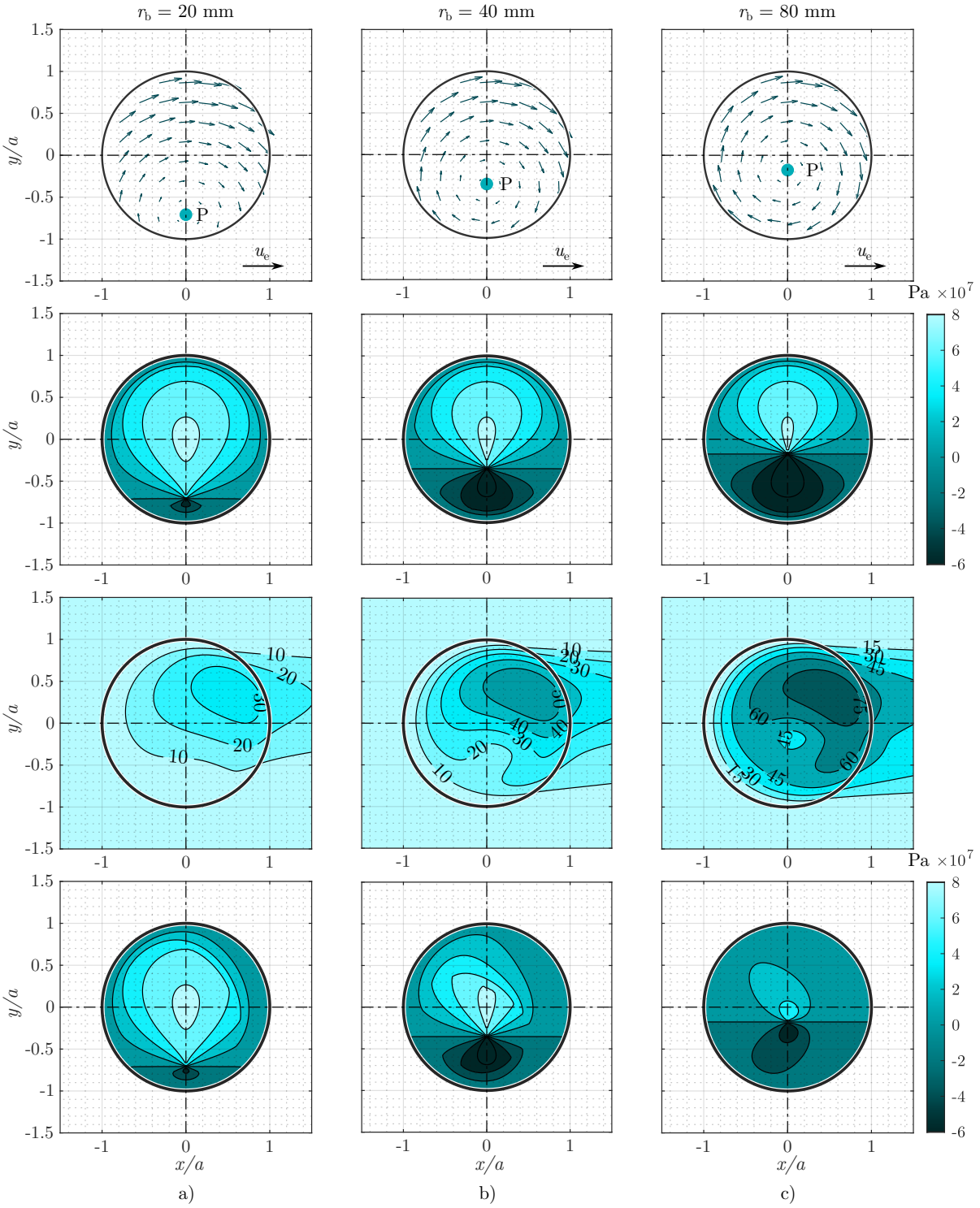

Figure 4.23: (From top to bottom) Surface sliding speed distribution, isothermal shear stresses in the rolling direction, temperature rise distribution and thermal shear stress under equal spinning speed conditions for $SRR = 10\%$ and a) $r_b = 20$ mm, b) $r_b = 40$ mm, and c) $r_b = 80$ mm.

4.3.3 *Equal spinning speed and normal load*

In T-CVT transmissions, normal load is required to transmit torque by traction forces regardless the applied contact pressure. The last case study consists on identifying the traction trends under equal normal force and spinning speed conditions; under different EHL conditions. Figure 4.24 shows the traction curves for the isothermal and thermally corrected traction. Differences between the three normal load conditions were identified in both curves.

- Under the isothermal condition, on the one hand, the lowest curvature ball revealed the highest traction coefficient across all the longitudinal sliding range. Since the contact pressure of the lowest interface is higher, the Newtonian viscosity is also higher. therefore higher traction coefficient is achieved. Additionally, the spin pole leaves the Hertzian contact zone at lower longitudinal sliding, therefore, less sliding in opposite direction to rolling appear in the contact interface.
- On other other hand, the thermally corrected curve illustrates that the low size condition has higher traction under low longitudinal sliding but while longitudinal sliding increases, a higher traction drop is achieved as a result of the thermal effects. The low size interface is subjected to higher contact pressures since an equal normal load in a lower area increases the contact pressure. Therefore, more thermal effects occur in the contact interfaces which causes a higher decrease on the traction coefficient.

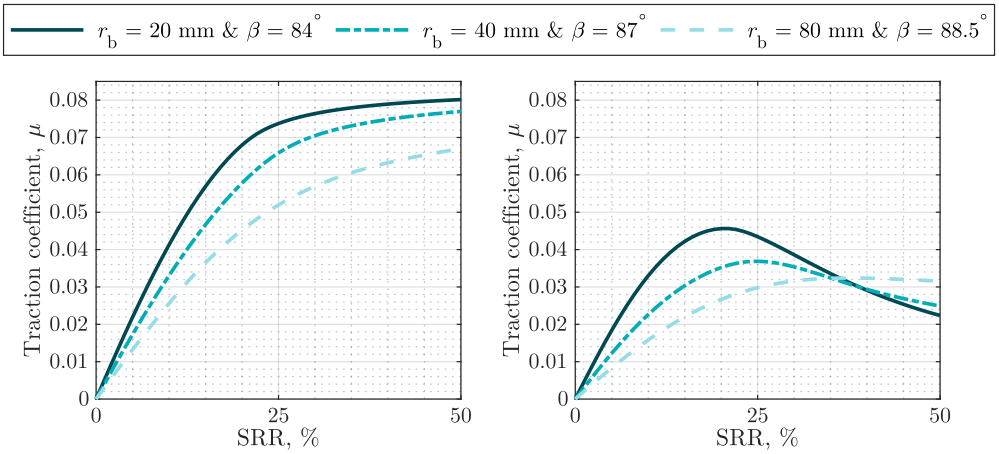

Figure 4.24: Traction coefficient for equal spinning speed and normal load conditions in a) isothermal and b) thermal conditions.

Figure 4.25 shows the main kinematic parameters as a function of the longitudinal sliding. It illustrates that the spinning speed is equal in the analysed three conditions, therefore, the spin pole position is equal. Nevertheless, since the contact interface size is different in the three conditions, the spin to roll ratio is no longer equal and the relative position of the spin pole to the interface radius neither. Therefore, the spin pole leaves the contact interface at different longitudinal sliding values for each of the conditions as shown in Figure 4.25c, where the greater the interface the later it leaves. Therefore, under equal longitudinal sliding conditions different kinematics are found in the interface which results in different traction behaviour as shown in Figure 4.24a.

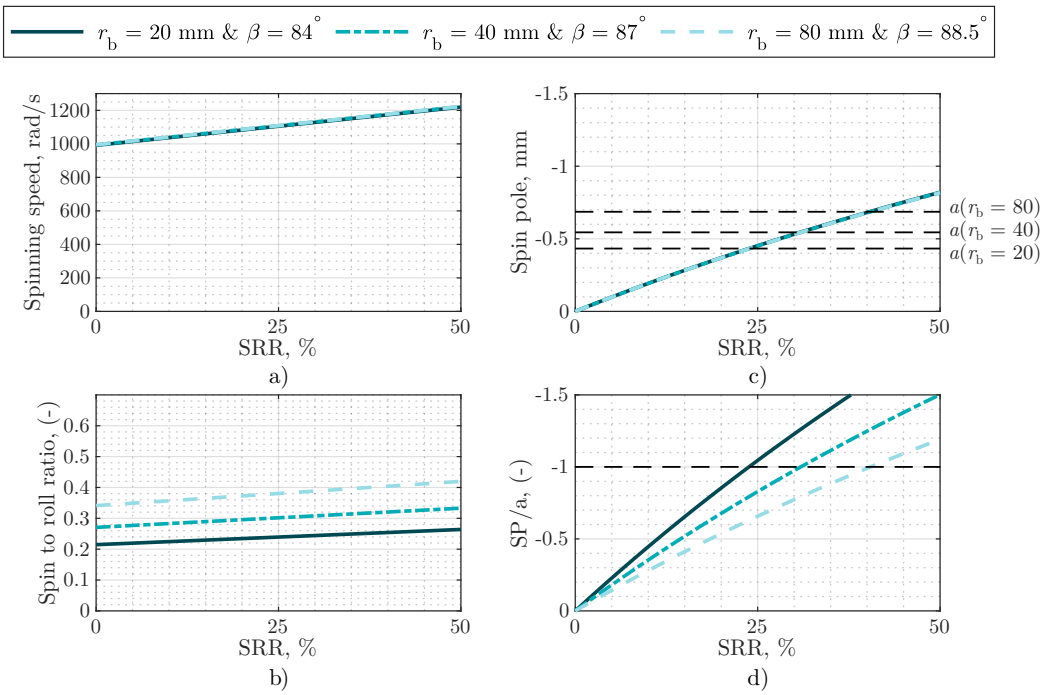

Figure 4.25: a) Spinning speed, b) spin to roll ratio, c) spin pole position and d) dimensionless spin pole position as a function of longitudinal sliding under equal spinning speed and normal load conditions.

The first row of Figure 4.26 represents the sliding speed distribution across the contact interface for the three scale conditions. Comparing the three conditions, it is represented that in one hand, the spin pole is closer to the contact centre for the large size interface. In this case also, the relation between the sliding speed distribution is given by $v_s(x,y)_{R20} = v_s(x,y)_{R40} = v_s(x,y)_{R80}$ Nevertheless, the differences between the sizes are not as high as in the previous case. Since the contact pressure on each of the interface sizes is no longer equal, the Newtonian viscosity neither, which explains the differences obtained in the isothermal shear stress distribution shown in the second row of Figure 4.26. The figure shows considerably higher shear stresses in the low size interface as a result of the higher viscosity of the lubricant. Thus higher traction can be expected after the integration, which is in agreement with the results depicted in Figure 4.21a.

The temperature rise distribution is depicted in the third row of Figure 4.26. Conversely to the previous case, the temperature rise is greater in the low size interface as a consequence of the greater contact pressure. It is as a consequence of the higher contact pressure, which generates more heat than the large interfaces which is subjected to a considerably lower contact pressure as expressed in Table 4.9. Accordingly, the bottom row of Figure 4.23 shows the distribution of thermally corrected shear stress in x-direction. The shear stresses are still higher under the low size interface for $SRR = 10\%$ as a result of the higher Newtonian viscosity. However, in high SRR conditions a higher decrease on lubricant viscosity explains the lower traction of the low size.

These findings reveal that higher traction is achieved under low longitudinal sliding conditions in all of the analysed conditions. Since T-CVTs work under this SRR range, it is preferable to consider low size interfaces in order to maximize the traction load which determined the transmissible torque.

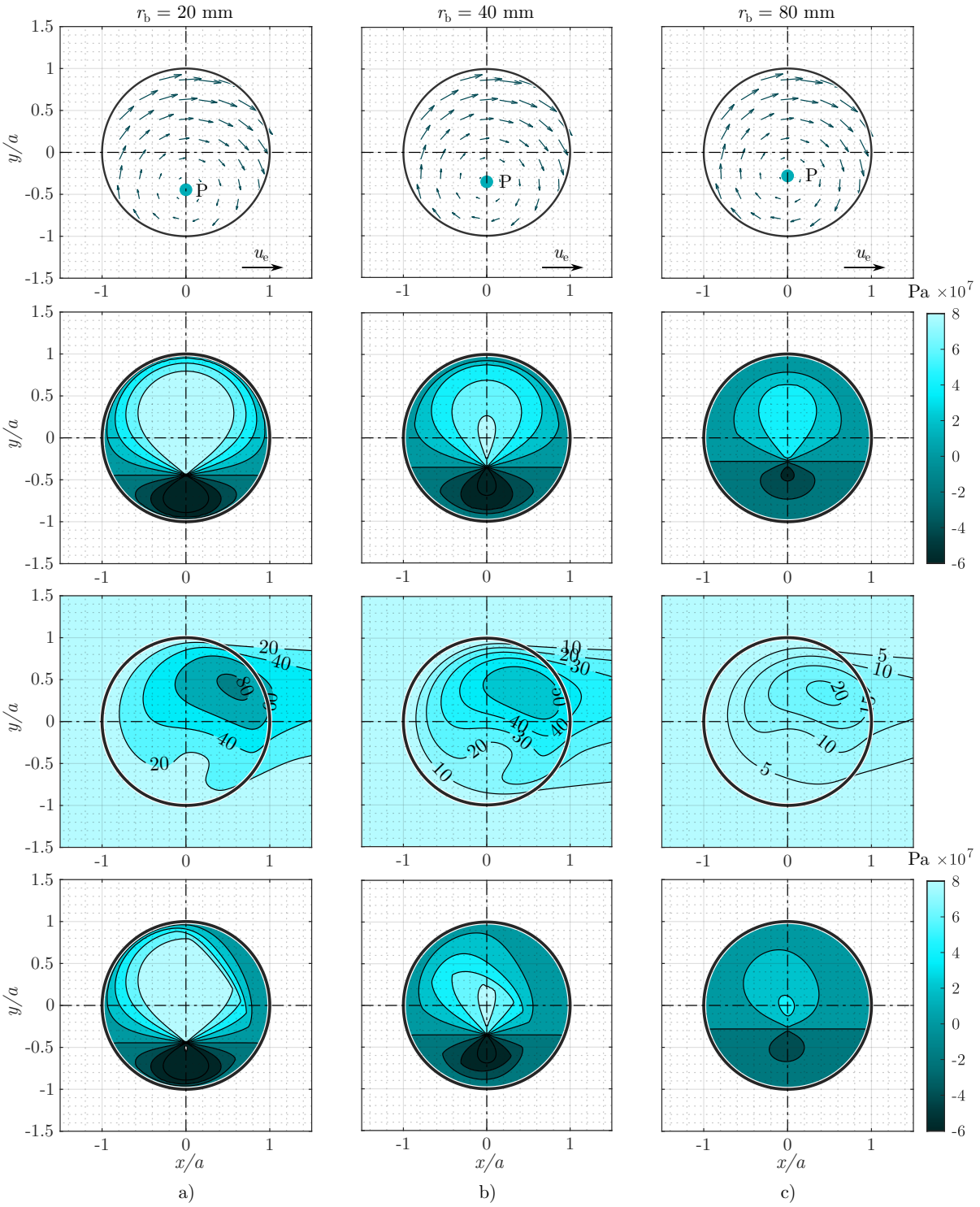

Figure 4.26: (From top to bottom) Surface sliding speed distribution, isothermal shear stresses in the rolling direction, temperature rise distribution and thermal shear stress under equal spinning speed and normal load conditions for $SRR = 10\%$ and a) $r_b = 20$ mm, b) $r_b = 40$ mm, and c) $r_b = 80$ mm.

4.4 CONCLUSIONS

A simplified semi-analytical traction prediction model has been presented, which analyses the impact of spinning motion on the traction coefficient, while also considering the influence of interface size. The results demonstrate that the model adequately represents the spin induced traction trends with a maximum and mean difference in traction coefficient that do not exceed 0.014 and 0.005 respectively. Although the simplified nature of the model led to some differences between simulated and experimental results, the model has proved effective in obtaining rapid insights into traction not achievable by complex numerical models. The results of this study can contribute to the enhanced design of mechanisms which include rolling, longitudinal sliding, and spinning contacts. The main conclusions are as follows:

- The traction coefficient is affected by both spinning motion and interface size. The presented study has reported that the spin to roll ratio provides a comprehensive description of the kinematic conditions, as the longitudinal sliding where the spin pole is located within the contact boundaries remains consistent across all conditions. However, it has been observed that decreasing the contact interface size mitigates the impact of spin motion. At equal spinning speed conditions, low sized interfaces show less sliding across the contact interface, therefore, less shear thinning of the lubricant and thermal effects of the fluid occur. Consequently, optimizing the traction coefficient may be achieved through the utilization of smaller interfaces.
- The spin to roll ratio properly represents the kinematic behaviour of the contact interface, and thus, traction under an equal spin to roll ratio is similar for different scale conditions under isothermal conditions. However, differences were found in the thermally corrected traction curve, since the interface size affects thermal behaviour. Large scale interfaces lead to a greater rise in temperature than small scale interfaces. As a result, the decrease in traction is greater for large interfaces.
- In equal spinning speed conditions, differences were observed between the contact sizes under isothermal conditions. Firstly, more shear thinning occurred in large scale interfaces due to the increased sliding speed on the surface. Secondly, these large interfaces reported higher shear stresses in the negative direction on the surface, since the spin pole is closer to the contact centre relative to the surface radius. However, it should be noted that the shear stresses below the spin pole act in the negative direction and do not contribute to enhancing traction.
- The integration of shear stresses in the rolling direction generates traction. Nevertheless, shear stresses in the negative direction cancel shear stresses in the positive, which leads to increased power losses. In addition, the shear stresses in the y-direction (transverse to rolling) do not generate traction load, but rather increase the energy dissipation, and hence power losses and efficiency. Larger interface sizes result in increased sliding in the negative or transverse direction to rolling, leading to higher energy dissipation. Consequently, both traction and contact efficiency are expected to reduce as the contact interface size increases.

Spin speed and contact interface size are independently controlled in the design of mechanisms such as toroidal continuously variable transmissions. While these parameters may vary during operation, they do so in a predetermined manner, and their operation is not actively controlled. The results presented in this paper would indicate that smaller surface sizes may be preferable in such mechanisms. In this way, transmissible torque (traction) and efficiency of the transmission would be considerably improved.

5 T-CVT EFFICIENCY PREDICTION MODEL

"There are things known and there are things unknown, and in between are the doors of perception."
Aldous Huxley

This chapter describes the modelling of the performance of T-CVTs under independently controlled input/output clamping load conditions. In the first section, the model is described, starting from the geometry, loads and kinematics of the transmission. In the calculation of the traction force, the traction prediction algorithm presented in Chapter 4 is implemented. It is worth mentioning that EHL conditions change together with the applied clamping load and transmission ratio, therefore, a computationally fast traction prediction model is required. Subsequently, the contact and transmission efficiency prediction algorithms are presented. The results are classified in three sections. The first one is focused on the effects that the transmission ratio has on the interface characteristics in terms of contact scale. The second section analyses the traction equilibrium and efficiency on the behaviour of a single point contact as a function of clamping load and torque. Finally, the last section determines the efficiency of the transmission under independently controlled input and output clamping load conditions. Thus, the main hypothesis of the thesis is numerically validated.

5.1 DESCRIPTION OF A T-CVT EFFICIENCY PREDICTION MODEL

This section describes the method to calculate the efficiency of this kind of transmission. For that purpose firstly the geometrical parameters, the forces and reactions are explained based on the model presented by Carbone et al. [27]. They are required for the power losses and efficiency calculation method subsequently explained following the calculation method proposed by Doki-Thonon [73]. The objective is to predict the behaviour of each contact point as a function of the working conditions.

Figure 5.1 shows a schematic representation of a T-CVT and the power flow of the transmission with the main geometrical parameters, loads, reaction forces, rotational speeds and power loss sources. As represented in the figure, losses can be calculated progressively, starting from the input shaft [179]. In the bottom of Figure 5.1 the power losses derived from the discs, rollers and contact points are represented, where $P_{\mathrm{D-in}}$ and $P_{\mathrm{D-out}}$ are power losses of the input and output discs, P_{R} is the power loss of the roller (multiplied by the number of rollers in the toroidal cavity) and $P_{\mathrm{CL-in}}$ and $P_{\mathrm{CL-out}}$ are the input and output contact power losses respectively. In this model losses derived from the discs are not considered since the objective is to identify the differences between the behaviour of the input and output contact points.

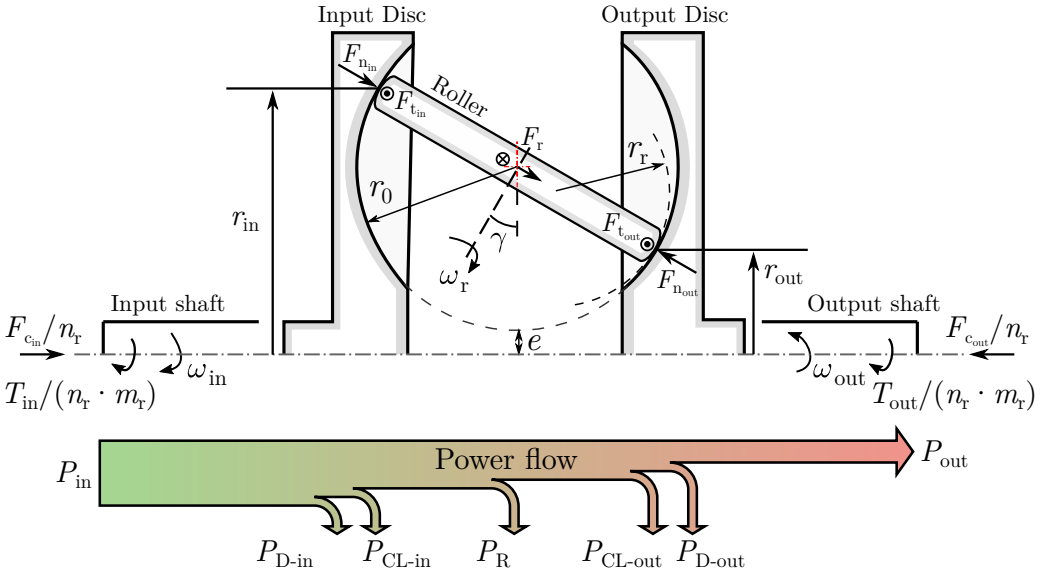

Figure 5.1: Schematic representation and power flow of a Toroidal type CVT.

5.1.1 *Geometry, loads and kinematics of a T-CVT*

T-CVT geometry

The geometrical parameters of a T-CVT are defined in Table 5.1. These parameters are also shown in Figure 5.1. They define the toroid geometry and they are required to determine the input and output radius as a function of the tilting angle of the rollers, defined by Equation 5.1.

Table 5.1: Geometrical parameters of a Toroidal type CVT.

r_0	Toroidal curvature radius
e	Toroidal minimum radius
γ	Roller tilting angle
n_r	Number of rollers in the toroidal cavity
m_r	Number of toroidal cavities
r_r	Roller curvature radius

$$\begin{aligned} r_\mathrm{in} &= r_0 \cdot [1 + k - \sin(\gamma)] \\ r_\mathrm{out} &= r_0 \cdot [1 + k + \sin(\gamma)] \end{aligned} \tag{5.1}$$

where, k is the aspect ratio between the toroidal minimum radius and the curvature radius of the toroidal cavity ($k = e/r_0$).

The ideal transmission ratio is defined by the relation between the input and output radius as shown in Equation 5.2. Therefore, adapting the inclination angle of the roller, the transmission ratio is adapted. Positive inclination angles (counter-clockwise direction) lead to decrease the input radius and increase the output one, therefore, the transmission ratio is adapted to reducer mode. The opposite happens for inclination angles in negative direction (the case represented in Figure 5.1).

$$i_{\text{ideal}} = \frac{r_{\text{out}}}{r_{\text{in}}} \tag{5.2}$$

The number of rollers in a toroidal cavity determine the number of contact points involved in the torque transmission. Increasing the number of rollers leads to an increase in transmissible torque since the loads are divided among additional contact points. In addition, the number of coaxial toroidal cavities increases the transmissible power, the more cavities, the higher the transmissible torque. Commonly one or two toroidal cavities are used in T-CVTs [180, 181].

An additional geometrical parameter to be considered in this kind of transmissions is the conformity ratio, CR. This parameter relates the curvatures of the toroidal cavity radius and roller curvature ($CR = r_{\text{r}}/r_0$). It has a significant impact in the contact mechanics (shape and size of the contact interface). The effect that this parameter has on the performance is analysed in Appendix B, where it has been concluded that low size interfaces lead to higher maximum achievable efficiency values.

Load and reactions

As stated in the introduction, it is important to ensure sufficient normal load in the contacts between the disc and rollers to transmit torque by means of traction forces. The applied normal load is commonly adapted as a function of the working conditions [17]. The relation between the clamping loads and normal loads is defined in Equation 5.3 for a full toroidal CVT.

$$F_{\text{n,in/out}} = \frac{F_{\text{c,in/out}}}{n_{\text{r}} \cdot \cos(\gamma)} \tag{5.3}$$

where F_{n} is the normal load, F_{c} is the applied clamping load, n_{r} represents the number of rollers in the toroidal cavity and γ represents the inclination angle of the rollers.

As a result of the normal loads acting on the contact points, elastic deflections of the components happen and therefore a contact area is generated [41, 123]. The basics of the contact mechanics are explained in Chapter 4, where it is highlighted that the contact curvatures of the toroid play an important role in the determination of the contact interface's shape, size and pressure distribution. The contact curvature of the components are shown in Table 5.2 which determine the effective radius in contact and therefore the ellipticity ratio of the contact. It is worth mentioning that negative radius of curvature implies that the curvature has higher conformity (concave curvature).

Table 5.2: Contact curvatures of the contact points of a T-CVT for the calculation of the Hertzian pressure and contact surface shape and size.

	Input	Output
R_{d_x}	$-r_0$	$-r_0$
R_{d_y}	$-\dfrac{(r_0+e)+r_0\cdot\sin(\gamma)}{\sin(\gamma)}$	$-\dfrac{(r_0+e)+r_0\cdot\sin(-\gamma)}{\sin(-\gamma)}$
R_{r_x}	$r_0 \cdot CR$	$r_0 \cdot CR$
R_{r_y}	r_0	r_0

Similarly to the relation between the clamping loads and normal forces, the torque is related to the traction forces and the radius. Equation 5.4 shows the relationship between torque and traction loads forces per roller.

$$\begin{aligned} T_{\text{in}} &= (F_{\text{t,in}} \cdot r_{\text{in}} + T_{\text{s,in}}) \cdot n_{\text{r}} \cdot m_{\text{r}} \\ T_{\text{out}} &= (F_{\text{t,out}} \cdot r_{\text{out}} - T_{\text{s,out}}) \cdot n_{\text{r}} \cdot m_{\text{r}} \end{aligned} \tag{5.4}$$

with T the torque, F_{t} the traction load, r the transmission radius, n_{r} and m_{r} the number of rollers and number of toroidal cavities respectively, and T_{s} is the spinning torque (later explained in Section 5.1.2). It has to be pointed out that the spinning torque is added to the input torque and subtracted from the output one due to the direction of the energy. Since energy is transmitted from the input disc to the rollers, the input torque should overcome the spinning torque. The output torque though, represents the effective torque of the output shafts, which is the traction between the roller and the output point after subtracting the spinning losses.

Since a T-CVT transmits torque by means of lubricated traction forces, the required traction is determined by Equation 5.5; obtained combining Equations 5.3 and 5.4; for a single toroidal cavity. In order to determine the EHL conditions where the required traction coefficient occurs, the traction prediction model presented in Chapter 4 is used. The traction coefficient of each of the contact points is calculated independently as shown in Equation 5.5.

$$\mu_{\text{in/out}} = \frac{F_{\text{t,in/out}}}{F_{\text{n,in/out}}} = \frac{(T_{\text{in/out}} \pm T_{\text{s,in/out}} \cdot n_{\text{r}}) \cdot \cos\gamma}{F_{\text{c,in/out}} \cdot r_{\text{in/out}}} \tag{5.5}$$

In addition, since the objective of this study is to analyse the performance of the transmission under different input and output clamping loads, the difference between the normal loads is supported by the roller bearings. Figure 5.2 shows a top view of the roller. It reveals that the load carried by the roller bearings is, on one hand the difference between both normal loads $F_{\text{r,n}} = F_{\text{n,in}} - F_{\text{n,out}}$. On the other hand, since both traction forces act in the same direction as a result of the power flow, the bearing of the roller supports the sum of both traction loads $F_{\text{r,t}} = F_{\text{t,in}} + F_{\text{t,out}}$. Consequently, the radial load carried by the roller's bearing is the the sum of both vectors $|F_{\text{r}}| = \sqrt{F_{\text{r,n}}^2 + F_{\text{r,t}}^2}$.

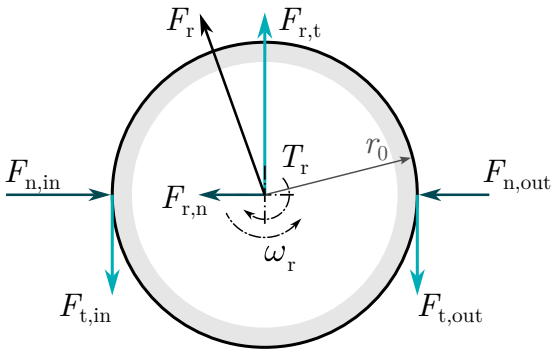

Figure 5.2: Free body diagram of the roller (top view of the roller).

Kinematics

Two different kinematic behaviour are distinguished in this kind of transmission: on one hand, the rotation speed of the disc and the rollers reflect the macro kinematics; on the other hand, the contact kinematics (rolling, longitudinal sliding and spinning) are defined. Nevertheless, both kinematics—macro and contact—are interdependent.

In Figure 5.1 it is represented that the speed of the shafts is inverted from the input to the output, therefore input and output torque are represented in the same direction. Furthermore, it has been shown in the previous chapter that longitudinal sliding is essential to have traction forces in lubricated rolling point contacts. Therefore, it is expected to achieve a lower output speed as a result of the longitudinal sliding happening in the contacts. Therefore a real transmission ratio is defined as shown in Equation 5.6.

$$i_{\text{real}} = \frac{|\omega_{\text{in}}|}{|\omega_{\text{out}}|} \tag{5.6}$$

where i_{real} is the real transmission ratio, ω_{in} and ω_{out} are the rotational speed of the input and output shafts of the transmission respectively, calculated as represented in Equation 5.7. Furthermore, in the determination of the real transmission ratio, longitudinal sliding occurring at two points is involved; the sliding between the input disc and the rollers and the sliding between the rollers and the output disc.

$$\begin{aligned} u_{\text{d,in}} &= \omega_{\text{in}} \cdot r_{\text{in}} \\ u_{\text{d,out}} &= \omega_{\text{out}} \cdot r_{\text{out}} \end{aligned} \tag{5.7}$$

where, $u_{\text{d,in}}$ and $u_{\text{d,out}}$ are the linear speed on the input and output contact points respectively. In addition, both linear speed are interdependent as a function of the longitudinal sliding happening on both contacts with respect to the speed of the roller. The longitudinal sliding happening in both contact points of this kind of transmission is calculated by Equation 5.8.

$$\begin{aligned} SRR_{\text{in}} &= \frac{v_{\text{s,in}}}{u_{\text{e,in}}} = 2 \cdot \frac{u_{\text{d,in}} - u_{\text{r}}}{u_{\text{d,in}} + u_{\text{r}}} \\ SRR_{\text{out}} &= \frac{v_{\text{s,out}}}{u_{\text{e,out}}} = 2 \cdot \frac{u_{\text{r}} - u_{\text{d,out}}}{u_{\text{r}} + u_{\text{d,out}}} \end{aligned} \tag{5.8}$$

with SRR_{in} and SRR_{out} the input and output slide to roll ratio respectively and u_{r} the linear speed of the roller calculated as $u_{\text{r}} = \omega_{\text{r}} \cdot r_0$; where, ω_{r} is the roller rotational speed and r_0 the radius of the roller (toroidal cavity radius).

In the contact points of a T-CVT transmission, spin motion occurs together with longitudinal sliding which affects the performance of the transmission. The spinning speed is calculated with Equation 5.9.

$$\omega_{\text{s,in/out}} = \omega_{\text{d,in/out}} \cdot \cos(\gamma) \tag{5.9}$$

The spin pole position and the sliding speed distribution are calculated by Equations 5.10 and 5.11. On one hand, the spin pole P is determined based on the spinning speed and longitudinal sliding happening on the centre of the contact interface O and subsequently the sliding

distribution is calculated with the spinning speed and the distance from point P to the evaluated point Q on the contact interface (see Figure 5.3).

$$\vec{\omega}_{\mathrm{s}} \times \overrightarrow{\mathrm{PO}} = \vec{v}_{\mathrm{s}}(0,0) \quad \rightarrow \quad |\overrightarrow{\mathrm{PO}}| = \frac{\vec{v}_{\mathrm{s}}(0,0)}{\vec{\omega}_{\mathrm{s}}} \tag{5.10}$$

$$\vec{v}_{\mathrm{s}}(x,y) = \vec{\omega}_{\mathrm{s}} \times \overrightarrow{\mathrm{PQ}} = \vec{\omega}_{\mathrm{s}} \times \left(\overrightarrow{\mathrm{PO}} + \overrightarrow{\mathrm{OQ}}\right) \tag{5.11}$$

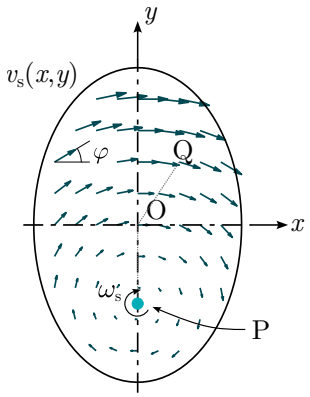

Figure 5.3: Contact sliding distribution representation.

5.1.2 *Contact power losses and efficiency calculation*

The contact power losses calculation is carried out by means of integration of the lubricant's shear stresses and the sliding speed over the contact surfaces (calculation procedure explained in Chapter 4). While traction is determined by the sliding components in x-direction ($\dot{\gamma}_{\mathrm{x}}$), the term in transverse direction (y-direction) still contributes to energy dissipation. Therefore, contrary to lubricated contacts with composite rolling-sliding movement in the x-direction, those interfaces subjected to an additional spin motion produce power loss. All the sliding vectors generate power losses regardless of the vector direction, therefore, contrary to Equation 4.28 (traction coefficient) the φ angle (see Figure 5.3) and the sliding component sign are not considered in Equation 5.12.

$$P_{\mathrm{CL}} = \int_{-a}^{a} \int_{-b}^{b} |v_{\mathrm{s}}| \cdot |\tau| \cdot \mathrm{d}x \cdot \mathrm{d}y \tag{5.12}$$

Two different power loss sources may be distinguished in this kind of contact dispositions (longitudinal sliding and spinning losses). Longitudinal sliding losses are the ones produced by the difference in linear speed at the centre of the contact interface of both components (see Equation 5.13). Nevertheless, spin motion generates an additional sliding speed distribution in the contact interface and hence increases the power losses (see Equation 5.14).

$$P_{\mathrm{LS}} = F_{\mathrm{t,x}} \cdot v_{\mathrm{s,x}} \tag{5.13}$$

$$P_{\mathrm{SP}} = \omega_{\mathrm{s}} \cdot T_{\mathrm{s}} = \omega_{\mathrm{s}} \cdot \int_{-b}^{b} \int_{-a}^{a} \left(\overline{\mathrm{OQ}}_{\mathrm{x}} \tau_{\mathrm{y}} - \overline{\mathrm{OQ}}_{\mathrm{y}} \tau_{\mathrm{x}} \right) \mathrm{d}x \cdot \mathrm{d}y \tag{5.14}$$

where P_{LS} is the longitudinal sliding power loss and P_{SP} is the spinning power loss.

The contact efficiency is defined as shown in Equation 5.15.

$$Eff_{\mathrm{CL}} = \frac{P_{\mathrm{out}}}{P_{\mathrm{in}}} = 1 - \frac{P_{\mathrm{CL}}}{P_{\mathrm{in}}} \tag{5.15}$$

where, Eff_{CL} represents the efficiency of the contact point, P_{in}, P_{out} and P_{CL} are the input, output and contact power loss values respectively. The input and output power values are calculated as shown in Equation 5.16 and Equation 5.17. On one hand, the input power is determined by the rotational speed and torque of the input disc. It is transformed into the traction power (longitudinal speed and traction force) and the spinning power loss (spinning torque and rotational speed). The former reflects the energy transferred to the roller while the latter corresponds to the energy dissipated in the contact interface. On the other hand, the output power is determined by the traction force and speed of the output point.

$$P_{\mathrm{in}} = T_{\mathrm{in}} \cdot \omega_{\mathrm{in}} = F_{\mathrm{t,x}} \cdot u_{\mathrm{in}} + T_{\mathrm{s}} \cdot \omega_{\mathrm{s}} \tag{5.16}$$

$$P_{\mathrm{out}} = F_{\mathrm{t,x}} \cdot v_{\mathrm{out}} \tag{5.17}$$

Furthermore, the efficiency drop caused by each of the two power loss sources may be determined as follows: longitudinal sliding efficiency (see Equation 5.18) and spinning efficiency (see Equation 5.19).

$$Eff_{\mathrm{LS}} = 1 - \frac{P_{\mathrm{LS}}}{P_{\mathrm{in}} - P_{\mathrm{SP}}} = \frac{v_{\mathrm{out}} \cdot F_{\mathrm{t}}}{v_{\mathrm{in}} \cdot F_{\mathrm{t}}} \tag{5.18}$$

$$Eff_{\mathrm{SP}} = 1 - \frac{P_{\mathrm{SP}}}{P_{\mathrm{in}} - P_{\mathrm{LS}}} \tag{5.19}$$

5.1.3 *Contact power and traction equilibrium calculation algorithm*

The power losses on the contact point have been calculated as shown in the flowchart of Figure 5.4 where the following steps are carried out:

1. Determine the geometry of the T-CVT transmission (parameters of Table 5.1).
2. Define input parameters: speed, torque, ideal transmission ratio and clamping loads.
3. Calculate the contact interface shape, size and pressure distribution following the Hertzian assumption.
4. Calculate a traction curve for the given working conditions and a range of predefined longitudinal sliding conditions and kinematics shown in the CVT contact disposition.

5. Calculate both, the transmissible power and the power losses for the given range of longitudinal sliding.

6. Find, via interpolation, the condition where the transmissible power as a function of longitudinal sliding coincides with the input power determined at operation 2.

7. Determine the longitudinal sliding, power loss and efficiency at the given equilibrium conditions.

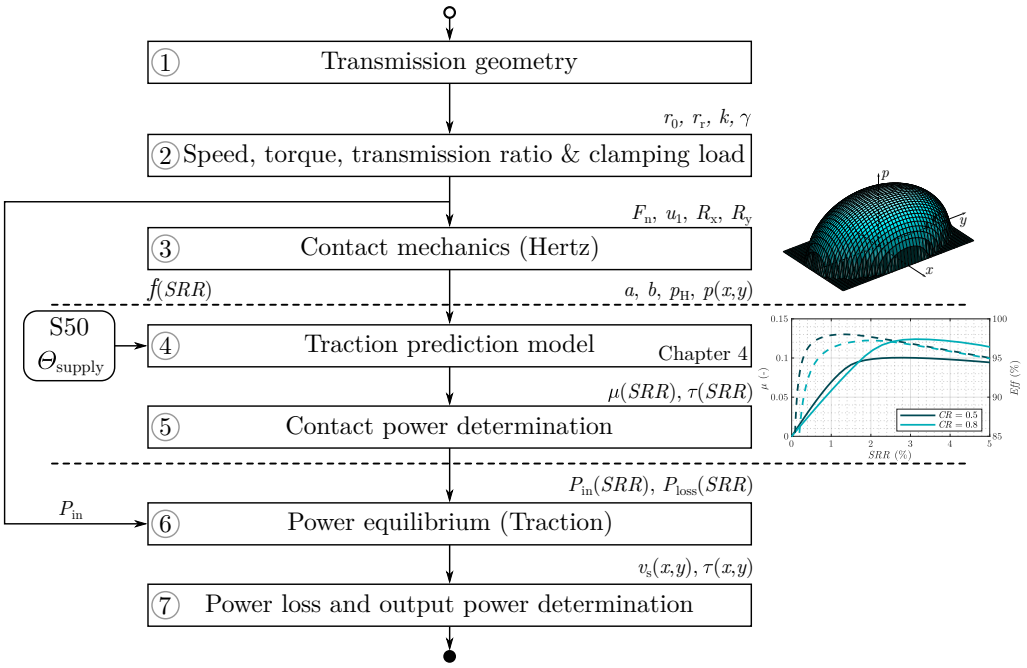

Figure 5.4: Contact power (traction) equilibrium and efficiency determination algorithm.

5.1.4 *Transmission's power loss and efficiency determination*

The efficiency of the whole transmission has been determined modelling the power flow shown in Figure 5.1 Firstly, the input contact power losses are calculated, then, the power losses generated in the rollers are calculated and finally, the output contact point power losses determine the output power. The efficiency of the transmission is calculated by Equation 5.20.

$$Eff = 1 - \frac{P_{\mathrm{CL-in}} + P_{\mathrm{R}} + P_{\mathrm{CL-out}}}{P_{\mathrm{in}}} \tag{5.20}$$

Two power loss sources occur in the rollers—the bearings and the lubricant churning. On one hand, the bearing losses have been calculated using the SKF model [182–185]. The friction torque of the bearings is calculated by Equation 5.21.

$$T_{\mathrm{be}} = T_{\mathrm{rr}} + T_{\mathrm{sl}} + T_{\mathrm{drag}} \tag{5.21}$$

where T_{be} represents the bearing frictional torque, T_{rr} is the rolling frictional moment, T_{sl} refers to the sliding friction torque and T_{drag} is the frictional moment of drag losses. The rolling frictional torque is calculated by Equation 5.22.

$$T_{\mathrm{rr}} = \phi_{\mathrm{ish}} \cdot \phi_{\mathrm{rs}} \cdot G_{\mathrm{rr}} \cdot (\nu_{\mathrm{visc}} \cdot N)^{0}.6 \tag{5.22}$$

where, ϕ_{ish} is the inlet shear heating reduction factor, ϕ_{rs} is the kinematic starvation reduction factor, G_{rr} is a variable depending on the bearing determined in [185], ν_{visc} is the lubricant's kinematic viscosity and N is the rotational speed (RPM). For the sliding frictional moment the calculation is carried out by Equation 5.23.

$$T_{\mathrm{sl}} = G_{\mathrm{sl}} \cdot \mu_{\mathrm{sl}} \tag{5.23}$$

where, G_{sl} is a variable depending on the bearing and μ_{sl} is the traction coefficient. Finally, the drag components of the bearing losses is calculated by Equation 5.24.

$$T_{\mathrm{drag}} = 0.4 \cdot V_{\mathrm{M}} \cdot K_{\mathrm{ball}} \cdot d_{\mathrm{m}}^{5} N^{2} + 1.093 \cdot 10^{-7} \cdot N^{2} \cdot d_{\mathrm{m}}^{3} \cdot \left(\frac{N \cdot d_{\mathrm{m}}^{2} \cdot f_{\mathrm{t}}}{\nu_{\mathrm{visc}}} \right)^{-1{,}379} R_{\mathrm{s}} \tag{5.24}$$

where, V_{M} is a drag loss factor, d_{m} is the bearing mean diameter, f_{t} and R_{s} are parameters as a function of the oil level and geometry of the bearing.

On the other hand, the lubricant churning losses have been calculated following the empirical model proposed by Bones et al. [186] for partially submerged smooth discs the friction torque is calculated following Equation 5.25, where drag torque increases together with the Reynolds number (flow regime) and low viscosity lubricants generate more power losses. They proposed different churning loss functions as a function of the Reynolds number (flow regime).

$$T_{\mathrm{ch}} = \frac{1}{2} \cdot C_{\mathrm{m}} \cdot \rho \cdot \omega^{2} \cdot r^{3} \cdot A \tag{5.25}$$

where, C_{m} represents the torque coefficient and it is defined as a function of the flow regime as shown in Table 5.3, ρ is the lubricant density, ω is the rotational speed (rad/s) and r and A represent the submerged disc radius and area respectively. The Reynolds number is calculated as shown in Equation 5.26.

$$Re = \frac{\omega \cdot r \cdot b}{\nu_{\mathrm{visc}}} \tag{5.26}$$

where, ω is the rotational speed, r is the disc radius, b is the disc width and ν_{visc} is the kinematic viscosity.

Table 5.3: Churning torque coefficients as a function of Reynolds number.

Flow regime	C_{m}
$Re < 2 \cdot 10^{3}$	$20 \cdot Re^{-1}$
$2 \cdot 10^{3} < Re < 10^{5}$	$8.6 \cdot 10^{-4} \cdot Re^{1/3}$
$10^{5} < Re$	$5 \cdot 10^{8} \cdot Re^{-2}$

The efficiency of the transmission has been modelled in a similar way to the previously explained contact efficiency. However, two points of contact and the losses of the rollers in the toroidal cavity have been considered:

1. Determine the geometry of the transmission.
2. Define the power in terms of input speed, torque and determine the ideal transmission ratio.
3. Calculate the contact power loss and on the input contact point for a range of clamping load values (algorithm of Figure 5.4).
4. Determine the power transmitted to the rollers and calculate the roller's churning and bearing power losses.
5. Repeat operation 2 for the output point contact.
6. Determine the output power and efficiency of the transmission.

The optimization of the clamping loads has been carried out gradually maximizing the efficiency of the afore mentioned loss sources. Figure 5.5 represents the optimization process, firstly, the input clamping load is optimized, then, the losses of the rollers are calculated and finally the output point contact is optimized.

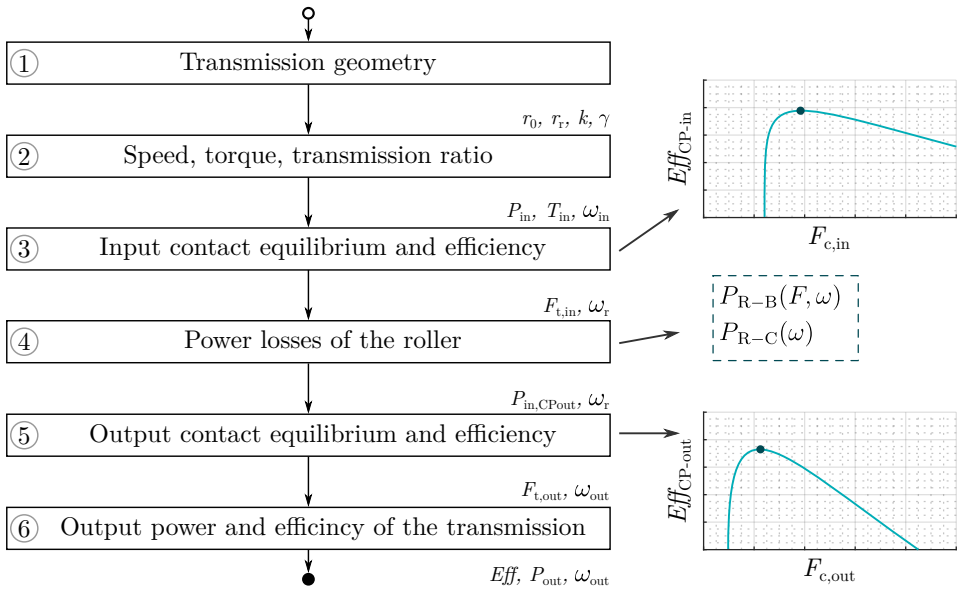

Figure 5.5: Transmission efficiency and clamping load optimization algorithm.

5.2 TRANSMISSION'S EFFICIENCY AND SLIDING EQUILIBRIUM RESULTS

This section resumes the results obtained from the model with the purpose to identify the effects of the clamping loads on the working conditions of the contact points. Then, the efficiency of the transmission is optimized by means of independently controlled input and output clamping loads. Table 5.4 shows the geometrical parameters of the CVT that has been used in this study. In the calculation Santotrac 50 (defined in Table 4.6) lubricant has been considered to determine the traction equilibrium. Additionally in order to estimate the losses of the rollers, the 4207 ATN9 double row ball bearings have been considered.

Table 5.4: Geometrical parameters needed to define a Toroidal type CVT.

r_0	e	γ	CR	n_r	m_r
110 mm	-20 mm	± 25°	0.5	3	1

The relation between the ideal transmission ratio and the tilting angle of the rollers is represented in Figure 5.6. The achievable transmission ratio range is between a reducer of 3:1 to a multiplier of 1:3 with a roller inclination angle range of ± 25°. Negative inclination angles (in clockwise direction) lead to multiplier mode of the transmission ratio and vice versa.

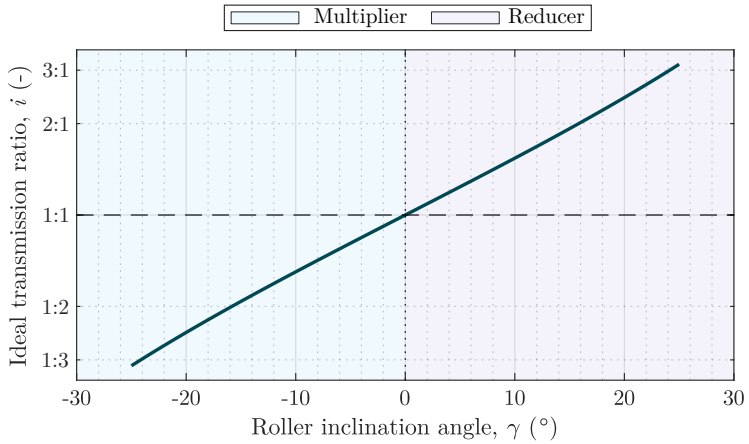

Figure 5.6: Ideal transmission ratio of the T-CVT as a function of the inclination angle of the rollers.

Three case studies are analysed in this section, which are as follows:

Case 1: In this case study the differences between the input and output points at equal clamping condition are analysed for the conditions in Table 5.5. Firstly, (i) clamping load effects on contact mechanics are determined. Then, (ii) the contact efficiency as a function of longitudinal sliding (SRR) is analysed under different ideal transmission ratio conditions.

Table 5.5: Working conditions of the first case study.

	(i)	(ii)
F_c	15 kN	
SRR	[-]	$0 \rightarrow 5\%$
i_ideal	1:3 → 3:1	[1:3, 1:1, 3:1]

Case 2: The second case study focuses on the traction equilibrium and contact efficiency on a single contact point as a function of the torque that has to be transmitted and the applied clamping load. The analysis shows the contact efficiency and longitudinal sliding behaviour as a function of (i) clamping load at constant torque and (ii) as a function of torque at constant clamping load. The working conditions analysed in this case study are determined in Table 5.6.

Table 5.6: Working conditions of the second case study.

	(i)	(ii)
F_c	$0 \rightarrow 15$ kN	[2, 4, 6, 10] kN
T	[10, 25, 50] Nm	$0 \rightarrow 50$ Nm
N_{in}	1500 RPM	
i_{ideal}	1:1	
Θ_0	30°C	

Case 3: The third case study lays the efficiency of the transmission by independently controlled input and output clamping loads. In this case two point contacts and roller's bearings and churning are considered. The working conditions studied in this case study are defined in Table 5.7, where, (i) the optimum clamping load conditions are identified, and the results are compared to (ii) equally loaded clamping load conditions maintaining the input load at the optimum clamping and to (iii) a 1 kN overclamped condition.

Table 5.7: Working conditions of the third case study.

	(i)	(ii)	(iii)
F_c	$F_{c,in} \neq F_{c,out}$	$F_{c,in} = F_{c,out}$	$F_{c,in} + 1\,\text{kN} = F_{c,out}$
T	[10, 25, 50] Nm		
N_{in}	1500 RPM		
i_{ideal}	[1:3, 1:2, 1:1, 2:1, 3:1]		
Θ_0	30°C		

5.2.1 *Case 1: Clamping load effects on interface characteristics*

Clamping load effects on the contact scale and pressure

Figure 5.7 shows the normal loads and Hertzian pressure of the input and output contact points as a function of the transmission ratio. On one hand, the normal load is affected by the transmission ratio as a result of the inclination angle of the rollers (see Equation 5.3), nevertheless, the figure reveals that the input and output normal loads are equal. On the other hand, differences were found between the input and output contact pressure values as a result of the differences on the contact curvatures. The unique condition where both point contacts have equal curvatures is under the 1:1 transmission ratio condition, therefore, the contact pressure is equal. The figure at the bottom shows the evolution of the input contact interface semiaxis as a function of the transmission ratio. As expected, the interface in more slender at reducer transmission ratios since the contact curvature R_{dy} is positive and therefore the contact pressure increases at equal normal load. It is worth mentioning that the opposite happens in the

output contact point. When the transmission ratio is in reducer mode, the contact pressure in the output decreases since the contact interface area increases. Based on the obtained pressure results, different performances may be expected between the input and output point contacts.

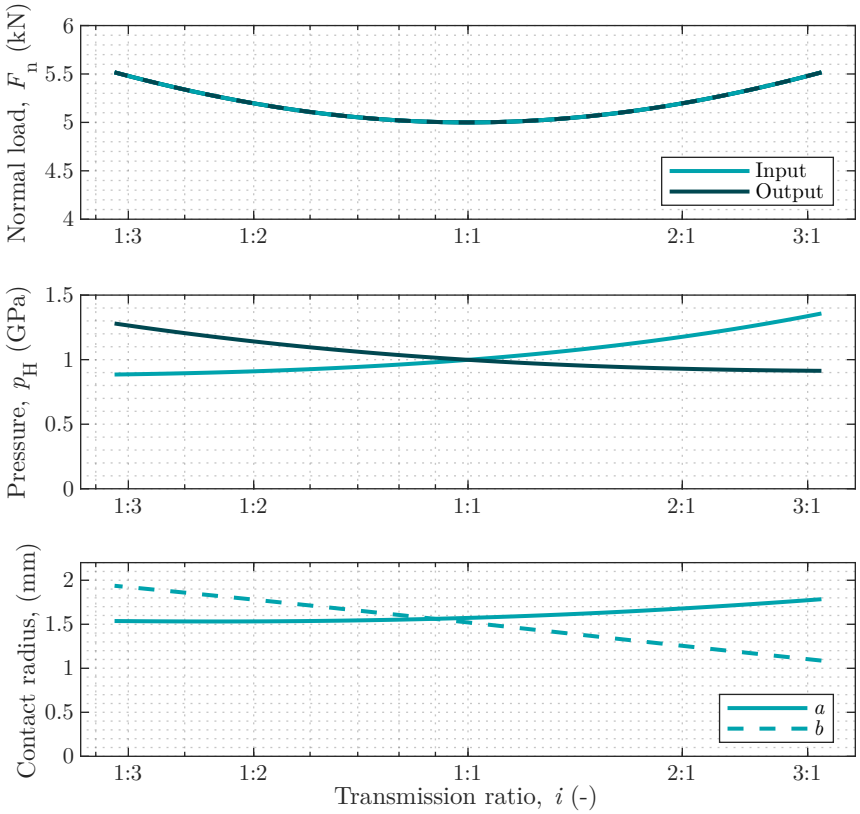

Figure 5.7: Normal load (top), Hertzian contact pressure (middle) and contact interface semiaxis (bottom) as a function of the transmission ratio.

It has been shown that differences between the input and output contact occur as a function of the transmission ratio. Variations in the contact curvature as a result of the tilting angle of the rollers generate differences between the input and output contacts as revealed in Table 5.2. Figure 5.8 shows how the curvature of both points is infinite when the tilting angle of the rollers tends to zero, therefore, in this condition the contact pressure is equal in both contact points. On the other hand, Figure 5.8 shows how the contact curvature of the input point is positive in the positive range of tilting angles (reducer mode), therefore, as represented in Figure 5.7 the contact interface is more elliptical when the transmission ratio is reducer mode.

Contact efficiency as a function of longitudinal sliding

Figure 5.9a shows the contact efficiency variation of each of the contact points as a function of the longitudinal sliding for different transmission ratio values. The figure reveals the efficiency curves for the input and output points are no longer equal, therefore, different behaviour between each contact point is achieved. It also reveals that the predominant power loss source varies as a function of longitudinal sliding. On one hand, Figure 5.9b shows that the spinning efficiency is low in low longitudinal sliding conditions and increases together with longitudinal sliding.

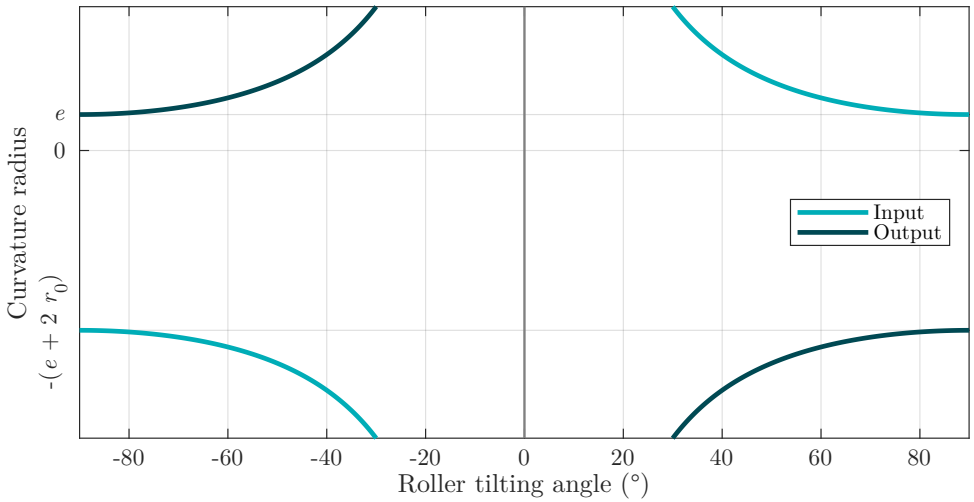

Figure 5.8: Contact curvature of the toroidal cavity as a function of the roller inclination angle.

On the other hand, Figure 5.9c shows that the longitudinal sliding efficiency decreases while longitudinal sliding increases. In addition, the figure shows that the longitudinal sliding loss is equal in both points and transmission ratio conditions, this is due to the fact that it does not depend on the traction force as represented in Equation 5.13.

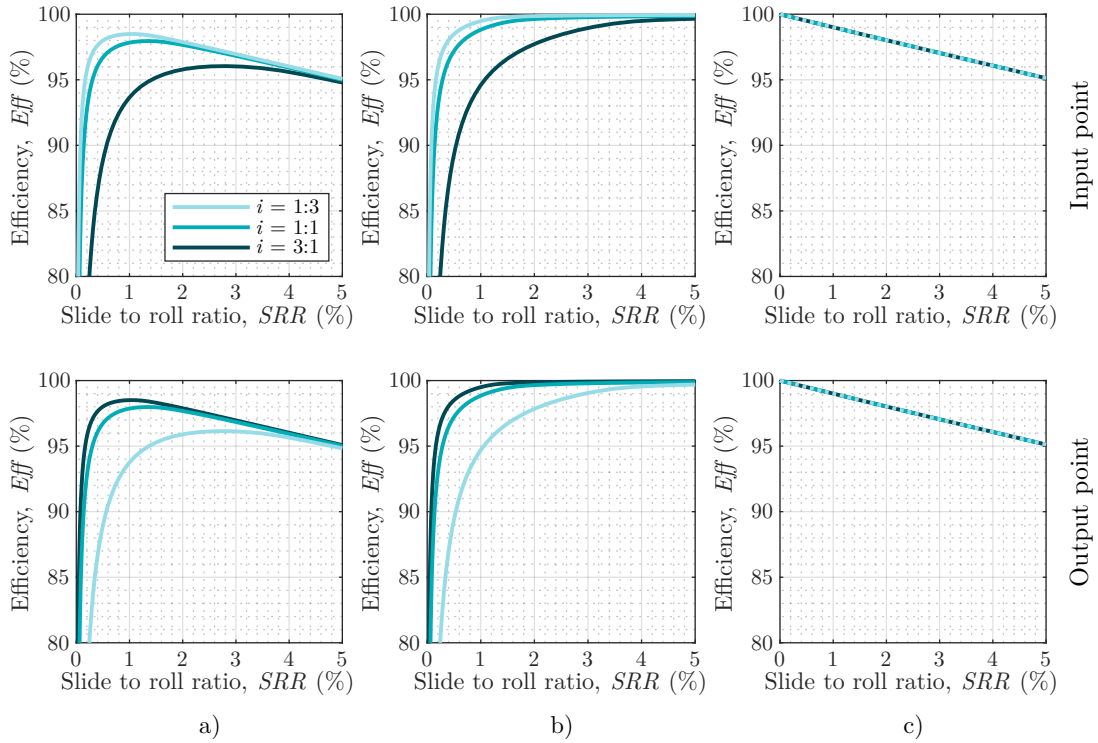

Figure 5.9: Contact efficiency as a function of longitudinal sliding for three transmission ratio of the input point (top) and b) output point (bottom); a) global efficiency b) spinning efficiency and c) longitudinal sliding efficiency.

Additionally, Figure 5.9 reveals that the difference between the efficiencies of the input point under 1:3 and 1:1 transmission ratio is not high. This is as a result of the semiaxis a, that it has little difference between both transmission ratio conditions. Figure 5.10 shows the evolution of the spin pole position relative to the interface semimajor axis for each point contact as a function of the longitudinal sliding. Since the contact interface shape and size changes as a function of the transmission ratio, the spinning efficiency is different at both point contacts. The spinning efficiency reaches the 100% when the spin pole is no longer inside the Hertzian contact interface—at $i = 3{:}1$, $SRR \approx 3.6\%$ for the input point and $SRR = 1.4\%$ for the output one. Furthermore, the figure illustrates that the spin pole moves in negative direction on the input point but in positive direction on the output one, this is caused by the power flow. Since in the input point the speed of the disc is higher than the speed of the roller, the spin pole appears closer to the rotation axis of the disc. Conversely, in the output point the disc is slower than the roller, therefore, the spin pole is further the rotation axis of the disc (positive y-direction).

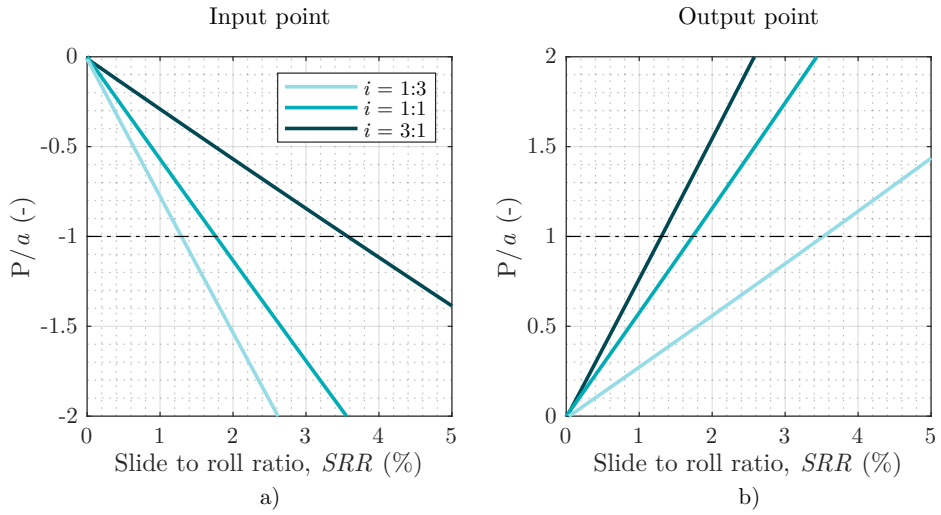

Figure 5.10: Relative spin pole position as a function of longitudinal sliding for different transmission ratio a) input point and b) output point.

These results showed the differences in the performance between the input and output point contacts. Additionally, it has been shown that the differences between both point contact were as a result of the contact scale since it affects the spinning power losses. The scale effects on efficiency as a result of the contact power losses source, calculated by Equation 5.12. The product between the local shear stresses and the local sliding speed gives a power loss distribution across the Hertzian contact region, which is shown in Figure 5.11. Three regions are represented in the figure: in the Hertzian contact region boundaries, the power losses became null as a result of the lack of shear stresses. Similarly, in the spin pole position, the power losses became null because there is no sliding speed in that point. Finally, there is a maximum point, where the product between shear stresses and sliding speed is maximum.

Similarly, it has been shown that spinning efficiency increases with longitudinal sliding. A representative distribution of the spinning torque is shown in Figure 5.12. On one hand, the figure shows the sliding speed distribution across the contact interface, for a certain longitudinal sliding condition (the spin pole P is below the contact interface centre O). On the other hand, since the torque is always calculated on the centre of the contact interface (point O), different torque regions may be distinguished. At certain longitudinal sliding condition, there are two regions; the first one is the region between the contact interface centre O and spin pole P,

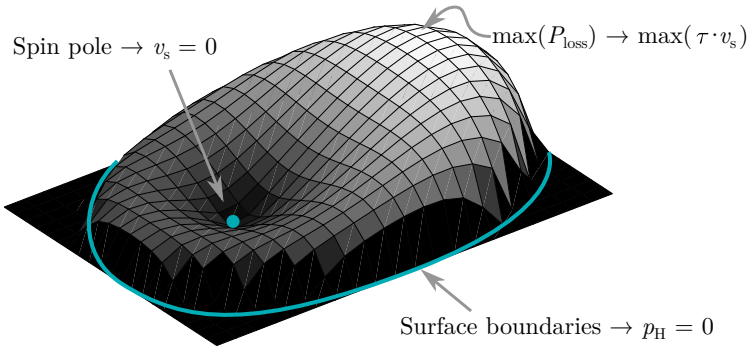

Figure 5.11: Contact power loss distribution.

where positive torque happens as a result of the direction of the sliding speed and radius from the contact centre to a point on the surface Q. The second region is the rest of the contact interface where negative torque occurs (due to sliding speed direction) that is below the spin pole location and above the contact interface centre. The figure gives an insight into what is happening in a pure rolling condition (pure spin condition), where the torque distribution is negative over the entire surface due to the sliding speed distribution. Nevertheless, at large longitudinal sliding, the positive torque below the interface centre is cancelled with the torque above it in the integration process.

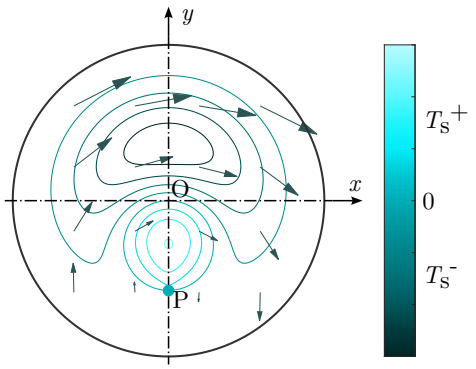

Figure 5.12: Spinning torque representation across the Hertzian contact region for a certain longitudinal sliding condition.

Equations 5.27 and 5.28 determine how the spinning torque is high at zero SRR conditions but it is negligible at high longitudinal sliding conditions. When the spin pole is far from the contact centre all the sliding vectors are aligned and therefore, the sliding speed at positive y-range is equal to the sliding in negative y-range.

$$T_{s,y}(SRR = 0) = r(y_+) \cdot F_{t,x}(y_+) + r(y_-) \cdot F_{t,x}(y_-) = 2 \cdot r(|y|) \cdot F_{t,x}(|y|) \tag{5.27}$$

$$T_{s,y}(SRR \gg 0) = r(y_+) \cdot F_{t,x}(y_+) + r(y_-) \cdot F_{t,x}(y_-) \approx r(|y|) \cdot F_{t,x}(|y|) - r(|y|) \cdot F_{t,x}(|y|) \approx 0 \tag{5.28}$$

where $T_{s,y}$ represents the spinning torque generated by the distance in y-direction of the sliding in x-direction of the surface, $r(y)$ represents the radius from the centre of the contact to any point on the contact interface in y-direction and $F_{t,x}$ determines the traction force in x-direction on each point of the interface.

Ehret et al. [24, 76] mentioned that spin motion affects the contact conditions when the spin pole is inside the Hertzian contact region; nevertheless, it has been found that the maximum contact efficiency occurs when the spin pole remains within the contact region under the analysed conditions. It should be noted that the overall efficiency decreases significantly when the spin pole reaches the contact boundaries, as a consequence of the longitudinal sliding losses.

5.2.2 *Case 2: Traction equilibrium and contact efficiency*

Figure 5.13 shows an efficiency map of the input contact point of the T-CVT for 1500 RPM of input speed and 1:1 transmission ratio as a function of the applied clamping load and the torque that has to be transmitted. Three regions are distinguished in the figure: the coloured region represents the working range of the contact where an equilibrium has been achieved, (nevertheless, as a function of the torque that has to be transmitted or the applied clamping loads, the efficiency of the transmission is considerably affected by the equilibrium condition). In addition, the region represented at low clamping conditions that increases with torque represents the gross slip region. The transition between the working range and gross slip region occurs rapidly since a small decrease on clamping load or a slight increase in torque lead to a condition where the needed traction coefficient is higher than the maximum on the traction curve, therefore, gross slip happens. Finally, at low torque conditions the overclamped region is observed, and it increases with the applied clamping load, from that condition on the efficiency of the transmission decreases, nevertheless contrary to the gross slip condition, energy transmission is achieved.

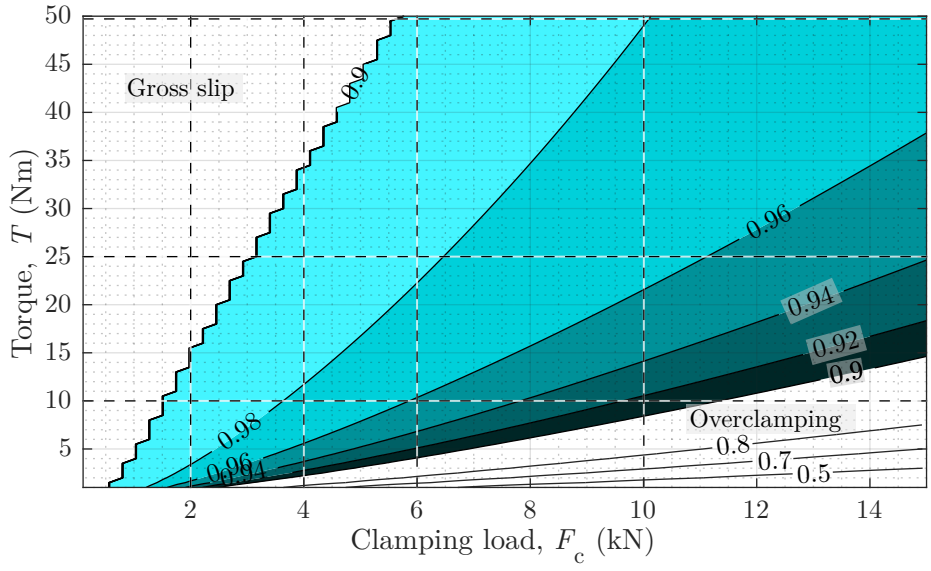

Figure 5.13: Contact efficiency map of a CVT for i = 1:1 and ω_{in} = 1500 RPM.

Contact efficiency as a function of clamping load

The efficiency trends as a function of the clamping load, maintaining the torque constant, are analysed in this section for the working conditions detailed in Table 5.6 (i). Figure 5.14 illustrates the contact efficiency for three different torque conditions (10, 25 and 50 Nm)—horizontal lines in Figure 5.13. The figure indicates that under low clamping load conditions, efficiency drops because there is insufficient traction capacity to transmit the required torque. Furthermore, the higher the torque to be transmitted, the wider the range of the underclamped condition. Conversely, in high clamping load conditions the condition with the lowest torque to be transmitted exhibits the lowest efficiency, as the transmission is in the overclamped region. In addition, the figure reveals that the optimum efficiency condition occurs always close to the gross slip limit.

The figure also depicts that the maximum efficiency value decreases as torque conditions increase. This trend is attributed to the greater clamping load required to transmit the higher torque, resulting in a larger contact interface area, hence at larger interface sizes the achievable maximum efficiency decreases.

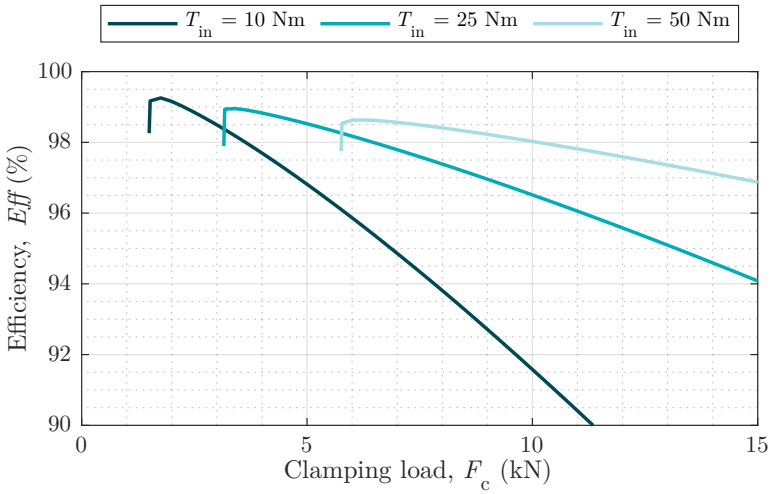

Figure 5.14: Efficiency of the point contact as a function of clamping load.

Figure 5.15a shows the SRR as a function of the clamping load. As expected, an increase in clamping load corresponds to a decrease in longitudinal sliding. Nevertheless, it is remarkable that at equal clamping load condition the longitudinal sliding increases with torque. This phenomenon is a consequence of the position of the required traction coefficient on the traction curve.

Similarly, Figure 5.15b shows the relative position of the spin pole to the semimajor axis of the contact interface. As anticipated, with reduced clamping loads, the spin pole appears further from the centre of the interface (higher longitudinal sliding conditions occur). The figure also illustrates that the gross slip region appears before the spin pole reaches the Hertzian contact boundary.

Figure 5.16 shows the needed traction coefficient represented as a function of the longitudinal sliding for the analysed three torque conditions and variable clamping load. The observed trends resemble to traction curves, where is no traction at conditions minimal longitudinal sliding. While longitudinal sliding increases, the traction coefficient also experiences an increase. It is worth mentioning that the traction curve of the figure represents a condition where the traction

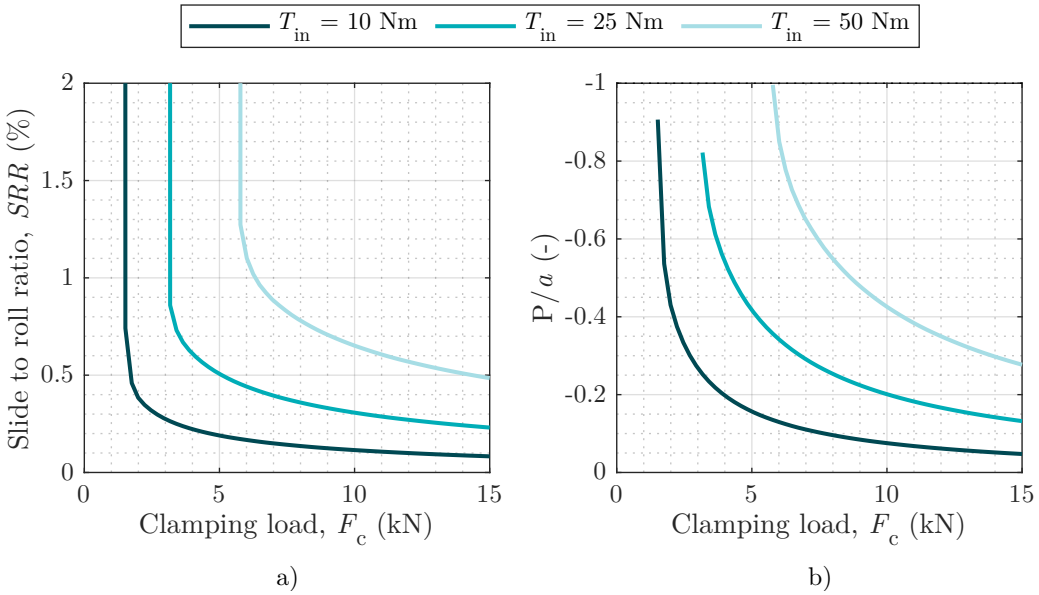

Figure 5.15: a) Longitudinal sliding and b) relative spin pole position as a function of clamping load of the input point.

force (torque) is fixed, and the normal force acting on the contact point varies. Therefore while longitudinal sliding increases the Hertzian contact pressure decreases. The following trends were observed in the curve:

- At low torque conditions, gross slip occurs at lower clamping loads (contact pressure), in addition, the maximum traction coefficient at low clamping loads is lower as a result of the EHL conditions (lower Newtonian viscosity of the lubricant).
- The traction curve does not exhibit a linear growth at low longitudinal sliding conditions. This phenomenon results from the changes in contact pressure. As slip increases as a consequence of decreasing the applied load, the EHL condition changes. Therefore, the Newtonian slope of the curve is not linear since different EHL conditions are represented on the same curve.
- The traction coefficient achieved at equal longitudinal sliding conditions is lower for the high clamping load condition. The author attributes this trend to the contact scale, when the same longitudinal sliding is achieved at different contact pressure conditions (normal load), the one with the highest normal load has the largest contact interface, resulting in the lowest traction coefficient. This observation aligns with the results presented by Meyer et al. [118] (see Figure 2.13 in Chapter 2).
- The figure does not depict a thermal region at high longitudinal sliding because after the gross slip limit the traction equilibrium is not achieved. Therefore, an horizontal asymptote was obtained (indicating the maximum achievable traction coefficient).

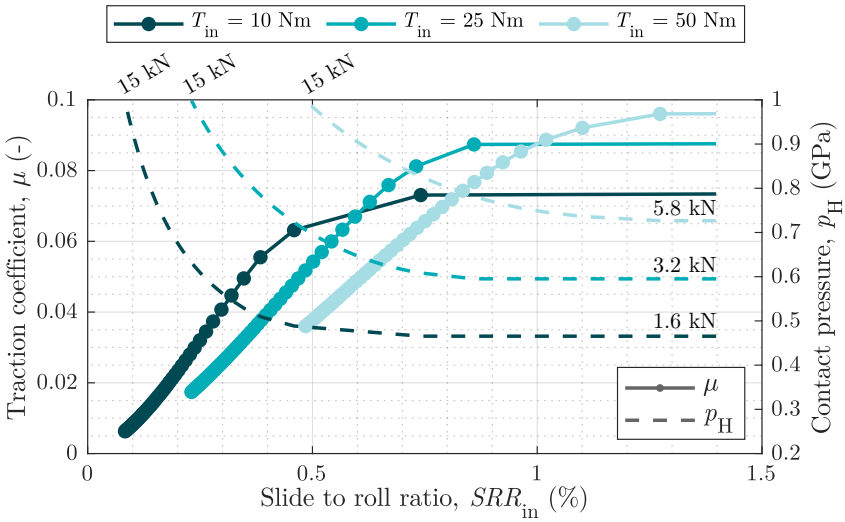

Figure 5.16: Traction curve as a function of SRR calculated adapting the applied clamping load.

Contact efficiency as a function of torque

The efficiency trends as a function of torque maintaining the clamping load constant are illustrated in Figure 5.17 for the working conditions defined in Table 5.6 (ii). Four clamping load conditions were analysed, corresponding to the vertical dashed lines at 2, 4, 6 and 10 kN shown in Figure 5.13. The figure indicates that the efficiency decreases under low and high torque conditions. On one hand, the efficiency drop in high torque conditions results from the gross slip occurring in the point contacts. On the other hand, the efficiency decrease at low torque conditions is a consequence of the overlamped condition. The contact efficiency under equal torque conditions is lower for high clamping load conditions; however, the gross slip region appears at higher torque values under these clamping load conditions. The obtained contact efficiency trends are similar to the ones shown in other studies [27, 38, 118].

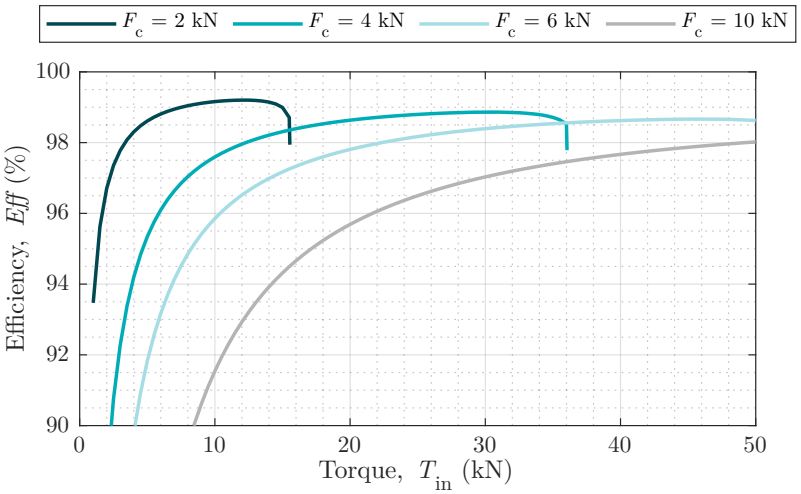

Figure 5.17: Efficiency of the point contact as a function of torque.

The longitudinal sliding as a function of torque is depicted in Figure 5.18a illustrating the relationship between the longitudinal sliding and torque. The figure indicates that the longitudinal sliding when the torque that has to be transmitted is negligible is almost null. The increase in longitudinal sliding corresponds with distinct regions in a traction curve. Initially, there is a linear increase in longitudinal sliding with torque, which aligns with the Newtonian region of a traction curve. As torque continues to increase, the longitudinal sliding increase accelerates, which corresponds to the non-Newtonian region of a traction curve. Finally, an asymptote is reached where the torque no longer increases, beyond this point gross slip occurs ($SRR = 200\%$). Similarly, the relative position of the spin pole as a function of torque is represented in Figure 5.18b; the higher the applied clamping load, the closer the spin pole is to the centre of contact interface. Consequently, in these clamping conditions, lower efficiencies are observed at low torque, but conversely, higher torque can be transmitted without experiencing gross slip.

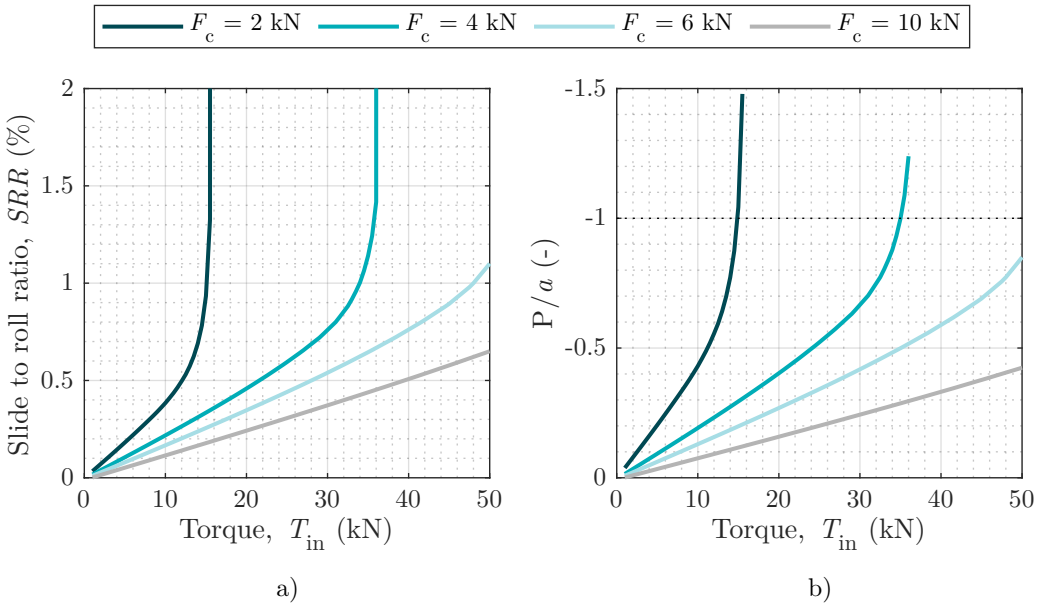

Figure 5.18: a) Longitudinal sliding and b) relative spin pole position as a function of torque of the input point.

The normal load has been maintained constant at each condition, the contact pressure is also maintained equal as a function of torque. Table, 5.8 indicates the contact pressure and contacts interface's semimajor axis results for each of the analysed clamping condition.

Table 5.8: Contact pressure and semimajor axis of the contact interface under each clamping condition.

F_c	2 kN	4 kN	6 kN	10 kN
p_H	0.51 GPa	0.65 GPa	0.74 GPa	0.87 GPa
a	0.80 mm	1.02 mm	1.16 mm	1.37 mm

Figure 5.19 illustrates the traction curves obtained maintaining the clamping load constant and adapting the torque for the four clamping load values. Different working insights may be inferred from the figure:

- A linear slope is obtained at low longitudinal sliding conditions conversely to the trends obtained in the previous case (see Figure 5.16). Since the clamping loads were maintained constant, the EHL conditions did not change and therefore, the Newtonian region is linear—the contact pressure is maintained equal in the four conditions.
- The obtained traction coefficient at low longitudinal sliding is lower under the high clamping load conditions. The author attributes this trend to the contact scale, since the contact interface is larger, the spin pole position relative to the interface size is lower—it is closer to the interface centre. Therefore, a lower traction coefficient acts in the contact. This trends was reported also by Meyer et al. [118], nevertheless it was not related with the contact scale.

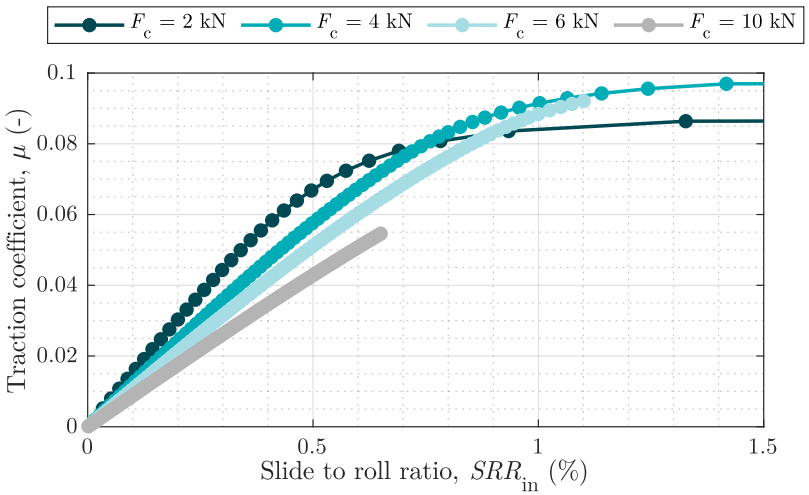

Figure 5.19: Traction curve as a function of SRR calculated adapting the torque to be transferred.

Discussion of the traction equilibrium

In this case study, it has been shown that the traction equilibrium varies as a function of the applied clamping load and/or the torque to be transferred. This phenomena may be explained by Figure 5.20, which shows a traction curve for S50 lubricant measured in a ball on disc tribometer. Therefore, the transmission equilibrates under different longitudinal sliding conditions as a function of the location of the required traction coefficient. Three possible traction equilibrium scenarios are represented in Figure 5.20, which are as follows:

- **A: Overclamped condition** is the condition where the applied clamping load is high in comparison to the torque that has to be transmitted. Hence, the needed traction coefficient is found at low longitudinal sliding conditions. In this region, rolling contact fatigue may decrease the durability of the components as a result of the excessive load (contact pressure).
- **B: Optimum clamping** refers to the condition where the needed traction coefficient is higher than in the previous condition, and therefore it is found at a higher longitudinal sliding condition. This longitudinal sliding means that the spin losses are decreases to the minimum without increasing the longitudinal sliding losses excessively (subsequently explained). Therefore, it corresponds to the optimum clamping condition.

- **C: Underclamped condition (Gross slip)** is related with the condition where the applied clamping load is too low. Therefore, the needed traction coefficient is higher than the maximum on the traction curve. No torque transmission is achievable in this condition as there is not enough traction force. Therefore, the driven component would be stopped efficiency drops to zero. This condition is the most critical condition because it may lead to different failures on the components such us scuffing.

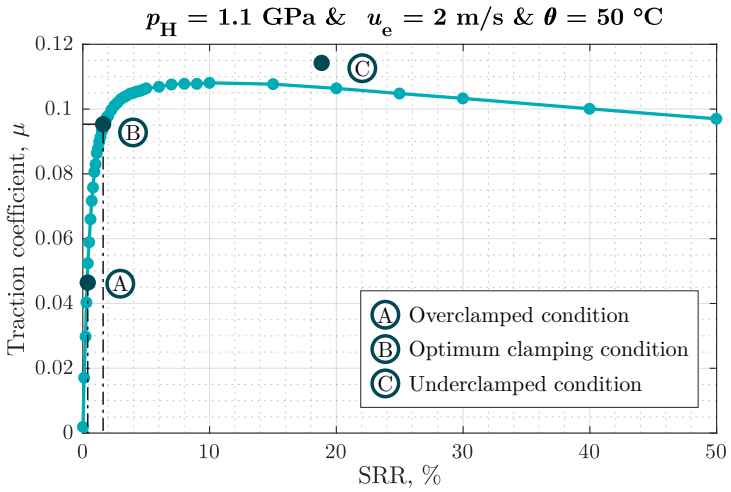

Figure 5.20: Traction equilibrium of representation by a representative traction curve.

The traction equilibrium affects the efficiency as represented in Figure 5.21. According to the efficiency determination, at low longitudinal sliding condition, the output power is considerably lower than the input power since the traction load (F_t) is low and the power losses increase in terms of spinning torque. Similarly, at high longitudinal sliding conditions the output linear speed would be lower than the input one, and therefore, the efficiency decreases also. Hence, there is an optimum efficiency condition as a function of longitudinal sliding.

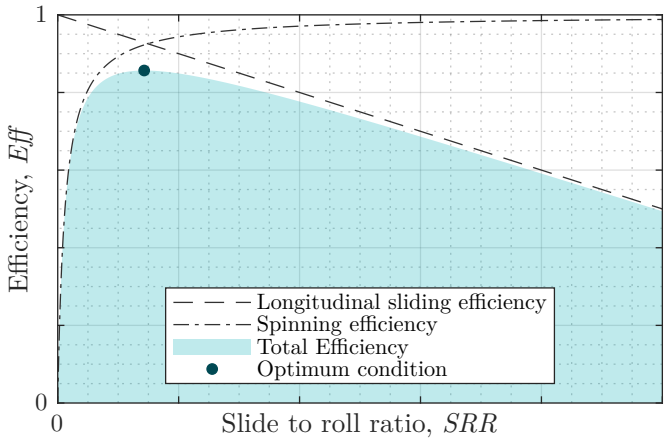

Figure 5.21: Contact efficiency representation as a function of longitudinal sliding.

5.2.3 *Case 3: Transmission performance; the impact of clamping loads*

Figure 5.22 presents the efficiency map of the transmission mapping clamping load and torque against efficiency at 1500 RPM of input speed and 1:1 of ideal transmission ratio. Differences were found in comparison to the contact efficiency map depicted in Figure 5.13. On one hand, the figure reveals an overall efficiency decrease as a consequence of the additional power loss sources: two contact points and rollers' bearing and churning losses. Therefore, the overclamped region increased in comparison to the contact efficiency map. On the other hand, the gross slip limit remains consistent with the previously observed conditions indicating that traction cannot be transmitted through the contact beyond this threshold.

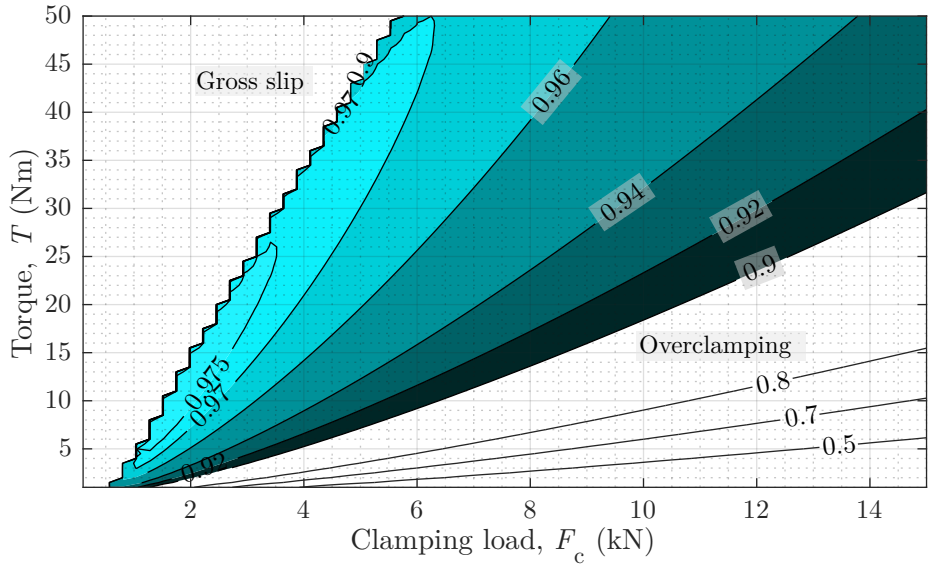

Figure 5.22: Efficiency map of a T-CVT for i = 1:1 and ω_{in} = 1500 RPM (considering equal input/output clamping loads).

Optimum clamping load determination

It may be expected that the optimum condition would be to gradually optimize each of the contact points to maximize the energy that goes to the following component. For that purpose, an input power is determined and the optimum input clamping condition (the minimum power loss condition) is determined. Then, the power losses of the rollers are calculated to end with the optimization of the clamping load of the output point. The obtained results are the optimum clamping conditions independently calculated for each point contact. In addition, the obtained results are compared to the equally loaded condition. The optimization has been carried out for one speed, three torque and five transmission ratio conditions determined in Table 5.7. The evolution of the efficiencies of each of the point contact as a function of the applied clamping load is depicted in Figure 5.23.

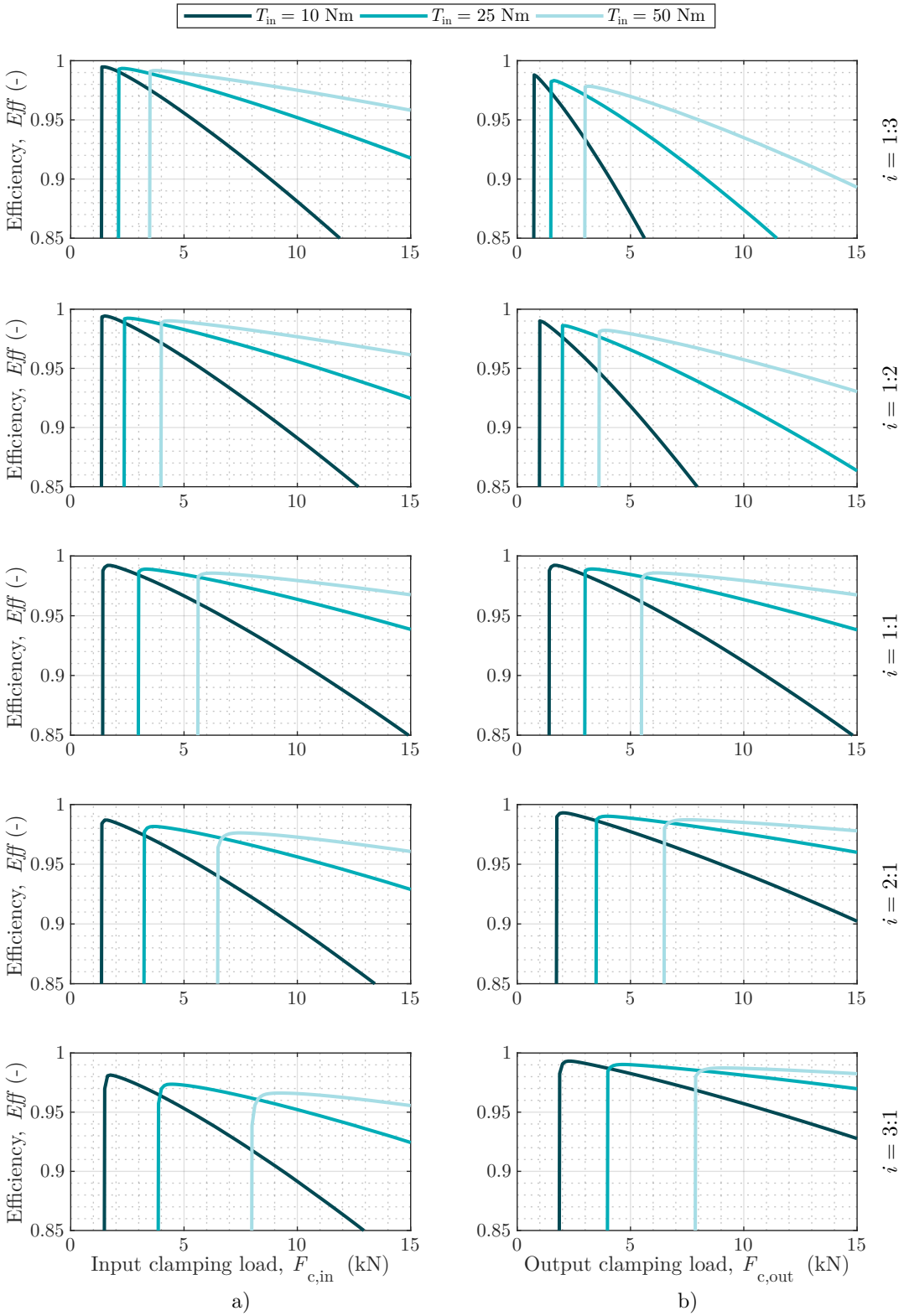

Figure 5.23: Clamping load optimization changing the transmission ratio from top to bottom i = 1:3; i = 1:2; i = 1:1; i = 2:1; i = 3:1 and a) input and b) output clamping load optimization curve.

Figure 5.23 shows the efficiency as a function of clamping load of each of the contact points, and the clamping values with the maximum efficiency condition are determined in Figure 5.24. The following trends where identified:

- Similarly as in the previously shown results. The higher the torque to be transmitted the higher the required clamping load will be across all the transmission ratio condition.
- Under the 10 Nm condition, the optimized input clamping load is almost equal for the five transmission ratio conditions. However, changes in the optimum output clamping load were identified. While transmission ratio turn from multiplier mode to reducer mode, higher output camping loads are required. In addition, in multiplier mode, the clamping load required on the output point contact is lower than the load on the input one.
- The optimum efficiency condition occurs close to the gross slip limit, therefore, it may be expected that under a slight variation on torque or clamping load the transmission may loss traction equilibrium and gross slip happen. Therefore, for security purposes,, it may be adequate to work under certain overclamped condition.
- The optimum clamping load for equal torque conditions vary as a function of the transmission ratio. Equation 5.5 determines the traction coefficient acting on the contact point and it shows that the transmission ratio (inclination angle and transmission radius) affects the the required traction coefficient. It is worth mentioning that the variation of the applied clamping load as a function of transmission ratio can not be achieved by passive clamping mechanisms such as loading cams.

On one hand, Figure 5.24 illustrates that the required clamping force at equal torque conditions increases in when the transmission ratio turns into reducer mode; since the same torque has to be transferred by a smaller radius more load is required (see Figure 5.25). On the other hand, the figure reveals that under reducer mode conditions the clamping load required in the output point is higher than the load required in the input one, nevertheless the differences decreases while the torque that has to transfer increases. This is a result of the increased losses; less energy than expected reaches to the output point and therefore less clamping load than expected has to be applied. In ideal conditions, it may be expected that the output point should be more clamped than the input under reducer mode conditions.

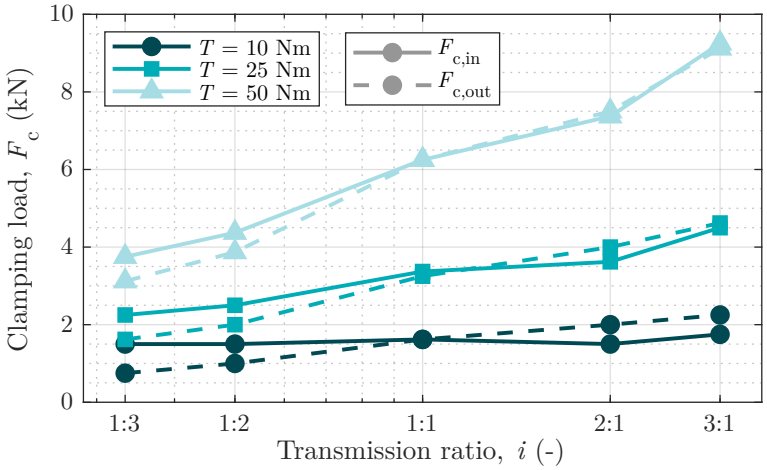

Figure 5.24: Optimum input and output clamping load values as a function of ideal transmission ratio.

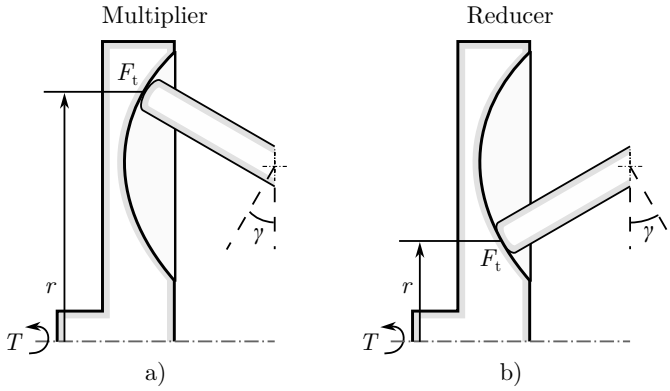

Figure 5.25: Transmission ratio effect on the required clamping load.

Figure 5.26 shows the efficiency values of the optimized clamping load conditions. In addition, each of the power losses—input contact, output contact and rollers—are shown. On one hand, the figure highlights that there are disparities in the power losses between the input and output points, resulting in different behaviours for each of the point contacts of the transmission. It is worth noting that at a 1:1 transmission ratio, the performance of both point contacts is almost equal. This equality arises from the contact conditions, which are only met at this transmission ratio. On the other hand, the losses in the rollers exhibit significant variations depending on the transmission ratio. This variation is caused by the the impact of the transmission ratio on the input radius (r_{in}). Therefore, maintaining a constant input speed, the speed of the rollers is altered. Particularly in the multiplier mode the roller speed increases due to the higher input radius, consequently, the rollers experience greater losses in this mode.

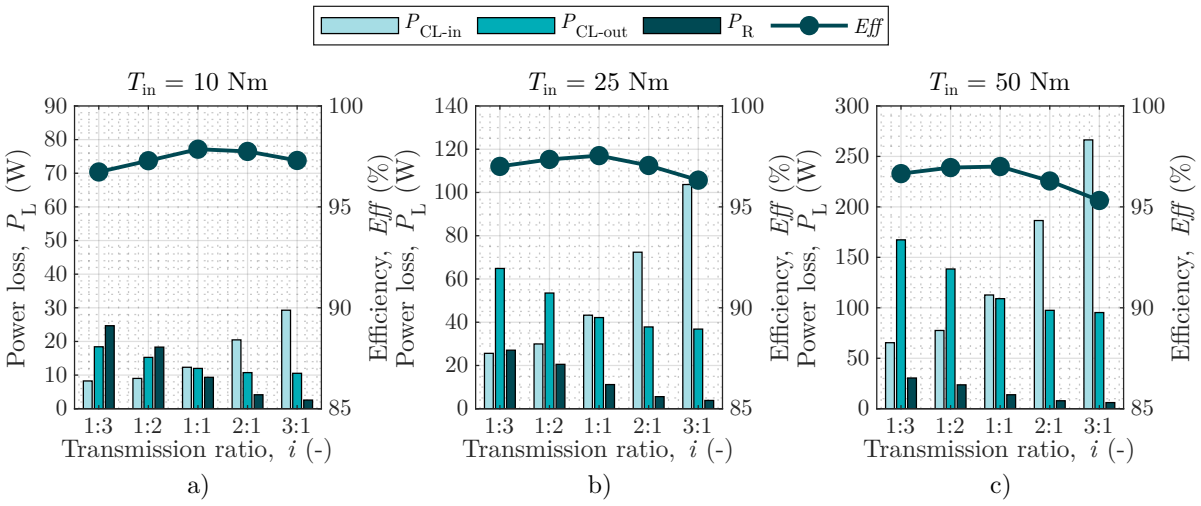

Figure 5.26: Power loss and efficiencies of the optimized clamping load conditions for a) T = 10 Nm b) T = 25 Nm and c) T = 50 Nm.

The influence of the transmission ratio on the power losses of each of the point contacts is a consequence of the contact scale (semimajor axis). The longitudinal sliding happening on each of the point contacts is illustrated in Figure 5.27. The figure reveals that in multiplier mode, the semimajor axis of the output point exceeds that of the input point, resulting in a shallower slope in the Newtonian region of the traction curve acting on the larger contact interface. Consequently, power losses are higher under conditions of increased longitudinal sliding. Conversely, the opposite occurs under reducer transmission ratio conditions. where the

semimajor axis of the input point surpasses that of the output point, leading to greater power losses in the output point. Unexpectedly, the maximum efficiency condition was observed under the 1:1 transmission ratio, where spinning speed is at its maximum. However, it is important to highlight that this condition remains unaffected by the contact scale, unlike other transmission ratio conditions.

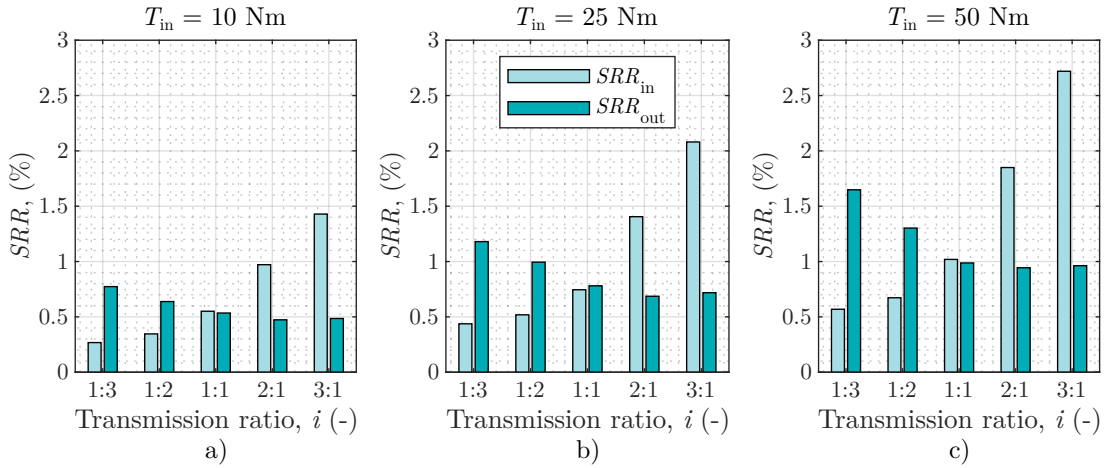

Figure 5.27: Longitudinal sliding occurring in each contact point under optimum input and output clamping load conditions for a) T = 10 Nm b) T = 25 Nm and c) T = 50 Nm.

Figure 5.28 shows the power loss and efficiency results for a condition where the input clamping load has been optimized but maintaining the output load equal to the input one. The most significant change is that generally, the output power losses increased across all the analysed conditions. Additionally, in the particular case of 10 Nm and reducer mode the zero efficiency was achieved as a consequence of the gross slip occurring on the output contact point. The dashed line on Figure 5.23b, in the reducer transmission ratio, indicates that gross slip occurs if the same load as at the input point were applied to the output. From this results, it can be inferred that not both contact points should be equally loaded since differences may occur and the transmission's performance is altered.

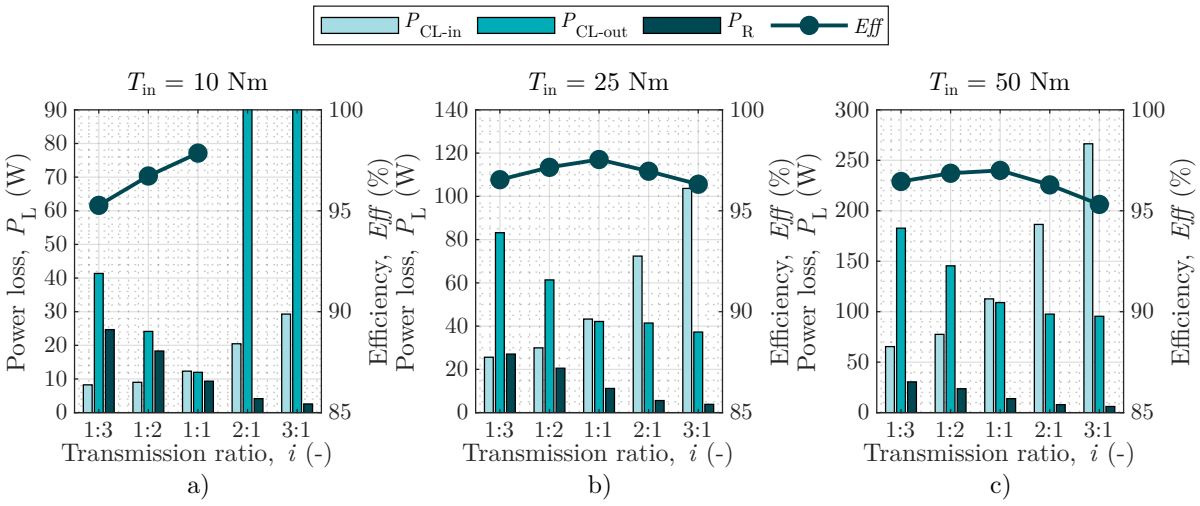

Figure 5.28: Power loss and efficiencies under the equally loaded and optimized input clamping load conditions for a) T = 10 Nm b) T = 25 Nm and c) T = 50 Nm.

As described previously, the optimum efficiency condition is close to the limit of the gross slip, which means that a small variation in the clamping loads and/or torque can destabilise the transmission. Therefore, the calculation has been repeated overclamping the transmission by 1 kN to the optimum input clamping condition (maintaining both clamping loads equal). The results shown in Figure 5.29 reveal an increase in the power losses of both point contacts. Therefore an overall decrease in the transmission's efficiency was observed. Nevertheless, the decrease in efficiency is lower at high torque conditions than in low torque conditions, since the 1 kN of overclamping has less effects in proportion to the low torque conditions.

Additionally, the results showed that the clamping load applied on the input point contact is crucial to maximize efficiency of the transmission. Since the power losses on the input point determine the energy on the second point, in an optimum clamping condition, the energy on the output is similar to the one in the input (high efficiency). Nevertheless, in a overclmaped condition, the energy transmitted from the input disc to the roller will be lowered, and therefore, the output point results to be more overclamped since it has less torque to transmit and more clamping load than the required. Therefore, in a condition of overclamped input point, the output clamping should decrease considerably not to increase excessively the output power losses.

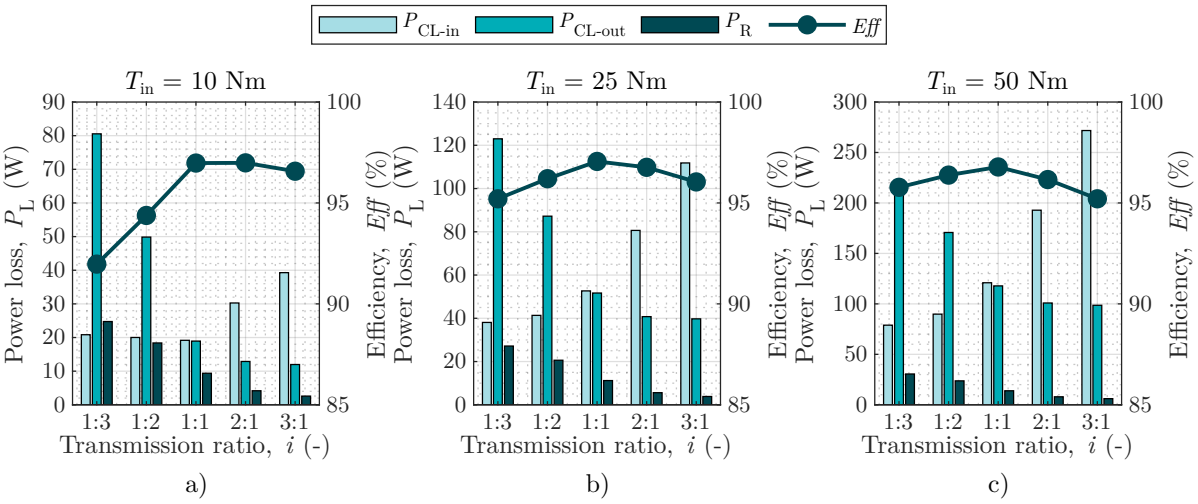

Figure 5.29: Power loss and efficiencies under the 1 kN overclamped equally loaded conditions for a) T = 10 Nm b) T = 25 Nm and c) T = 50 Nm.

The efficiencies of the three clamping conditions have been represented together at Figure 5.30. The figure reveals that the independent clamping loads may have an impact under low torque conditions since the decrease in efficiency is considerably higher under these conditions. Nevertheless, at large torque conditions the decrease in efficiency is negligible even at 1 kN overclamped condition. In addition, based on the premise that the optimum clamping condition always occurs close to the gross slip limit, it may be preferable to consider higher clamping load conditions (overclamped by 1 kN) to ensure that the traction equilibrium is always achieved. It can be concluded that even if different behaviour was found in each of the contact points of the transmission, similar normal loads are required in both point contacts, hence, equal normal load may be applied in both point contacts with the purpose of simplifying the design of the transmission, furthermore, less actuators would be required.

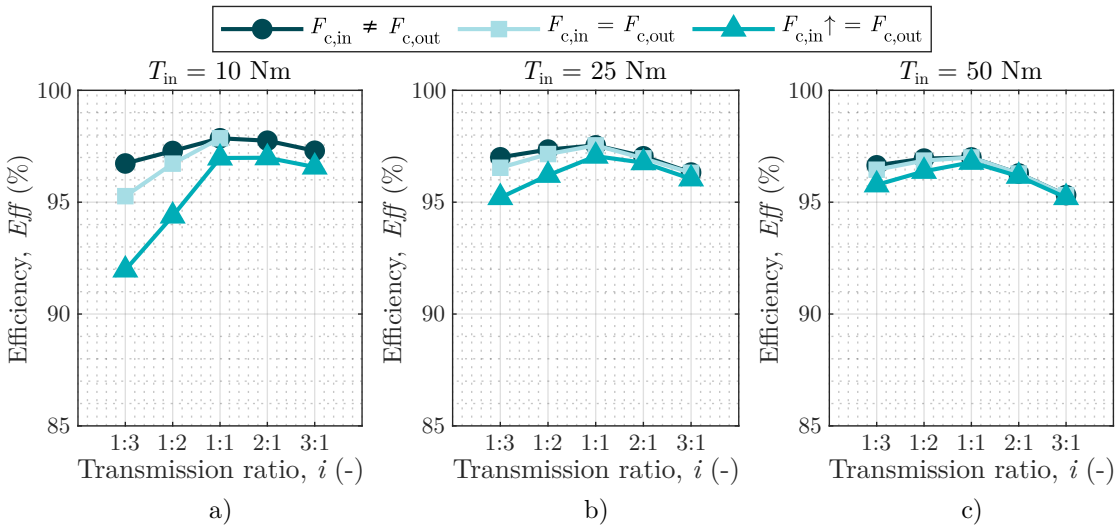

Figure 5.30: Comparison of the efficiency of the transmission under equal working conditions and different clamping conditions for a) $T = 10$ Nm b) $T = 25$ Nm and c) $T = 50$ Nm.

5.3 CONCLUSIONS

In the present chapter a working performance and efficiency prediction model of a T-CVT has been presented to find the optimum clamping conditions. It has been found that the applied clamping loads are critical in the proper performance of this kind of transmission. The following conclusions were inferred:

- On one hand, low clamping loads lead to underclamped conditions and gross slip occur, which will cause no power transmission. On the other hand, too high clamping condition decreases the efficiency of the transmission due to spinning losses, nevertheless, torque transmission is achieved. Therefore, the optimum longitudinal sliding may be achieved adapting the clamping loads.
- It has been identified that the input clamping load plays an important role on the performance of the output point. The power at the output point depends on the losses than happened in the input point as represented in the power flow diagram of Figure 5.1. In a condition where the input power losses are high, less power reaches the output one, resulting in overclamped condition and therefore the efficiency of the transmission decreases.
- It has been revealed that the optimum clamping occurs close to the gross slip limit. Therefore, it may be preferable to work under certain overclamped conditions in order to prevent possible traction equilibrium losses as a result of any peak torque while operation.
- It has been shown that optimum clamping loads changes with transmission ratio due to size effects. Higher loads are required in reducer conditions due to the low input radius (see Figure 5.24). Thus, passive clamping devices have drawbacks, where load is proportional to torque, therefore it leads to inadequate clamping conditions.
- The hypothesis has been theoretically answered, since an efficiency increase of 1% is found under low torque conditions and multiplier transmission ratio conditions by means of independently controlled clamping loads. Nevertheless, under high torque conditions the increase on the efficiency is negligible. Different behaviour is found in each of the contact points, however, similar clamping load are required in both of them.

6 EXPERIMENTAL STUDY

"The most exciting phrase to hear in science,
the one that heralds the most discoveries, is not
"Eureka!" but "that's funny...""
Isaac Asimov

This chapter presents the experimental study of the Toroidal type CVT to meet the demands of Objective O.3 of this thesis. In order to test the longitudinal sliding equilibrium and efficiency of the transmission a full toroidal CVT prototype has been developed with the main peculiarity of enabling to independently control the input and the output clamping loads. The measurements have been carried out in a transmission test bench which is based on two electric motors to achieve different working conditions as a function of speed and torque.

The first section of the chapter contains the description of the developed prototype: the design, manufacturing and assembly process as well as the sensors and actuators of the transmission. Afterwards the experimental procedure is defined, for that purpose the testing facilities are presented, then testing process is explained and subsequently, the data processing is explained. In the following section the results are presented; efficiency and longitudinal sliding trends are presented as a function of (i) torque maintaining the clamping loads equal, and (ii) independently controlled clamping load maintaining the torque constant. Finally, the results are discussed and some conclusions are inferred.

6.1 TOROIDAL TYPE CVT DESCRIPTION

6.1.1 *Transmission design, manufacturing and assembly*

A single cavity full toroidal CVT has been designed, Figure 6.1 shows a cut view of the designed transmission, which considers three rollers on a central base. The developed prototype has the peculiarity to independently control the input and output clamping loads in order to have different normal loads in each contact point between disc and rollers. The geometrical parameters of the designed transmission are defined in Table 6.1. A transmission ratio range from 1:3 to 3:1 is achieved by a set of ± 25° of tilting angle of the rollers. In addition, a conformity ratio of 0.5 has been chosen since it leads to higher efficiencies as stated in Appendix B. For further details of the designed components the drawings of the discs and rollers of the designed transmission are in Appendix C.

Table 6.1: Geometrical parameters of the designed and manufactured T-CVT.

r_0	e	γ	CR	n_r	m_r
110 mm	-20 mm	± 25°	0.5	3	1

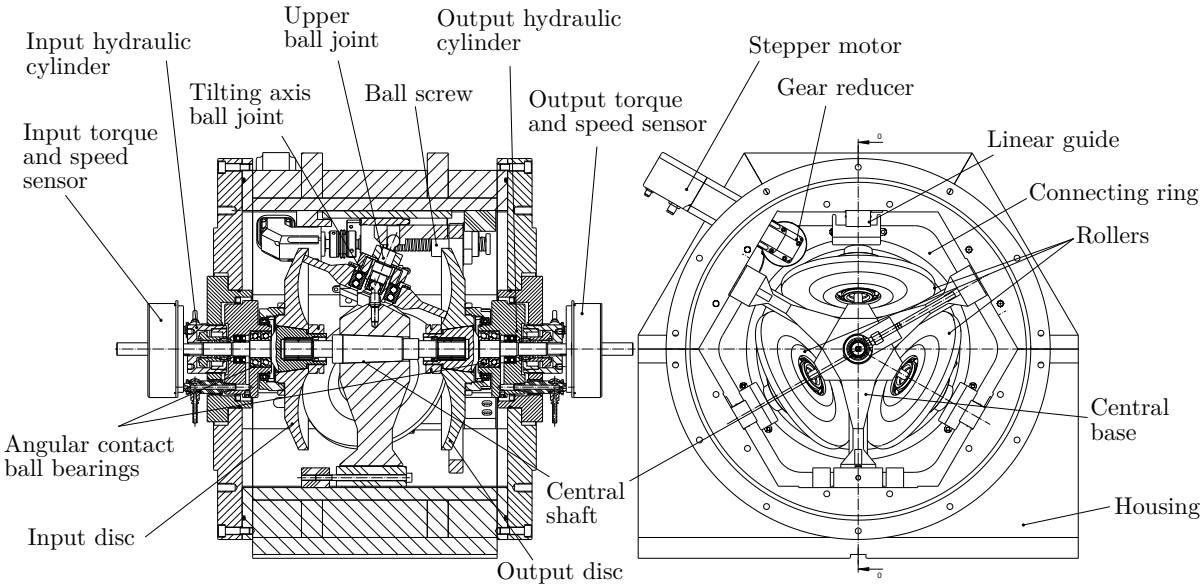

Figure 6.1: Drawing of the designed T-CVT transmission.

The designed transmission has been divided in three assemblies, an input and an output assembly, where the input and the output discs are positioned respectively and a central assembly with the central base and the three rollers. A central shaft has been positioned on the central assembly in order to determine the position of the discs with the purpose to align them with the rollers of the central base. The discs are mounted on two needle roller bearings on the central shaft (SKF NKI 20/20 bearing). Furthermore, they allow an axial displacement of the disc, which is of interest in order to avoid possible reactions when adapting the clamping forces. Additionally, the transmission's shafts are connected by grooved couplings that allow axial displacement of both shafts. This design helps to prevent undesired reactions that may occur as a result of the axial displacement of the shaft during the clamping process.

Transmission ratio shifting mechanism

The transmission ratio of this kind of transmission is controlled by means of changing the tilting angle of the rollers. For that purpose, the rollers have been placed on ball joints that determine their tilting axis, which is positioned in the centre of the toroidal cavity (see Figure 6.1). The rollers have been placed on double row ball bearings in order to withstand the tilting moment generated during the transmission ratio shifting (4207 ATN9 bearings of SKF). Additionally, in order to tilt the rollers, an upper ball joint is connected to a linear guide, hence, moving the linear guide forward and backward the transmission ratio is controlled. The tilting angle of the rollers is controlled by a stepper motor, a gear reducer and a ball screw represented in Figure 6.1. The ball screw moves a connecting ring, which is attached to the three linear guides of the rollers, and thus the upper ball joints.

The ideal transmission ratio of this kind of transmission is determined by the inclination angle of the roller γ calculated by Equation 6.1. Subsequently, the γ values is used on Equation 5.1 and 5.2. The angle is determined from the distance from the ball joint of the centre of the rollers to the upper ball joint ($d_{\text{joint}} = 71$ mm) and the displacement of the ball screw nut d_{nut}. The displacement is calculated from the ball screw (5 mm pitch), the gear reducer ($i = 10{:}1$) and the stepper motor (12800 steps per revolution): $d_{\text{nut}} = 5 \cdot n_{\text{step}} / (12800 \cdot 10)$.

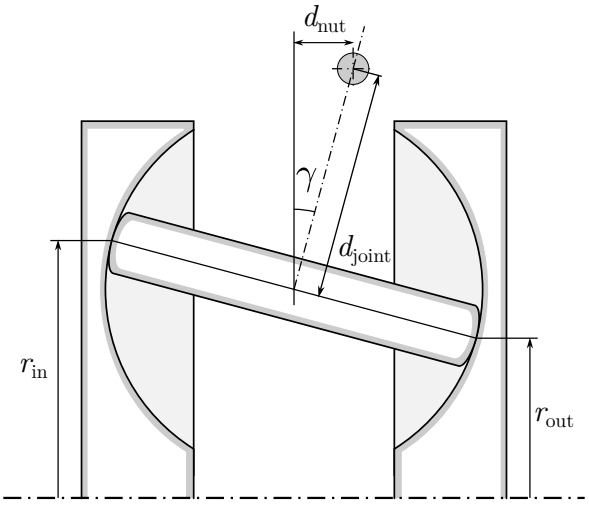

Figure 6.2: Determination of the transmission ratio (γ) of the prototype.

$$\sin\gamma = \frac{d_{\text{nut}}}{d_{\text{joint}}} \tag{6.1}$$

Two limit switches were positioned in the geometrical limits of stroke of the connecting ring (transmission ratio limits). Therefore, by means of a homing process and the geometry of the ball joints and rollers the transmission ratio is determined counting the number of steps of the stepper motor.

Clamping load mechanism

The normal load between the disc and rollers is controlled during the operation of the transmission in order to control the losses of the contact points since it has been identified that overclamping the points leads to a decrease on the efficiency of the transmission.

The control of the normal loads is carried out by two hollow plunger hydraulic cylinders on the input and output assemblies as represented in Figure 6.1. The hydraulic pressure of the cylinder is converted into clamping load, subsequently, the clamping load is transferred to the the contact points of the transmission by means of two angular contact ball bearings in tandem disposition (7205 BECBP bearings of SKF). The shafts of the discs are passed from the central hole of the hollow plunger hydraulic cylinders therefore, the force is in line with the shafts and undesired reactions are avoided.

The clamping load is determined from the hydraulic pressure and the effective area of the cylinder (see Equation 6.2). with p_{c} the hydraulic pressure inside the cylinder and A the effective area of the cylinder. The Enerpac RWH 120 cylinder has an effective area of 1718 mm^2.

$$F_{\text{c}} = p_{\text{c}} \cdot A \tag{6.2}$$

Additionally, differences in the normal loads happening on the rollers are generate a reaction force which is transferred to the central base from the ball joints.

Manufacturing and assembly

Figure 6.3 shows a photograph of the central part of the manufactured and assembled transmission where the three rollers are placed on the ball joints located on the central base.

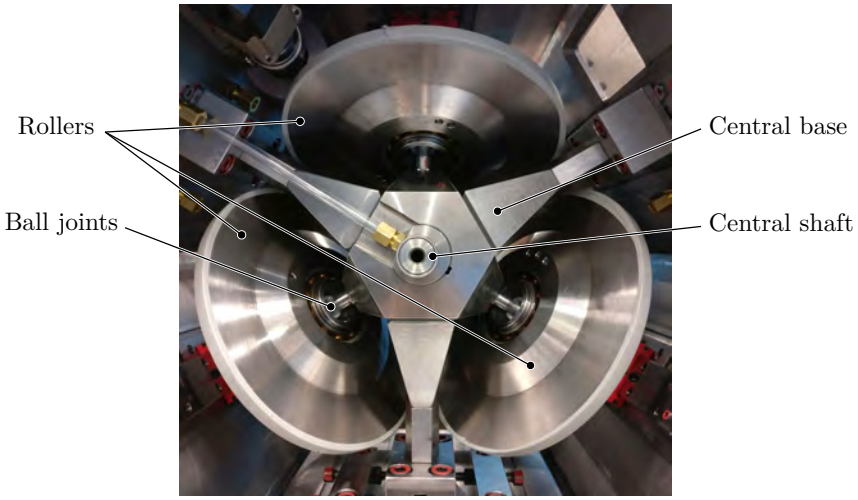

Figure 6.3: Photograph of the manufactured T-CVT transmission.

The following aspects were considered in the manufacturing process:

- Discs and the rollers are made of 16MnCr5 case hardened steel with the purpose to achieve a surface hardness of 59 HRC (equivalent to 700 HV). In rolling and sliding contacts the surface hardness plays an important in the durability of the components, the harder the better. Nevertheless, hardness makes the steel fragile, therefore instead of bearing steel (through hardened), gear steel (case hardened) has been used [169].
- This kind of transmission works under EHL lubrication regime, and it is interesting not to have direct metal to metal contacts while the operation with the purpose of preventing the components from wear. Additionally, the literature has revealed that polished surfaces prevent the components from rolling contact fatigue [181]. For that purpose, the disc and the rollers were designed considering polished surfaces similar to the roughness that can be found in bearings and/or tribometer samples. Once the components were manufactured, the surface roughness was measured by means of optical profilometers (Alicona IFG4) and it was stated that the surface roughness was under $\sigma_q = 50$ nm.
- The dimensional and geometrical tolerances of the manufactured components were measured in a coordinate measuring machine (CMM) to ensure the proper performance of the prototype and that load were correctly transferred into the contact points. The verification of the tolerances of disc and rollers are in Appendix C.

The assembly process was carried out similarly. The alignment of each of the components of the transmission was ensured by the CMM machine, and when the alignment was not enough the components were modified in order to correct their alignment.

The transmission was filled with Santotrac 50 which is a commercially available traction lubricant. Furthermore, a series of ducts have been considered to supply lubrication to all the bearings as shown in Figure 6.3, where a duct is shown from the housing to the central shaft to lubricate the needle bearings.

6.1.2 *Sensors and actuators of the transmission*

Sensors and actuators are required in order to monitor the performance of the CVT transmission and to make decisions about how to adapt the transmission ratio and clamping loads as a function of the measured conditions. Table 6.2 shows the sensors and actuators considered in the developed transmission prototype.

Table 6.2: Sensors and actuators of the T-CVT.

Sensors	Device	Range	Communication
Speed	Encoder	0 - 8000 RPM	TCP-IP
Torque	Strain gauges on shafts	-50 - 50 Nm	0 - 10 V
Hydraulic pressure	Parker SCPSDi-100	0 - 100 bar	4 - 20 mA
Lubricant temperature	Pt100	-20 - 100 °C	4 - 20 mA
Actuators			
Linear actuators (F_c)	MecVel ALI1		
Stepper motor	IGUS (NEMA 23)		
Lubricant pump	Hydac UKF-1		

Input and output speed measurements are essential in order to calculate both, the longitudinal sliding happening in the transmission as well as the efficiency of the mechanism. Similarly, the torque is needed in order to determine the efficiency of the transmission. The hydraulic pressure is monitored to determine the clamping load acting in each of the contact points of the transmission. Additionally, the lubricant temperature has been measured since it is widely known that the lubricated traction depends on the lubricant's temperature; the higher the temperature, the lower the traction.

It is worth mentioning that the torque sensors have been specifically developed in this project in a partnership with ARC company from Italy. They are integrated in the shafts of the transmission, where measurement is accomplished using strain gauges attached to the input and output shafts. The sensor's output signal ranges from 0 to 10 V, where 0 V corresponds to -50 Nm, and 10 V corresponds to 50 Nm. The data transference and power supply of the sensor is carried out wirelessly through a coil. For that purpose, the sensor comprises a stator and a rotor, with the rotor directly connected to the strain gauges, transmitting data to the stator, which is subsequently linked to the control cabinet.

The actuators of the designed prototype are mainly the clamping and transmission ratio controlling device. On one hand, two linear actuators were used to comprise two springs and thus control the hydraulic pressure (based on the stiffness of the spring) needed for the clamping load. On the other hand, an stepper motor was used to move the ball screw and change the tilting angle of the rollers. Additionally, a hydraulic power pump was used in order to recirculate the lubricant inside the transmission and to carry it to all the bearings and rolling contacts as well as to filter and refrigerate it.

A control cabinet has been built to measure the signals obtained from the transmission. For that purpose a CompactRIO 9047 controller of National Instruments was used and programmed together with Mondragon Sistemas company by LabView. The drivers of the actuators used on the prototype were included in the control cabinet.

6.2 EXPERIMENTAL PROCEDURE

6.2.1 *Test bench*

The tests were carried out in a transmission test bench on MGEP facilities. The experimental setup consists on two three-phase synchronous motors placed one against the other and the transmission placed between both of them as represented in Figure 6.4. One of them works in motor mode, which fixes the input speed and adapts the needed torque in order to maintain it. The other one works as a generator (brake), it fixes the braking torque and the speed is self balanced. A photograph of the setup is shown in Figure 6.5 identifying the main components.

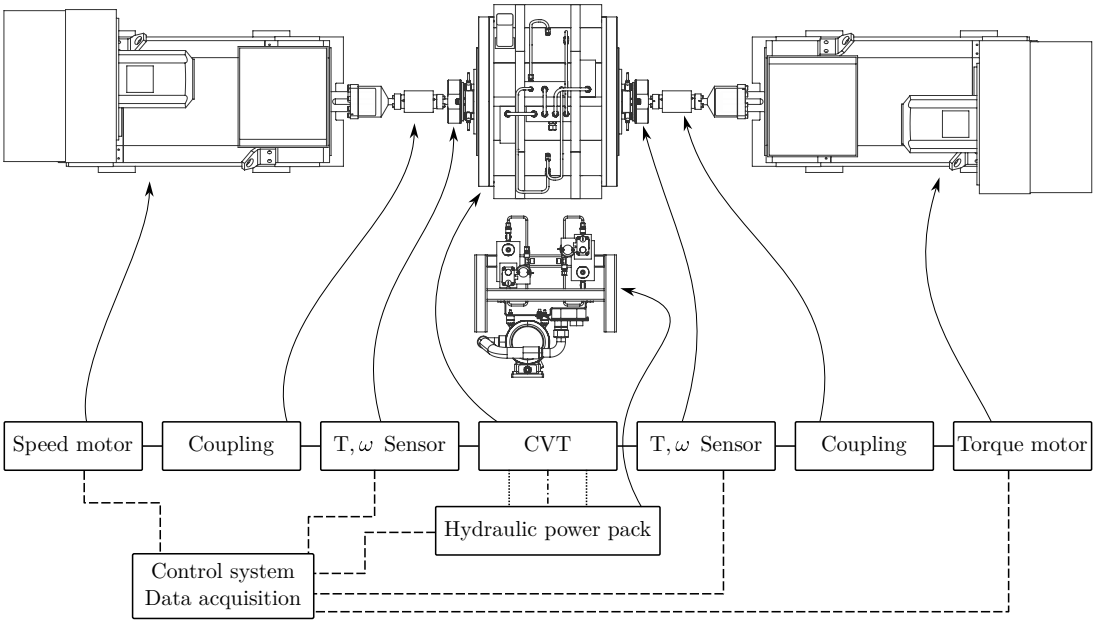

Figure 6.4: Schematics representation of the transmission test bench and control and acquisition system.

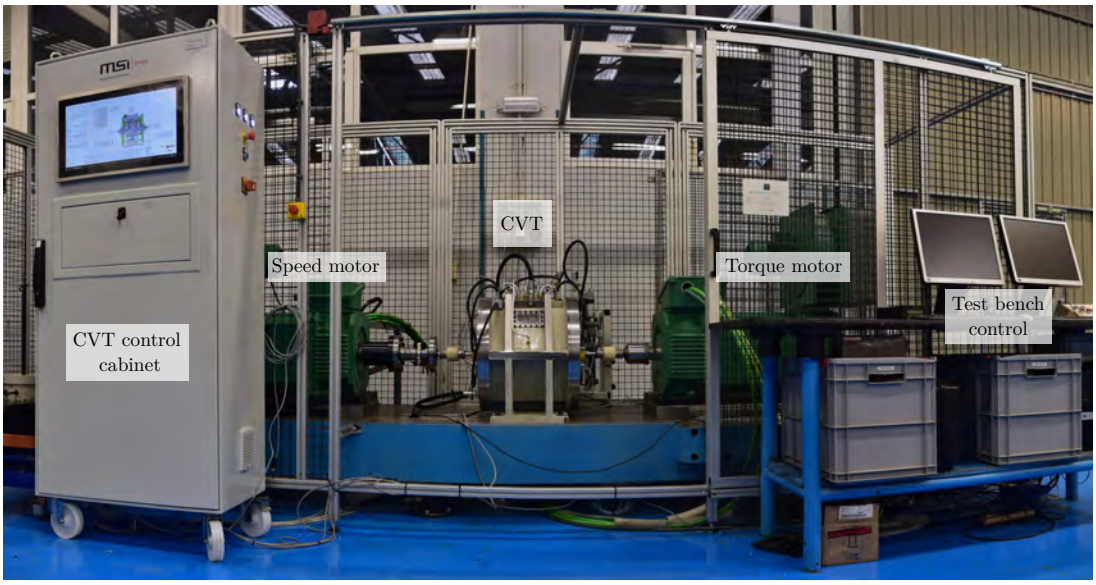

Figure 6.5: Transmission test bench photograph.

6.2.2 *Measurement procedure*

Tests are carried out as follows:

1. Firstly, the control cabinet of the CVT is switched on, the lubrication pump is turned on and the homing process of the stepper motor (transmission ratio) is carried out. Subsequently, the testing transmission ratio is established and the transmission is clamped to up to the desired clamping load. At this point the measurement is initiated.
2. Then, the two motors are turned on and gradually accelerated until the desired input speed is achieved.
3. Subsequently the torque/clamping load is adapted to test the behaviour of the transmission under different torque/clamping load conditions until gross slip happens or the measured torque exceeds 50 Nm. It has to be pointed out that when the output torque increases and gross slip happens the output shaft may stop.
4. Finally, the braking torque is set to zero, and the transmission is stopped. The measured data is saved for the subsequent analysis.

6.2.3 *Data processing*

After the test, the obtained data is processed by Matlab software. The efficiency and te longitudinal sliding has been calculated as follows based on the measured data.

Power and efficiency

The input and output power of the transmission are determined by the speed (ω) and torque (T) of the shafts as determined in Equation 6.3.

$$\begin{aligned} P_{\text{in}} &= \omega_{\text{in}} \cdot T_{\text{in}} \\ P_{\text{out}} &= \omega_{\text{out}} \cdot T_{\text{out}} \end{aligned} \tag{6.3}$$

Subsequently, the efficiency of the transmission is determined by Equation 6.4 relating both power values.

$$Eff_{\text{exp}}\,(\%) = 100 \cdot \frac{P_{\text{out}}}{P_{\text{in}}} \tag{6.4}$$

Longitudinal sliding

It has already been stated that longitudinal sliding is essential in order to transmit torque by means of lubricated traction forces, which is determined by the lubrication regime of EHL. In the transmission, longitudinal sliding occurs in the input and the output point contacts. However, the speed of the rollers is not measured. Therefore, the sliding happening in each of the contact points can not be measured. Nevertheless, Equation 6.5 gives the relation between the sliding motion happening in each contact point and the global longitudinal sliding, their relation is depicted in Figure 6.6a.

$$SRR_{\text{global}} = \frac{4 \cdot SRR_{\text{in}} + 4 \cdot SRR_{\text{out}}}{4 + SRR_{\text{in}} \cdot SRR_{\text{out}}}, \quad SRR_{\text{in,out}} \in [0, 2] \tag{6.5}$$

where SRR_{global} is the measured longitudinal sliding, combination the sliding happening in the input (SRR_{in}) and the output contact points (SRR_{out}). Note that the values of the longitudinal sliding are inside the range between 0 and 2. In addition, developing the equation, the definition of Equation 6.6 is achieved. There, the rotational speed of both shafts (ω_{in} and ω_{out}) and the ideal transmission ratio (i_{ideal}) determine the longitudinal sliding occurring in the transmission.

$$SRR_{\text{global}} = \frac{2\left(\omega_{\text{in}} - \omega_{\text{out}} \cdot i_{\text{ideal}}\right)}{\omega_{\text{in}} + \omega_{\text{out}} \cdot i_{\text{ideal}}} \tag{6.6}$$

Similarly, the relation between the real and the ideal transmission ratio is given by Equation 6.7, which is obtained combining the equation of the real transmission ratio ($i_{\text{real}} = \omega_{\text{in}}/\omega_{\text{out}}$) and Equation 6.6.

$$i_{\text{real}} = i_{\text{ideal}} \cdot \left(\frac{2 + SRR_{\text{global}}}{2 - SRR_{\text{global}}}\right) \tag{6.7}$$

Figure 6.6 depicts the effects of the longitudinal sliding on the transmission. On one hand, Figure 6.6 illustrates the relation between the longitudinal sliding occurring in each point contact and the global longitudinal sliding happening in the transmission. As expected, once the SRR of 2 (200%) is achieved in any of the point contacts the global longitudinal sliding (SRR_{global}) is also 200%.

On the other hand, the global longitudinal sliding relates the ideal and real transmission ratio as represented in Figure 6.6b. The longitudinal sliding leads to decrease the output speed, therefore the real transmission ratio turns to a reduction of the expected transmission ratio. The figure shows that a longitudinal sliding up to 100% at 1:1 of ideal transmission ratio leads to a real transmission ratio of 3:1 of reduction. Furthermore, under a SRR condition of 200% the transmission ratio would be infinite since there would be no output speed.

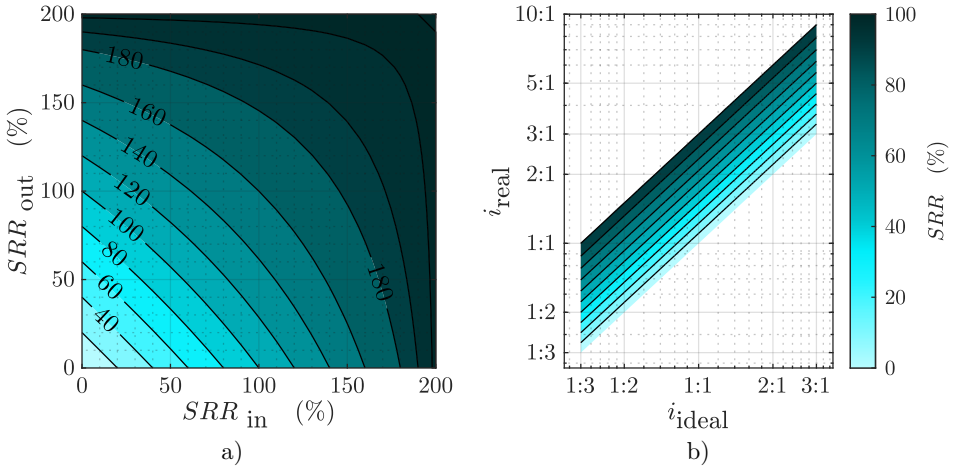

Figure 6.6: a) Relation between the local sliding and the global sliding (SRR_{global}) and b) Relation between the ideal and real transmission ratio by means of the global longitudinal sliding.

Figure 6.7 illustrates a variable output torque measurement of the CVT performance under 1:1 ideal transmission ratio (i_{ideal}), input speed (N_{in}) of 750 RPM and a equally loaded clamping load (F_{c}) of 4 kN, where 0% reveals the 0 Nm of output torque and 100% the 50 Nm. Firstly, Figure 6.7a illustrates the evolution of torque, since the test was carried gradually increasing the output torque the deviation of the output torque is low. Furthermore, since the 50 Nm of torque was not achieved, the test finishes at 60%. Additionally, an interesting insight is given by the torque values at the beginning of the test (0%), where the output torque is negligible but there is a certain amount of input torque produced by spinning losses (overclamping) and peripheral losses (churning bearings and sealing components). Figure 6.7b shows the evolution of rotational speed of the input and output shafts, the input speed is fixed while the output speed decreases while torque increases. Furthermore, Figure 6.7c and Figure 6.7d represents this trend in form of efficiency and longitudinal sliding respectively. At the beginning, there is a negligible output torque, consequently the efficiency is zero and increases gradually with torque until the gross slip condition is achieved. Similarly, a small amount of longitudinal sliding occurs at the beginning of the test since a certain longitudinal sliding is required, and it increases with torque. Additionally, Figure 6.7e depicts that both input and output clamping loads are equal and that have been maintained constant during the test. Finally, Figure 6.7f shows the comparison between the ideal and real transmission ratio, which is given by the longitudinal sliding, it depicts how increasing SRR the transmission turns into reducer mode.

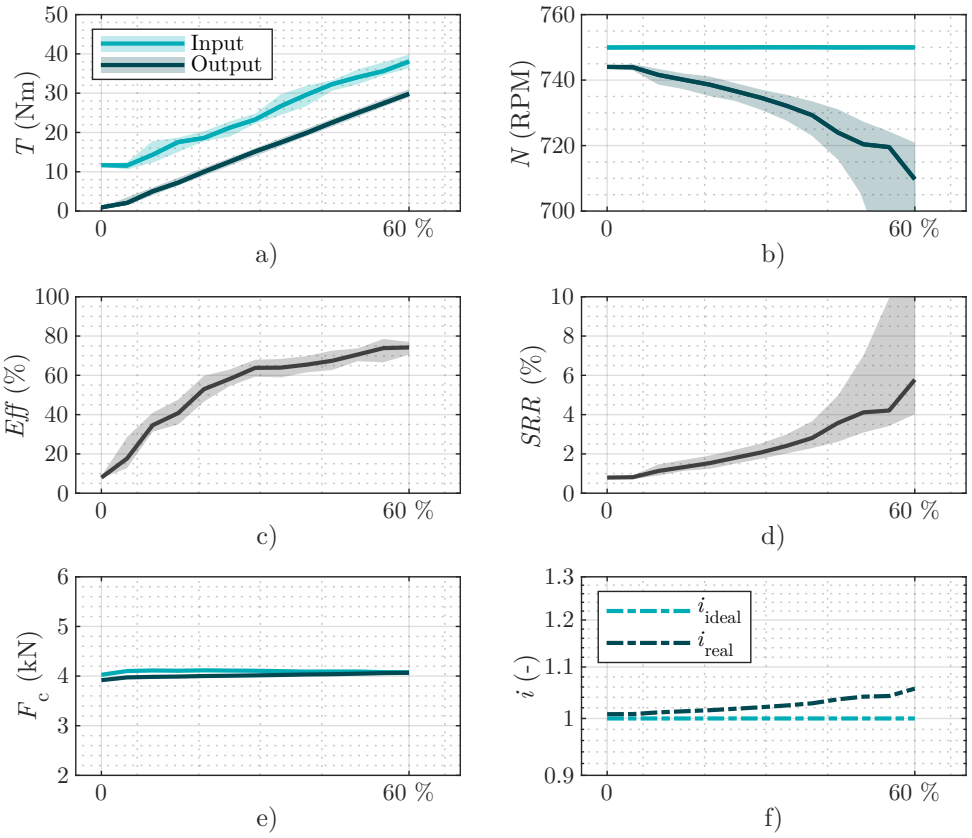

Figure 6.7: Variable torque measurement example under i = 1:1, N_{in} = 750 RPM and $F_{\text{c,in/out}}$ = 4 kN condition where: a) T, b) N, c) Eff, d) SRR, e) F_{c} and f) i.

6.3 EXPERIMENTAL EFFICIENCY AND LONGITUDINAL SLIDING TESTS

The following two case studies have been analysed:

Case 1: Efficiency and longitudinal sliding evolution tests as a function of the output torque. Three different transmission ratio and two equally loaded clamping load conditions have been tested. As a function of the transmission ratio the input speed has been adapted with the purpose of maintaining the output speed at 750 RPM; three transmission ratios were tested: i = 1:2, i = 1:1 and i = 2:1.
The tested conditions are determined in Table 6.3.

Table 6.3: Constant clamping load and variable torque test conditions.

ω_{in}	[375, 750, 1500] RPM
$\omega_{\text{out},SRR=0\%}$	750 RPM
T_{out}	0 → 50 Nm
$F_{\text{c,in}}$	[4, 8] kN
$F_{\text{c,out}}$	[4, 8] kN
i	[1:2, 1:1, 2:1]
Θ_0	20 °C

Case 2: Variable clamping load tests under low output torque conditions, since independent input/output clamping loads are preferable under low torque conditions. Two different tests were carried out in this case study.
On one hand, (i) independently controlled clamping load test were carried out. Firstly, the output load was maintained constant at 5 kN and the input clamping load was adapted to identify the performance trends. Then, the input clamping load was maintained constant at 5 kN and the output clamping load was adapted.
On the other hand, (ii) two input clamping load conditions were fixed (3.5 and 5 kN) and the output clamping load has been adapted to identify the efficiency and longitudinal sliding evolution with the objective to identify the effects of the input point on the output one.
The tested working conditions are defined in Table 6.4.

Table 6.4: Constant torque and variable clamping load test conditions.

	(i)	(ii)
ω_{in}	[500, 300] RPM	500 RPM
$\omega_{\text{out},SRR=0\%}$	[500, 600] RPM	500 RPM
T_{out}	10 Nm	10 Nm
$F_{\text{c,in}}$	($\Delta F_{\text{c,in}}$, 5 kN)	[3.5, 5] kN
$F_{\text{c,out}}$	(5 kN, $\Delta F_{\text{c,out}}$)	$\Delta F_{\text{c,out}}$
i	[1:1, 1:2]	1:1
Θ_0	20 °C	20 °C

6.3.1 *Variable torque at constant clamping force tests*

Efficiency and longitudinal sliding trends as a function of the output torque under two clamping load conditions are depicted in Figure 6.8 for three transmission ratio conditions. The efficiency trends illustrated in Figure 6.8a reveal that the efficiency of the transmission depends on the torque that has to be transmitted, when the torque is negligible, the efficiency is low since the output power approaches zero. While output torque increases, the peripheral losses are lower in proportion to the transmitted power and therefore the efficiency rises.

The applied clamping load also affects the efficiency of the transmission. The low clamped case leads to higher efficiency values in mos of the conditions; however, the maximum transmissible torque is lower. The high clamped case, though, transmits higher torque, additionally, its efficiency keeps gradually increasing after the condition where gross slip occur in the the low clamped condition.

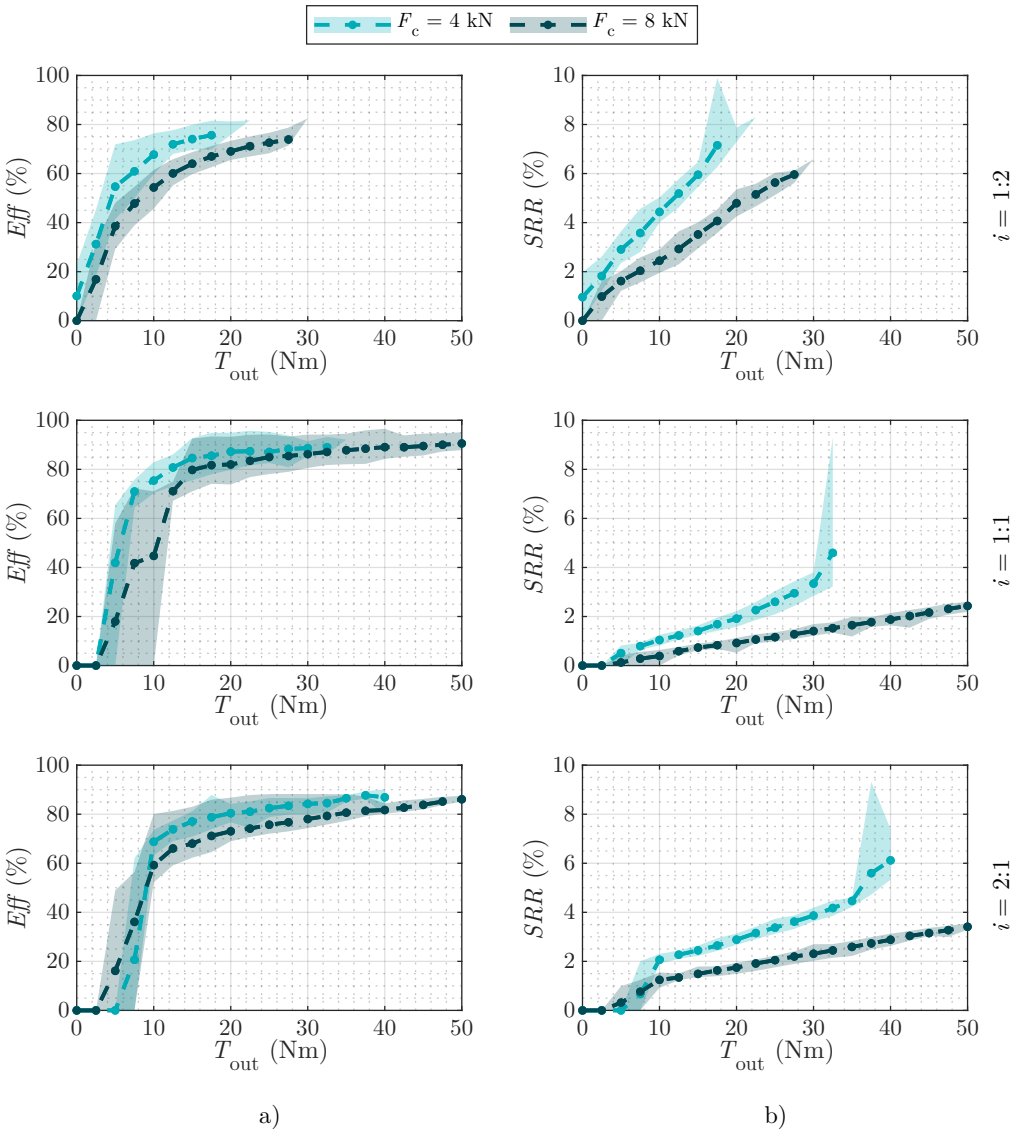

Figure 6.8: a) Efficiency and b) longitudinal sliding evolution as a function of torque for two different clamping conditions at (from top to bottom) i = 1:2, i = 1:1, i = 2:1.

Figure 6.8b shows the longitudinal sliding evolution as a function of the output torque. As expected, the longitudinal sliding trend resembles to a traction curve. At low torque conditions, the longitudinal sliding increases linearly with torque, which corresponds to the linear region of a traction curve. Subsequently, the non-Newtonian region and the thermal region appears in th low clamped conditions, where a rise of the SRR slope was achieved until gross slip occur. The figure reveals that once the traction equilibrium is lost, the measured data has a high deviation bound in positive SRR. Additionally, all the sliding trends reveal that the longitudinal sliding is lower in the high clamping load condition due to the lower traction that is required to transmit the same torque.

Figure 6.9 shows the values as a function of the transmission ratio of the afore shown figure under 15 Nm of output torque. Since the input speed has been adapted to maintain the power constant, the output speed and the output torque are equal ni the three conditions.

On one hand, Figure 6.9a illustrates the mean efficiency values. As expected across the three transmission ratio values, the mean efficiency is higher under low clamping load condition. Additionally, the maximum efficiency was measured under the 1:1 transmission ratio. Note that a similar trend was achieved in modelled transmission behaviour of the previous Chapter (see Figure 5.30), where the maximum efficiency occur under 1:1 transmission ratio.

On the other hand, the longitudinal sliding mean values are depicted in Figure 6.9b. The measured longitudinal sliding was lower for the high clamping load value. Since lower traction coefficient is required with a higher normal load, the transmission is equilibrated at lower SRR values. Additionally, the measured longitudinal sliding is minimum in the 1:1 transmission ratio condition. It has to be pointed out that this trend was also achieved in the previous chapter (see Figure 5.27). The maximum spinning speed condition occurs under the 1:1 transmission ratio [27, 28], however, since the contact interface shape and size changes with the transmission ratio; the position of the spin pole as a function of SRR is affected. Therefore, the increase of the longitudinal sliding changing the transmission ratio to a conditions with lower spinning speed is as a consequence of the scale effect, where the semimajor axis of the contact interface increases and therefore, lower Newtonian slope appears in the traction curve acting on the contact points.

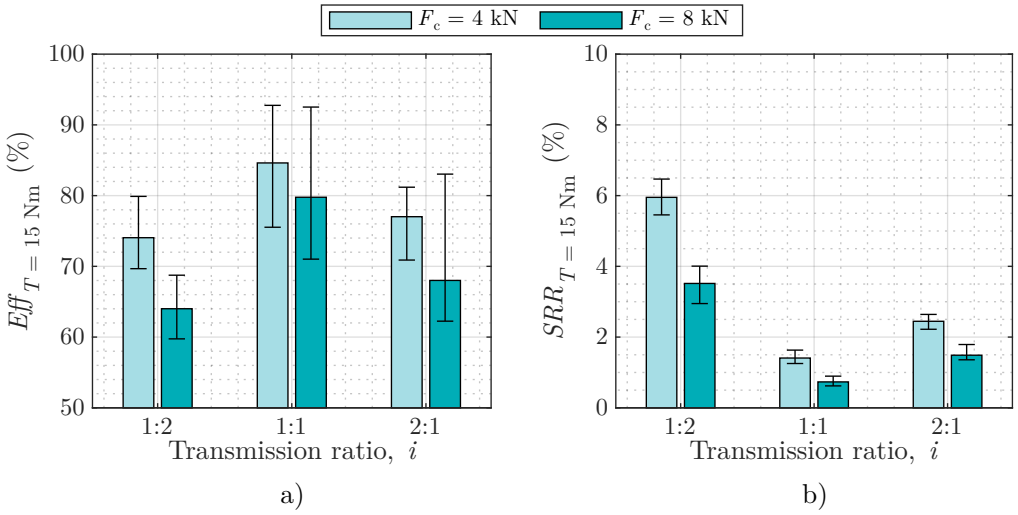

Figure 6.9: Main experimental results as a function of transmission ratio, a) efficiency and b) longitudinal sliding under T_{out} = 15 Nm.

6.3.2 *Variable clamping load at constant torque*

Figure 6.10 illustrates the efficiency and longitudinal sliding trends as a function of the clamping load for the conditions of Table 6.4(i). On one hand, the output clamping load has been maintained constant at 5 kN and the input load was adapted ($\Delta F_{c,in}$ in Figure 6.10). The figure illustrates that gross slip happened at 3 kN of clamping load for both transmission ratio conditions. This trend reveals that no torque transference can be carried out applying lower clamping loads on the input contact points.

On the other hand, the input clamping load was maintained constant at 5 kN and the output load was adapted ($\Delta F_{c,out}$ in Figure 6.10). The figure depicts that the gross slip condition happened at 1.5 kN of clamping load for both transmission ratio scenarios; a considerably lower load than the critical clamping load of the input point. Additionally, decreasing the applied clamping load indicates an increase on the mean efficiency value caused by the overclamping losses. Furthermore, an efficiency drop was measured for lower clamping load values to the gross slip limit.

This trend reveals differences in the performances between the input and output contact points. If gross slip on te input point occur at 3 kN the limit of the output one occurs under lower clamping load conditions. Since losses occur gradually in the power flow diagram (see Figure 5.1) the input point transmits more energy than the output one.

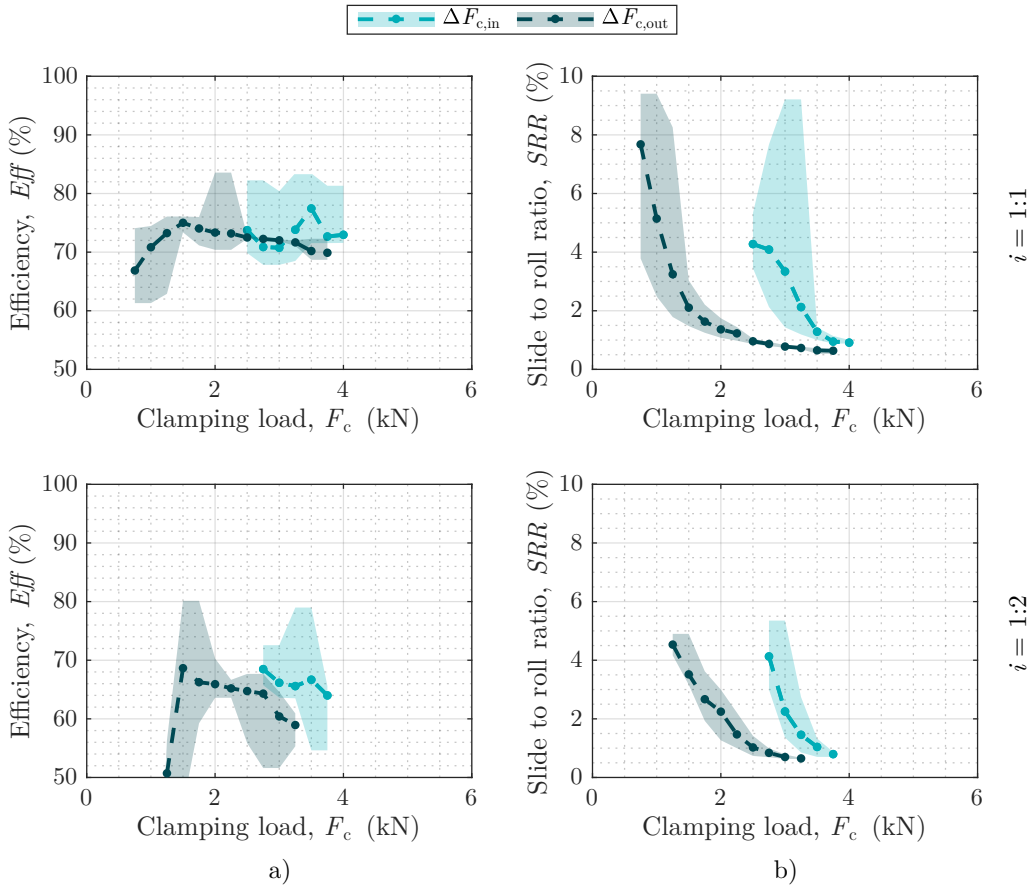

Figure 6.10: a) Efficiency and b) longitudinal sliding evolution as a function of independently controlled input and output clamping loads.

Figure 6.11 shows the efficiency and longitudinal sliding trends as a function of the output clamping load under two different input clamping conditions for the working conditions determined in Table 6.4(ii):

Scenario 1: The input point is clamped up to 5 kN and the output clamping load has been adapted. The longitudinal sliding and efficiency trends are depicted in Figure 6.11 corresponding to the $F_{\mathrm{c,in}} \uparrow$ condition. The result revealed that gross slip occur at 1.5 kN of output clamping load. Additionally, the efficiency curve showed a gradual increase while clamping load decreased until the gross slip limit.

Scenario 2: The input clamping load has been set up to 3.5 kN and the output clamping load has been adapted to identify the performance trends. Results are shown in Figure 6.11 as $F_{\mathrm{c,in}} \downarrow$. In this scenario, the gross slip occur at 2 kN of clamping load a considerably higher clamping load than in the afore shown condition. Additionally, the efficiency curve showed a higher mean efficiency value across most of the clamping load conditions above the gross slip limit of $F_{\mathrm{c,out}} = 2$ kN.

Different behaviours of the output point were illustrated in Figure 6.11, where differences were caused by the clamping load applied in the input point. The phenomena happening in the contact may be explained by the block diagram represented in Figure 6.12. The blocks represent each of the contact point in the transmission; the input power is transferred to the rollers by the input contact point (block of the left), subsequently, the power of the rollers is transferred to the output point by the output contact point (block of the right). Overclamping the input contact point leads to decrease the efficiency of the input contact point (low $Eff_{\mathrm{CP-in}}$ in the first block of first row in Figure 6.12). Therefore, less energy reaches the output contact point and therefore the critical clamping load occurs at 1.5 kN. Decreasing the input clamping load, lead to increase the efficiency of the input point (high $Eff_{\mathrm{CP-in}}$ in the first block of the second row in Figure 6.12). Consequently, the energy reaching the output point rises, and therefore the gross slip condition happens under higher clamping load conditions ($F_{\mathrm{c,out}} \approx 2$ kN). Similarly, the efficiency of te entire transmission increases avoiding overclamping effects.

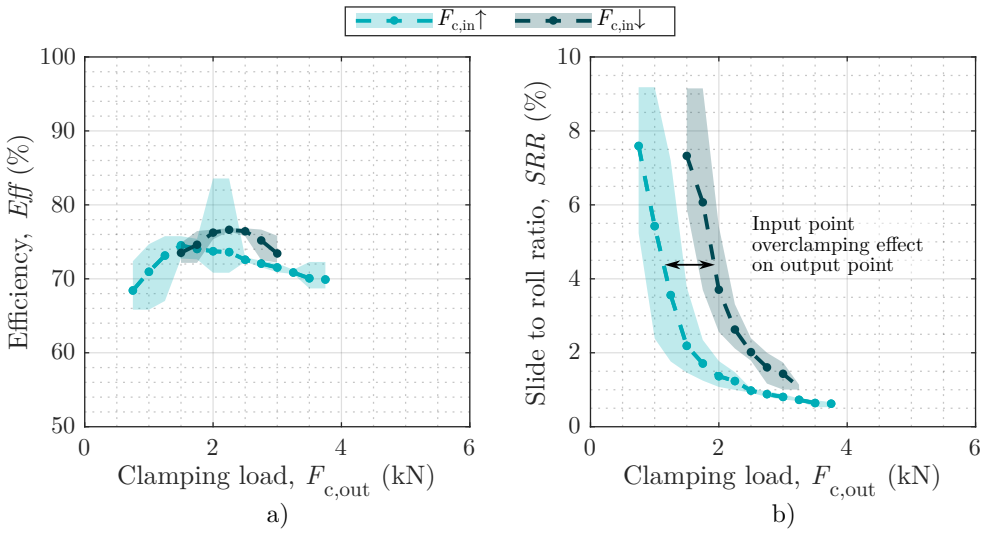

Figure 6.11: a) Efficiency and b) longitudinal sliding evolution as a function of the output clamping force under two different input clamping load conditions.

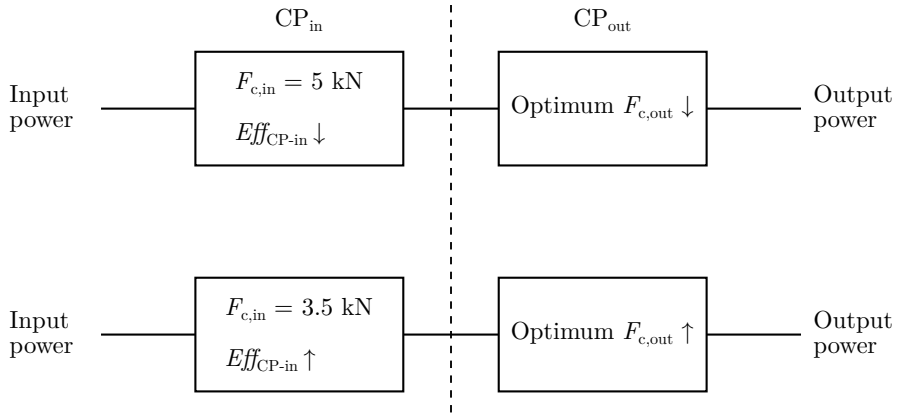

Figure 6.12: Box diagram of the T-CVT transmission: input clamping load effects on the output point.

6.3.3 *Discussion of the results*

The results obtained from the model have been compared to the experimentally measured performance trends in order to correlate the efficiency and longitudinal sliding trends of the transmission. The results obtained from the model proposed in Chapter 5 were modified including the losses derived from the input and output discs (the losses before and after both contact points represented in Figure 5.1). The churning losses of each of the disc is calculated by the empirical model proposed by Boness et al. [186] already presented in Chapter 5; nevertheless the geometry of the discs will be considered as well as their speed under each working condition.

The power losses of the bearings of the discs are calculated by the SKF model [185] presented also in the previous chapter. The working conditions to calculate the power losses of the bearings are determined in Table 6.5, where the angular contact ball bearings are used to transmit the clamping loads while the needle bearings are used to align the discs with the rollers and little load is supported there.

Table 6.5: Working conditions of the bearings of the T-CVT prototype.

	Input 7205 BECBP	Input NKI 20/20	Output 7205 BECBP	Output NKI 20/20
Speed	N_{in}	N_{in}	N_{out}	N_{out}
Axial load	$F_{c_{in}}$	-	$F_{c_{out}}$	-
Radial load	-	Disc weight	-	Disc weight

Additionally, the frictional losses caused by the sealing elements of the input and output shafts should be considered. Lip seal losses were calculated by Equation 6.8 [187], which it is an empirical equation determined based on many friction torque measurements of lip seals where the lubricant temperature, viscosity and rotational speed of the shafts are considered.

$$P_{loss-S} = (145 - 1.6 \cdot \Theta + 350 \cdot \log(\log(\nu_{visc} + 0.8))) \cdot 10^{-7} \cdot d^2 \cdot N \tag{6.8}$$

where, Θ is the temperature, ν_{visc} is the kinematic viscosity defined as the relation between dynamic viscosity and density of the lubricant ($\nu_{visc} = \eta/\rho$), d is the diameter of the shaft and N represents the rotational speed in RPM.

Measurements under four clamping load conditions (F_c = 3, 5, 7, 10 kN), an input speed of 500 RPM and 1:1 ideal transmission ratio were carried out for the correlation of the results considering variable output torque conditions. Similarly, the same conditions were modelled by the model presented in Chapter 5.

Figure 6.13a illustrates the efficiency results and Figure 6.13b shows the longitudinal sliding of both, modelled and tested conditions. It is noteworthy that the obtained calculated and tested trends exhibit considerable differences. On one hand, for th conditions where gross slip occur, it appears under different torque conditions; in the tests gross slip occur at lower torque values than in the modelled results. On the other hand, the measured efficiency values at low torque conditions are higher than the modelled values. The conducted experiments entail a significant source of uncertainty, which is defined as follows:

- The torque sensors were purpose-built for this project. The sensors had to be calibrated before assembly into the transmission; however, due to their sensitive nature, deviations in the measured torque may have occurred. A correction factor, denoted as C_f of 1.48 applied to the measured torque aligns the experimental and modelled efficiency curves (see Equation 6.9). Furthermore, it can be inferred that the error in all measurements is of the same order, thus validating the trends.

$$T_{\text{in/out,cor}} = T_{\text{in/out}} \cdot C_f \tag{6.9}$$

  where, $T_{\text{in/out,cor}}$ is the corrected input or output torque, $T_{\text{in/out}}$ is the measured one and C_f is the correction factor.

- Furthermore, differences are observed in longitudinal sliding. The difference in the measured SRR may be caused by the definition of the ideal transmission ratio where it has been seen that an error of 2% on the definition of the transmission ratio may result in a error of 2% on the SRR. Additionally differences may be caused by the differences in the Newtonian slope of the measured and calculated traction curves [88].

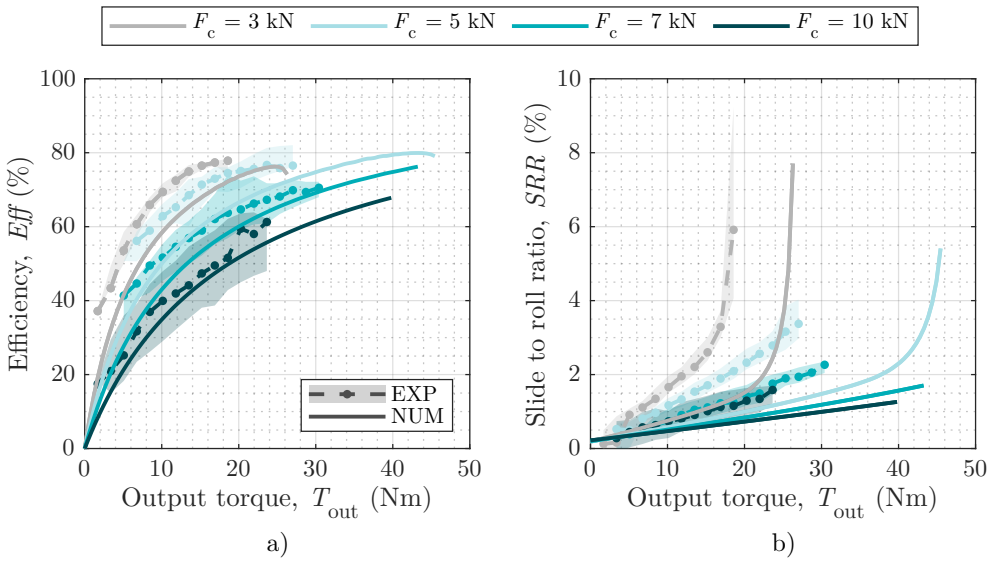

Figure 6.13: Raw a) efficiency and b) longitudinal sliding evolution as a function of torque in four clamping conditions at i = 1:1.

The results with the torque values corrected are shown in Figure 6.14. Since both the input and output torque sensors have the same correction factor, the efficiency values remain unchanged, but the curve has been shifted to higher torque values. The trends obtained by both, the model and the experiments are comparable. However, the increase on the longitudinal sliding under the Newtonian region of the lubricant is still higher in the experimental result than in the modelled ones. The author attributes this trend to the Newtonian region of a traction curve, the literature has also revealed deviations in this region [88].

The results indicate that longitudinal sliding and efficiency can be controlled by the clamping loads; the following trends were observed:

- Under low output torque conditions the measured efficiency is low since the power losses are higher in proportion to the transmitted power. While output torque increases the efficiency increases also. Additionally, increasing clamping loads leads to decrease the efficiency as a result of overclamping effects (spinning losses).
- Nevertheless, decreasing clamping loads leads to decrease the transmissible maximum power. Gross slip occurs after a certain torque condition, which represents the achievable maximum traction coefficient.
- The longitudinal sliding happening in the contact interfaces may be controlled by the relation between the torque and the applied lamping loads. At a constant torque, increasing the clamping loads decreases the measured SRR since the traction acting on the contact interface is achieved in a lower longitudinal sliding condition. Similarly, increasing torque and maintaining the clamping loads constant lead to increase the longitudinal sliding.

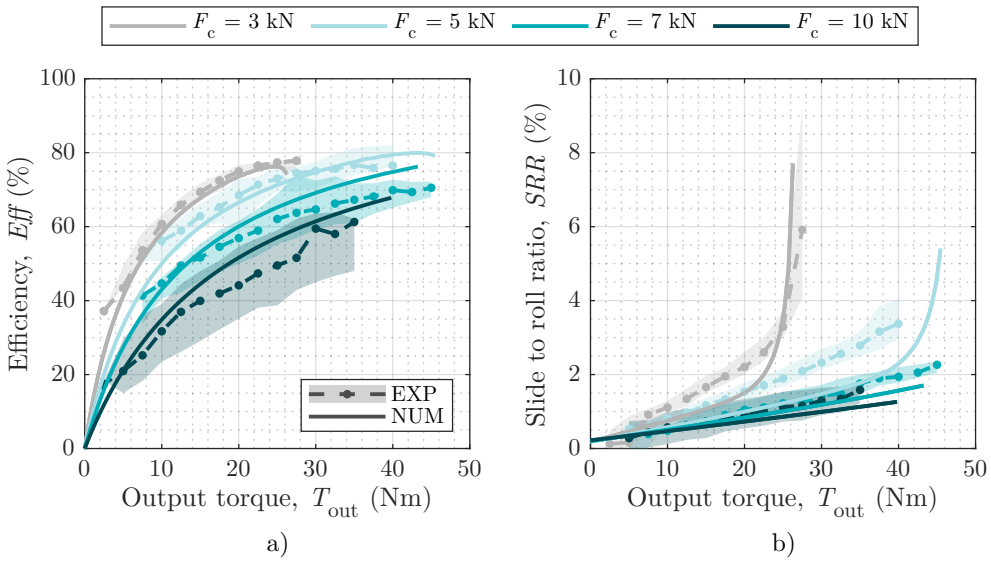

Figure 6.14: Corrected a) efficiency and b) longitudinal sliding evolution as a function of torque in four clamping conditions at i = 1:1.

6.4 CONCLUSIONS

In this chapter the experimental tests of a T-CVT prototype were shown. This prototype, was designed to allow to control independently the input and output clamping loads in order to study their influence in longitudinal sliding and efficiency of the transmission. The following conclusion were inferred from this work:

- The sliding motion happening in the transmission increases with torque (see Figure 6.8) and decreases with clamping load (see Figure 6.10). Therefore, and equilibrium between torque and clamping should be achieved to control the longitudinal sliding motion occurring on the transmission as well as the efficiency of the mechanism.
- As expected, a decrease in efficiency was measured at overclamped working conditions as represented in the high clamping load conditions shown in Figure 6.11. This trend has also been seen in the modelled transmission behaviour trends on Chapter 5 and in the literature as mentioned by Gecim et al. [17]. Additionally, similar efficiency curves as a function of torque (see Figure 6.14) were presented by Carbone et al. [27] and Meyer [118], where maintaining the clamping load constant the efficiency is low under low torque conditions as a result of overclamping and in high torque as a result of gross slip.
- It has been identified the importance of the input clamping load on the performance of the output point. In a condition when the input point is overclamped, the input power losses are high, consequently, the energy transmitted to the output point decreases. Clamping both point contacts equal, means that the energy losses of the output point is high since it is even more overclamped, therefore, overall efficiency decreases. Additionally, decreasing the input clamping load, increases the energy transmitted to the output one, therefore the gross slip condition of the output point occurs under higher clamping load conditions (therefore in optimum clamping conditions, the the optimum clamping load values resemble more than in overclamped conditions).

7 CONCLUSIONS AND FUTURE WORK

"The aim of argument or of discussion, should not be victory but progress"
Karl Popper

This chapter resumes the principal contributions of the thesis.

7.1 CONCLUSIONS

In this thesis the effects of clamping load on the performance of T-CVTs were analysed considering the combined effects that the contact interface size and spin motion have on the lubricated traction and contact power losses. For that purpose three research objectives were defined and the main conclusions inferred fulfilling each objective are determined as follows:

O.1: Lubricated traction prediction considering the combined effect of contact interface and spin motion.

A traction coefficient prediction model has been generated to identify the combined effect between the contact scale and spin motion in rolling and longitudinal sliding lubricated contacts. It has observed the importance to consider low size interfaces in order to maximize the traction capacity of T-CVTs.

- The spin to roll ratio correctly represents the kinematic behaviour of this kind of contacts under isothermal conditions. However, differences in effective traction coefficient were found in the thermally corrected traction, the higher the contact interface size the lower the traction coefficient.
- Under equal spinning speed conditions differences were found between the scale conditions even in isothermal analysis, the maximum traction coefficient was obtained for low size interface, therefore the author attributed this trend to the spin pole position as a function of longitudinal sliding. Additionally, under high contact interface conditions the maximum traction coefficient occur at higher longitudinal sliding conditions.
- In many applications where spin motion occur, the size and spin motion are governed independently, therefore, an analysis at equal normal load and equal spinning speed analysis was carried out for different contact curvature (scale) conditions. Results revealed that under low longitudinal sliding condition, the low size interface show a higher traction coefficient, however, in high longitudinal sliding conditions more thermal heating occur.

O.2: Modelling the efficiency and sliding equilibrium of T-CVTs under independent input and output clamping loads.

A T-CVT traction equilibrium and performance prediction model has been developed which calculates the traction coefficient acting on the contact interface by the afore mentioned traction prediction model. The hypothesis is theoretically answered, different behaviour was found in each of the contact point, however, it was found that similar clamping load was required in both of them.

- Differences between the input and output contact points were observed since the transmission ratio causes differences in their characteristics. Transmission ratio changes the contact geometries of the points, consequently, the contact interface size and contact pressure differs between the input and output points. Therefore, the contact efficiency as a function of the longitudinal sliding is no longer equal in both points.
- Traction equilibrium analysis was carried out to identify the performance of a single point contact. On one hand, variable clamping load at equal torque analysis showed that efficiency decreases under high and low clamping values as a result of gross slip and overclamping effects respectively. Similarly, at constant clamping load and variable torque the same trend was revealed, overclamping occur at low torque conditions and gross slip at high torque.
- It was observed that the optimum clamping condition occurs close the gross slip limit. Therefore, if the CVT is clamped at such optimum load, any torque peak could cause gross slip and disruptive torque transmission. As a result, it may be preferable to assume a small amount of overclamping with the purpose of ensuring torque transmission.
- The transmission efficiency trends showed differences between the equilibrium of the input and output contact points. On one hand, as a result of the changes on the contact conditions (pressure and interface size) each contact point equilibrates under different longitudinal sliding condition. Additionally, as a consequence of the transmission ratio, different clamping loads are required on the transmission. It was demonstrated that it is possible to increase the efficiency of the transmission with independent load control. Nevertheless, under high torque conditions the increase on the efficiency of the transmission was negligible by the independently controlled clamping loads.

O.3: Experimental observation of T-CVTs longitudinal sliding equilibrium and efficiency.

A T-CVT prototype has been developed with the main innovation that allows to independently control the input and output clamping loads. Measurements revealed consistent working trend comparable to the modelled results.

- Efficiency increased together with torque, obtaining higher efficiency under the lowest clamping load condition tested. Nevertheless, the maximum transmissible torque is lower under low clamping conditions. Hence, it has been stated the importance to control the applied clamping loads as a function of the torque that has to be transmitted.
- The maximum efficiency and lower longitudinal sliding was achieved at 1:1 ideal transmission ratio.
- It has been observed that the clamping load applied in the input point considerably affects to the behaviour of the output point. This reflects the importance to adequately control the clamping loads of this kind of transmissions in order to obtain an adequate performance.

7.2 FUTURE WORK

This dissertation has provided valuable insight into the effects of clamping forces on the behaviour of T-CVT transmissions. The analytical and experimental observations serve as an inspiration to define the future work directions as follows:

O.1: Lubricated traction prediction.

A traction prediction model has been created for rolling and longitudinal sliding with spin motion. Effects that ellipticity ratio has on the traction behaviour should be specifically analysed, constant spin to roll ratio may be achieved with different ellipticity ratios, nevertheless, different kinematic behaviour may be found, causing considerable differences in traction. A new spin to roll ratio definition may be of interest considering the ellipticity ratio and rolling direction.

O.2: Modelling of the performance of T-CVTs under independent clamping load conditions.

Traction equilibrium and efficiency predictions were carried out by the model that was generated in this thesis. Nevertheless, rolling contact fatigue has not been analysed and independent normal loads may be preferable when the rolling contact fatigue is considered since exponential decrease on durability is achieved under high contact pressure.

O.3: Experimental observation of T-CVT performance.

Experimental measurements of a toroidal type CVT were performed in this thesis under steady-state conditions. However, clamping load control strategies under variations of transmission ratio are valuable since this kind of transmissions work under dynamic scenarios were the transmission should be adapted continuously.

7.3 SCIENTIFIC CONTRIBUTIONS

The work presented in this thesis has been disseminated in scientific conferences, journals and participation in innovation projects:

On lubricated traction prediction considering spin and scale effects [O.1]:

M. Iribecampos, I. Ulacia, A. Arana, and J. Larrañaga. "The combined effect of contact interface size and spin on lubricated traction in rolling-sliding point contacts." In: *Tribology International* 188 (2023), p. 108822. DOI: 10.1016/j.triboint.2023.108822.

On Toroidal type CVT transmission modelling [O.2]:

M. Iribecampos, A. Arana, I. Ulacia, J. Larrañaga, "Contact model for toroidal type continuously variable transmissions". *Lubmat, Lubrication, Tribology and condition monitoring, conference and exhibition.* 15th - 17th December 2020, Basque Country (online).

M. Iribecampos, A. Arana, J. Larrañaga, I. Ulacia, "Modelo para el análisis geométrico de Transmisiones Variables Continuas Toroidales", *CNIM, XXIII Congreso Nacional de Ingeniería Mecánica.* 20th - 22nd October 2021. Jaen, Spain.

Experimental characterization of Toroidal type CVT transmissions [O.3]:

M. Iribecampos, E. Errazkin, A. Arana, I. Ulacia, J. Larrañaga, "Sliding performance of toroidal type CVT transmissions". *7th World Tribology Congress, WTC 2022.* 10th - 15th July 2022, Lyon, France.

On a industrial application of a T-CVT:

The CIRMET project funded by the European Union's Horizon 2020 research and innovation programme. There a Waste Heat Recovery System was developed and the T-CVT prototype was used to transmit and adapt the mechanical energy of the Organic Rankine Cycle to an air compressor. The results showed that the clamping loads play an important role on the correct performance of the entire system, since overclamping it decreases the efficiency of the system considerably. Additionally, the continuous transmission ratio shifting enables to maintain the input speed as close as possible to the optimum working condition in order to maximize the recovered energy. Appendix D shows the main results obtained on the project.

M. Iribecampos, U. Morales, M. Merchan, G. Urchegui, J. Calviño, M. Baraldi, J. Larrañaga, I. Ulacia, "Beroa berreskuratzeko sistema berritzaile baten garapena", *MZT, Materialen Zientzia eta Teknologia V. Kongresua.* 29th - 30th November 2021, Bilbo, Basque Country.

APPENDICES

A SURFACE TEMPERATURE RISE CALCULATION

"The answers you get depend upon the questions you ask"
Thomas Kuhn

SURFACE TEMPERATURE RISE CALCULATION

The temperature rise calculation procedure of an arbitrary shaped heat source moving along x-direction on a solid is explained in the following paragraphs. The temperature of one of the solids in contact may be written as [167, 168]:

$$\bar{\Theta}_1(\bar{x},\bar{y}) = \frac{1}{2\pi\sqrt{k}} \iint_{A_H} \frac{\bar{\dot{q}} \cdot \alpha_\Theta(\bar{x}',\bar{y}') e^{-Pe\{R-(\bar{x}-\bar{x}')\}}}{R} d\bar{x}' d\bar{y}' \tag{A.1}$$

where k is the ellipticity b/a, $\bar{\dot{q}}$ the dimensionless heat generation rate calculated as $\dot{q} \cdot a \cdot b/Q$ (Q is the rate of flow heat, W), Pe the Peclet number calculated as shown in Equation A.2, where χ is the thermal diffusivity calculated as $K/(\rho \cdot c_p)$ and $R = \sqrt{(\bar{x}-\bar{x}')^2 + (\bar{y}-\bar{y}')^2}$.

$$Pe = \frac{v_s \cdot a}{2 \cdot \chi} \tag{A.2}$$

Discretizing the contact region in a uniform grid of element size g, we obtain the following solid temperature distribution:

$$\bar{\Theta}\left(\bar{x}_i,\bar{y}_j\right) = \frac{1}{2\pi}\frac{1}{\sqrt{k}} \sum_{k=0}^{n_x}\sum_{l=0}^{n_y} K_{ijkl}^{gggg}\bar{\dot{q}}_{kl} \tag{A.3}$$

where K is the kernel of the thermal resistance:

$$K_{ijkl}^{gggg} \equiv \int_{x_m}^{x_p}\int_{y_m}^{y_p} \frac{dvdu}{\sqrt{u^2+v^2}} \exp\left(-\frac{1}{2}Pe\left(\sqrt{u^2+v^2}-u\right)\right) \tag{A.4}$$

with,

$$\begin{aligned} u &= \bar{x}_i - \bar{x}, & v &= \bar{y}_j - \bar{y} \\ x_p &= \bar{x}_i - \bar{x}_k + g/2, & x_m &= \bar{x}_i - \bar{x}_k - g/2, \\ y_p &= \bar{y}_j - \bar{y}_l + g/2, & y_m &= \bar{y}_j - \bar{y}_l - g/2. \end{aligned} \tag{A.5}$$

Carslaw and Jaeger [164] found an analytical expression for this surface integral which reduces it to a line integral, where E_1 is the exponential integral.

$$\begin{aligned} K_{ijkl}^{gggg} = & \\ & y_m E_1 \left\{ Pe \left(\sqrt{x_m^2 + y_m^2} - x_m \right) \right\} \\ & - y_m E_1 \left\{ Pe \left(\sqrt{x_p^2 + y_m^2} - x_p \right) \right\} \\ & - y_p E_1 \left\{ Pe \left(\sqrt{x_m^2 + y_p^2} - x_m \right) \right\} \\ & + y_p E_1 \left\{ Pe \left(\sqrt{x_p^2 + y_p^2} - x_p \right) \right\} \\ & - \int_{y_m}^{y_p} \frac{e^{-Pe\left(\sqrt{v^2+x_m^2}-x_m\right)} v^2}{\sqrt{v^2 + x_m^2} \left(\sqrt{v^2 + x_m^2} - x_m \right)} dv \\ & + \int_{y_m}^{y_p} \frac{e^{-Pe\left(\sqrt{v^2+x_p^2}-x_p\right)} v^2}{\sqrt{v^2 + x_p^2} \left(\sqrt{v^2 + x_p^2} - x_p \right)} dv \end{aligned} \tag{A.6}$$

Thus, the surface temperature distribution is calculated by means of the space convolution of the heat generation rate $\dot{q}(x', y')$ and the kernel of the thermal resistance of the solids $K(x - x', y - y')$ calculated as simple multiplication of their FFT.

$$\Theta(x, y) = \mathrm{IFFT} \left\{ \mathrm{FFT}(\dot{q}) \cdot \mathrm{FFT}(K(x, y)) \right\} \tag{A.7}$$

Dimensionless surface temperature rise results are depicted in Figure A.1, same results as the ones presented by Tian et al. [166] were obtained (the figure shows the results of the Peclet number of $Pe = 10$).

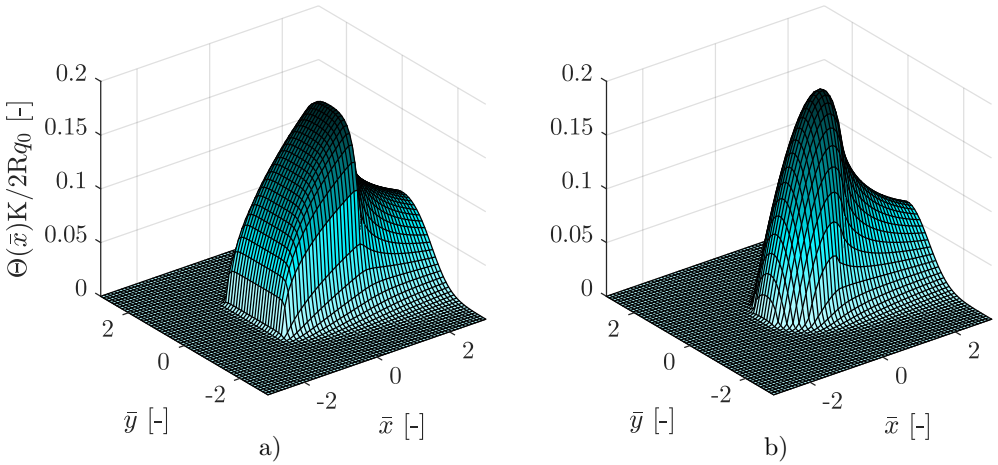

Figure A.1: Surface temperature rise results for a) square heat source and b) parabolic heat source where $Pe = 10$.

B CONFORMITY RATIO EFFECTS ON CONTACT EFFICIENCY

"Thinking is the talking of the soul with itself."
Plato

CONFORMITY RATIO EFFECTS ON CONTACT EFFICIENCY

The effects of the conformity ratio on the interface characteristics and contact efficiency are analysed in the following pages. For that purpose two conformity ratio conditions were tested, $CR = 0.5$ and $CR = 0.8$. This changes the values of the curvature of the contact, therefore, clamping both contact points up to $F_c = 15$ kN and adapting the transmission ratio from 1:3 to 3:1, the results obtained in Figure B.1 are obtained. It shows the normal loads and Hertzian pressure of the input and output contact points as a function of the transmission ratio.

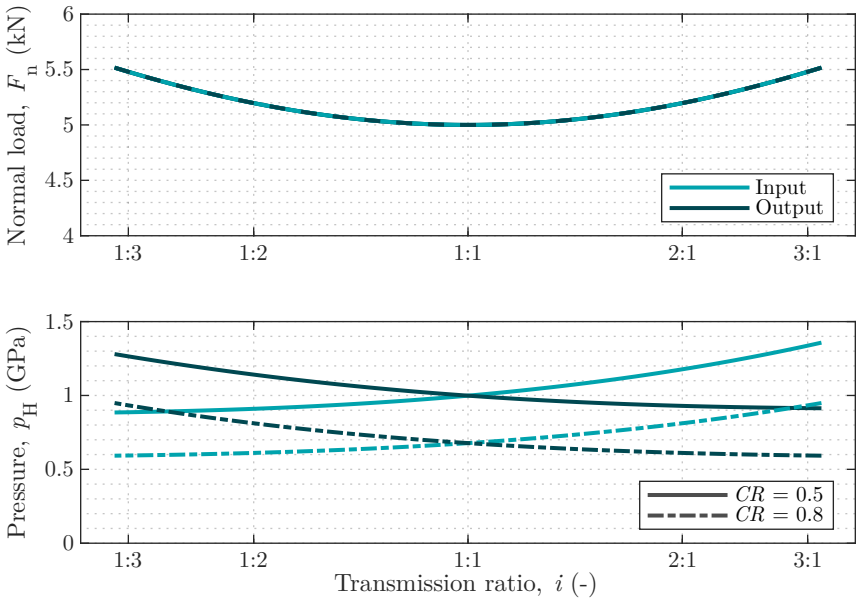

Figure B.1: Normal load (top) and Hertzian contact pressure (bottom) for two CR values as a function of the transmission ratio.

Figure B.2a shows the input contact interface shape and size for two different conformity ratios at 15 kN of clamping load and 1:1 transmission ratio. The figure reveals that the conformity ratio plays an important role on the shape and size of the contact interface. Large conformities increases the ellipticity of the contact interface having the semiminor axis aligned with rolling

motion (x-direction). Low conformities though, generates smaller contact interfaces, therefore, the contact pressure increases in comparison to the high conformity values. Similarly, the semi axis of the input contact interface as a function of the transmission ratio are represented in Figure B.2b. As expected, the interface in more slender at reducer transmission ratio due to the positive contact curvature R_{dy}, thus the contact pressure increases at equal normal load.

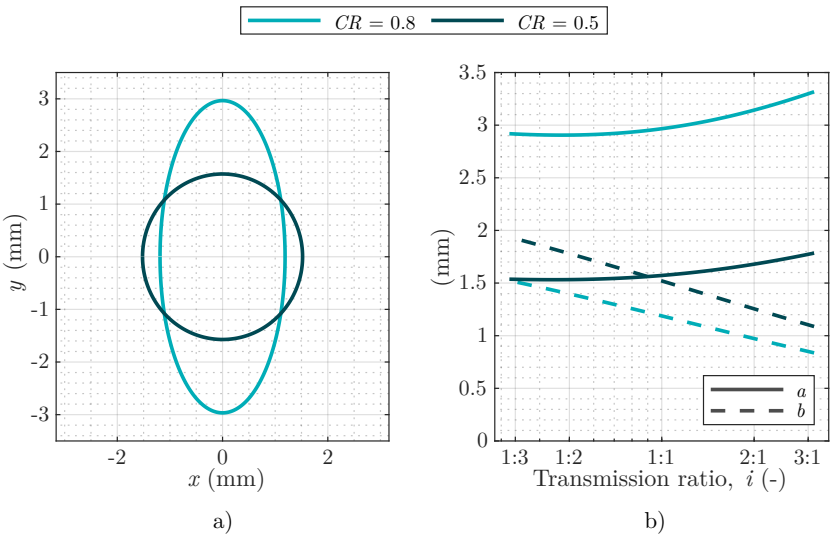

Figure B.2: a) Contact surface shape and size for different CR (i = 1:1) and b) evolution of the semi axis values as a function of transmission ratio.

Figure B.3 shows the contact efficiency of the input contact point as a function of longitudinal sliding for the two conformity ratios. As expected, the efficiency of the high conformity condition decreases. On one hand, the figure reveals that differences in the spinning efficiency, where the increase of the efficiency together with longitudinal sliding decreases for the high conformity case. On the other hand, is is shown that the longitudinal sliding efficiency is equal for both conditions since it depends only on the longitudinal sliding. Therefore, once the spinning power losses became negligible, the efficiency of both conformity ratios converges.

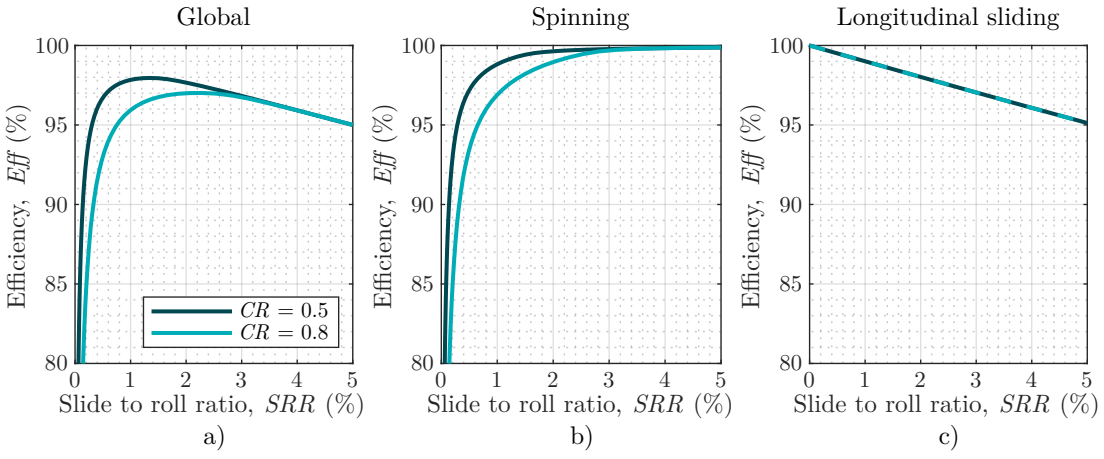

Figure B.3: Contact efficiency as a function of longitudinal sliding for different conformity ratio; $i = 1:1$ and F_c = 15 kN. a) Global efficiency b) Spinning efficiency and c) Longitudinal sliding efficiency.

The afore shown figure has revealed that differences between both conformity ratio values were a consequence of the spinning efficiency. Which increases rapidly with longitudinal sliding becoming negligible on SRR 1.8 % for the low conformity condition and at $SRR = 3.3$ % for the high conformity. These two longitudinal sliding conditions correspond to the conditions when the spin pole is positioned within the boundaries of the Hertzian contact region as shown in Figure B.4.

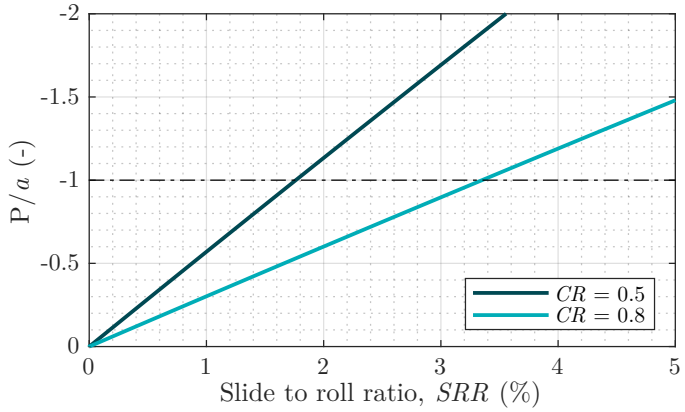

Figure B.4: Relative spin pole position as a function of longitudinal sliding for different conformity ratio; $i = 1{:}1$ and $F_c = 15$ kN.

These results revealed the effects of the contact interface size on the contact efficiency. It has been revealed that the spinning power losses are causing a decrease on the contact efficiency while the spin pole is inside the Hertzian contact region. Nevertheless, Figure B.3 revealed that the optimum efficiency condition happens when the spin pole is still inside the Hertzian contact region, which is in contrast to what Ehret et al. [24] said. The optimum efficiency conditions occurs under a certain longitudinal sliding condition where the spinning efficiency has increased considerably without increasing the longitudinal sliding losses excessively: $SRR = 1.3$ % for the low conformity and $SRR = 2.1$ % for the high conformity condition. Similar results were also obtained by several researchers [38, 45, 90], nevertheless, it was not analysed deeply to relate their effects with the contact scale.

From this result it is concluded that low conformities are preferable to maximize the efficiency of this kind of contacts. Additionally, the maximum efficiency condition is found under lower longitudinal sliding conditions for lower conformity ratio values, which is a valuable aspect to be considered in T-CVT transmission design. However, the contact pressure increases considerably as a result of the decrease of the contact interface size, therefore the contact fatigue may considerably decrease the durability of the components.

C DRAWINGS AND VERIFICATION OF DISCS AND ROLLERS

"If we spoke a different language, we would perceive a somewhat different world"
Ludwig Wittgenstein

DISC DRAWING AND VERIFICATION

Figure C.2 shows the drawing of the discs (input and output equal).

Figure C.1a illustrates toroidal cavity radius measurements carried out on both discs on the coordinate measuring machine (CMM) machine. Additionally, Figure C.1b depicts the differences between the reference value ($r_0 = 110$ mm) and the measured radius, furthermore, the tolerance limits are also represented.

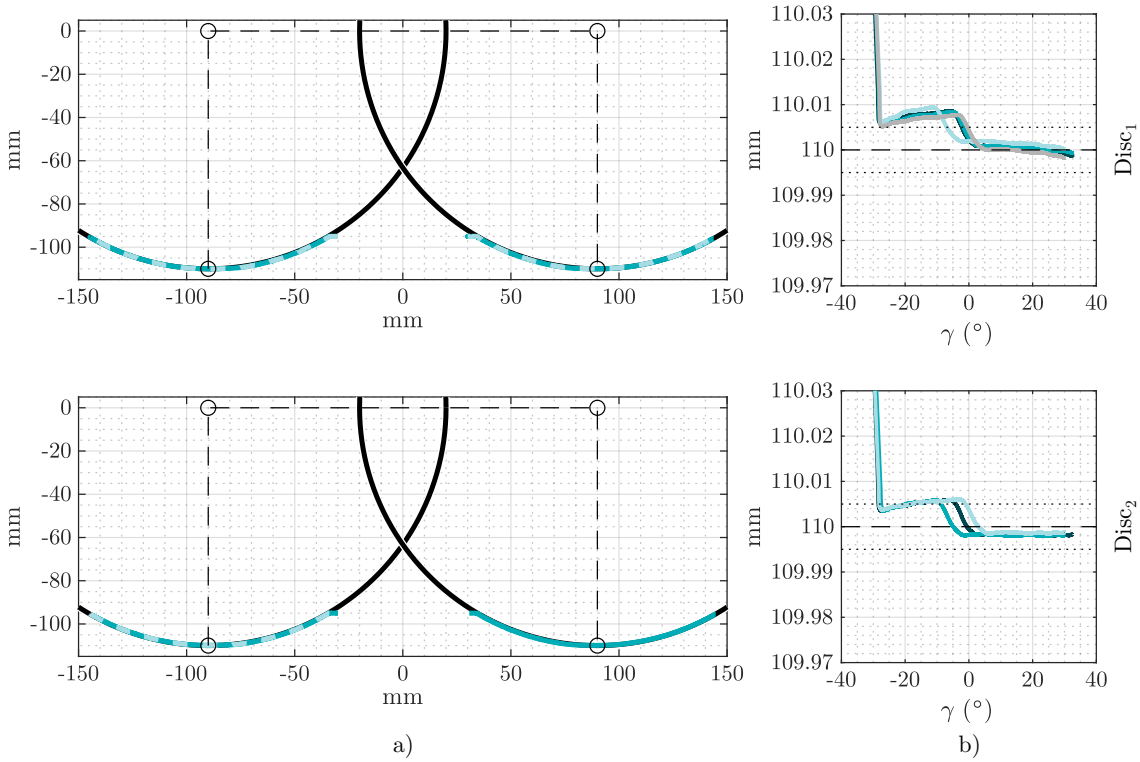

Figure C.1: Measured toroidal cavity radius of both discs.

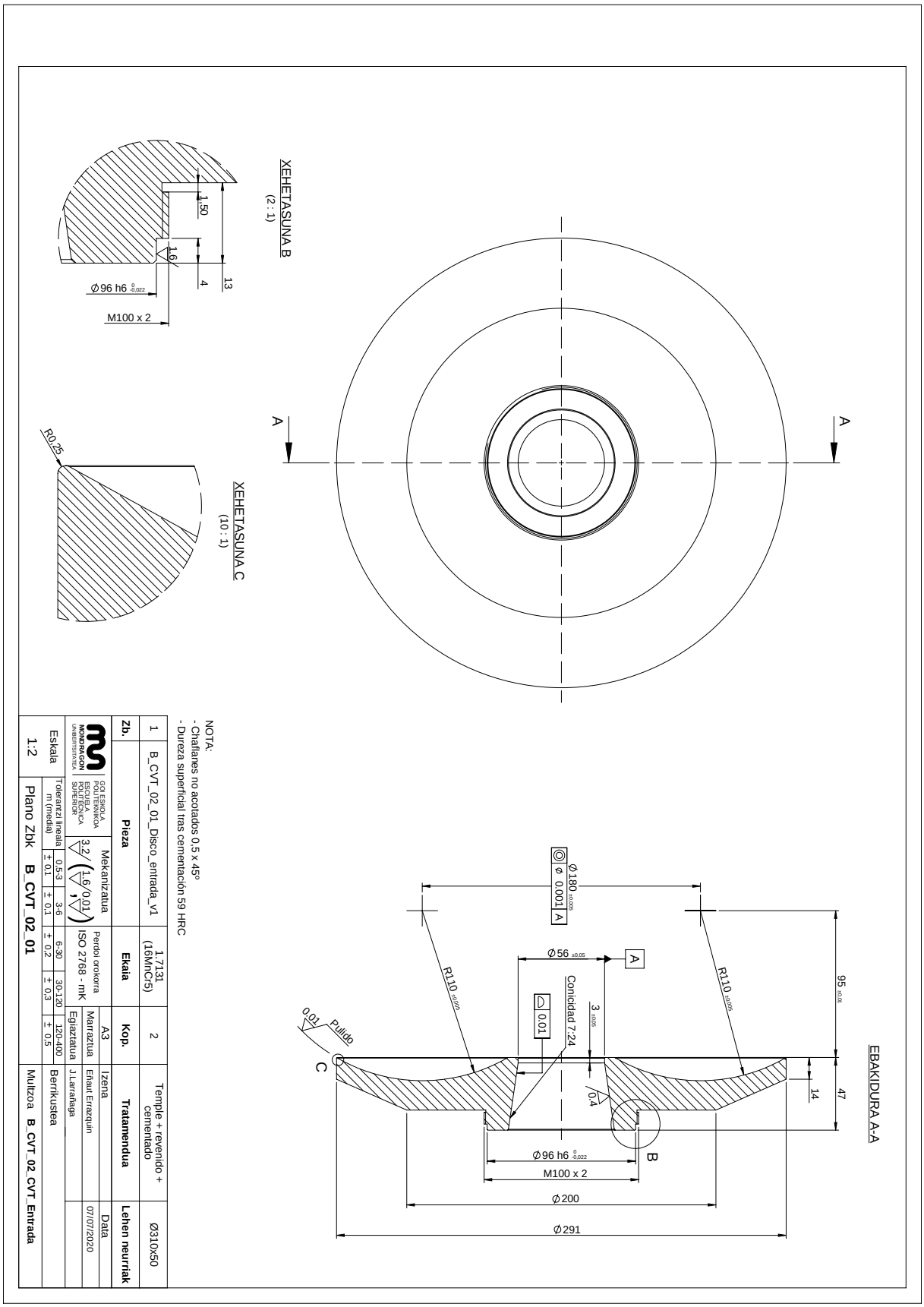

Figure C.2: Drawing of the disc of the T-CVT prototype.

ROLLER DRAWING AND VERIFICATION

Figure C.4 depicts the drawing of the rollers.

Figure C.3a illustrates circularity of the three rollers, the figure shows that two of them are close to the lower limit of the tolerance and that one of them is above the upper limit of the tolerance. Additionally, Figure C.3b depicts the curvature of the roller curvature radius, the responsible of determining the conformity ratio of the transmission for the three rollers.

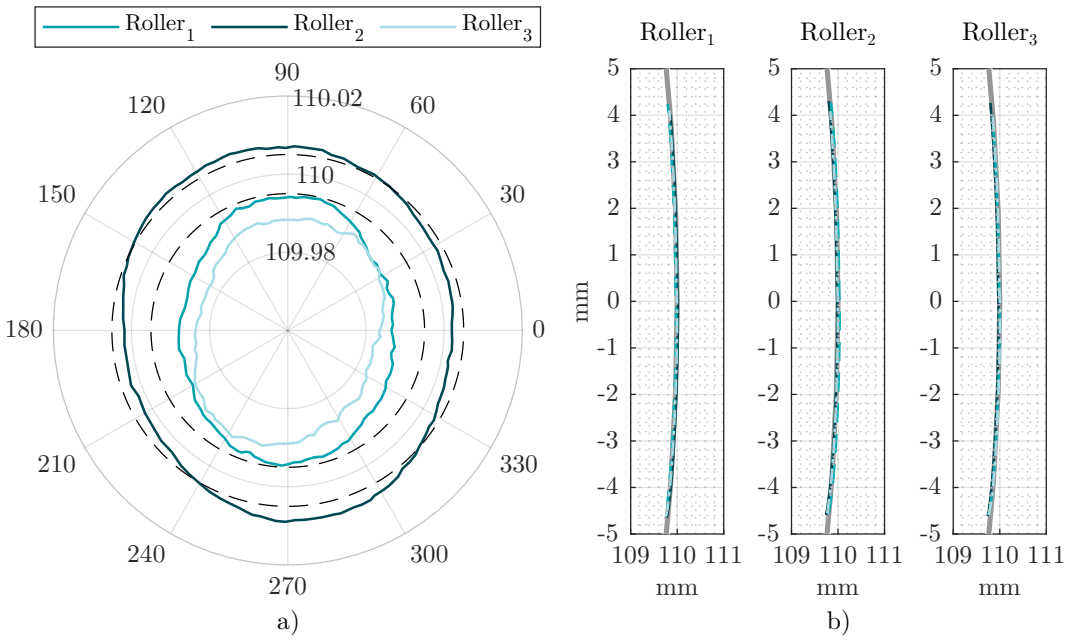

Figure C.3: Measured a) diameter and b) curvature of the three rollers.

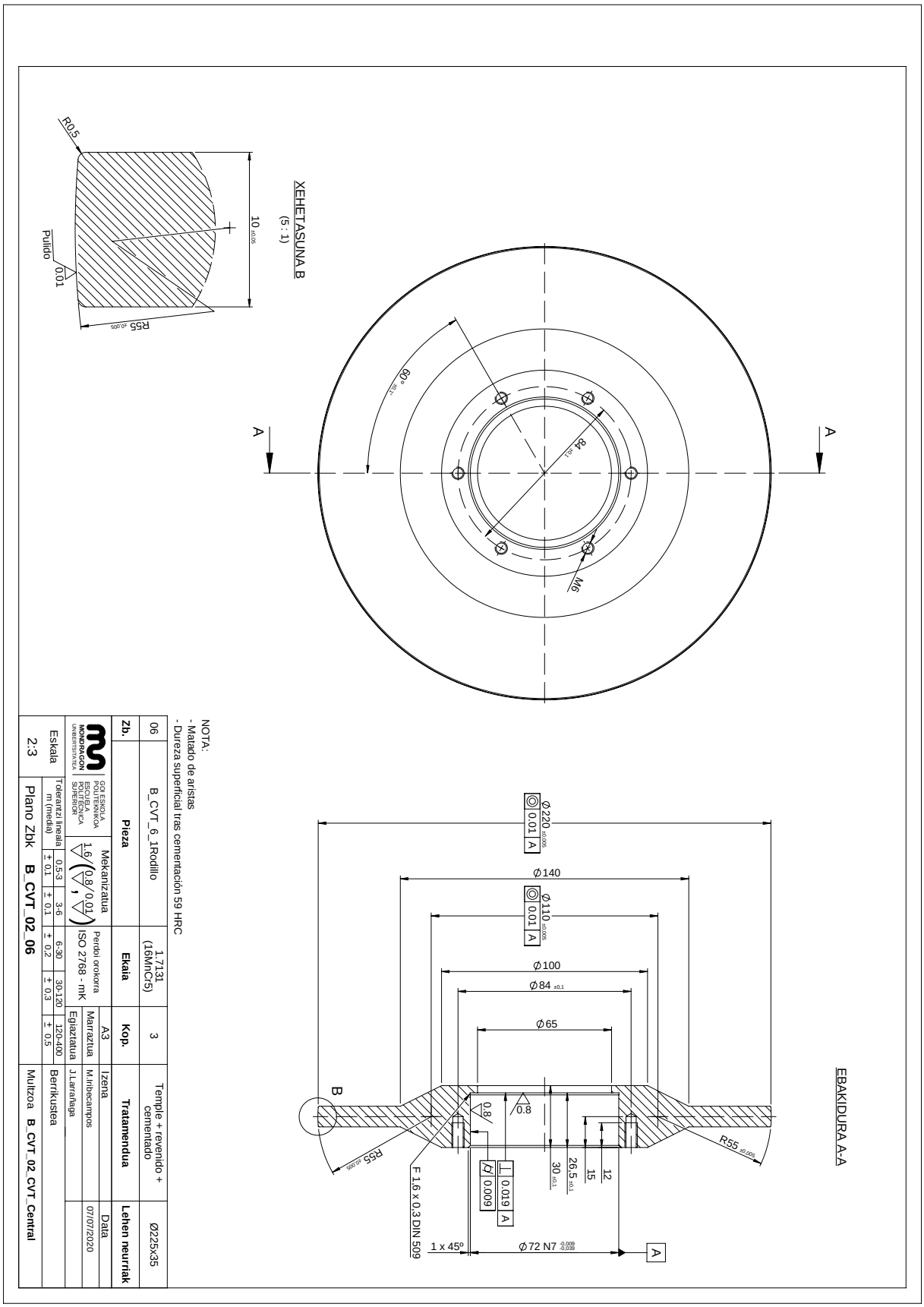

Figure C.4: Drawing of the roller of the T-CVT prototype.

D T-CVT IN A INDUSTRIAL APPLICATION: CIRMET PROJECT

"Life is like riding a bicycle. To keep your balance you must keep moving."
Albert Einstein

INDUSTRIAL WASTE HEAT RECOVERY SYSTEM

An industrial Waste Heat Recovery System (WHRS) is a device used to recover the energy coming from the industrial heat. Historically, this heat has been expelled to the atmosphere by means of heat exchangers after using it in the industrial production. For instance, this is an important social concern. Different research have been made about the energy that is being wasted and expelled to the atmosphere even if it may have some other applications[1].

The RECUWASTE system was developed in order to transfer the industrial energy waste into compressed air. It was studied that the compression is an expensive activity for many industries, therefore, the heat may be used there in order to decrease costs and reuse the expelled heat. The system was based on an Organic Rankine Cycle (ORC) device, a T-CVT and and air compressor (see Figure D.1). The importance of the CVT was to deal with the energy fluctuations in both, air consumption and expelled heat, as the energy source and demand are no more constant. The ORC is a device that can transfer low heat (100 - 150 °C) into mechanical energy.

The actuators of the CVT prototype were programmed to be controlled automatically. On one hand, the clamping loads were controlled based on the measured longitudinal sliding. If the measured SRR is lower than 1 % the clamping loads were gradually decreased until it reached the range between 1 - 3 %. Then, if the measured SRR is greater than 3 % the clamping load was increased. On the other hand, the transmission ratio control was based on the measured input speed. If there was no enough energy on the ORC the system speed decreased, therefore, the transmission ratio was set into reducer mode to maintain the input speed. Conversely, if the system begins to accelerate, the transmission ratio is turned into multiplier mode to increase the input torque and therefore control the speed of the system.

[1] "Industrian bero jario handia alferrik galtzen ari da; energia, alegia" Pello Larrinaga, EHU (Berria egunkaria, 2021-08-24)
In a Basque newspaper, a news regarding the utilisation of the industrial waste heat for other purposes was published. The key ideas of the news were that heat is being dissipated in industry, which is in fact energy, additionally they mentioned that in the Basque Country there are many companies that are dissipating heat to the atmosphere after using it in their production. They mentioned that the investment of a WHRS would be profitable within a period of five years in many cases. Nevertheless, they remarked that the main drawback is the negativity of the industries in order to implement this kind of solutions since requires changes in the production facilities. Therefore, they concluded with the importance to apply public policies to help to implement WHRS in order to decrease the excessive energy waste.

Figure D.1: RECUWASTE solution. The manufactured and tested WHRS.

The torque that the transmission has to move is defined by the pressure in the air compressor. Figure D.2 shows the relation between the compressed air and the torque. It shows how the torque does not increase until 4 bar of air pressure and increases gradually from that point.

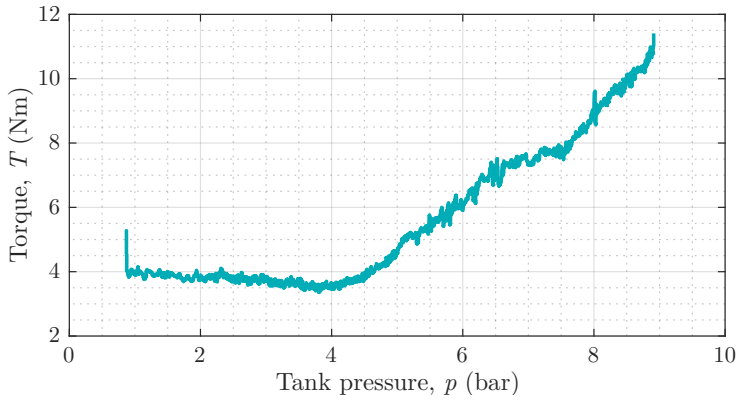

Figure D.2: Measured compressor torque as a function of tank pressure.

RECUWASTE TESTS

The results of the RECUWASTE tests are illustrated in Figure D.3, the following behaviour trends were identified:

- On the one hand, while the pressure of the tank increases (see FigureD.3c), the speed of the ORC decreases (see Figure D.3a), therefore, less air is being compressed.
- On the other hand, while the air consumption is higher than the generation, the pressure of the tank decreases and the system is accelerated, which leads to an increase on the compressed air generation.

This trend shows that the system is self-stabilized. When compressed air generation has to increase the system is accelerated automatically (as a result of the low pressure on the tank) as can be seen in the range between the 15$^{\text{th}}$ and the 25$^{\text{th}}$ minute of Figure D.3, where the output torque decreases considerably as a consequence of the drop on the tank pressure and therefore the shafts are accelerated. Conversely, while pressure in the tank increases since there is no a high air consumption (period from the 25$^{\text{th}}$ minute to the 40$^{\text{th}}$ minute on Figure D.3), the system is self-decelerated and the compressed air generation decreases.

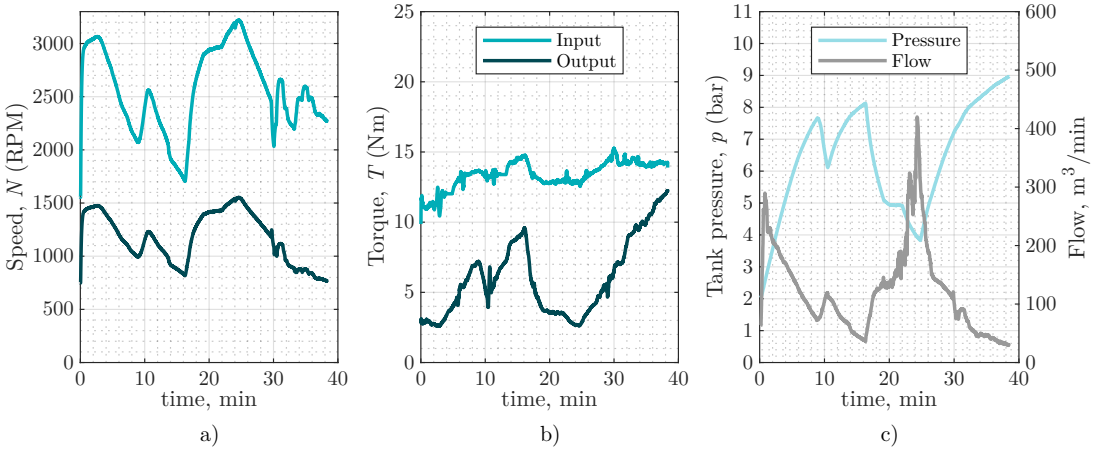

Figure D.3: WHRS auto-stabilization as a function of compressed air tank pressure.

Nevertheless, it was identified that the maximum recovered energy of the ORC occur under the speed range between 3000 and 4000 RPM; furthermore, the efficiency of the ORC decreases drastically below 2000 RPM. Therefore, the T-CVT allows to work as close as possible in the optimum operation range and to ensure that the system works always above the minimum speed limit. Figure D.4 depicts that the output torque of the T-CVT increases as a result of the increasing the pressure of the tank. Consequently, the speed of the transmission decreases since the ORC has not enough energy. Although output speed decreases, adapting the transmission ratio, the input speed is maintained above the 2000 RPM limit.

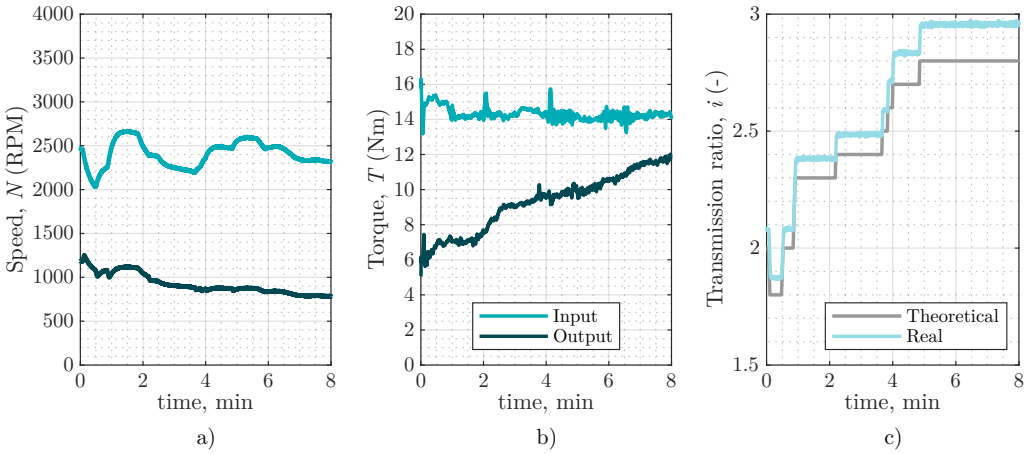

Figure D.4: WHRS optimization by means of the transmission ratio.

In addition, it has been seen that the clamping loads affect the performance of the WHRS as illustrated in Figure D.5. The applied clamping load should be carefully controlled for two reasons:

- On one hand, under too low clamping conditions, gross slip happens and therefore there would be no energy transference. Additionally, the durability of the components would be considerably reduced since scuffing may happen when gross slip occur under high sliding speed conditions.
- On the other hand, under overclamped conditions, the performance of the demonstrator is also affected. Since the efficiency of the T-CVT decreases at overclamped conditions, the energy demand of the ORC increases, as a consequence the speed of the entire system decreases and the efficiency of the whole system drops. Decreasing the clamping loads, the system equilibrates under higher speed conditions, decreasing the losses of the transmission and increasing the recovered energy. This trend is shown in Figure D.5 in the interval between minutes 10 and 12. The clamping load were decreased and therefore the input torque of the transmission decreased while the output torque was maintained constant (it is affected by the tank pressure). Consequently, the losses of the T-CVT decreased, the speed of the entire system increased; consequently the recovered energy raised.

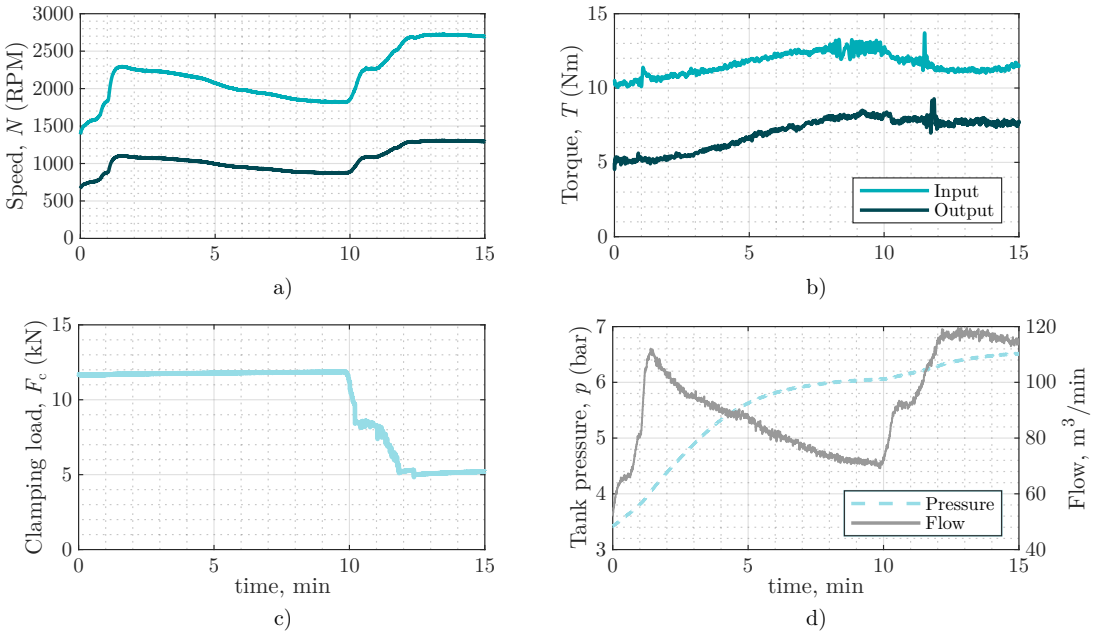

Figure D.5: Clamping load effects on the WHRS behaviour.

REFERENCES

[1] A. Agrawal. "Review on Continuous Variable Transmission (CVT)." In: *International Conference on Intelligent Emerging Methods of Artificial Intelligence & Cloud Computing* (2022). DOI: 10.1007/978-3-030-92905-3_61.

[2] B. Bonsen, M. Steinbuch, and P. A. Veenhuizen. "CVT ratio control strategy optimization." In: *Vehicle Power and Propulsion Conference* (2005). DOI: 10.1109/vppc.2005.1554561.

[3] M. Delkhosh. "Modelling and Optimization of Toroidal Continuously Variable Transmission in ECE Driving Cycle." In: *International Journal of Engineering* (2012). DOI: 10.5829/idosi.ije.2013.26.12c.14.

[4] C. Brockbank and D. Burtt. "Developments in Full Toroidal Traction Drive Infinitely and Continuously Variable Transmissions." In: *SAE Technical Paper Series* (2007). DOI: 10.4271/2007-01-3740.

[5] W. Shabbir and S. A. Evangelou. "Efficiency analysis of a continuously variable transmission with linear control for a series hybrid electric vehicle." In: *IFAC Proceedings Volumes* (2014). DOI: 10.3182/20140824-6-za-1003.01770.

[6] R. Pfiffner, L. Guzzella, and C. H. Onder. "Fuel-optimal control of CVT powertrains." In: *Control Engineering Practice* (2003). DOI: 10.1016/s0967-0661(02)00219-8.

[7] G. Ch. Tyreas and P. G. Nikolakopoulos. "Development and friction estimation of the Half-Toroidal Continuously Variable Transmission: A wind generator application." In: *Simulation Modelling Practice and Theory* (2016). DOI: 10.1016/j.simpat.2015.11.007.

[8] E. M. Berge and A. Pramanik. "Analysis and Material Selection of a Continuously Variable Transmission (CVT) for a Bicycle Drivetrain." In: *Introduction to Mechanical Engineering* (2018). DOI: 10.1007/978-3-319-78488-5_2.

[9] M. Tomaselli, F. Bottiglione, P. Lino, and G. Carbone. "NuVinci drive: Modeling and performance analysis." In: *Mechanism and Machine Theory* (2020). DOI: 10.1016/j.mechmachtheory.2020.103877.

[10] C. Brockbank and C. Greenwood. "Fuel Economy Benefits of a Flywheel & CVT Based Mechanical Hybrid for City Bus and Commercial Vehicle Applications." In: *SAE International Journal of Commercial Vehicles* (2009). DOI: 10.4271/2009-01-2868.

[11] F. Bottiglione, G. Carbone, L. Novellis, L. Mangialardi, and G. Mantriota. "Mechanical Hybrid KERS Based on Toroidal Traction Drives: An Example of Smart Tribological Design to Improve Terrestrial Vehicle Performance." In: *Advances in Tribology* (2013). DOI: 10.1155/2013/918387.

[12] P. Seshadri Venkatesh, V. Chandran, and S. Anil. "Study of Flywheel Energy Storage in a Pure EV Powertrain in a Parallel Hybrid Setup and Development of a Novel Flywheel Design for Regeneration Efficiency Improvement." In: *SAE Technical Paper Series* (2021). DOI: 10.4271/2021-01-0721.

[13] S. Motaman, M. Eltaweel, M. R. Herfatmanesh, T. Knichel, and A. Deakin. "Numerical analysis of a flywheel energy storage system for low carbon powertrain applications." In: *Journal of Energy Storage* (2023). DOI: 10.1016/j.est.2023.106808.

[14] I. M. Hutchings. “Leonardo da Vinci’s studies of friction.” In: *Wear* (2016). DOI: 10.1016/j.wear.2016.04.019.

[15] I. M. Hutchings and P. Shipway. *Tribology. Friction and Wear of Engineering Materials*. Butterworth-Heinemann, 2017.

[16] T. Yamamoto, T. Osidari, and M. Nakano. “Improvement of loading cam performance in a toroidal CVT.” In: *JSAE Review* (2002). DOI: 10.1016/s0389-4304(02)00223-0.

[17] B. A. Gecim. “Modeling and Experimental Validation of Optimized Clamp Loading in a Toroidal-CVT.” In: *SAE Technical Paper Series* (2004). DOI: 10.4271/2004-01-0351.

[18] I. Hutchings and P. Shipway. “Lubricants and lubrication.” In: *Tribology* (2017). DOI: 10.1016/b978-0-08-100910-9.00004-0.

[19] R. Ahmed. “Rolling Contact Fatigue.” In: *Failure Analysis and Prevention* (2002). DOI: 10.31399/asm.hb.v11.a0003563.

[20] M. Laithy, L. Wang, T. J. Harvey, B. Vierneusel, M. Correns, and T. Blass. “Further understanding of rolling contact fatigue in rolling element bearings - A review.” In: *Tribology International* (2019). DOI: 10.1016/j.triboint.2019.105849.

[21] P. M. Lugt and G. E. Morales-Espejel. “A Review of Elasto-Hydrodynamic Lubrication Theory.” In: *Tribology Transactions* (2011). DOI: 10.1080/10402004.2010.551804.

[22] H. C. Liu. “Traction prediction in rolling/sliding EHL contacts with reference fluids.” PhD thesis. Leibniz Universitaet Hannover, 2020. DOI: 10.15488/10206.

[23] H. C. Liu. “Scale and contact geometry effects on friction in thermal EHL: twin-disc versus ball-on-disc.” In: *Tribology International* (2020). DOI: 10.1016/j.triboint.2020.106694.

[24] P. Ehret, F. Chevalier, D. Dowson, C.M. Taylor, H. Okamura, and T. Sano. “Traction in EHL Elliptical Contacts with Spin Conditions.” In: *Thinning Films and Tribological Interfaces, Proceedings of the 26th Leeds-Lyon Symposium on Tribology* (2000), pp. 71–83. DOI: 10.1016/s0167-8922(00)80113-3.

[25] S. H. Loewenthal. “A Historical Perspective of Traction Drives and Related Technology.” In: *NASA Lewis Research Center* (1983).

[26] M. Patterson. “Paper X (iv) Traction Drive Contact Optimisation.” In: *Vehicle Tribology* (1991), pp. 295–300. DOI: 10.1016/s0167-8922(08)70145-7.

[27] G. Carbone, L. Mangialardi, and G. Mantriota. “A comparison of the performances of full and half toroidal traction drives.” In: *Mechanism and Machine Theory* (2004). DOI: 10.1016/j.mechmachtheory.2004.04.003.

[28] L. Novellis, G. Carbone, and L. Mangialardi. “Traction and Efficiency Performance of the Double Roller Full-Toroidal Variator: A Comparison With Half- and Full-Toroidal Drives.” In: *Journal of Mechanical Design* (2012). DOI: 10.1115/1.4006791.

[29] Q. Li, H. Li, D. Yu, and J. Yao. “A novel continuously variable transmission with logarithmic disc generatrix.” In: *Mechanism and Machine Theory* (2015). DOI: 10.1016/j.mechmachtheory.2015.07.001.

[30] Q. Li, J. Wu, H. Li, and J. Yao. “A Mathematical Method for Eliminating Spin Losses in Toroidal Traction Drives.” In: *Mathematical Problems in Engineering* (2015). DOI: 10.1155/2015/501878.

[31] Q. Li, M. Liao, and S. Wang. “A Zero-Spin Design Methodology for Transmission Components Generatrix in Traction Drive Continuously Variable Transmissions.” In: *Journal of Mechanical Design* (2017). DOI: 10.1115/1.4038646.

[32] C. Li, H. Li, Q. Li, S. Zhang, and J. Yao. "Modeling, kinematics and traction performance of no-spin mechanism based on roller-disk type of traction drive continuously variable transmission." In: *Mechanism and Machine Theory* (2019). DOI: 10.1016/j.mechmachtheory.2018.11.017.

[33] A. Afrabandpey and H. Ghariblu. "Performance Evaluation of Ball CVT and Comparison with Half Toroidal CVT." In: *International Journal of Automotive Technology* (2018). DOI: 10.1007/s12239-018-0052-x.

[34] M. Tomaselli, P. Lino, and G. Carbone. "Modelling and efficiency formulation of a planetary traction drive CVT." In: *IFAC-PapersOnLine* (2019). DOI: 10.1016/j.ifacol.2019.09.066.

[35] O. S. Cretu and R. P. Glovnea. "Constant Power Continuously Variable Transmission (CP-CVT): Operating Principle and Analysis." In: *Journal of Mechanical Design* (2005). DOI: 10.1115/1.1828457.

[36] C. Bell. "Constant power - continuously variable transmission (CP-CVT): Optimisation and simulation." PhD thesis. Brunel University School of Engineering, 2011. URL: http://bura.brunel.ac.uk/handle/2438/6279.

[37] H. Tanaka. "Speed ratio control of a parallel layout double cavity half-toroidal CVT for four-wheel drive." In: *JSAE Review* (2002). DOI: 10.1016/s0389-4304(02)00163-7.

[38] F. Verbelen, S. Derammelaere, P. Sergeant, and K. Stockman. "A comparison of the full and half toroidal continuously variable transmissions in terms of dynamics of ratio variation and efficiency." In: *Mechanism and Machine Theory* (2018). DOI: 10.1016/j.mechmachtheory.2017.10.026.

[39] F. Verbelen, J. Druant, S. Derammelaere, H. Vansompel, F. De Belie, K. Stockman, and P. Sergeant. "Benchmarking the permanent magnet electrical variable transmission against the half toroidal continuously variable transmission." In: *Mechanism and Machine Theory* (2017). DOI: 10.1016/j.mechmachtheory.2017.03.005.

[40] G. K. Nikas. "Fatigue Life and Traction Modeling of Continuously Variable Transmissions." In: *Journal of Tribology* (2002). DOI: 10.1115/1.1491976.

[41] Q. J. Wang and Dong Zhu. "Hertz Theory: Contact of Spherical Surfaces." In: *Encyclopedia of Tribology* (2013). DOI: 10.1007/978-0-387-92897-5_492.

[42] H. Machida, H. Itoh, T. Imanishi, and H. Tanaka. "Design principle of high power traction drive CVT." In: *SAE Technical Papers* (1995). DOI: 10.4271/950675.

[43] S. Akehurst, D. A. Parker, and S. Schaaf. "CVT Rolling Traction Drives—A Review of Research Into Their Design, Functionality, and Modeling." In: *Journal of Mechanical Design* (2005). DOI: 10.1115/1.2214737.

[44] J. Zhang and H. Spikes. "Measurement of EHD Friction at Very High Contact Pressures." In: *Tribology Letters* (2020). DOI: 10.1007/s11249-020-1281-5.

[45] M. Delkhosh and M. S. Foumani. "Multi-objective geometrical optimization of full toroidal CVT." In: *International Journal of Automotive Technology* (2013). DOI: 10.1007/s12239-013-0077-0.

[46] M. Delkhosh and M. S. Foumani. "Optimisation of full-toroidal continuously variable transmission in conjunction with fixed ratio mechanism using particle swarm optimisation." In: *Vehicle System Dynamics* (2013). DOI: 10.1080/00423114.2013.765588.

[47] H. Itagaki, H. Hashiguchi, M. Kita, and H. Nishii. "Development of a High-Power Two-Roller Traction Tester and Measurement of Traction Curves." In: *Tribology Online* (2016). DOI: 10.2474/trol.11.661.

[48] O. S. Cretu and R. P. Glovnea. "Traction Drive With Reduced Spin Losses." In: *Journal of Tribology* (2003). DOI: 10.1115/1.1538192.

[49] T. Doki-Thonon, N. Fillot, G. E. Morales Espejel, M. Querry, D. Philippon, N. Devaux, and P. Vergne. "A Dual Experimental/Numerical Approach for Film Thickness Analysis in TEHL Spinning Skewing Circular Contacts." In: *Tribology Letters* (2013). DOI: 10.1007/s11249-013-0122-1.

[50] M. Raghavan. "Kinematics of the Full-Toroidal Traction Drive Variator." In: *Journal of Mechanical Design* (2002). DOI: 10.1115/1.1480816.

[51] S. H. Loewenthal. "Spin Analysis of Concentrated Traction Contacts." In: *Journal of Mechanisms Transmissions and Automation in Design* (1986). DOI: 10.1115/1.3260788.

[52] M. Taniguchi, D. Dowson, and C. M. Taylor. "The effect of spin motion upon elastohydrodynamic elliptical contacts." In: *Elastohydrodynamics - '96 Fundamentals and Applications in Lubrication and Traction, Proceedings of the 23rd Leeds-Lyon Symposium on Tribology held in the Institute of Tribology, Department of Mechanical Engineering* (1997). DOI: 10.1016/s0167-8922(08)70486-3.

[53] A. Porras-Vazquez, N. Fillot, P. Vergne, D. Philippon, and G. E. Morales-Espejel. "Influence of spin on film thickness in elastohydrodynamic starved point contacts." In: *Tribology International* (2020). DOI: 10.1016/j.triboint.2020.106825.

[54] S. Y. Poon. "Some Calculations to Assess the Effect of Spin on the Tractive Capacity of Rolling Contact Drives." In: *Proceedings of the Institution of Mechanical Engineers* (1970). DOI: 10.1243/pime_proc_1970_185_115_02.

[55] Q. Zou, C. Huang, and S. Wen. "Elastohydrodynamic Film Thickness in Elliptical Contacts With Spinning and Rolling." In: *Journal of Tribology* (1999). DOI: 10.1115/1.2834124.

[56] H. A. Spikes and Z. Jie. "History, Origins and Prediction of Elastohydrodynamic Friction." In: *Tribology Letters* (2014). DOI: 10.1007/s11249-014-0396-y.

[57] S. Bair. *High Pressure Rheology for Quantitative Elastohydrodynamics*. Cambridge, MA: Elsevier, 2019. ISBN: 9780444641564. DOI: 10.1016/c2017-0-03927-7.

[58] J. Echávarri Otero, E. de la Guerra Ochoa, E. Chacón Tanarro, and B. del Río López. "Friction coefficient in mixed lubrication: A simplified analytical approach for highly loaded non-conformal contacts." In: *Advances in Mechanical Engineering* (2017). DOI: 10.1177/1687814017706266.

[59] M. Björling. "Friction in Elastohydrodynamic Lubrication." PhD thesis. Luleå University of Technology, 2014. URL: http://urn.kb.se/resolve?urn=urn:nbn:se:ltu:diva-17478.

[60] R. F. Duckworth, G. R. Paul, and A. Cameron. "The Elastic Properties of Films in EHL Contacts." In: *Proceedings of the Royal Society A: Mathematical, Physical and Engineering Sciences* (1980). DOI: 10.1098/rspa.1980.0107.

[61] J. F. Archard. "The temperature of rubbing surfaces." In: *Wear* (1959). DOI: 10.1016/0043-1648(59)90159-0.

[62] L. Martinie and P. Vergne. "Lubrication at Extreme Conditions: A Discussion About the Limiting Shear Stress Concept." In: *Tribology Letters* (2016). DOI: 10.1007/s11249-016-0709-4.

[63] H. A. Spikes. "Mixed lubrication — an overview." In: *Lubrication science* (1997). DOI: 10.1002/ls.3010090302.

[64] H. A. Spikes and A. V. Olver. "Basics of mixed lubrication." In: *Lubrication Science* (2003). DOI: 10.1002/ls.3010160102.

[65] A. Almqvist. "On the Effects of Surface Roughness in Lubrication." PhD thesis. Luleå University of Technology, 2006.

[66] J. Echávarri Otero, E. de la Guerra Ochoa, I. Bellón Vallinot, and E. Chacón Tanarro. "Optimising the design of textured surfaces for reducing lubricated friction coefficient." In: *Lubrication Science* (2016). DOI: 10.1002/ls.1363.

[67] J. Hansen, M. Björling, and R. Larsson. "Lubricant film formation in rough surface non-conformal conjunctions subjected to GPa pressures and high slide-to-roll ratios." In: *Scientific Reports* (2020). DOI: 10.1038/s41598-020-77434-y.

[68] J. Hansen, M. Björling, and R. Larsson. "A New Film Parameter for Rough Surface EHL Contacts with Anisotropic and Isotropic Structures." In: *Tribology Letters* (2021). DOI: 10.1007/s11249-021-01411-3.

[69] T. Zapletal, P. Sperka, I. Krupka, and M. Hartl. "The effect of surface roughness on friction and film thickness in transition from EHL to mixed lubrication." In: *Tribology International* (2018). DOI: 10.1016/j.triboint.2018.07.047.

[70] A. Porras-Vazquez. "Lubricant starvation in elastohydrodynamic large-size spinning contacts." PhD thesis. L'Institut National des Sciences Appliquées de Lyon, 2020.

[71] S. Y. Poon. "An experimental study of the shear traction distribution in rolling with spin." In: *Wear* (1967). DOI: 10.1016/0043-1648(67)90107-x.

[72] H. Dormois. "Frottement dans les contacts EHD de grandes dimensions, role du pivotement." PhD thesis. L'Institut National des Sciences Appliquées de Lyon, 2008.

[73] T. Doki-Thonon. "Thermal effects in elastohydrodynamic spinning circular contacts." PhD thesis. L'Institut National des Sciences Appliquées de Lyon, 2012.

[74] J. D. Wheeler. "Non-Elliptical Point Contacts: the Torus-on-Plane Conjunction." PhD thesis. L'Institut National des Sciences Appliquées de Lyon, 2016.

[75] H. Itagaki. "Method for estimating traction curves under practical operating conditions." In: *Tribology International* (2020). DOI: 10.1016/j.triboint.2019.02.047.

[76] P. Ehret, D. Dowson, and C. M. Taylor. "Thermal Effects in Elliptical Contacts with Spin Conditions." In: *Tribology Series* (1999). DOI: 10.1016/s0167-8922(99)80088-1.

[77] E. Bergseth, Y. Zhu, and A. Söderberg. "Study of Surface Roughness on Friction in Rolling/Sliding Contacts: Ball-on-Disc Versus Twin-Disc." In: *Tribology Letters* (2020). DOI: 10.1007/s11249-020-01310-z.

[78] D. Philippon, L. Martinie, and P. Vergne. "Discussion on "Scale and contact geometry effects on friction in thermal EHL: twin-disc versus ball-on-disc" by Liu, Zhang, Bader, Venner, Poll, Tribology International 154, 106694, 2021." In: *Tribology International* (2021). DOI: 10.1016/j.triboint.2021.106877.

[79] A. M. Plint. "Third paper: traction in elastohydrodynamic contacts." In: *Proceedings of the Institution of Mechanical Engineers* (1967).

[80] J. P. Ewen, H. A. Spikes, and D. Dini. "Contributions of Molecular Dynamics Simulations to Elastohydrodynamic Lubrication." In: *Tribology Letters* (2021). DOI: 10.1007/s11249-021-01399-w.

[81] H. C. Liu and G. Poll. "Reply to the Discussion by Philippon, Martinie, Vergne on "Scale and Contact Geometry Effects in Thermal EHL: Twin-Disc versus Ball-on-Disc" by Liu, Zhang, Bader, Venner and Poll in Tribology International." In: *Tribology International* (2022). DOI: 10.1016/j.triboint.2022.108204.

[82] A. V. Olver and H. A. Spikes. "Prediction of traction in elastohydrodynamic lubrication." In: *Proceedings of the Institution of Mechanical Engineers, Part J: Journal of Engineering Tribology* 212.5 (1998), pp. 321–332. DOI: 10.1243/1350650981542137.

[83] H. C. Liu, B. B. Zhang, N. Bader, C. H. Venner, and G. Poll. "Simplified traction prediction for highly loaded rolling/sliding EHL contacts." In: *Tribology International* (2020). DOI: 10.1016/j.triboint.2020.106335.

[84] N. F. Bader. "Traction in EHL-Contacts - the influence of local fluid rheology and temperatures." PhD thesis. Leibniz Universitaet Hannover, 2018. DOI: https://doi.org/10.15488/4459.

[85] S. Lingard. "Tractions at the spinning point contacts of a variable ratio friction drive." In: *Tribology* (1974). DOI: 10.1016/0041-2678(74)90121-3.

[86] B. Jacod, C. H. Venner, and P. M. Lugt. "A Generalized Traction Curve for EHL Contacts." In: *Journal of Tribology* (2000). DOI: 10.1115/1.1308021.

[87] M. Björling, R. Larsson, P. Marklund, and E. Kassfeldt. "EHL friction mapping : the influence of lubricant, roughness, speed and slide to roll ratio." In: *14th Nordic Symposium on Tribology : NORDTRIB 2010 : Storforsen, Sweden, June 8-11, 2010* (2010).

[88] M. Björling, W. Habchi, S. Bair, R. Larsson, and P. Marklund. "Towards the true prediction of EHL friction." In: *Tribology International* (2013). DOI: 10.1016/j.triboint.2013.04.008.

[89] E. Chacón Tanarro. "Modelización de contactos termoelastohidrodinámicos." PhD thesis. Universidad Politecnica de Madrid, 2012.

[90] J. Newall and A. Lee. "Measurement and prediction of spin losses in the EHL point contacts of the full toroidal variator." In: *Tribology Series* (2003). DOI: 10.1016/s0167-8922(03)80105-0.

[91] O. Reynolds. "On the theory of lubrication and its application to Mr. Beauchamp tower's experiments, including an experimental determination of the viscosity of olive oil." In: *Philosophical Transactions of the Royal Society of London* (1886). DOI: 10.1098/rstl.1886.0005.

[92] P. Sperka, I. Krupka, and M. Hartl. "Lubricant flow in thin-film elastohydrodynamic contact under extreme conditions." In: *Friction* (2016). DOI: 10.1007/s40544-016-0134-6.

[93] P. Sperka, I. Krupka, and M. Hartl. "Analytical Formula for the Ratio of Central to Minimum Film Thickness in a Circular EHL Contact." In: *Lubricants* (2018). DOI: 10.3390/lubricants6030080.

[94] M. Omasta, J. Adam, P. Sperka, I. Krupka, and M. Hartl. "On the Temperature and Lubricant Film Thickness Distribution in EHL Contacts with Arbitrary Entrainment." In: *Lubricants* (2018). DOI: 10.3390/lubricants6040101.

[95] J. P. Chaomleffel, G. Dalmaz, and P. Vergne. "Experimental Results and Analytical Predictions of EHL Film Thickness." In: *33rd Leeds Lyon Symposium on Tribology "Tribology at the Interface"* (2006). URL: https://hal.archives-ouvertes.fr/hal-00141919.

[96] B. J. Hamrock and D. Dowson. "Isothermal Elastohydrodynamic Lubrication of Point Contacts: Part 1—Theoretical Formulation." In: *Journal of Lubrication Technology* (1976). DOI: 10.1115/1.3452801.

[97] R. J. Chittenden, D. Dowson, J. F. Dunn, and C. M. Taylor. "A Theoretical Analysis of the Isothermal Elastohydrodynamic Lubrication of Concentrated Contacts. II. General Case, with Lubricant Entrainment along Either Principal Axis of the Hertzian Contact Ellipse or at Some Intermediate Angle." In: *Proceedings of the Royal Society A: Mathematical, Physical and Engineering Sciences* (1985). DOI: 10.1098/rspa.1985.0015.

[98] G. Nijenbanning, C. H. Venner, and H. Moes. "Film thickness in elastohydrodynamically lubricated elliptic contacts." In: *Wear* (1994). DOI: 10.1016/0043-1648(94)90150-3.

[99] H. Moes. *Lubrication and Beyond*. University of Twente, 2000.

[100] J. D. Wheeler, P. Vergne, N. Fillot, and D. Philippon. "On the relevance of analytical film thickness EHD equations for isothermal point contacts: Qualitative or quantitative predictions?" In: *Friction* (2016). DOI: https://doi.org/10.1007/s40544-016-0133-7.

[101] R. I. Popovici. "Friction in wheel - rail contacts." PhD thesis. University of Twente, 2010. DOI: 10.3990/1.9789036529570.

[102] R. I. Popovici and D. J. Schipper. "Stribeck and traction curves for elliptical contacts: isothermal friction model." In: *International Journal Sustainable Construction & Design* (2014). DOI: 10.21825/scad.v4i2.1042.

[103] G. E. Morales-Espejel and A. W. Wemekamp. "An engineering approach on sliding friction in full-film, heavily loaded lubricated contacts." In: *Proceedings of the Institution of Mechanical Engineers, Part J: Journal of Engineering Tribology* (2004). DOI: 10.1243/1350650042794806.

[104] P. Lafont Morgado, J. Echávarri Otero, J. B. Sánchez-Peñuela Lejarraga, J. L. Muñoz Sanz, A. Díaz Lantada, J. M. Muñoz-Guijosa, H. Lorenzo Yustos, and P. Leal Wiña. "Models for Predicting Friction Coefficient and Parameters with Influence in Elastohydrodynamic Lubrication." In: *Advanced Tribology* (2009). DOI: 10.1007/978-3-642-03653-8_48.

[105] A. Arana, J. Larrañaga, and I. Ulacia. "Partial EHL friction coefficient model to predict power losses in cylindrical gears." In: *Proceedings of the Institution of Mechanical Engineers, Part J: Journal of Engineering Tribology* (2018). DOI: 10.1177/1350650118778655.

[106] J. L. Tevaarwerk and K. L. Johnson. "The Influence of Fluid Rheology on the Performance of Traction Drives." In: *Journal of Lubrication Technology* (1979). DOI: 10.1115/1.3453346.

[107] J. L. Tevaarwerk. "Traction calculations using the shear plane hypothesis." In: *Proc. Of Leeds-Lyon Symposium on Tribology* (1979).

[108] J. L. Tevaarwerk. "A Simple Thermal Correction for Large Spin Traction Curves." In: *Journal of Mechanical Design* (1981). DOI: 10.1115/1.3254936.

[109] S. Aihara, S. Natsumeda, and H. Achiha. "EHL Traction in Traction Drives with high contact pressure." In: *Elastohydrodynamics - '96 Fundamentals and Applications in Lubrication and Traction, Proceedings of the 23rd Leeds-Lyon Symposium on Tribology held in the Institute of Tribology, Department of Mechanical Engineering* (1997). DOI: 10.1016/s0167-8922(08)70485-1.

[110] M. Delkhosh, M. S. Foumani, M. Boroushaki, M. Ekhtiari, and M. Dehghani. "Geometrical optimization of half toroidal continuously variable transmission using particle swarm optimization." In: *Scientia Iranica* (2011). DOI: 10.1016/j.scient.2011.08.005.

[111] F. Verbelen, S. Derammelaere, P. Sergeant, and K. Stockman. "Half toroidal continuously variable transmission: Trade-off between dynamics of ratio variation and efficiency." In: *Mechanism and Machine Theory* (2017). DOI: 10.1016/j.mechmachtheory.2016.09.013.

[112] Q. Li, L. Liang, C. Li, R. Li, C. Yan, and S. Liu. "Characteristic Investigation and Torque Distribution Diagram-Based Computational Method for Continuously Variable Power-Split Transmission." In: *Mathematical Problems in Engineering* (2022). DOI: 10.1155/2022/6136766.

[113] T. Doki-Thonon, N. Fillot, P. Vergne, and G. E. Morales Espejel. "Numerical insight into heat transfer and power losses in spinning EHD non-Newtonian point contacts." In: *Proceedings of the Institution of Mechanical Engineers, Part J: Journal of Engineering Tribology* (2011). DOI: 10.1177/1350650111419567.

[114] M. Tanaka, T. Saito, and K. Miyamoto. "Prediction of Power Transmission Efficiency for Two-Mode Half-Toroidal IVT." In: *SAE Technical Paper Series* (2018). DOI: 10.4271/2018-01-1060.

[115] T. Saito, Y. Tamoto, and E. Inoue. "Prediction Methodology for Traction Drive Characteristics of Half-Toroidal Variator System." In: *Volume 9: 13th ASME/IEEE International Conference on Mechatronic and Embedded Systems and Applications* (2017). DOI: 10.1115/detc2017-67515.

[116] T. Saito and A. Lewis. "Development of Traction Fluid Property Tables for a Toroidal CVT Multi-Body Simulation." In: *SAE Technical Paper Series* (2018). DOI: 10.4271/2018-01-1061.

[117] P. Walker, J. Durack, and M. Durack. "Laboratory testing of a new form of toroidal CVT." In: *FISITA* (2014).

[118] C. Meyer. "Reibung in hoch belasteten EHD-Wälzkontakten." PhD thesis. Leibniz Universitaet Hannover, 2010. DOI: 10.15488/7473.

[119] A. Arana. "Thermal Distortion Effects on Cylindrical Gear Teeth Contact." PhD thesis. Mondragon Unibertsitatea, Faculty Of Engineering, 2019.

[120] A. V. Olver. "Testing Transmission Lubricants: The Importance of Thermal Response." In: *Proceedings of the Institution of Mechanical Engineers, Part G: Journal of Aerospace Engineering* (1991). DOI: 10.1243/pime_proc_1991_205_235_02.

[121] V. L. Popov. *Contact Mechanics and Friction*. Springer-Verlag GmbH, 2010.

[122] F. Chevalier. "Modélisation des conditions d'alimentation dans les contacts élastohydrodynamiques ponctuels." PhD thesis. Ecole Doctorale Mecanique, Energetique, Genie Civil, Acoustique (MEGA) (Villeurbanne), 1996.

[123] Q. J. Wang. "Conformal-Contact Elements and Systems." In: *Encyclopedia of Tribology* (2013). DOI: 10.1007/978-0-387-92897-5_22.

[124] Q. J. Wang and D. Zhu. *Interfacial Mechanics: Theories and Methods for Contact and Lubrication*. CRC Press, 2019. DOI: https://doi.org/10.1201/9780429131011.

[125] K. L. Johnson. *Contact Mechanics*. Cambridge University Press, 1985. DOI: 10.1017/cbo9781139171731.

[126] G. Stachowiak and A. W. Batchelor. *Engineering Tribology*. Elsevier S&T, 2011.

[127] A. Porras-Vazquez, D. Philippon, N. Fillot, P. Vergne, N. Devaux, L. Lafarge, and G. E. Morales-Espejel. "An Experimental Approach to Evaluate Film Thickness in Starved Large-Size Spinning Contacts." In: *Journal of Tribology* (2022). DOI: 10.1115/1.4054863.

[128] K. L. Johnson. "Regimes of Elastohydrodynamic Lubrication." In: *Journal of Mechanical Engineering Science* (1970). DOI: 10.1243/jmes_jour_1970_012_004_02.

[129] K. L. Johnson and A. D. Roberts. "Observations of viscoelastic behaviour of an elastohydrodynamic lubricant film." In: *Proceedings of the Royal Society of London. A. Mathematical and Physical Sciences* (1974). DOI: 10.1098/rspa.1974.0046.

[130] H. van Leeuwen. "The determination of the pressure-viscosity coefficient of two traction oils using film thickness measurements." In: *Faseb Journal - FASEB J* (2010).

[131] W. Habchi, P. Vergne, S. Bair, O. Andersson, D. Eyheramendy, and G. E. Morales-Espejel. "Influence of pressure and temperature dependence of thermal properties of a lubricant on the behaviour of circular TEHD contacts." In: *Tribology International* (2010). DOI: 10.1016/j.triboint.2009.10.002.

[132] J. A. Greenwood and J. J. Kauzlarich. "Inlet Shear Heating in Elastohydrodynamic Lubrication." In: *Journal of Lubrication Technology* (1973). DOI: 10.1115/1.3451844.

[133] H. Liu, L. Han, and Y. Cao. "Improving transmission efficiency and reducing energy consumption with automotive continuously variable transmission: A model prediction comprehensive optimization approach." In: *Applied Energy* (2020). DOI: 10.1016/j.apenergy.2020.115303.

[134] P. Jiang, X. M. Li, F. Guo, and J. Chen. "Interferometry Measurement of Spin Effect on Sliding EHL." In: *Tribology Letters* (2008). DOI: 10.1007/s11249-008-9399-x.

[135] X. M. Li, F. Guo, B. Fan, and P. Yang. "Influence of spinning on the rolling EHL films." In: *Tribology International* (2010). DOI: 10.1016/j.triboint.2010.05.005.

[136] C. Barus. "Isothermals, isopiestics and isometrics relative to viscosity." In: *American Journal of Science* (1893). DOI: 10.2475/ajs.s3-45.266.87.

[137] C. J. A. Roelands, J. C. Vlugter, and H. I. Waterman. "The Viscosity-Temperature-Pressure Relationship of Lubricating Oils and Its Correlation With Chemical Constitution." In: *Journal of Basic Engineering* (1963). DOI: 10.1115/1.3656919.

[138] P. Vergne and S. Bair. "Classical EHL Versus Quantitative EHL: A Perspective Part I—Real Viscosity-Pressure Dependence and the Viscosity-Pressure Coefficient for Predicting Film Thickness." In: *Tribology Letters* (2014). DOI: 10.1007/s11249-014-0302-7.

[139] S. Bair, C. Mary, N. Bouscharain, and P. Vergne. "An improved Yasutomi correlation for viscosity at high pressure." In: *Proceedings of the Institution of Mechanical Engineers, Part J: Journal of Engineering Tribology* (2013). DOI: 10.1177/1350650112474394.

[140] K. J. Sharif, H. P. Evans, R. W. Snidle, and J. P. Newall. "Modeling of Film Thickness and Traction in a Variable Ratio Traction Drive Rig." In: *Journal of Tribology* (2004). DOI: 10.1115/1.1609490.

[141] S. Bair. "The high pressure rheology of some simple model hydrocarbons." In: *Proceedings of the Institution of Mechanical Engineers, Part J: Journal of Engineering Tribology* (2002). DOI: 10.1243/1350650021543960.

[142] S. Bair and W. O. Winer. "The Pressure-Viscosity Coefficient at Hertz Pressure And Its Relation To Concentrated Contact Traction." In: *Thinning Films and Tribological Interfaces, Proceedings of the 26th Leeds-Lyon Symposium on Tribology* (2000). DOI: 10.1016/s0167-8922(00)80148-0.

[143] S. Bair. "The unresolved definition of the pressure-viscosity coefficient." In: *Scientific Reports* (2022). DOI: 10.1038/s41598-022-07470-3.

[144] H. van Leeuwen. "The determination of the pressure—viscosity coefficient of a lubricant through an accurate film thickness formula and accurate film thickness measurements." In: *Proceedings of the Institution of Mechanical Engineers, Part J: Journal of Engineering Tribology* (2009). DOI: 10.1243/13506501jet504.

[145] H. van Leeuwen. "The determination of the pressure–viscosity coefficient of a lubricant through an accurate film thickness formula and accurate film thickness measurements. Part 2: high L values." In: *Proceedings of the Institution of Mechanical Engineers, Part J: Journal of Engineering Tribology* (2011). DOI: 10.1177/1350650111398405.

[146] H. C. Liu, B. B. Zhang, V. Schneider, C. H. Venner, and G. Poll. "Two-dimensional generalized non-Newtonian EHL lubrication: Shear rate-based solution versus shear stress-based solution." In: *Proceedings of the Institution of Mechanical Engineers, Part J: Journal of Engineering Tribology* (2021). DOI: 10.1177/13506501211050484.

[147] P. J. Carreau. "Rheological Equations from Molecular Network Theories." In: *Transactions of the Society of Rheology* (1972). DOI: 10.1122/1.549276.

[148] S. Bair, P. Vergne, P. Kumar, G. Poll, I. Krupka, M. Hartl, W. Habchi, and R. Larsson. "Comment on "History, Origins and Prediction of Elastohydrodynamic Friction" by Spikes and Jie." In: *Tribology Letters* (2015). DOI: 10.1007/s11249-015-0481-x.

[149] S. Bair. "The rheological assumptions of classical EHL: What went wrong?" In: *Tribology International* (2019). DOI: 10.1016/j.triboint.2018.10.020.

[150] S. Bair, C. McCabe, and P. T. Cummings. "Calculation of Viscous EHL Traction for Squalane Using Molecular Simulation and Rheometry." In: *Tribology Letters* (2002). DOI: 10.1023/a:1021011225316.

[151] S.-N. Ndiaye, L. Martinie, D. Philippon, N. Devaux, and P. Vergne. "A Quantitative Friction-Based Approach of the Limiting Shear Stress Pressure and Temperature Dependence." In: *Tribology Letters* (2017). DOI: 10.1007/s11249-017-0929-2.

[152] S. Bair and W. O. Winer. "Shear Strength Measurements of Lubricants at High Pressure." In: *Journal of Lubrication Technology* (1979). DOI: 10.1115/1.3453339.

[153] B. Jacobson. "A High Pressure-Short Time Shear Strength Analyzer for Lubricants." In: *Journal of Tribology* (1985). DOI: 10.1115/1.3261024.

[154] E. Hoglund and B. Jacobson. "Experimental Investigation of the Shear Strength of Lubricants Subjected to High Pressure and Temperature." In: *Journal of Tribology* (1986). DOI: 10.1115/1.3261267.

[155] C. R. Evans and K. L. Johnson. "The Rheological Properties of Elastohydrodynamic Lubricants." In: *Proceedings of the Institution of Mechanical Engineers, Part C: Journal of Mechanical Engineering Science* (1986). DOI: 10.1243/pime_proc_1986_200_134_02.

[156] K. T. Ramesh. "On the Rheology of a Traction Fluid." In: *Journal of Tribology* (1989). DOI: 10.1115/1.3261985.

[157] M. F. Workel, D. Dowson, P. Ehret, and C. M. Taylor. "The influence of mean contact pressure on the friction coefficient of a traction fluid at high pressure." In: *Proceedings of the Institution of Mechanical Engineers, Part C: Journal of Mechanical Engineering Science* (2000). DOI: 10.1243/0954406001522976.

[158] M. F. Workel, D. Dowson, P. Ehret, and C. M. Taylor. "Measurements of the coefficients of friction of different lubricants during impact under high pressure and shear." In: *Proceedings of the Institution of Mechanical Engineers, Part J: Journal of Engineering Tribology* (2003). DOI: 10.1243/13506500360603543.

[159] J. P. Ewen, D. M. Heyes, and D. Dini. "Advances in nonequilibrium molecular dynamics simulations of lubricants and additives." In: *Friction* (2018). DOI: 10.1007/s40544-018-0207-9.

[160] P. an Yang. "Thermal Effect on EHL." In: *Encyclopedia of Tribology* (2013). DOI: 10.1007/978-0-387-92897-5_648.

[161] E. Chacon-Tanarro. "Modelización de contactos termoelastohidrodinamicos." PhD thesis. Universidad Politécnica de Madrid, 2012.

[162] R. Larsson and O. Andersson. "Lubricant thermal conductivity and heat capacity under high pressure." In: *Proceedings of the Institution of Mechanical Engineers, Part J: Journal of Engineering Tribology* (2000). DOI: 10.1243/1350650001543223.

[163] Q. Liu. "Friction in Mixed and Elastohydrodynamic Lubricated Contacts Including Thermal Effects." PhD thesis. University of Twente, 2002.

[164] H. S. Carslaw and J. C. Jaeger. *Conduction of heat in solids*. Oxford University Press, 1959.

[165] Y-C. Liu, H. Wang, W-Z. Wang, Y-Z. Hu, and D. Zhu. "Methods comparison in computation of temperature rise on frictional interfaces." In: *Tribology International* (2002). DOI: 10.1016/s0301-679x(02)00062-2.

[166] X. Tian and F. E. Kennedy. "Maximum and Average Flash Temperatures in Sliding Contacts." In: *Journal of Tribology* (1994). DOI: 10.1115/1.2927035.

[167] J. Bos. "Frictional heating of tribological contacts." PhD thesis. University of Twente, 1995. DOI: 10.3990/1.9789090089201.

[168] J. Bos and H. Moes. "Frictional Heating of Tribological Contacts." In: *Journal of Tribology* (1995). DOI: 10.1115/1.2830596.

[169] W. Habchi and S. Bair. "The role of the thermal conductivity of steel in quantitative elastohydrodynamic friction." In: *Tribology International* (2020). DOI: 10.1016/j.triboint.2019.105970.

[170] T. Reddyhoff, A. Schmidt, and H. Spikes. "Thermal Conductivity and Flash Temperature." In: *Tribology Letters* (2019). DOI: 10.1007/s11249-018-1133-8.

[171] J. Lu, T. Reddyhoff, and D. Dini. "A study of thermal effects in EHL rheology and friction using infrared microscopy." In: *Tribology International* (2020). DOI: 10.1016/j.triboint.2020.106179.

[172] H. C. Liu, B. B. Zhang, N. Bader, G. Poll, and C. H. Venner. "Influences of solid and lubricant thermal conductivity on traction in an EHL circular contact." In: *Tribology International* (2020). DOI: 10.1016/j.triboint.2019.106059.

[173] C. D. Tipton, F. Qureshi, and M. E. Huston. "Automotive Traction Fluids: A Shift in Direction for Transmission Fluid Technology." In: *SAE Technical Paper Series* (2000). DOI: 10.4271/2000-01-2906.

[174] J. Lu, Q. J. Wang, N. Ren, and F. E. Lockwood. "Correlation between pressure-viscosity coefficient and traction coefficient of the base stocks in traction lubricants: A molecular dynamic approach." In: *Tribology International* (2019). DOI: 10.1016/j.triboint.2019.02.013.

[175] L. D. Wedeven, G. G. Wedeven, S. H. Kratz, T. E. King, J. L. Linden, F. Caracciolo, and D. G. Mcwatt. "USCAR Traction Test Methodology for Traction-CVT Fluids." In: *SAE Technical Paper Series* (2002). DOI: 10.4271/2002-01-2820.

[176] W. Habchi and S. Bair. "Effect of lubricant rheology on friction in coated elastohydrodynamic lubricated contacts." In: *Proceedings of the Institution of Mechanical Engineers, Part J: Journal of Engineering Tribology* (2016). DOI: 10.1177/1350650116684657.

[177] S. Bair and M. Kotzalas. "The Contribution of Roller Compliance to Elastohydrodynamic Traction." In: *Tribology Transactions* (2006). DOI: 10.1080/05698190600614817.

[178] H. Dormois, N. Fillot, P. Vergne, G. Dalmaz, M. Querry, E. Ioannides, and G. E. Morales-Espejel. "First Traction Results of High Spinning Large-Size Circular EHD Contacts from a New Test Rig: Tribogyr." In: *Tribology Transactions* (2009). DOI: 10.1080/10402000802105448.

[179] C. Bell and R. Glovnea. "Tribological optimization of a toroidal-type continuously variable transmission." In: *Proceedings of the Institution of Mechanical Engineers, Part J: Journal of Engineering Tribology* (2011). DOI: 10.1177/2041305x10394054.

[180] M. Nakano, T. Hibi, and K. Kobayashi. "Dual-Cavity Half Toroidal CVT for Passenger Cars." In: *SAE Technical Paper Series* (1992). DOI: 10.4271/922105.

[181] A. P. Lee, J. Newall, Y. Ono, and T. Hoshino. "Developing the Durability of a Dual-Cavity Full-Toroidal IVT Variator." In: *SAE Technical Paper Series* (2002). DOI: 10.4271/2002-01-0587.

[182] C. Fernandes, P. Marques, R. Martins, and J. Seabra. "Gearbox power loss. Part II: Friction losses in gears." In: *Tribology International* (2015). DOI: 10.1016/j.triboint.2014.12.004.

[183] C. Fernandes, P. Marques, R. Martins, and J. Seabra. "Gearbox power loss. Part I: Losses in rolling bearings." In: *Tribology International* (2015). DOI: 10.1016/j.triboint.2014.11.017.

[184] M. M. Khonsari and E. R. Booser. *Applied Tribology: Bearing Design and Lubrication*. John Wiley & Sons, Ltd, 2017. DOI: 10.1002/9781118700280.

[185] SKF. *Rolling bearings*. Catalogue. 2018.

[186] R. J. Boness. "Churning losses of discs and gears running partially submerged in oil." In: *Proceedings of the ASME International Power Transmission and Gearing Conference* (1989).

[187] H. Linke, J. Börner, and R. Heß. *Cylindrical Gears*. Carl Hanser Verlag GmbH & Co. KG, 2016. DOI: 10.3139/9781569904909.